



## Photochemistry and Photocatalysis of Alcohols on Bare and Metal Cluster-Loaded TiO<sub>2</sub>(110)

Moritz Maximilian Joachim Eder

Vollständiger Abdruck der von der Fakultät für Chemie der Technischen Universität  
München zur Erlangung des akademischen Grades eines

**Doktors der Naturwissenschaften**

genehmigten Dissertation.

**Vorsitzender:**

Prof. Dr. Klaus Köhler

**Prüfende der Dissertation:**

1. Prof. Dr. Ulrich K. Heiz
2. Hon.-Prof. Dr. Richard W. Fischer
3. Prof. Gareth S. Parkinson, Ph.D.,  
Technische Universität Wien

Die Dissertation wurde am 19.11.2021 bei der Technischen Universität München  
eingereicht und durch die Fakultät für Chemie am 11.01.2022 angenommen.



*„...verzeihen Sie, dass ich so furchtbar gescheit daherrede, aber wenn man an der Universität ist, kommt einem eine Menge vertrottelter Bücher unter die Hände; unwillkürlich verfällt man dann in eine deppenhafte Ausdrucksweise.“*

- Gustav Meyrink, *Der Golem*





# Danksagung

Ich danke meinem Chef, dem Exilschweizer Ueli Heiz, für die herzliche Aufnahme in sein Team, für sein bodenständiges Vertrauen und die große Freiheit, die wir beim Arbeiten stets genießen durften.

Ich danke meinem Betreuer, dem Exilösterreicher Martin Tschurl, der seine geliebte Heimat weit hinter sich ließ, um uns seine weise Führung durch die Klippen des Promotionswerdegangs zuteil werden zu lassen, für seine Aufopferungsbereitschaft und für den großen Spaß, den ich bei unserer humorvollen Zusammenarbeit habe.

Ich danke meiner Weggefährtin, der Exilluxemburgerin Carla Courtois, für die großartige gemeinsame Zeit im immerwährenden Kampf gegen die Nanokat und den Rest der Welt.

Ich danke meiner Schwester im heterogenkatalytischen Geiste, der Exilchwäbin Clara Aletsee.

Ich danke unseren Nanokat-Labornachbarn und Erzfeinden, dem Exilluxemburger Kevin Bertrang, dem Exilrosenheimer Tobias Hinke und dem Exilniederbayern Max Krause, für ihren unermesslichen Beitrag zum schönsten Arbeitsplatz der ganzen Chemiefakultät.

Ich danke meinem Lohhofer Stammesgenossen und Mentor Constantin Walenta sowie seiner besseren Hälfte Sebastian Kollmannsberger, die mich auf den rechten Weg der physikalischen Chemie geleitet haben, und ohne die der Fluoreszenzversuch im fünften Semester nicht möglich gewesen wäre.

Ich danke Philip Petzoldt und Sonia Mackewicz, um deren lange Begleitung während meiner Promotion ich sehr froh bin, und durch deren Nachfolge ich das Projekt in besten Händen weiß.

Ich danke meinen Kollegen am Lehrstuhl, die zu einer großartigen Atmosphäre beigetragen haben, die ich in anderen Gruppen so nicht erlebt habe.

Ich danke unseren Studenten in der Photokat. Kordula Schnabl, Carina Schramm, Laura Fuchs, Mirza Grebo, Natalie Rosen, Viktoria Brandt, Marko Medugorac, Lucia Mengel und Matías Wegner haben meinen Arbeitsalltag enorm bereichert.

I want to thank Ulrike Diebold and Gareth Parkinson for letting me be a part of their scientific family in Vienna, and for giving me the invaluable opportunity of working with them.

Ich danke meiner Familie und meinen Freunden, besonders meinen Eltern, für ihre unschätzbare Unterstützung.



# Abstract

Photocatalysis has emerged as a large research field during the last decades, but even on much investigated systems like titania, a molecular understanding of the surface chemistry and the role of the co-catalyst is still lacking. To acquire a better understanding, the photochemical and photocatalytic reactivity of alcohols was studied on bare and Ni or Pt cluster-loaded rutile  $\text{TiO}_2(110)$  under well-defined conditions in ultra high vacuum. The photochemistry of tertiary alcohols was investigated on bare and Pt-loaded titania. Both proved to be suitable catalysts for the selective photoconversion of the substrates. It was shown that the photochemical pathway is determined by the semiconductor, and is therefore analogous to that of primary and secondary alcohols. Pt as co-catalyst induces an additional thermal desorption pathway facilitating  $\text{H}_2$  evolution. Notably, tertiary alcohols can be photoconverted without  $\text{H}_2$  formation on the bare surface in a truly catalytic way, which is not the case for primary and secondary alcohols.

Furthermore, catalyst deactivation was investigated for the photoconversion of methanol on bare titania. When photooxidizing primary alcohols on bare  $\text{TiO}_2(110)$ , a rapid decline in photocatalytic activity is commonly observed. A deactivation mechanism under constant illumination was proposed in the scope of this work. The loss in photoactivity was ascribed to the fact that hydrogen cannot desorb from the  $\text{TiO}_2(110)$  surface at room temperature in the absence of a co-catalyst. Since the photoconversion of alcohol surface species yields surface hydrogen species and is thermally reversible, hydrogen accumulation shifts the reaction equilibrium to the reactant site.

For the first time, Ni clusters were used as co-catalysts for methanol photocatalysis on  $\text{TiO}_2(110)$ , where they showed the same reactivity as Pt clusters in methanol photoreforming. A truly catalytic photoconversion of the alcohol is enabled by hydrogen recombination and desorption at the metal co-catalyst. Contrary to Pt, the Ni-loaded photocatalyst deactivates over time due to the formation of surface carbon species under illumination. The activity can be partially restored by thermal treatment.

The findings of this work extend the mechanistic understanding of surface processes in photocatalysis and the role of the co-catalysts, contributing to a rational design of tailored photocatalysts.



# Zusammenfassung

Die Photokatalyse hat sich während der letzten Jahrzehnte zu einem großen Forschungsfeld entwickelt. Dennoch fehlt sogar auf ausgiebig untersuchten Systemen wie Titanoxid ein molekulares Verständnis der Oberflächenchemie und der Rolle des Co-Katalysators. Um ein besseres Verständnis zu bekommen, wurde die photochemische und photokatalytische Reaktivität von Alkoholen auf reinem sowie mit Pt- oder Ni-Clusterbeladenem Rutil  $\text{TiO}_2(110)$  unter sehr definierten Bedingungen im Ultrahochvakuum untersucht. Die Photochemie tertiärer Alkohole wurde auf reinem und Pt-beladenem Titanoxid untersucht. Beide Systeme erwiesen sich als geeignete Katalysatoren für die selektive Umsetzung der Edukte. Es wurde gezeigt, dass der photochemische Reaktionsweg durch den Halbleiter bestimmt wird und daher analog zu dem primärer und sekundärer Alkohole verläuft. Pt als Co-Katalysator ermöglicht einen zusätzlichen thermischen Desorptionsweg, welcher  $\text{H}_2$ -Entwicklung ermöglicht. Tatsächlich können tertiäre Alkohole auf der reinen Oberfläche echt katalytisch photochemisch umgesetzt werden ohne  $\text{H}_2$  zu bilden, was bei primären und sekundären Alkoholen nicht der Fall ist.

Zudem wurde die Katalysatordeaktivierung bei der Photoumsetzung von Methanol auf Titanoxid untersucht. Bei der Photooxidation primärer Alkohole auf reinem  $\text{TiO}_2(110)$  wird allgemein eine rasche Abnahme der photokatalytischen Aktivität beobachtet. Ein Deaktivierungsmechanismus unter konstanter Beleuchtung wurde im Rahmen dieser Arbeit vorgeschlagen. Der Verlust an Photoaktivität wurde auf die Tatsache zurückgeführt, dass Wasserstoff bei Raumtemperatur nicht von der  $\text{TiO}_2(110)$ -Oberfläche desorbieren kann, wenn kein Co-Katalysator vorhanden ist. Da die Photoumsetzung alkoholischer Oberflächenspezies Wasserstoff-Oberflächenspezies bildet und thermisch reversibel ist, verschiebt die Akkumulation von Wasserstoff das Reaktionsgleichgewicht auf die Seite der Edukte.

Zum ersten Mal wurden Ni-Cluster als Co-Katalysatoren für die Methanol-Photokatalyse auf  $\text{TiO}_2(110)$  verwendet, wo sie dieselbe Reaktivität wie Pt in der Methanol-Photoreformierung zeigten. Eine echt katalytische Photoumsetzung des Alkohols wird durch Wasserstoffrekombination und -desorption am Metall-Co-Katalysator ermöglicht. Im Gegensatz zu Pt deaktiviert der Ni-beladene Photokatalysator im Laufe der Zeit aufgrund der Bildung von Kohlenstoffspezies auf der Oberfläche. Die Aktivität kann zum Teil durch Hitzebehandlung wiederhergestellt werden.

Die Ergebnisse dieser Arbeit erweitern das mechanistische Verständnis von Oberflächenprozessen in der Photokatalyse und von der Rolle des Co-Katalysators, womit sie zu einem verständigen Design maßgeschneiderter Photokatalysatoren beitragen.



# Contents

<b>Danksagung</b>	<b>v</b>
<b>Abstract</b>	<b>vii</b>
<b>Zusammenfassung</b>	<b>ix</b>
<b>Contents</b>	<b>xi</b>
<b>1 Introduction</b>	<b>1</b>
<b>2 Scientific Literature on Titanium Dioxide Photocatalysis</b>	<b>3</b>
2.1 General Remarks . . . . .	3
2.2 Fundamentals of Semiconductor Photocatalysis . . . . .	5
2.3 Alcohols on Bare TiO <sub>2</sub> (110) . . . . .	7
2.3.1 Methanol Photochemistry on Bare TiO <sub>2</sub> (110) . . . . .	9
2.3.2 The Photochemistry of Secondary Alcohols on Bare TiO <sub>2</sub> (110) . . . . .	11
2.3.3 The Photochemistry of Tertiary Alcohols on Bare TiO <sub>2</sub> (110) . . . . .	11
2.4 The Photochemically Active Site . . . . .	12
2.5 Alcohol Photochemistry on Metal-Loaded TiO <sub>2</sub> (110) . . . . .	14
<b>3 Experimental Methods</b>	<b>17</b>
3.1 Cluster Source . . . . .	17
3.2 Analysis and Reaction Main Chamber . . . . .	18
3.3 Laser System for Photocatalytic Studies . . . . .	19
3.4 Sample Preparation . . . . .	19
3.5 Temperature Programmed Desorption . . . . .	20
3.6 Photocatalytic Measurements and Photon-Stimulated Desorption . . . . .	21
<b>4 Results - Publication Summaries</b>	<b>23</b>
4.1 Reactions in the Photocatalytic Conversion of Tertiary Alcohols on Rutile TiO <sub>2</sub> (110) . . . . .	24
4.2 Origin of Poisoning in Methanol Photoreforming on TiO <sub>2</sub> (110): The Importance of Thermal Back-Reaction Steps in Photocatalysis . . . . .	58
4.3 Nickel clusters on TiO <sub>2</sub> (110): thermal chemistry and photocatalytic hydrogen evolution of methanol . . . . .	75
<b>List of Figures</b>	<b>93</b>

*CONTENTS*

<b>5 Bibliographic Details</b>	<b>95</b>
5.1 Reactions in the Photocatalytic Conversion of Tertiary Alcohols on Rutile TiO <sub>2</sub> (110) . . . . .	95
5.2 Origin of Poisoning in Methanol Photoreforming on TiO <sub>2</sub> (110): The Importance of Thermal Back-Reaction Steps in Photocatalysis . . . . .	96
5.3 Nickel clusters on TiO <sub>2</sub> (110): thermal chemistry and photocatalytic hydrogen evolution of methanol . . . . .	97
<b>6 Conclusion &amp; Outlook</b>	<b>99</b>
<b>Bibliography</b>	<b>103</b>
<b>A Further Publications</b>	<b>119</b>
<b>B Contributions to the Publications</b>	<b>157</b>
<b>C Reprint Permissions</b>	<b>159</b>
<b>D Prepared Manuscripts</b>	<b>165</b>



# 1 Introduction

The energy transported as sunlight to the earth's surface is hardly utilized anywhere near its full potential by mankind, even though its total amount of energy exceeds the demands of modern civilization by orders of magnitude.[1, 2] In fact, solar collectors for generating thermal and electrical energy are the only wide-spread commercial technology used to harvest a small fraction of this tremendous energy supply. In the chemical industry, light energy is hardly used for processes on a large scale, which is surprising for several reasons. First, utilizing sunlight for converting abundant molecules into valuable substances is long-known by the name of photosynthesis, with the natural process occurring in plants as a role model reaction. Second, the continuing reliance on fossile feedstocks as fuel for combustion engines is irresponsible not only from an ecological but also from an economical point of view, since these feedstocks are a starting point for modern functional materials. While there are many technologically advanced alternatives for fuels (e.g. Li ion batteries, hydrogen, or materials derived from biomass), there are hardly any alternatives for these synthetic building blocks.[3] Third, the industrial processes which modern society relies on are extremely energy-intensive. For example, the Haber-Bosch-Process, which is an essential technology for worldwide food supply, consumes more than 1% of the world's daily energetic demand.[4] For these reasons, utilizing more energy from sunlight seems not only advisable but virtually imperative. In this regard, heterogeneous photocatalysis is a potential key methodology. For example, photocatalytic CO<sub>2</sub> reduction to synthesize small organic molecules,[5] water splitting for hydrogen evolution,[6] or decomposition of toxic organic compounds in water[7, 8] have been shown to be well feasible. The upscaling of these bench-scale processes would certainly help in tackling the problems listed above. However, a major drawback is the low efficiency of photocatalysts developed so far, independent of the reaction they have been designed for.[9] Their improvement is therefore strictly necessary for applicability, and potentially very rewarding given the possibilities. Hydrogen evolution by photo(electro)catalytic methods would be an economically competitive technology if the catalytic efficiency was sufficiently high. By reaching solar-to-hydrogen ratios of at least 5% to 15% (depending on the process and catalyst design), the prices for photocatalytically generated hydrogen would be as low as 1.60\$ to 4.10\$ per kg H<sub>2</sub> and thus cost-competitive with fossil-based fuels.[10]

One of the most promising photocatalyst materials is rutile TiO<sub>2</sub> due to its low cost, abundance, stability, and non-toxicity. However, the band gap of titania lies in the UV range and is therefore not suitable for the utilization of sunlight, which contains only a small portion of UV irradiation.[11] Nevertheless, TiO<sub>2</sub> is a prominent model system due to the aforementioned advantages and well-suited for investigating photocatalytic principles. It has been thoroughly investigated in the last decades, and it can be em-

## 1 Introduction

ployed for a number of photocatalytic reactions. Among them, the photoreforming of alcohols is of particular interest. Not only are alcohols hydrogen carriers and precursors for biomass; they also provide a rich chemistry due to a variety of different bonds, and their oxidation products are of considerable chemical and economical value as synthetic building blocks.[12]

The optimization of the photocatalytic performance of titania, most often as rutile or anatase powder, is usually conducted by screening different co-catalyst materials in a reaction of choice. This approach is problematic from two points of view. On the one hand, most studies lack the normalization of their results to certain parameters or descriptors, making literature results difficult to compare.[13] On the other hand, the heterogeneity of the titania powder particles and their surfaces impede the elucidation of structure-performance relationships, which are crucial for the optimization of photocatalysts.

In this respect, the surface science approach offers an alternative for the mentioned problems. By conducting photochemical reactions on model systems in ultra high vacuum (UHV) on atomically defined semiconductor single crystal surfaces, the comparability of results as well as the possibility of elucidating chemical surface mechanisms and the impact of certain physical parameters is given.[14, 15] Importantly, the co-catalyst, which usually comprises metal(oxide) nanoparticles or clusters, can be investigated more thoroughly as well. This approach towards fundamental understanding of photocatalytic processes therefore allows to construct a holistic picture of the investigated reaction.

In this dissertation, the photocatalytic oxidation of alcohols on Pt and Ni cluster-loaded rutile  $\text{TiO}_2(110)$  is studied. The photoreactivity of tertiary alcohols is investigated on bare and Pt-loaded  $\text{TiO}_2(110)$ . The observations are mechanistically explained and compared to primary and secondary alcohols. Additionally, the deactivation of the photocatalyst by primary alcohols in the absence of co-catalysts is elucidated. An alternative explanation to those found in the literature is provided based on the results. Furthermore, Ni clusters are examined as co-catalyst for hydrogen evolution and possible alternative to Pt. Their suitability as co-catalyst material for photocatalytic hydrogen evolution by methanol photoreforming is demonstrated and the differences between Ni and Pt as co-catalyst material are discussed.

## 2 Scientific Literature on Titanium Dioxide Photocatalysis

This chapter gives an overview on titania photocatalysis, especially with respect to its crystalline (110) facet and its reactivity towards alcohols. The aim is to summarize the key results from the vast amount of publications on the topic, in order to put the findings of this thesis into context.

### 2.1 General Remarks

The first internationally published experiments using titanium dioxide as photocatalyst date back to the middle of the 20th century.[16] However, only when Fujishima and Honda presented their findings on photoelectrochemical water splitting using a titania electrode, the topic gained considerable momentum.[17] During the following decades, numerous papers on titania-based photocatalysis and water splitting have been published by scientists from different fields, such as semiconductor and surface physics, chemical kinetics, inorganic synthesis or chemical engineering.[18] Apart from different focuses of the studies, this has also caused some inconsistencies in terminology and methodology, which has been criticized by some authors as it complicates the comparison of results in the literature.[19, 20, 13]

Titania has three crystalline modifications, two of which - anatase and rutile - are commonly investigated for photocatalytic applications. In this regard, they differ in the size of their band gap, which amounts to 3.2 eV for anatase and 3.0 eV for rutile, corresponding to an excitation wavelength of 413 nm and 387 nm, respectively.[11] Rutile is the thermodynamically most stable modification. Many ways of preparing various titania photocatalysts have been introduced, and due to the complexity of the chemical systems, different interpretations and reaction mechanisms have been proposed (a summary can be found e.g. in a review by Bahnemann and coworkers[18]). P25 (Degussa) is the most often applied photocatalyst in studies under applied conditions. According to the manufacturer, it comprises a mixture of rutile and anatase particles. However, Ohtani and coworkers also found a small fraction of amorphous  $\text{TiO}_2$  in their samples.[21] Apart from this inherent inhomogeneity given by the mixture, the authors found evidence that samples taken from a batch are not homogeneous compared to each other, making the comparison of results in the literature on P25 questionable.[21]

In contrast, surface science studies on titania single crystal facets have elaborated reliable, reproducible recipes for catalyst preparation. The basic structure and surface properties of single crystalline  $\text{TiO}_2$  have been comprehensively reviewed by Diebold.[22] This accounts particularly for the  $\text{TiO}_2(110)$  facet (see figure 2.1), which is in general

the most investigated one. Structurally, it consists of a plane of oxygen anions and titanium cations, arranged in alternating rows in the [001] direction. On top of every second Ti row lies another chain of oxygen ions, whose species are called bridge-bonded oxygen (BBO) since they "bridge" two oxygen rows below. The titanium species underneath the BBO-row resemble the 6-fold coordinated bulk  $\text{Ti}^{4+}$  cations ( $\text{Ti}_{6c}$ ), whereas the "uncovered" Ti species are 5-fold coordinated  $\text{Ti}^{4+}$  cations ( $\text{Ti}_{5c}$ ). In addition, certain defects are always present. A fraction of the BBOs is missing, and the Ti species underneath are accessible for potential adsorbates which take the position of the missing BBO. Furthermore, reduced  $\text{Ti}^{3+}$  species are present on or underneath the surface plane as so-called interstitials. Moreover, adsorbates like single oxygen species on top of  $\text{Ti}_{5c}$  ( $\text{O}_{ad}$ ) or hydrogen (bound to BBO as hydroxyl) are commonly present and affect the reactivity.[23, 24, 25, 26, 27] Importantly, a specific preparation procedure to obtain desired properties of the  $\text{TiO}_2(110)$  surface will never exclusively yield one defect type, but simply change the ratios between all types described above. This makes the elucidation of (photo-)catalytically active sites difficult, since the impact of one particular defect species can be seldomly completely excluded. For example, adsorbing  $\text{O}_2$  on the titania surface or annealing it in oxygen atmosphere oxidizes the surface, but some BBO vacancies still remain.[28, 29, 30] Under UHV, different treatments are conductible

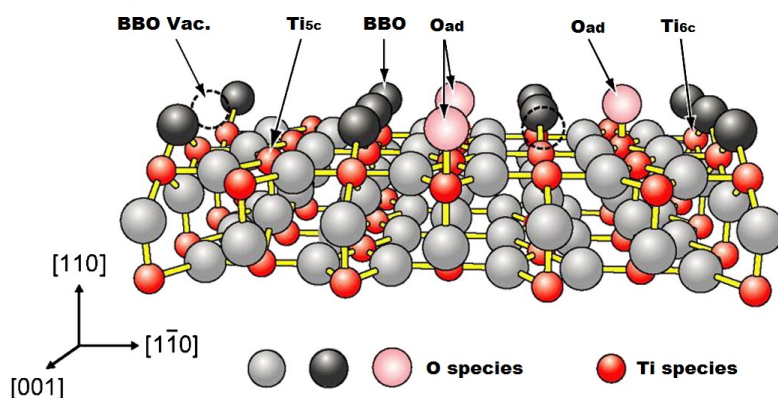


**Figure 2.1:** Ball and stick model of the rutile  $\text{TiO}_2(110)-(1 \times 1)$  surface with BBO vacancies and  $\text{O}_{ad}$  adatoms. Black spheres represent BBO species, grey spheres in-plane O ions, pink spheres  $\text{O}_{ad}$  adatoms and red spheres Ti cations. Adapted from [31].

for preparing the  $\text{TiO}_2(110)$  surface. For studies on chemical reactivity, the surface is usually oxidized (o- $\text{TiO}_2(110)$ ) or reduced (r- $\text{TiO}_2(110)$ ). Treating the surface with  $\text{O}_2$  will result in an oxidized surface, als already mentioned.[32, 33, 28] The degree of oxidation is determined by the temperature during exposure,[34] and leads not only to the partial healing of BBO defects but also to the creation of  $\text{O}_{ad}$ .[29, 35] The chemistry of  $\text{O}_2$  on titania, that is, the different kinds of oxygen species and their interaction with other molecules, is not trivial.[31] Furthermore, the elucidation of structure-reactivity relationships is challenging, since scanning tunneling microscopy (STM) studies have to be taken with care due to  $\text{O}_2$  dissociation induced by the tip.[36] The reduced surface is most commonly obtained by sputtering and annealing the crystal in UHV. Apart from

the removal of surface contaminations, this leads to the creation of BBO vacancies and to the surface or sub-surface migration of Ti interstitials.[37, 28] Both the reduced and the oxidized surface have been thermo- and photochemically investigated, although the reduced surface has received more attention since it is structurally and chemically better defined.

Independent of the surface preparation, the behavior of the material under illumination determines the photoreactivity to a major degree. In order to gain fundamental insights into titania photocatalysis, one has to consider the chemical properties of the surface as well as the basic aspects of semiconductor physics.

## 2.2 Fundamentals of Semiconductor Photocatalysis

In surface science studies on semiconductors, it is important to consider that the chemistry occurs on extended surface facets of a single crystal, whose electronic structure has considerable impact on the photoreactivity.[38] One of the most important concepts is that of semiconductor band bending, which may result from adsorbates, defects, material contacts or external fields (for details see the comprehensive review by Zhang and Yates[39]). Briefly, the band bending concept describes a continuous, smooth shift of the upper and lower energies of valence and conduction band, respectively, from the bulk towards the surface. This shift occurs naturally due to the alignment of the fermi levels at the junction of semiconductor and the chemical environment at the surface. This description allows to implement local changes of charge distribution into the band model.

Independent of its modification or surface facets, titania is naturally an n-type semiconductor due to the oxygen and titania defect species described above, which cause an accumulation of negative charges on the surface as depicted in figure 2.2. The Fermi level alignment of surface and bulk of the n-type semiconductore results in an upward band bending.[40, 41, 42] Furthermore, these surface and subsurface defects also generate states within the band gap.[28, 43] By irradiating the semiconductor with light whose photon energy is above the band gap, electrons are being excited from the valence band into the conduction band. A formally positive charge (a so-called (photo-)hole) remains in the valence band to ensure charge balance. With respect to titania, the issue of diffusion dynamics of electron and hole, as well as the question of how "excitonic" they behave, is not comprehensively resolved.[14] In a simplified but useful picture, the charge carriers are considered to be point charges which diffuse inside the crystal under the influence of the electrostatic forces. The impact of the upward band bending in n-type  $\text{TiO}_2$  attracts holes towards the surface, whereas electrons are being repelled and travel preferentially towards the bulk. Upon their arrival at the surface, holes may quench negative surface states, thus flattening the upward band bending and lowering its impact on electron and hole migration.[44, 45] Then, charge carrier recombination becomes predominant for the majority of electrons and holes in the bulk as well as on the surface.[46, 47]

The electronic structure and hence the band bending is obviously altered when chemi-

cal processes occur on the photocatalyst, e.g. by the adsorption of reactants or metal particles as co-catalysts. Nevertheless, these influences can hardly be quantified or even disentangled *in situ*, which is why the simplified band bending scheme described above is being applied to qualitatively explain chemical experimental results as well. In this sense, the photocatalytic reactivity of titania can be regarded to be hole-driven (i.e. the initial reaction step being an oxidation) due to the upward band bending.

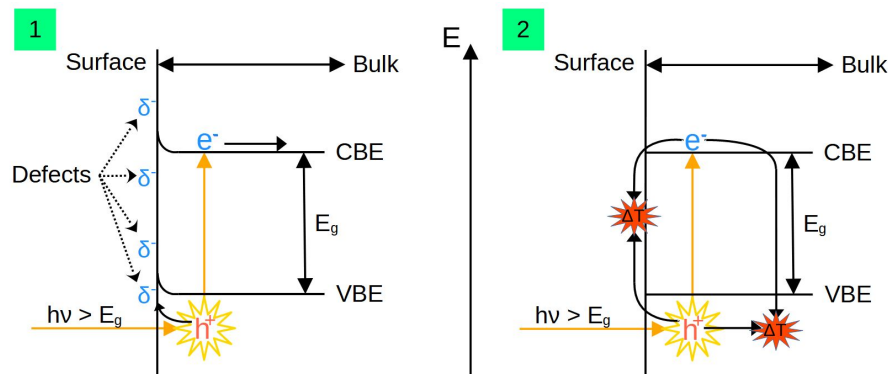


**Figure 2.2:** Schematic representation of band bending and charge carrier dynamics in titania upon illumination with light whose energy  $h\nu$  is above the band gap  $E_g$ . 1: The negatively charged defects at the surface cause an upward band bending, i.e. a repulsive and attractive potential for electrons and holes, respectively. Therefore, electrons travel preferentially towards the bulk and holes towards the surface. 2: When the negative surface states have been extinguished by the holes, the formerly bent bands are flattened. Electrons and holes diffuse towards the surface and the bulk to finally recombine, releasing the absorbed light energy as heat. CBE: Conduction band edge; VBE: Valence band edge.

The work which started the gold rush on titania photocatalysis was actually based on electrochemistry.[17] The vast majority of follow-up works adapted the mechanistic picture even if no bias were applied or the reaction environment was fundamentally different.[18] As described above, the absorption of light whose energy exceeds the band gap leads to the creation of an electron-hole pair (eq. 2.1) in the semiconductor, which induce the reduction (compound  $A$  in eq. 2.2) and oxidation (compound  $B$  in eq. 2.3) of adsorbates, respectively.



Consequently, photocatalytic hydrogen evolution was generally imagined to occur by a reduction of protonic surface species on  $\text{TiO}_2(110)$  according to



For every proton reduced according to eq. 2.4, one photohole has to be consumed in order to fulfill charge balance. Alcohols are organic compounds which are easily oxidized, and have therefore been used as hole scavengers in photocatalysis, in order to enhance the yield of hydrogen evolution reactions by more efficient charge carrier separation and photohole consumption.[48, 49, 50, 51] However, this approach has received considerable criticism. On the one hand, the fate of the hole scavenger after its oxidation remains largely unknown in most studies, but further reaction steps which affect the overall outcome cannot be ruled out. On the other hand, alcohol hole scavengers are often active for H<sub>2</sub> evolution themselves, but usually their contribution to an overall H<sub>2</sub> yield is not taken into account.[52, 53, 54]

Apart from that, alcohols have become substrates of interest themselves for photochemical conversion. Their intrinsic potential as hydrogen carriers, their valuable oxidation products and their role as precursors for more complex organic substrates was being acknowledged in the recent years.[55, 56, 57, 58, 59] On TiO<sub>2</sub>(110), Dohnálek, Henderson and others have set a solid foundation for alcohol (photo-)chemistry. In this regard, methanol is to a high degree representative for compounds of this class, as discussed in the following.

## 2.3 Alcohols on Bare TiO<sub>2</sub>(110)

With respect to scanning probe techniques, the Dohnálek group presented the first atomically resolved STM images of methanol adsorbed on TiO<sub>2</sub>(110).[60] It became clear that methanol dissociates in BBO vacancies not by C-O but *via* O-H bond scission, yielding adsorbed methoxy and hydroxyl species. At methanol coverages below the BBO concentration, the pairs remained in stationary vicinity. If the amount of methanol exceeded the BBO density, molecularly adsorbed methanol on the Ti rows was mobile and facilitated hydroxyl migration at room temperature. This suggested transport mechanism is similar to the one proposed by Wendt *et al.* for water-assisted hydroxyl migration on reduced TiO<sub>2</sub>(110).[61] The adsorption behavior of alcohols deduced from the experimental results were confirmed by theoretical investigations. The groups of Kresse as well as Petrik and co-workers found the dissociative adsorption in BBO-vacancies to be thermodynamically favorable, while molecular and dissociative adsorption on the Ti<sub>5c</sub> sites were shown to be energetically close.[62, 63] Qualitatively, the same results were obtained by the Dohnálek group for 2-butanol instead of methanol with respect to adsorption, diffusion and dissociation behavior.[64] In accordance, Besenbacher and coworkers investigated ethanol on TiO<sub>2</sub>(110) by means of STM. They found molecular and dissociated ethanol on Ti<sub>5c</sub> sites and dissociated ethanol in BBO vacancies.[65] Considering thermal reactivity studies, Gamble *et al.* had found the same ethanol surface species by means of temperature programmed desorption (TPD) and X-ray photoelectron spectroscopy (XPS) as in the work by the Besenbacher group mentioned above. Ethanol desorbed both as molecular alcohol and as thermal decomposition products, respectively.[66] Henderson *et al.* conducted a systematic study of methanol on

TiO<sub>2</sub>(110).[67] The TPD spectra yielded prominent features at 150, 165, 295, 350, and 480 K. The low-temperature peaks were both assigned to multilayer desorption. The 295 K feature was assigned to molecularly adsorbed methanol on Ti<sub>5c</sub> sites. The high temperature peak as well as the shoulder at 350 K was attributed to recombinative desorption of dissociated methanol in BBO vacancies and from Ti<sub>5c</sub> sites, respectively. If the surface had been exposed to O<sub>2</sub> before methanol adsorption, the residual oxygen species enhanced methanol dissociation and the thermal conversion of the alcohol to formaldehyde above 600 K. Partially dissociated methanol on defective and nondefective sites was also found by Farfan-Arribas and Madix after room temperature adsorption. The thermal conversion of remaining methanol to formaldehyde at high temperatures was also observed, in line with Henderson's results.[68] A representative TPD spectrum with the mentioned features is shown in figure 2.3.

Subsequently, the Dohnálek group found the adsorption and dissociation behavior

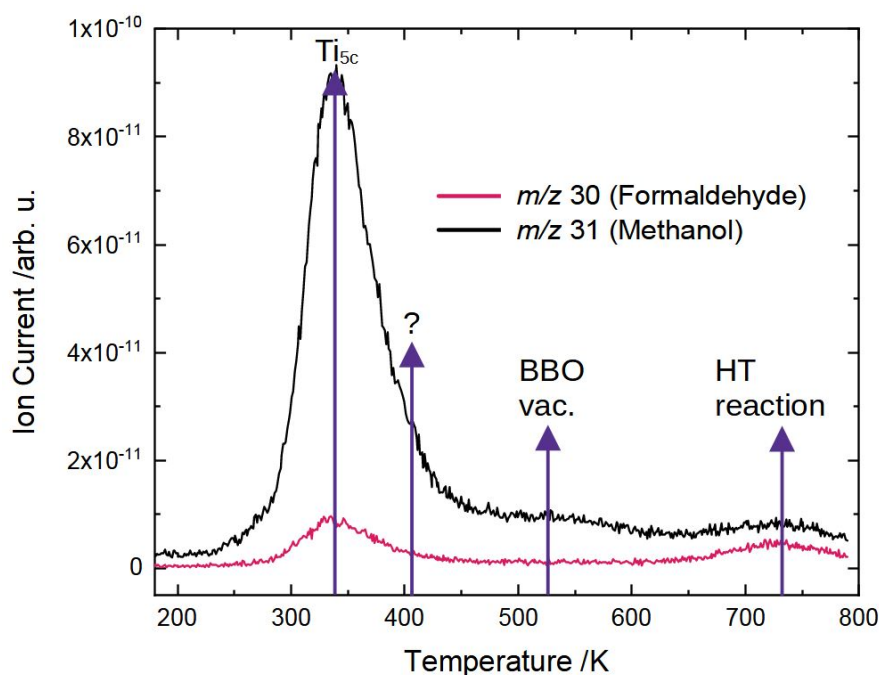


**Figure 2.3:** TPD spectrum of 1.5 ML methanol on reduced TiO<sub>2</sub>(110) recorded in the course of this thesis. While the multilayer peak is absent due to the low coverage, the four features highlighted by the arrows are in good agreement with the literature.[67, 68] Deviations in the desorption temperature from the literature values can be traced back to experimental differences such as heating rate, heat transfer, or location of the thermocouples.

described above for a number of aliphatic C<sub>2</sub> to C<sub>8</sub> alcohols on TiO<sub>2</sub>(110). They elucidated different temperature- and moiety-dependent reaction pathways, namely dehydration, dehydrogenation and recombination.[69] In good agreements with these results, Farfan-Arribas and Madix created oxygen vacancies on TiO<sub>2</sub>(110) by means of electron



bombardment and found that ethanol, 2-propanol and *n*-propanol adsorb dissociatively at room temperature by O-H bond cleavage. This resulted in the formation of the respective alkoxy species and a hydroxyl group with a BBO. Heating the sample led to recombination and high-temperature decomposition of the alcohols. The amount of dissociated and decomposed molecules scaled with the number of defects.[70]

By extending the investigations to secondary and tertiary alcohols, it was found that the dehydration reaction to alkenes was favored over dehydrogenation to aldehydes with increasing chain length and chain number.[71] Furthermore, the absolute coverage also decreased according to the same trend, which was mainly ascribed to an increasing steric hinderance.[72]

The gist from the studies above is that the adsorption and dissociation behavior of alcohols appears to be qualitatively equal for the molecules of this compound class. Upon adsorption on the reduced TiO<sub>2</sub>(110) surface, the alcohol dissociates in BBO vacancies and partially also on Ti<sub>5c</sub> sites:



The same reaction behavior can therefore be expected when introducing new alcohols to be studied on TiO<sub>2</sub>(110). This is an important axiom for the photochemistry in this work, as discussed in section 4.

### 2.3.1 Methanol Photochemistry on Bare TiO<sub>2</sub>(110)

In 2010, Yang and coworkers published a photochemical study of methanol on TiO<sub>2</sub>(110) based on STM, theory and time-dependent 2-photon photoemission experiments. They claimed that molecularly adsorbed methanol on Ti<sub>5c</sub> sites dissociates under UV irradiation at a wavelength below 400 nm by O-H bond cleavage to form a methoxy species and a hydroxyl group with a neighbouring BBO.[73] In a follow-up study, the dissociation rate was observed to be an order of magnitude faster on a defective surface compared to a stoichiometric one.[74]

A photochemical TPD study by Henderson strongly suggested that methoxy species are at least an order of magnitude more reactive than adsorbed methanol for hole-mediated oxidation, in agreement with later computational studies.[75, 76] Upon hole capture, a C-H bond from methoxy was cleaved, forming the aldehyde which desorbed molecularly during post-illumination TPD (PI-TPD), and a BBO-H (see figure 2.4). The latter cannot be desorbed as molecular hydrogen by recombination on two BBO-H, but as water with an oxygen atom from the titania surface.[77] Shen and Henderson extended the photochemical investigation of methanol to the presence of co-adsorbed water. The latter promoted neither the thermal nor photochemical conversion of methanol to methoxy. However, the photo-oxidation of methoxy to formaldehyde was hampered by water adsorbed on BBO rows, which led the authors to the conclusion that these sites accept the hydrogen from the light-induced C-H bond cleavage.[78] Shen *et al.* furthermore highlighted the importance of diffusion for methanol chemistry on TiO<sub>2</sub>(110). In order to thermally decompose to methoxy on reduced TiO<sub>2</sub>(110), methanol has to migrate to an H-accepting site. This was not possible at 100 K, and formaldehyde formation was

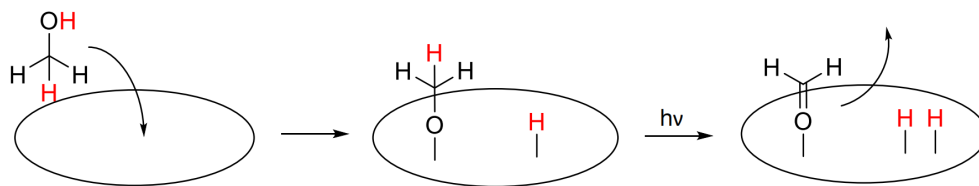


**Figure 2.4:** Schematic illustration of alcohol photochemistry on TiO<sub>2</sub>(110) using methanol as an example based on the literature results discussed in the text. Upon adsorption, the alcohol partially dissociates to form the photoactive alkoxy species. Upon illumination, the alcohol is oxidized by a homolytic  $\alpha$ -H bond cleavage. At sufficiently high temperatures (e.g. at room temperature), the aldehyde/ketone desorbs into the gas phase, whereas the hydrogen species remain on the surface.

not observed at cryogenic temperatures. The reactivity was enhanced when oxygen was co-adsorbed at cryogenic temperatures (providing more H-accepting sites), and further increased when the sample was heated above 200 K where methanol diffusion on Ti<sub>5c</sub> occurs.[79]

Phillips *et al.* evidenced that formaldehyde can be converted further to methyl formate on TiO<sub>2</sub>(110) by light-induced coupling of methoxy with formaldehyde.[80] The methyl formate yield could be enhanced by pre-oxidizing the surface, since this step led to a higher fraction of thermally dissociated methanol. Methyl formate formation was corroborated by other groups[81, 82, 83] and had also been evidenced in a study at ambient conditions on anatase particles.[84] Walenta *et al.* addressed the question of how much formaldehyde formed from methoxy under illumination is further converted to methyl formate. Using kinetic description and modeling, they correlated the methyl formate yield to the surface residence time of the intermediate formaldehyde. This residence time is governed by the sample temperature, since elevated temperatures favor formaldehyde desorption over its consecutive reaction.[85]

The findings by the Friend group put the interpretation of the previously mentioned combined STM and 2-photon photoemission study by Zhou *et al.* into question.[73] Evidence for two distinct photochemical steps was found in the photoemission spectra. This was the basis for the presumption of photon-induced dissociation of molecular methanol to methoxy. One may speculate that the two photon-induced features observed spectroscopically could stem from the formaldehyde and methyl formate surface species, not from photochemically dissociated methanol. This accounts all the more since the sample was cooled in the presence of oxygen, which increases methyl formate production by enhanced preceding thermal methoxy formation.[80] The fact that no methyl formate was evident in STM according to Zhou *et al.* could be traced back to the stark contrast in methanol coverage between their spectroscopic and scanning probe experiments. While the STM images were recorded at a coverage of 0.02 ML, the photoemission spectra were taken at 0.16, 0.50, and 1.00 ML (i.e., at least the eight-fold coverage than for STM). Nevertheless, the groups of Huang and Yang evidence photochemical O-H bond cleavage in other spectroscopic studies, but assigned the superior photoactivity to methoxy

groups.[86, 87, 88, 89, 88]

In summary, while methanol O-H bond may be photochemically broken, the majority of studies presume a defect-mediated thermal dissociation of this bond.[75, 76, 77, 78, 79, 80, 90, 91, 92] Indeed, thermal O-H dissociation of methanol was later also confirmed by Yang's group, too.[93] Importantly, they also found that the photon-driven reaction to formaldehyde is thermally reversible even at low temperatures, which will be discussed in the course of section 3.2.[94]

### 2.3.2 The Photochemistry of Secondary Alcohols on Bare TiO<sub>2</sub>(110)

Compared to the considerable interest in the recent years in methanol photocatalysis on TiO<sub>2</sub>(110), photochemical studies on higher alcohols in an ideal environment are comparably rare. Brinkley and Engel reported the formation of small amounts of acetone from isopropanol on the reduced surface. They claimed that BBO vacancies are not the photoactive site, but enhance the reaction yield. [95, 96, 97] In a photochemical study combining Fourier-transform infrared spectroscopy (FTIR), TPD, and PI-TPD, Al-Shamery and coworkers observed the formation of propane and propene as thermal products and acetone as photoproduct. UV illumination before temperature treatment was found to inhibit propene and propane formation for the benefit of acetone.[98] Kershis and White investigated ethanol and 2-propanol in a combined TPD and pump-probe laser ionization study on TiO<sub>2</sub>(110). They detected methyl radicals whose energy was close to those from decomposed acetaldehyde and acetone, respectively. The authors suggested that both alcohols are at first photo-oxidized to the corresponding aldehyde or ketone *via* C-H cleavage by the photohole, and subsequently oxidized further by another hole which cleaves a C-C bond.[99] Friend and coworkers investigated the photochemistry of isobutanol. After the thermal formation of surface isobutoxy species, a hole-mediated oxidation yielded isobutanal. Depending on the temperature, the aldehyde desorbed or underwent another oxidation step to yield propane and CO.[100]

The parallels between the photoreactivity of primary and secondary alcohols on TiO<sub>2</sub>(110) are strong, although the final product spectra are different. The latter are evidently affected by the presence of adsorbed oxygen species. However, the first photon-driven reaction is in principle identical, which is the oxidation of the surface alkoxy species to the corresponding aldehyde or ketone. This step seems to be independent of the moieties. Depending on the temperature, the oxidation product desorbs or is photo-oxidized further to substrate-specific products.[80, 100] The first oxidation step is therefore the same as for primary and secondary alcohols, and differences in selectivity emerge in the second photo-oxidation step.

### 2.3.3 The Photochemistry of Tertiary Alcohols on Bare TiO<sub>2</sub>(110)

While the literature on photochemistry of secondary alcohols is already moderate compared to primary ones, even fewer studies exist for tertiary alcohols. Even in the liquid phase only few papers were published on this topic, in which tertiary alcohols are often

merely among a selection of reactants but are not systematically examined as a compound class.[101, 102, 103, 104, 105, 106, 107] This might be due to the fact that tertiary alcohols are commonly considered to be inert towards oxidation, especially in a selective manner.[108, 109] Recently, Heiz and coworkers investigated the photo-oxidation of *tert*-butanol on TiO<sub>2</sub>(110) in UHV. Similar to ketones,[99] the hole-mediated oxidation of the alcohol led to the ejection of a methyl radical into the gas phase at low temperatures. Near room temperature and above, isobutene formation by dehydration of the alcohol was evident.[110, 83] These studies suggested on the one hand, that the photoreaction pattern of tertiary alcohols at elevated temperatures is more complex than for primary and secondary alcohols. On the other hand, the photoreactivity seems similar at low temperatures. Instead of cleaving a C-H bond, a C-C bond is cleaved upon hole capture, leading to the corresponding ketone, as in the case of primary and secondary alcohols. For tertiary alcohols, systematic studies on the nature of the photochemically active site are scarce, while for primary and secondary alcohols the issue is still under discussion.

### 2.4 The Photochemically Active Site

State-of-the-art spectroscopic techniques are not sufficiently sensitive to enable an exact *in situ* discrimination between different sites of the TiO<sub>2</sub>(110) surface under illumination. Therefore, a direct identification of the sites where adsorbed molecules are photoconverted has not been accomplished so far. Nevertheless, one can make a set of considerations deduced from the results of alcohol photochemistry discussed above. An illustration of the discussed defects and the alcohol species on TiO<sub>2</sub>(110) is given in figure 2.5.

The results of many STM and TPD studies suggest methoxy to be the photochemically active species. Since alcohols adsorb dissociatively in BBO vacancies, it seems obvious to presume those surface sites to be photochemically active centers.[70, 65, 67, 60, 64, 69, 71, 77, 78, 79, 80, 91, 92] This assumption is consolidated by the fact that the amount of alcohol molecules photoconverted at low temperatures (which suppresses diffusion) is 5 - 20% of its total coverage, corresponding to typical values of the atomic surface concentration of BBO vacancies.[95, 77, 81, 92, 110] One may argue that in PI-TPDs, thermal products formed in BBO vacancies are still detectable even after maximal low temperature photoconversion, suggesting that at least some of these sites are not photochemically active. However, it must be taken into account that the adsorbates become mobile during the heating process. Since photoproducts such as aldehydes or ketones usually desorb at lower temperatures than alkoxy species, the thermal alcohol decomposition products detected in PI-TPDs may well stem from alkoxy diffusion into vacancies where a photoproduct was previously adsorbed.[79, 111, 80, 99, 92] After the refilling of BBO sites upon diffusion, further photoconversion at these defects is certainly possible. These arguments against considering the BBO vacancies to be photochemically active sites therefore do not hold.

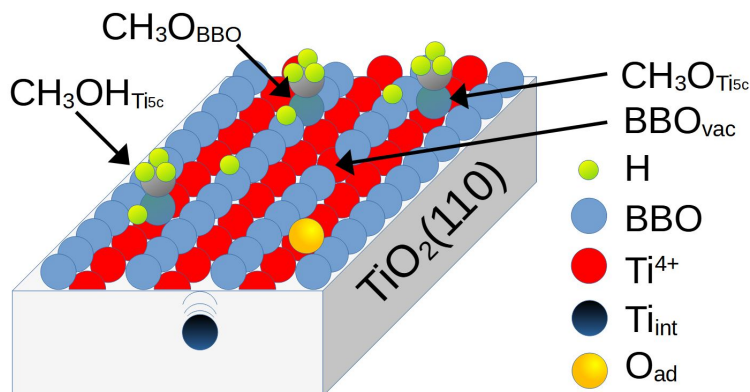


**Figure 2.5:** Schematic illustration of the surface sites, defects, and methanol adsorbates present on  $\text{TiO}_2(110)$ . [23, 24, 25, 26, 27] The ideal  $\text{TiO}_2(110)$  surface consists of  $\text{Ti}^{4+}$  and BBO sites. Additionally, defects (sub-surface Ti interstitials ( $\text{Ti}_{int}$ ), BBO vacancies,  $\text{O}_{ad}$ , hydroxyls (H on BBO)) are present. These defects influence the adsorption states of methanol, leading to methoxy groups on the Ti rows ( $\text{CH}_3\text{O}_{\text{Ti}_{5c}}$ ) and in BBO vacancies ( $\text{CH}_3\text{O}_{\text{BBOvac}}$ ) next to molecular methanol ( $\text{CH}_3\text{OH}_{\text{Ti}_{5c}}$ ).

Apart from BBO vacancies, some authors speculated that subsurface species such as Ti interstitials or lattice oxygen defects may also affect or be active sites for the titania photochemistry. [112, 113] Indeed, many studies suggest a strong impact on the electronic structure as well as the thermal  $\text{TiO}_2(110)$  surface chemistry by these defects. [31, 114, 115, 116, 117, 28, 43, 118] However, direct evidence is difficult to obtain as the detection of these subsurface species on titania is challenging by means of scanning probe techniques. [119] Furthermore, the creation of e.g. Ti subsurface interstitials is facilitated by bulk reduction of the titania crystal, as is the creation of BBO vacancies. Since both species are therefore interconnected in their creation, their individual impact on the surface photochemistry can hardly be disentangled, and their effect on the photochemistry is ambiguous. [14]

Apart from defect sites, there is also evidence for regular  $\text{Ti}_{5c}$  surface sites being photochemically active. It should be noted that although nominally equal, the chemical surrounding of the Ti ions in the troughs may vary significantly due to the near presence of e.g. defects, hydroxyls or adsorbed oxygen. In this regard, the photoreactivity of  $\text{Ti}_{5c}$  remains elusive, since many studies on this issue were conducted on an oxidized  $\text{TiO}_2(110)$  surface. [77, 78, 80, 120] As mentioned before, even on the reduced  $\text{TiO}_2(110)$  surface defects and adsorbates are present. An impact on  $\text{Ti}_{5c}$  sites can also not be excluded in studies on the reduced surface. [121] Recently, Diebold and coworkers investigated the UV-induced photoreactivity of adsorbed oxygen species on reduced  $\text{TiO}_2(110)$  using atomic force microscopy. They found that molecular oxygen was photoreactive both on  $\text{Ti}_{5c}$  sites (hole-induced direct desorption) as well as BBO vacancies (electron-induced dissociation). [122] Naturally, a direct comparison of oxygen and alcohol photochemistry should be taken with care. Nevertheless, no work has hitherto ruled out that regular Ti sites can be photochemically active.

Regardless of what the photoactive sites may be, it is clear that the surface reactivity is to a certain degree determined by band bending, which dictates the main charge carrier dynamics.[39] As described above, band bending is caused by negative surface states such as BBO vacancies (double negative charge) or Ti interstitials (single negative charge).[123, 124, 125, 126] Notably, hydroxylating the surface by water adsorption fills the BBO vacancies, but does not seem to alter their electronic structure.[127, 28] Upon O<sub>2</sub> adsorption and dissociation, charge from the BBO vacancies is being transferred to the oxygen adatoms.[127, 128, 129] Due to the locally different electronic structure, it is clear that the interaction and (photo)chemistry of molecules is significantly dominated and impacted by these sites as well.[130, 131, 132] However, quantifying the effect on charge carrier dynamics and hence the chemical impact of a defect site is difficult since charges near the surface are probably not strictly localized. The fact that sub-surface electrons may be delocalized to a certain degree has for example led to the concept of polarons (electrons which strongly interact with the surrounding crystal lattice), and their further sub-division into near- and wide-range polarons.[133, 134, 135, 136, 137] Therefore, an assignment of which defect or lattice ion is photochemically active and which is not is difficult, all the more since the defects described above all carry negative charges and can therefore potentially attract holes.

### 2.5 Alcohol Photochemistry on Metal-Loaded TiO<sub>2</sub>(110)

In the liquid phase, hydrogen production from titania powder in aqueous environments was early shown to be possible, albeit very slow, while the presence of a metal co-catalyst accelerated the reaction significantly.[138, 139] Hydrogen evolution from water or alcohols is also hardly feasible on bare TiO<sub>2</sub>(110) in UHV. Pure photocatalytic water splitting has so far not been observed, and only very small amounts of hydrogen were detected at best during methanol photoreforming.[140]

The deposition of metal particles on the TiO<sub>2</sub>(110) surface facilitated H<sub>2</sub> production from photochemical methanol reforming. Using a laser ablation cluster source, Heiz and coworkers demonstrated in two studies that small Pt clusters deposited on rutile TiO<sub>2</sub>(100) facilitated truly photocatalytic methanol reforming to yield molecular hydrogen and the corresponding carbonyl compound as depicted in figure 2.6.[83, 141] Assuming a dissociative adsorption of the alcohol on a negatively charged surface state, the authors described the oxidation of the alkoxy as a hole-mediated homolytic  $\alpha$ -H cleavage, followed by the thermal desorption of the aldehyde or ketone. The Pt co-catalyst was suggested to subsequently facilitate thermal hydrogen recombination and desorption. Finally, the photoelectron was proposed to travel to the adsorption site and re-establish the initially negative surface state extinguished by the hole. This last step is not only crucial for maintaining the charge balance, but also for re-establishing the upward band bending which had been flattened by the consumption of the photo-hole. This is illustrated by schematically extending the common band bending scheme, as illustrated in figure 2.7. The fact that the Pt clusters facilitated hydrogen evolution thermally and not photochemically implies that photocatalytic methanol conversion on

$\text{TiO}_2(110)$  is a one-photon-process, in line with a linear (i.e. first order) dependency of hydrogen yield on the photon flux.[141] While contradicting the electrochemical picture of hydrogen formation by the reduction of surface-bound protons by photoelectrons, which would require a higher-order dependency on the photon flux, this finding agreed with other results in the literature.[53, 142]

In a subsequent study, Walenta *et al.* provided evidence that the Pt clusters are cov-

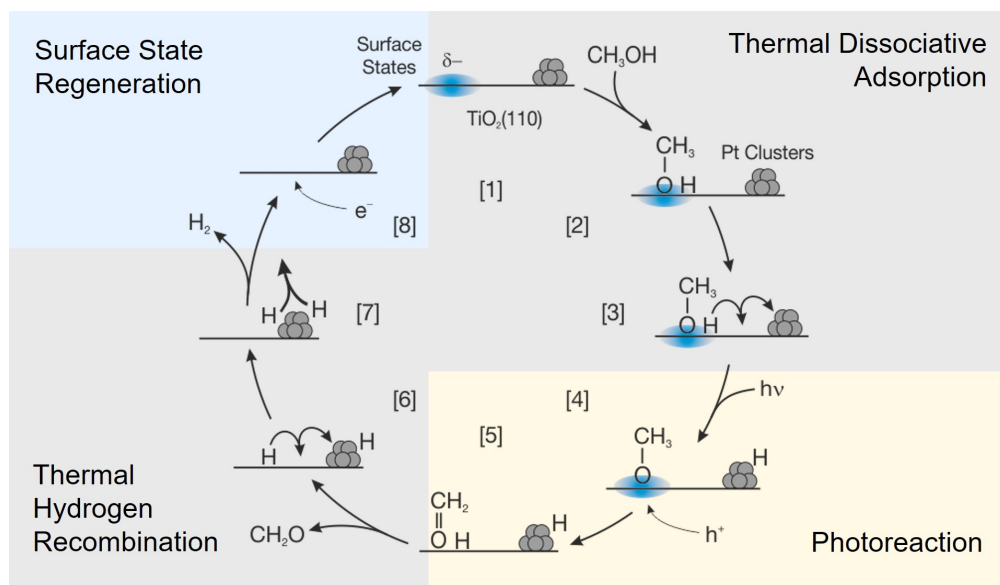


**Figure 2.6:** Photocatalytic reaction mechanism for methanol conversion at a co-catalyst-loaded  $r\text{-TiO}_2(110)$  surface as described in the text. Upon adsorption, a methoxy and hydroxyl species [2] is formed thermally. The latter diffuses across the surface at sufficiently high temperature[3]. Upon illumination, methoxy is oxidized by a photohole [4] yielding formaldehyde [5], which eventually desorbs thermally. The thus formed atomic hydrogen diffuses on the surface [6] and recombines with another hydrogen at a co-catalyst, desorbing as  $\text{H}_2$  [7]. The negatively charged surface states (e.g. BBO vacancies or  $\text{Ti}^{3+}$  interstitials) of the n-type semiconductor get replenished by the photoelectron [8]. The catalyst remains unchanged after the completion of the cycle [1]. The reaction mechanism facilitates an overall charge-neutral stoichiometric reaction comprising thermal and photochemical steps. Adapted from [141].

ered by carbon monoxide under the reaction conditions, which supposedly originates from methanol decomposition. Since the catalyst showed no signs of deactivation over hours of steady-state photocatalytic methanol conversion, the authors assumed a protective effect of the CO adsorbates.[85] On the same system, Hao *et al.* observed a significant increase in the reaction rate for higher Pt loadings.[143] The groups of Idriss and Yang further reported photocatalytic hydrogen evolution from methanol on gold cluster-covered  $\text{TiO}_2(110)$ . Idriss and coworkers interpreted their results based on an electrochemical picture assuming the clusters to be charge carrier traps, and concluded that the reaction rate did not scale with cluster density or size.[144] In contrast, Yang and coworkers claimed  $\text{H}_2$  evolution during photocatalytic methanol conversion on  $\text{TiO}_2(110)$

to occur thermally on the Au clusters, in agreement with the catalytic cycle proposed by the Heiz group.[145, 141]

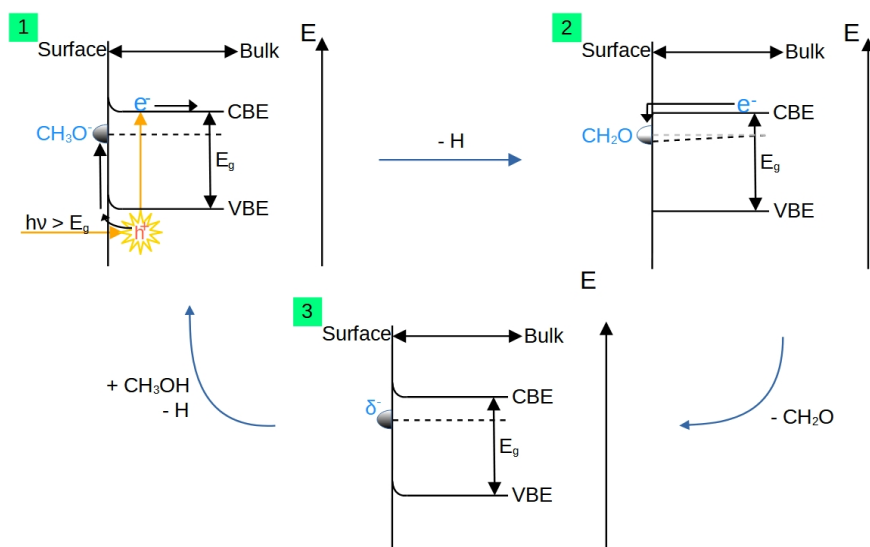


**Figure 2.7:** The band bending scheme adapted to the photocatalytic cycle proposed by Walenta *et al.*. The photoactive methoxy group is bound to a negatively charged surface state, which causes an upward band bending. The adsorbate affects the surface density of states, as indicated by the dashed lines and the hemisphere. A photo-hole created by illumination migrates to the surface state, and by its consumption reduces the electron density there, leading to a C–H bond cleavage. Formaldehyde subsequently desorbs, the reduction of negative surface charge creates a band flattening and enables the diffusion of photoelectrons to the surface, where it regenerates the initial negatively charged surface state. Black dotted line: actual occupation, grey dotted line: previous occupation.



## 3 Experimental Methods

The UHV is depicted in figure 3.1. It consists of an analysis and a reaction chamber with a laser vaporization cluster source attached to it. The chambers are differentially pumped, with a pressure between  $1 \cdot 10^{-1}$  mbar at the skimmer and  $2 \cdot 10^{-7}$  mbar in the main chamber when depositing clusters. The main chamber has a base pressure of less than  $1 \cdot 10^{-10}$  mbar and is equipped with a liquid N<sub>2</sub>-cooled  $(x, y, z, \phi)$ -manipulator, a sputter gun, an Auger electron spectrometer, a quadrupole mass spectrometer (QMS), leak valves, a molecular beam doser, and a gasline of in-house design. Photocatalytic experiments were conducted using the second harmonic (241.8 nm) of an optical parametric oscillator pumped by the third harmonic of a Nd:YAG laser. The cluster source has a base pressure lower than  $2 \cdot 10^{-8}$  mbar at the quadrupole bender and is operated using a frequency-doubled Nd:YAG laser. More details about the setup are given below.

### 3.1 Cluster Source

The laser vaporization cluster source enables the generation of small clusters with a defined and variable number of atoms between 1 amu to 16 000 amu.[146] These clusters are deposited on the TiO<sub>2</sub>(110) surface under soft-landing conditions ( $<1$  eV/atom).[147] At a constant cluster current, the deposition time is adjusted to deposit a desired amount of atoms in the range of 0.1 % to 2 % of a monolayer with respect to the total number of surface atoms. Hence, cluster size and coverage can be controlled independently.

The second harmonic of a diode-pumped Nd:YAG laser (DPPS Spitlight, 100 Hz, 6 W, 9 ns pulse width) is focused onto a hypocycloidically rotating metal target disc (99.95% purity for Pt (ESG Edelmetalle); the purity of the Ni target was checked by mass scans). Synchronous to the laser pulses, the produced metal plasma is mixed with of He gas (5.0 for Pt, 6.0 for Ni, Air Westfalen), whose inlet is triggered by a piezo valve with pulses of 40  $\mu$ s in length (3 bar to 4 bar gas pressure at the piezo). The metal plasma is thermalized by the He pulses, and the mixture expands adiabatically into the vacuum through a nozzle of 3 mm in diameter. The mixing of plasma and rare gas pulses and their expansion counterpropagating to the laser beam leads to cluster cation formation and their cooling below room temperature.[148] Using Einzel lenses, the ions are first guided through a linear octupole (HT Transceiver TS-5700, Kenwood) operating at radio frequency. Subsequently, a 90° quadrupole bender deflects the cations rectangularly towards the main chamber. This way, the neutral clusters are separated and dumped onto a glass slab. The cations are guided through a quadrupole mass filter (QMF) (150 QC, Extrel) which facilitates the selection of certain cluster sizes in a mass range of 1 amu to 16 000 amu assuming singly charged particles. Alternatively, the QMF operates in radio frequency mode, serving as high pass filter and facilitating

### 3 Experimental Methods

the deposition of clusters of a certain size distribution. The clusters enter the main chamber through a gate, where they reach the single crystal surface in direction of the surface normal. An intact landing without fragmentation is ensured by the soft-landing conditions mentioned above. Upon landing, the cluster cations are neutralized, which is measured as electric current using a picoammeter (Keithley 6487). A home-written LabVIEW program converts the neutralization current to the total cluster surface coverage (in % of all surface atoms) during the deposition. The cluster current typically amounts to 100 pA to 300 pA for size-selected and 2 nA to 5 nA for unselected clusters.

## 3.2 Analysis and Reaction Main Chamber

The UHV main chamber (base pressure lower than  $1 \cdot 10^{-10}$  mbar) consists of a liquid N<sub>2</sub>-cooled ( $x, y, z, \phi$ )-manipulator (VAB Vakuum), a sputter gun for surface purification and TiO<sub>2</sub> reduction (IQE 11/35, Specs), an Auger electron spectrometer for surface analysis (CMA 100, Omicron Nanotechnology), an electron-ionization QMS (QMA 430, Pfeiffer Vacuum), leak valves (Pfeiffer Vacuum), a molecular beam doser for directed water dosage, and a gasline of in-house design (base pressure  $5 \cdot 10^{-8}$  mbar) which allows for the dosage of all other substrates through the leak valves. All liquids are purified by freeze-pump-thaw cycles prior to their use, and the absence of contaminants is checked by dosing the reactant into the chamber and performing QMS mass scans. A transfer chamber with a ( $z, \phi$ )-manipulator (Ferrovac MDG40) with a transfer tool enables the exchange of samples.

The manipulator carries three sample holders, two of which are identical. All three are heated resistively using wires made of a W-Re alloy (26% Re, Omega Engineering). The temperature is monitored using a calibrated readout of a twisted thermocouple (type C).[149] The two identical sample holders are based on a design by the Yates group[150, 151] and hold cylindrical TiO<sub>2</sub> single crystals (SurfaceNet GmbH) of 1 mm in diameter with the (110) facet exposed. Two notches are cut vis-a-vis into the sides of the crystal. This way, Ta plates of 0.125 mm thickness clamp the crystal onto a Ta heating plate with a gold foil of 0.025 mm thickness in between. The thermocouple is inserted directly into a hole drilled sideways into the crystal without any adhesive. The samples of these holders are not compatible with the load lock and cannot be mounted or removed without breaking the vacuum. They were used for the study discussed in section 4.1.

The second sample holder is also made of Ta and carries exchangeable Ta plates into which the actual sample is put. The latter have a cutout spacing to carry TiO<sub>2</sub> single crystals (SurfaceNet GmbH, 10 mm × 10 mm × 0.3 mm with the (110) facet exposed), with a gold foil of 0.025 mm thickness in between. The crystal is stabilized by two Ta sheets spot-welded vis-a-vis onto the exchangeable Ta plate. This system was used for the studies discussed in section 4.2 and 4.3.

### 3.3 Laser System for Photocatalytic Studies

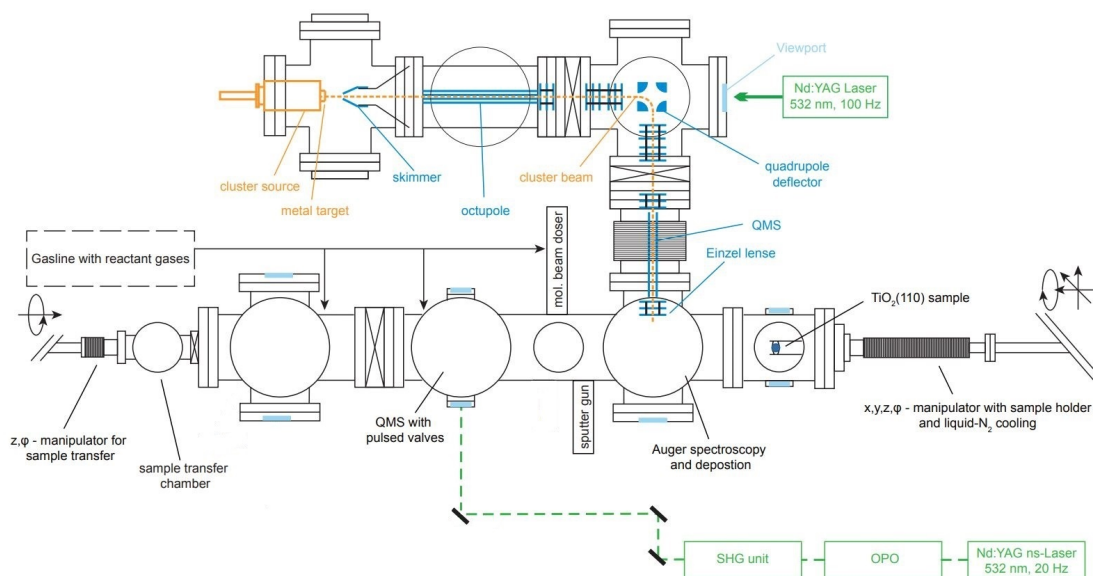


**Figure 3.1:** Sketch of the experimental setup used in this work which is divided into two parts: the laser vaporization cluster source for the generation of Pt or Ni clusters as co-catalysts (top) and the analysis chamber for surface preparation, characterization, and reactivity measurements (bottom). Adapted with permission from [83]. Copyright 2018 American Chemical Society.

### 3.3 Laser System for Photocatalytic Studies

Photocatalytic experiments were conducted using the second harmonic (241.8 nm) of an optical parametric oscillator (premiScan ULD/400, GWU) pumped by the third harmonic of a Nd:YAG laser (Spitlight 1200, 20 Hz, Innolas). Idler and signal beam are separated using a Pellin-Broca prism. The resulting laser beam has a wavelength of 241.8 nm and a pulse energy of 500  $\mu\text{J}$  to 1000  $\mu\text{J}$  after exiting the prism and being deflected by a metal mirror (protected Al). The power can be further lowered using a grey filter. The UV beam is then guided into the UHV chamber with two mirrors and a periscope (CVI Melles Griot), where it reaches the single crystal at an angle of  $30^\circ$  with respect to the surface normal. The pulse energy on the crystal surface is approximately 1/3 of the energy measured after the deflection mirror behind the laser housing exit.

### 3.4 Sample Preparation

The reduced TiO<sub>2</sub>(110) surface is generally obtained by cycles of Ar ion sputtering (1.0 keV,  $5 \cdot 10^{-6}$  mbar, 12  $\mu\text{A}$  ion current, 20 min) and vacuum annealing (800 K, 10 min). A hydroxylated surface is prepared from the reduced surface by dosing water onto the sample using the molecular beam doser (usually 420 mbar 420 mbar backpressure at the micro-capillary plate for 4 min) at cryogenic temperatures and a subsequent short annealing at 350 K. The surface purity is confirmed using Auger electron spectroscopy

### 3 Experimental Methods

(AES) and the thermal reactivity is checked by means of water and methanol TPD. The photochemical activity is probed by the photocatalytic conversion of 2-methyl-2-pentanol.

## 3.5 Temperature Programmed Desorption

The reactant of choice is adsorbed onto the crystal surface at cryogenic temperatures using a leak valve and Langmuir dosing or the molecular beam doser in case of water. The sample is then placed at a distance of approximately 2 mm below the skimmer of the QMS in a line of sight geometry. For PI-TPD measurements, the sample is irradiated at a wavelength of 241.8 nm for a certain duration prior to heating. The heating ramp is performed resistively and monitored using a temperature readout (Eurotherm 2408) with a rate of 0.8 K/s. The desorbing species are monitored by the QMS.

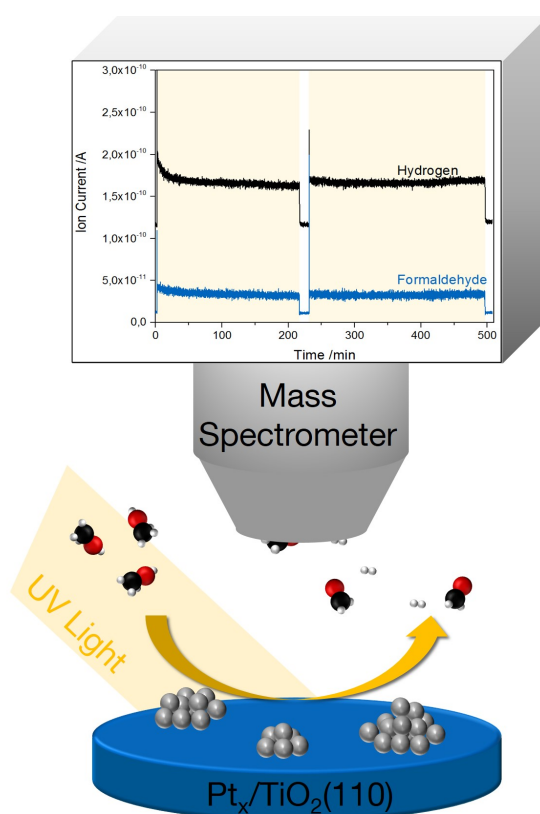


**Figure 3.2:** Principle behind the photocatalytic measurements with the example of methanol photoreforming on Pt-loaded  $TiO_2(110)$ . The reaction is started by UV illumination (yellow background) at a certain background pressure of the reactant. Upon light exposure, the traces of the desorbing reaction products are detected in the QMS.

### **3.6 Photocatalytic Measurements and Photon-Stimulated Desorption**

For photon-stimulated desorption (PSD) measurements, the reactant is dosed onto the crystal at cryogenic temperatures. The sample is moved to a fixed distance below the skimmer of the QMS in a line of sight geometry and heated to a temperature of choice. The crystal is illuminated and the desorption products are detected by the QMS.

For photocatalytic experiments, the crystal is first brought to the same position as for PSD experiments and heated to the desired temperature. The reactant is then continuously dosed into the chamber using a leak valve in a way that a certain substrate background pressure is established. The  $\text{TiO}_2(110)$  surface is illuminated and the desorbing photoproducts are detected by the QMS as depicted in figure 3.2.



## 4 Results - Publication Summaries

This chapter includes short summaries of the journal articles published in the course of this thesis. The focus is set on the chemical and physical insights obtained from the results.

## 4.1 Reactions in the Photocatalytic Conversion of Tertiary Alcohols on Rutile TiO<sub>2</sub>(110)

According to chemistry textbooks, tertiary alcohols are very difficult to oxidize in the liquid phase under ambient conditions.[109] Only specifically functionalized substrates, often combined with an appropriate catalyst, are suitable for selective oxidation. However, Walenta *et al.* demonstrated the selective photo-oxidation of *tert*-butanol on Pt<sub>x</sub>/TiO<sub>2</sub>(110) in UHV.[141] More complex tertiary alcohols can be photoreformed in a similar way, with the selectivity depending on the respective moieties and chain lengths. As discussed in section 2.3, tertiary alcohols adsorb to a certain extent dissociatively on the TiO<sub>2</sub>(110) surface, yielding a hydroxyl species and the corresponding alkoxy molecule.[71, 72] Here, it is found that under UV light, a photohole mediates the homolytic C-C bond cleavage between the carbonyl carbon and a hydrocarbon chain. Generally, this oxidation step forms a ketone and an alkyl radical species. The selectivity is determined by the length of the individual chains attached to the carbonyl group. The ketone desorbs into the gas phase at sufficiently high temperatures. On bare TiO<sub>2</sub>(110), the alkyl radical recombines with the hydrogen species that stems from the dissociative adsorption of the alcohol, and desorbs as alkane. On Pt-loaded titania, an additional pathway is facilitated, which becomes more dominant at elevated reactant pressure. The Pt clusters enable the recombinative adsorption of surface hydrogen species to form H<sub>2</sub>, while the alkyl surface species may also recombine with each other to yield the corresponding longer-chain alkane.

Since the bare titania surface facilitates the recombinative desorption of the alkyl and hydrogen surface species, i.e. all reaction products are removed from the equilibrium. Thus, the photo-oxidation of tertiary alcohols can be conducted on TiO<sub>2</sub>(110) catalytically in the absence of any co-catalyst. This is different to primary and secondary alcohols, where an  $\alpha$ -H is cleaved in the oxidation step. The thus formed hydroxyl species cannot desorb from the surface as H<sub>2</sub> in the absence of metal cluster co-catalysts such as Pt and hence poison the surface (see section 4.2).

The chain lengths of the tertiary alcohol determine the selectivity of photo-oxidation step. Methyl groups are not cleaved at all in the presence of longer alkyl moieties. The photoreforming of 2-methyl-2-butanol and 2-methyl-2-pentanol, both of which contain two methyl groups, exclusively yields acetone next to propane and ethane, respectively. The photoconversion of 3-methyl-3-hexanol allows both the ethyl and the propyl group to be cleaved, yielding the respective alkanes next to ethane and propane in molecular ratio of 2:1. The tendency of bond cleavage can be qualitatively estimated from thermodynamics by comparing their free energies of formation in the gas phase.

Apart from different selectivities, the presence of Pt clusters generally also enhances the overall reaction rate, expressed by the TOF. Yet while the selectivity changes due to the presence of platinum (which allows an additional reaction pathway), it does not change further by increasing coverages of this co-catalyst.



## Photocatalysis

 International Edition: DOI: 10.1002/anie.201907917  
 German Edition: DOI: 10.1002/ange.201907917

# Reactions in the Photocatalytic Conversion of Tertiary Alcohols on Rutile TiO<sub>2</sub>(110)

Carla Courtois<sup>+</sup>, Moritz Eder<sup>+</sup>, Kordula Schnabl, Constantin A. Walenta, Martin Tschurl, and Ulrich Heiz<sup>\*</sup>

**Abstract:** According to textbooks, tertiary alcohols are inert towards oxidation. The photocatalysis of tertiary alcohols under highly defined vacuum conditions on a titania single crystal reveals unexpected and new reactions, which can be described as disproportionation into an alkane and the respective ketone. In contrast to primary and secondary alcohols, in tertiary alcohols the absence of an  $\alpha$ -H leads to a C–C-bond cleavage instead of the common abstraction of hydrogen. Surprisingly, bonds to methyl groups are not cleaved when the alcohol exhibits longer alkyl chains in the  $\alpha$ -position to the hydroxyl group. The presence of platinum loadings not only increases the reaction rate but also opens up a new reaction channel: the formation of molecular hydrogen and a long-chain alkane resulting from recombination of two alkyl moieties. This work demonstrates that new synthetic routes may become possible by introducing photocatalytic reaction steps in which the co-catalysts may also play a decisive role. Open access funding enabled and organized by Projekt DEAL.

The selective oxidation of alcohols to aldehydes and ketones is a fundamental topic in various fields of chemistry ranging from heterogeneous catalysis to synthetic organic chemistry.<sup>[1]</sup> In contrast to the facile oxidation of primary and secondary alcohols, tertiary alcohol typically do not react analogously, due to the required cleavage of a C–C instead of a C–H bond to establish the carbonyl functionality.<sup>[2]</sup> As tertiary alcohol oxidation is generally difficult, in particular in a selective manner, publications on this subject are thus scarce and often a broad product spectrum results.<sup>[1c,2,3]</sup> Conventional synthetic methods often rely on auxiliary compounds or quantitative amounts of oxidants to enable the reaction in the first place.<sup>[4]</sup>

Often the conversion is conducted with the use of toxic metal oxides such as chromium(VI) oxides.<sup>[5]</sup>

An alternative approach for alcohol reforming is photocatalysis using semiconductors.<sup>[6]</sup> For example, Teichner and co-workers successfully photooxidized 2-methyl-2-butanol by means of UV irradiation on a nonporous anatase catalyst in the presence of oxygen. The proposed reaction pathways take place via olefin intermediates, leading to the reaction products acetone, ethanal, and 2-butanone.<sup>[7]</sup>


In general, titania is by far the most used material in photocatalysis due to its reaction properties and availability.<sup>[8]</sup> While it is commonly applied in a nanostructure form (e.g. as P25), the material's structural complexity often prevents the elucidation of exact reaction mechanisms.<sup>[9]</sup> As in thermal catalysis, defined single-crystal surfaces under highly defined conditions in ultra-high vacuum (UHV) are more suitable for this purpose.<sup>[10]</sup> In heterogeneous photocatalysis, rutile TiO<sub>2</sub>(110) surfaces have been comprehensively employed in alcohol conversion thermally<sup>[11]</sup> and photochemically.<sup>[12]</sup> Thus, this material represents the best-suited model system, even though other titania systems (e.g. anatase) may exhibit better photoactivities.


For this report, we investigated the photochemical reaction behavior of longer-chain tertiary alcohols (3-methyl-3-hexanol, 2-methyl-2-pentanol, and 2-methyl-2-butanol) on bare and platinum-loaded rutile TiO<sub>2</sub>(110) in an UHV environment in the absence of oxygen and water. We demonstrate that the alcohols undergo unexpected and new photocatalytic reactions, which enable general mechanistic insights. Furthermore, we show that the rich chemistry of tertiary alcohols makes them an interesting model system for photocatalysis. For example, they enable the elucidation of the behavior of alkyl radicals on surfaces, important for the photo-Kolbe reaction<sup>[13]</sup> and the Fischer–Tropsch process.<sup>[14]</sup> In the latter, TiO<sub>2</sub> represents a common support material.<sup>[15]</sup>

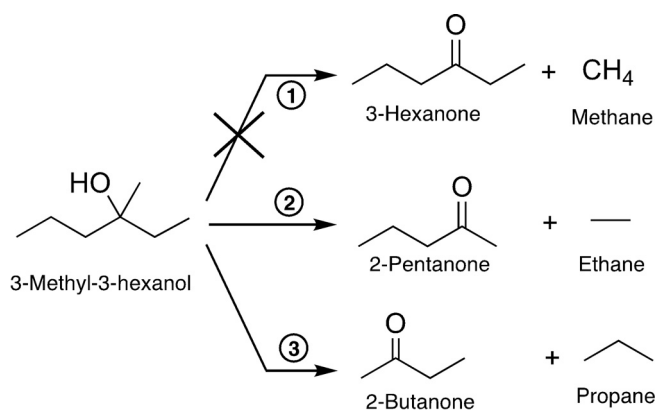
The UV illumination of a TiO<sub>2</sub>(110) crystal, decorated with a defined coverage (0.1 % monolayer (ML)) of platinum clusters ranging in size range from Pt<sub>8</sub> to about Pt<sub>25</sub>, leads to a photocatalytic reaction of 3-methyl-3-hexanol, which results in a complex fragmentation pattern in the mass spectrum. However, a detailed analysis reveals (see Figure S2) that only two parallel reactions occur, both of which are an oxidation to a ketone and a corresponding alkane (2-pentanone and ethane, 2-butanone and propane, see Scheme 1). While the formation of higher alkanes is observed, a reaction yielding methane is not. Monitoring mass traces specific for a particular molecule (Figure 1) demonstrates that the reaction is truly catalytic under illumination and formation of unwanted surface species leading to catalyst poisoning does not occur.

[\*] C. Courtois,<sup>[†]</sup> M. Eder,<sup>[‡]</sup> K. Schnabl, Dr. C. A. Walenta, Dr. M. Tschurl, Prof. Dr. U. Heiz  
 Chair of Physical Chemistry  
 Department of Chemistry & Catalysis Research Center  
 Technische Universität München  
 Lichtenbergstraße 4, 85748 Garching (Germany)  
 E-mail: ulrich.heiz@mytum.de

[†] These authors contributed equally to this work

 Supporting information and the ORCID identification number(s) for the author(s) of this article can be found under:  
<https://doi.org/10.1002/anie.201907917>.

 © 2019 The Authors. Published by Wiley-VCH Verlag GmbH & Co. KGaA. This is an open access article under the terms of the Creative Commons Attribution License, which permits use, distribution and reproduction in any medium, provided the original work is properly cited.



**Scheme 1.** Reaction scheme for the photoreforming of 3-methyl-3-hexanol on Pt<sub>x</sub>/r-TiO<sub>2</sub>(110) and on r-TiO<sub>2</sub>(110) under UV illumination. The reaction can be seen formally as a hole-mediated disproportionation yielding an alkane and the respective ketone; however, this does not occur for the formation of methane.

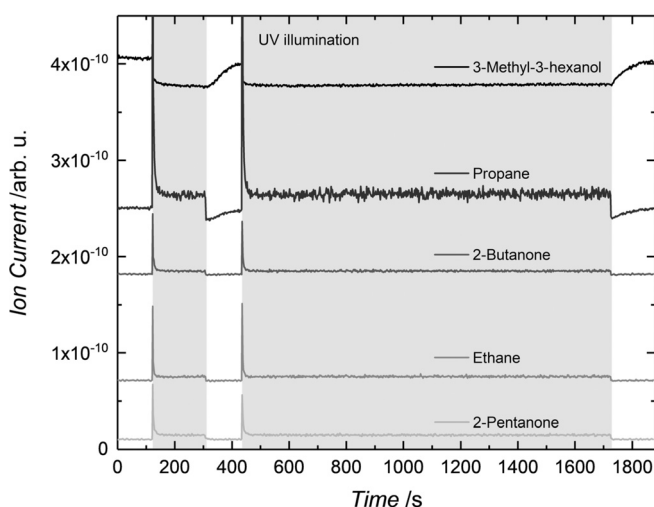


**Figure 1.** Photocatalytic products of 3-methyl-3-hexanol photoreforming on Pt<sub>x</sub>/r-TiO<sub>2</sub>(110) (0.1% monolayer (ML) cluster coverage). Signals for 3-methyl-3-hexanol ( $m/z$  73), propane ( $m/z$  29), 2-butanone ( $m/z$  72), ethane ( $m/z$  30), and 2-pentanone ( $m/z$  86) are shown at 340 K under a 3-methyl-3-hexanol background pressure of  $1.7 \times 10^{-7}$  mbar. The gray region highlights the period of UV laser irradiation. The initial burst of the signal originates from higher surface concentrations of the alcohol before the start of the illumination. Note that the traces are offset for clarity. The traces demonstrate that two different photocatalytic reactions occur in parallel yielding a ketone and the respective alkane.

Compared to the photoreforming of other alcohols, the observed reaction pathways are unexpected. The absence of an  $\alpha$ -H precludes the common C–H cleavage to form H<sub>2</sub> and the respective aldehyde or ketone, as detected for primary and secondary alcohols.<sup>[2,16]</sup> Therefore, the ejection of radicals and concomitant stoichiometric production of H<sub>2</sub> is expected in analogy to *tert*-butanol photoreforming.<sup>[17]</sup> Neither radical abstraction nor significant molecular hydrogen formation is detected for prolonged reaction times. Instead, this reaction, which to the best of our knowledge has never been described before, can be viewed as a photocatalytic disproportionation

yielding higher alkanes and the respective ketones. Interestingly, reaction products originating from the cleavage of the methyl group are not observed (Figure S9). In the same way, dehydration reactions, common in thermal reactions, also do not occur (Figure S9). The same reaction is observed for tertiary alcohols with two methyl groups at the  $\alpha$ -C position (namely, 2-methyl-2-butanol and 2-methyl-2-pentanol), for which only the long carbon chain is abstracted with 100% selectivity (see Figures S3 and S4). Consequently, the formation of acetone and the respective alkane results exclusively. This demonstrates the generality of our findings. The same products are observed under ambient conditions even for 2-methyl-2-butanol, but the presence of oxygen and water leads to additional by-products.<sup>[7,18]</sup>

This new reaction can be explained with the mechanism we suggested for the photoreforming of alcohols on TiO<sub>2</sub> in the gas phase.<sup>[17a]</sup> The photoactive alkoxy species, which are already formed upon surface adsorption in the dark<sup>[12,19]</sup> undergo a hole-mediated oxidation reaction, resulting in the cleavage of a C–C bond. The role of alkoxy compounds as the photoactive species on TiO<sub>2</sub>(110) in alcohol photoreforming has been demonstrated convincingly in the works of Henderson and others.<sup>[12,20]</sup> Methyl radical ejection observed with *tert*-butanol demonstrates that the photocatalytic oxidation reaction occurs via a homolytic C–C bond scission. In contrast to methyl groups, longer alkyl chains such as ethyl and propyl exhibit stronger interactions with the TiO<sub>2</sub> surface in their adsorption geometry and thus remain on the surface. This is in perfect agreement with their absence in the mass spectra.

These surface alkyl radicals undergo recombination in a consecutive thermal reaction step with hydrogen atoms originating from the dissociative adsorption of the alcohol. This reaction is also facilitated on bare TiO<sub>2</sub>(110) (i.e., in the absence of Pt) in contrast to the recombination of two hydrogen atoms. Consequently, photoreforming of higher tertiary alcohols occurs in a photocatalytic manner even without any co-catalyst (Figure 2a) and on a hydroxylated surface (as shown in Figure S13 for 2-methyl-2-pentanol photoreforming), in contrast to  $\alpha$ -H-containing alcohols. For the latter, surface hydroxylation results in the poisoning of the photocatalyst.<sup>[17a]</sup> The deposition of small amounts of Pt clusters significantly increases the overall reaction rate, with higher loadings leading only to a small increase in the turnover frequency (TOF) (Figure 2a). This trend is in good agreement with findings from methanol photoreforming in UHV<sup>[17a]</sup> and with colloidal systems.<sup>[21]</sup>

In good accordance with the interpretation of the photo-oxidation on the semiconductor and a consecutive alkane formation, the selectivity of the reaction of 3-methyl-3-hexanol remains unaffected by the degree of Pt coverage (Figure 2b). It also remains constant at temperatures (Figure S8b) between 230 and 360 K, further demonstrating the photocatalytic nature of the reaction. In order to explain the observed selectivity of pentanone to butanone of about 2:1 (i.e., the preferred cleavage of ethyl over propyl and the general absence of methyl), the thermochemistry of the reactions may be used to obtain qualitative insights. All three possible reactions displayed in Scheme 1 are endothermic by about 20 to 30 kJ mol<sup>-1</sup> (see the corresponding chapter in the

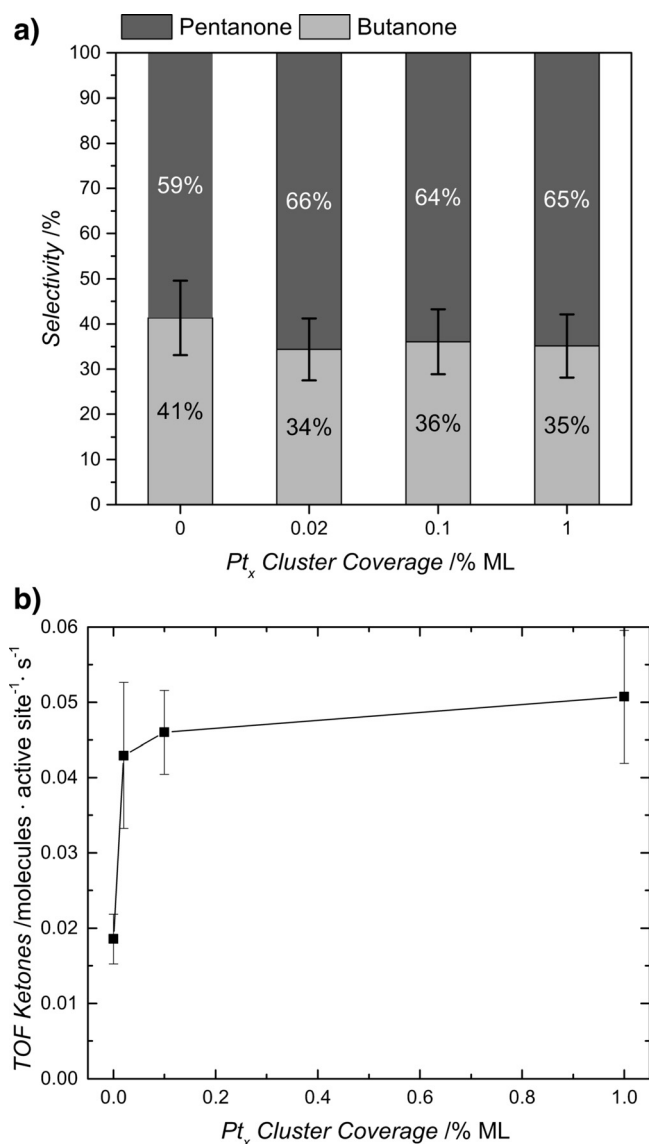
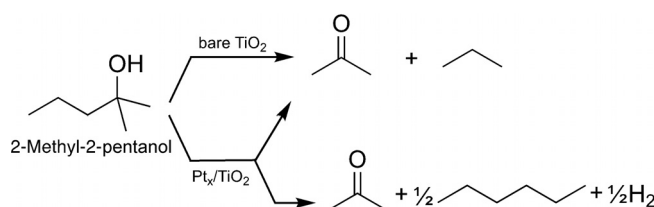


**Figure 2.** Photocatalytic conversion of 3-methyl-3-hexanol on Pt-decorated *r*-TiO<sub>2</sub>(110). In (a) the TOF of the ketones (sum of 2-butanone and 2-pentanone) is shown for different Pt<sub>x</sub> cluster coverages. In (b) the selectivities for 2-pentanone and 2-butanone based on the TOFs are displayed for bare *r*-TiO<sub>2</sub>(110) and for different Pt loadings on *r*-TiO<sub>2</sub>(110). A monolayer ML refers to the surface atoms. 0% ML stands for the bare *r*-TiO<sub>2</sub>(110). While the deposition of Pt clusters does not affect the reaction's selectivity, it initially increases the TOF. However, higher loadings do not have a similar effect.

Supporting Information). Model reactions for the photocatalytic C–C bond cleavage suggest that the formation of methyl radicals requires significantly more energy than ethyl or propyl formation (see details in the Supporting Information). In addition, longer-chain alkyl moieties than methyl exhibit stronger interactions with the surface. These radicals are therefore not detected in the gas phase, in contrast to the ejection of methyl radicals in *tert*-butanol photoreforming. For ethyl and propyl formation, the difference in thermochemistry is less pronounced compared to methyl. However, reactions yielding ethyl are generally more endothermic than propyl formation. This trend is reflected in the observed

selectivity of the reaction; pentanone and an ethyl radical are preferentially formed over butanone and a propyl radical. Therefore, thermodynamic values may be used as a rule-of-thumb to predict preferential bond cleavage in similar photoreactions.

Performing the reaction at different pressures ( $3 \times 10^{-8}$  mbar to  $5 \times 10^{-6}$  mbar) with the Pt-loaded photocatalyst does not affect the branching ratio for the two reactions (Figure S8a). The overall TOFs exhibit typical 1<sup>st</sup> order behavior when the reaction is limited by reactant adsorption and 0<sup>th</sup> order in the case of limitation by product desorption (see Figures S5 and S6). Similarly, the illumination-dependent TOFs (see Figure S7) suggest a first-order behavior at lower irradiation intensities, which transfer into a saturation regime (zeroth order) at higher photon fluxes, as in the photoreforming of other alcohols.<sup>[17a]</sup> However, and more importantly, for platinum-decorated TiO<sub>2</sub>(110) an additional side reaction becomes evident at higher pressures. This is best illustrated for 2-methyl-2-pentanol photoreforming (Scheme 2), for which all reaction products can clearly be



**Scheme 2.** Reaction scheme for the photoreforming of 2-methyl-2-pentanol on bare *r*-TiO<sub>2</sub>(110) and Pt<sub>x</sub>/*r*-TiO<sub>2</sub>(110) under UV illumination. While on bare titania only the hole-mediated disproportionation yielding acetone and propane occurs, a second reaction pathway is enabled for Pt-decorated TiO<sub>2</sub> above  $2.0 \times 10^{-7}$  mbar alcohol pressure. In the latter reaction, hydrogen recombines on the Pt clusters and two propyl radicals recombine forming hexane.

quantified and their analysis is not affected by isobaric interference. As deposited platinum clusters enable the efficient thermal recombination of hydrogen atoms,<sup>[17a]</sup> the surface coverage of alkyl increases in the steady state with increasing pressure. Consequently, the recombination product of two radicals (i.e., hexane) accompanied by H<sub>2</sub> formation is detected at  $5 \times 10^{-6}$  mbar of alcohol pressure (Figure 3a).

As the formation of H<sub>2</sub> is not facilitated on bare titania, this side reaction is not observed in the absence of a cocatalyst (Figure 3b). Consequently, this result also demonstrates that with the addition of noble-metal clusters, not only unwanted consecutive reactions (as for example the hydrogenation of ketones recently studied mechanistically by electrochemistry<sup>[22]</sup>), but also an intrinsically different outcome of the photoreaction cycle must be considered in applied systems.

To summarize, we discovered a new reaction for the photoreforming of tertiary alcohols on rutile, which can be described as hole-mediated disproportionation yielding an alkane and the respective ketone. Surprisingly, the abstraction of methyl groups does not occur and only  $\alpha$ -C bonds to longer alkyl chains are selectively cleaved, in contrast to the reaction

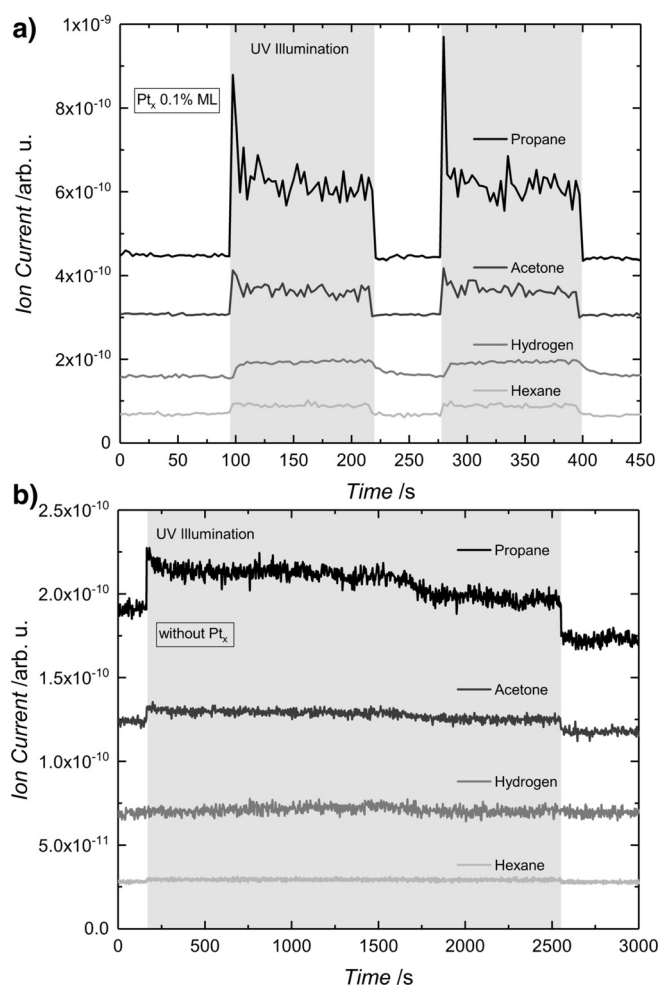


**Figure 3.** Photocatalytic products of 2-methyl-2-pentanol photoreforming on a) Pt<sub>x</sub>/r-TiO<sub>2</sub>(110) (0.1% ML cluster coverage) and b) r-TiO<sub>2</sub>(110). Propane (*m/z* 29), acetone (*m/z* 58), hydrogen (*m/z* 2), and hexane (*m/z* 86) signals are shown at 336 K under a 2-methyl-2-pentanol background pressure of  $5.0 \times 10^{-6}$  mbar. The gray region highlights the period of UV laser irradiation. Note that the traces are offset for clarity. In contrast to bare TiO<sub>2</sub>(110), the co-catalyst-loaded semiconductor enables another side reaction, alkyl radical recombination and molecular hydrogen formation.

of *tert*-butanol. The thermochemistry of radical formation may supply a qualitative measure to predict the selectivity of the photoreaction. As the recombination of the alkyl radical and hydrogen is enabled on bare titania, in contrast to the recombination of two hydrogen atoms, the reaction is fully catalytic even without a co-catalyst. While already small amounts of Pt clusters on the rutile crystal increase the overall reaction rate, they also induce another reaction pathway yielding molecular hydrogen and the recombination product of two radicals observed at increasing pressures.

The observed mechanisms may explain the variety of product distributions from ambient pressure and liquid photoreforming studies and have set mechanistic research in photocatalysis on a solid foundation.

## Acknowledgements

We thank Martin Stutzmann (TU Munich) for helpful discussions and the DFG for project funding via grant HE3435/22-1. C.C. acknowledges the support by the Luxembourg National Research Fund (FNR), project code 12531916 and by the TUM International Graduate School of Science and Engineering (TUM-IGSSE). Open access funding enabled and organized by Projekt DEAL.

## Conflict of interest

The authors declare no conflict of interest.

**Keywords:** alcohol reforming · photocatalysis · reaction mechanisms · tertiary alcohols · titania

**How to cite:** *Angew. Chem. Int. Ed.* **2019**, *58*, 14255–14259  
*Angew. Chem.* **2019**, *131*, 14393–14397

- [1] a) J. H. J. Kluytmans, A. P. Markusse, B. F. M. Kuster, G. B. Marin, J. C. Schouten, *Catal. Today* **2000**, *57*, 143; b) G. Tojo, M. I. Fernández, *Oxidation of Alcohols to Aldehydes and Ketones: A Guide to Current Common Practice*, 1st ed., Springer, New York, **2006**; c) M. N. Kopylovich, A. P. C. Ribeiro, E. C. B. A. Alegria, N. M. R. Martins, L. M. D. R. S. Martins, A. J. L. Pombeiro, *Adv. Organomet. Chem.* **2015**, *63*, 91; d) R. A. Sheldon, H. v. Bekkum, *Fine chemicals through heterogeneous catalysis*, 1st ed., Wiley-VCH, Weinheim, **2001**.
- [2] K. Wietzerbin, J. Bernadou, B. Meunier, *Eur. J. Inorg. Chem.* **2000**, 1391.
- [3] a) D. F. Chen, Y. C. Zhang, X. Y. Pan, F. Wang, S. L. Huang, *Adv. Synth. Catal.* **2018**, *360*, 3607; b) K. Matsunaga, H. Hirajima, A. Kishida, K. Takatori, H. Nagaoka, *Tetrahedron Lett.* **2015**, *56*, 5941.
- [4] a) E. Brenna, M. Crotti, M. De Pieri, F. G. Gatti, G. Manenti, D. Monti, *Adv. Synth. Catal.* **2018**, *360*, 3677; b) H. G. Yayla, H. J. Wang, K. T. Tarantino, H. S. Orbe, R. R. Knowles, *J. Am. Chem. Soc.* **2016**, *138*, 10794; c) J. M. Vatèle, *Tetrahedron* **2010**, *66*, 904.
- [5] a) G. Cainelli, G. Cardillo, *Chromium oxidations in organic chemistry*, Springer, Berlin, New York, **1984**; b) S. V. Ley, A. Madin, in *Comprehensive Organic Synthesis* (Eds.: B. M. Trost, I. Fleming), Pergamon, Oxford, **1991**, p. 251; c) F. A. Luzzio in *Organic Reactions* (Eds.: P. A. Evans, S. Weinreb), Vol. 53, Wiley, **1998**, DOI: 10.1002/0471264180.or053.01.
- [6] “Photocatalytic Synthesis of Chemicals”: M. Kobielusz, P. Mikrut, W. Macyk, in *Materials for Sustainable Energy*, Vol. 72, Academic Press, San Diego, **2018**, pp. 93–144.
- [7] A. Walker, M. Formenti, P. Meriaudeau, S. J. Teichner, *J. Catal.* **1977**, *50*, 237.
- [8] a) M. A. Henderson, *Surf. Sci. Rep.* **2011**, *66*, 185; b) A. Fujishima, X. T. Zhang, D. A. Tryk, *Surf. Sci. Rep.* **2008**, *63*, 515; c) J. Schneider, M. Matsuoka, M. Takeuchi, J. L. Zhang, Y. Horiuchi, M. Anpo, D. W. Bahnemann, *Chem. Rev.* **2014**, *114*, 9919.
- [9] B. Ohtani, O. O. Prieto-Mahaney, D. Li, R. Abe, *J. Photochem. Photobiol. A* **2010**, *216*, 179.
- [10] a) U. Diebold, *Appl. Phys. A* **2003**, *76*, 681; b) U. Diebold, *Surf. Sci. Rep.* **2003**, *48*, 53.
- [11] a) Y. K. Kim, B. D. Kay, J. M. White, Z. Dohnalek, *J. Phys. Chem. C* **2007**, *111*, 18236; b) Z. Dohnálek, I. Lyubinetsky, R. Rousseau, *Prog. Surf. Sci.* **2010**, *85*, 161; c) Z. J. Li, R. S. Smith, B. D. Kay, Z. Dohnalek, *J. Phys. Chem. C* **2011**, *115*, 22534.



- [12] a) M. A. Henderson, I. Lyubinsky, *Chem. Rev.* **2013**, *113*, 4428; b) M. Shen, D. P. Acharya, Z. Dohnalek, M. A. Henderson, *J. Phys. Chem. C* **2012**, *116*, 25465; c) M. M. Shen, M. A. Henderson, *J. Phys. Chem. Lett.* **2011**, *2*, 2707.
- [13] a) B. Kraeutler, C. D. Jaeger, A. J. Bard, *J. Am. Chem. Soc.* **1978**, *100*, 4903; b) D. Yang, X. Y. Ni, W. K. Chen, Z. Weng, *J. Photochem. Photobiol. A* **2008**, *195*, 323.
- [14] W. A. Herrmann, *Angew. Chem. Int. Ed. Engl.* **1982**, *21*, 117; *Angew. Chem.* **1982**, *94*, 118.
- [15] E. Iglesia, *Appl. Catal. A* **1997**, *161*, 59.
- [16] M. B. Smith, *March's Advanced Organic Chemistry: Reactions, Mechanisms, and Structure*, 7<sup>th</sup> ed., John Wiley & Sons, Inc, Hoboken, **2013**, pp. 1433–1497.
- [17] a) C. A. Walenta, S. L. Kollmannsberger, C. Courtois, R. N. Pereira, M. Stutzmann, M. Tschurl, U. Heiz, *Phys. Chem. Chem. Phys.* **2019**, *21*, 1491; b) S. L. Kollmannsberger, C. A. Walenta, C. Courtois, M. Tschurl, U. Heiz, *ACS Catal.* **2018**, *8*, 11076.
- [18] J. Cunningham, B. K. Hodnett, A. Walker, *Proc. R. Ir. Acad. Sect. B* **1977**, *77*, 411.
- [19] a) Z. R. Zhang, R. Rousseau, J. L. Gong, B. D. Kay, Z. Dohnalek, *J. Am. Chem. Soc.* **2009**, *131*, 17926; b) E. Farfan-Arribas, R. J. Madix, *J. Phys. Chem. B* **2002**, *106*, 10680; c) M. A. Henderson, S. Otero-Tapia, M. E. Castro, *Faraday Discuss.* **1999**, *114*, 313.
- [20] K. R. Phillips, S. C. Jensen, M. Baron, S.-C. Li, C. M. Friend, *J. Am. Chem. Soc.* **2013**, *135*, 574.
- [21] G. R. Bamwenda, S. Tsubota, T. Nakamura, M. Haruta, *J. Photochem. Photobiol. A* **1995**, *89*, 177.
- [22] C. J. Bondue, M. T. M. Koper, *J. Catal.* **2019**, *369*, 302.
- [23] U. Heiz, F. Vanolli, L. Trento, W. D. Schneider, *Revi. Sci. Instruments* **1997**, *68*, 1986.
- [24] C. A. Walenta, S. L. Kollmannsberger, J. Kiermaier, A. Winbauer, M. Tschurl, U. Heiz, *Phys. Chem. Chem. Phys.* **2015**, *17*, 22809.
- [25] M. A. Henderson, *Langmuir* **1996**, *12*, 5093.
- [26] Z. H. Geng, X. C. Jin, R. M. Wang, X. Chen, Q. Guo, Z. B. Ma, D. X. Dai, H. J. Fan, X. M. Yang, *J. Phys. Chem. C* **2018**, *122*, 10956.
- [27] a) Y. Watanabe, X. Y. Wu, H. Hirata, N. Isomura, *Catal. Sci. Technol.* **2011**, *1*, 1490; b) N. Isomura, X. Y. Wu, H. Hirata, Y. Watanabe, *J. Vac. Sci. Technol. A* **2010**, *28*, 1141.

Manuscript received: June 25, 2019

Accepted manuscript online: August 7, 2019

Version of record online: August 28, 2019

## Supporting Information

### **Reactions in the Photocatalytic Conversion of Tertiary Alcohols on Rutile TiO<sub>2</sub>(110)**

*Carla Courtois<sup>+</sup>, Moritz Eder<sup>+</sup>, Kordula Schnabl, Constantin A. Walenta, Martin Tschurl, and Ulrich Heiz\**

anie\_201907917\_sm\_miscellaneous\_information.pdf

# Supporting Information:

## Experimental Overview

The details of the experimental setup are described below and also elsewhere.<sup>S1</sup> In brief, measurements are performed with a complex UHV apparatus featuring a laser vaporization cluster source for the deposition of clusters with an atomically precise number of atoms.<sup>S2</sup> The cluster coverage is controlled by the deposition time and determined by recording the neutralization current with a picoammeter. The UHV chamber is equipped with an Auger spectrometer and an ion gun for Ar<sup>+</sup> sputtering for the preparation of a defined semiconductor surface. The sample is mounted on a sample holder,<sup>S3</sup> which is attached to a heatable and

liquid-N<sub>2</sub>-coolable manipulator in order to set the sample on a selected and defined temperature. The TiO<sub>2</sub>(110) crystal is cleaned following established procedures of sputtering and annealing cycles. The degree of surface reduction and absence of platinum is determined by H<sub>2</sub>O temperature-programmed desorption and the evaluation of traces of water<sup>S4</sup> and H<sub>2</sub>,<sup>S5</sup> respectively. The Pt/TiO<sub>2</sub>(110) model catalysts have been thoroughly characterized by a variety of local and integral techniques.<sup>S6</sup> Photocatalytic measurements are performed by illuminating the sample with a Nd:YAG-pumped, frequency-doubled OPO laser beam at 242 nm in an alcohol background. Product evolution is followed by a quadrupole mass spectrometer placed in line of sight with the photocatalyst.

## Experimental Details

The setup consists of a laser vaporization cluster generation source and an ultra-high vacuum (UHV) setup. For cluster generation, a focused beam of the frequency-doubled of a Nd:YAG (532 nm, 100 Hz, Spitlight DPSS, Innolas) ablates a rotating Pt target (99.96% purity, ESG Edelmetalle, Germany). The resulting plasma is cooled by the expansion of a He gas pulse (He 6.0, Air Westfalen) into the vacuum. The cationic cluster beam is guided and bent into a quadrupole mass filter (QMF; Extrel, USA), which enables either the selection of a particular cluster size or the guidance of the clusters in ion-guide mode.<sup>S2</sup> For this study, the latter mode was used and was operated as high-pass filter transmitting only ions larger than Pt<sub>7</sub>. The settings resulted in a cluster size distribution with a maximum from Pt<sub>11</sub> to Pt<sub>13</sub> (see S1). 0.1% monolayer (ML) of Pt<sub>x</sub> clusters (relative to surface atoms) were deposited onto a TiO<sub>2</sub>(110) single crystal under soft landing conditions (<1eV/atom in kinetic energy). Cluster loadings were determined by recording the cluster neutralization current during the deposition with a picoammeter (Keithley, 6587). For experiments with different cluster coverages, the desired amount of platinum, which is specified in the presented data, was deposited by varying the deposition time (in the order of minutes). The as-obtained Pt-



decorated  $\text{TiO}_2(110)$  catalysts have been well-characterized in previous works by means of scanning probe microscopy and photoelectron spectroscopy.<sup>S6-S9</sup>

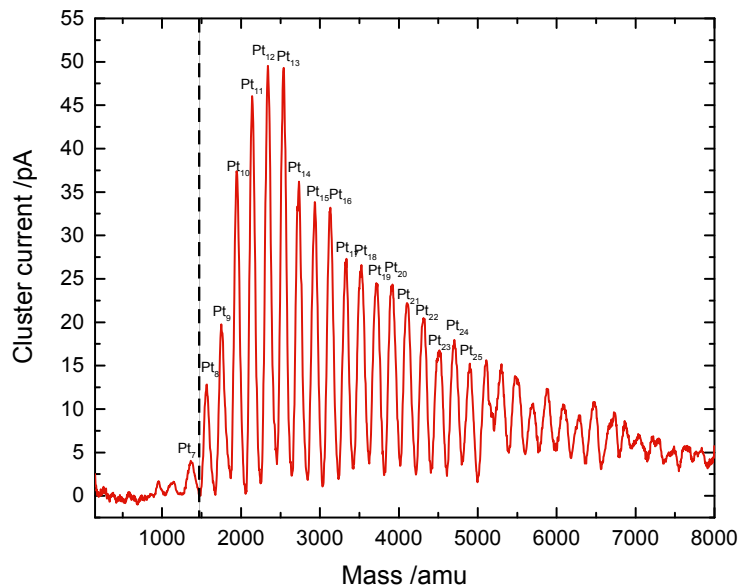


Figure S1: Size-distribution of platinum clusters from  $\text{Pt}_7$  to  $\text{Pt}_{35}$  with a maximum from  $\text{Pt}_{11}$  to  $\text{Pt}_{13}$  from the laser vaporization cluster source. The solid black line denotes the cut-off mass of the quadrupole mass filter during deposition.

In the UHV setup, a base pressure lower than  $9.8 \cdot 10^{-11}$  mbar is achieved. The sample in the chamber is mounted on a sample holder,<sup>S3</sup> which is attached to a  $(\phi, x, y, z)$ -manipulator (VAB Vakuum GmbH) in order to enable the movement of the sample to different positions. The sample holder enables liquid nitrogen cooling and the resistive heating of the crystal. For analysis, an auger spectroscope (MDC, HLM-275-3), an electron ionization quadrupole mass spectrometer (EI-QMS; QMA 430, Pfeiffer Vacuum GmbH) and a home-built photoionization time-of-flight mass spectrometer (PI-TOF-MS) are attached to the main chamber. The chamber is further equipped with a leak valve (Pfeiffer Vacuum) for Langmuir dosing and a molecular beam doser in order to introduce reactant gases into the vacuum via a gas line. The vapor pressure of 3-methyl-3-hexanol (99%, Alfa Aesar), 2-methyl-2-pentanol (99%, Sigma Aldrich) and 2-methyl-2-butanol ( $\geq 99\%$ , Sigma Aldrich) is exploited in order to introduce the reactants in the reaction chamber via a leak valve with a constant background pressure.

The surface of the rutile  $\text{TiO}_2(110)$  single crystal (SurfaceNet GmbH) is prepared by cycles of  $\text{Ar}^+$  (100% N60; Air Liquide) sputtering (1 keV,  $4 \cdot 10^{-5}$  mbar for several hours), oxygen ( $\geq 99\%$ ; Westfalen) annealing (800 K,  $1 \cdot 10^{-6}$  mbar, 20 min) and vacuum annealing (800 K, 10 min) until no contamination is observed by Auger electron spectroscopy with a respective spectrometer (Omicron Nanotechnology). The absence of Pt is further confirmed by the evaluation of the  $\text{H}_2$  trace in a  $\text{H}_2\text{O}$  thermal programmed desorption (TPD) experiment.<sup>S5</sup> The resulting light blue  $\text{TiO}_2$  has a bridge-bonded oxygen (BBO) vacancy concentration of  $6 \pm 1\%$  of Ti lattice sites, which is determined by  $\text{H}_2\text{O}$  TPD.<sup>S4</sup> All the experiments are performed on such a reduced  $\text{TiO}_2(110)$  crystal. Photoexcitation experiments are conducted with a frequency doubled OPO laser (GWU, premiScan ULD/400), which is pumped with the third harmonic of a Nd:YAG (Innolas Spitlight HighPower 1200, 7 ns pulse width, 20 Hz repetition rate), in order to achieve a wavelength of 242 nm (with a power of  $3.6 \pm 0.3$  mW at the crystal surface, if not otherwise noted). Product identification is performed with the above-mentioned QMS with mass scans under catalytic conditions (see for example figure S2) and the recording of specific mass traces for the quantification of the reaction rates (see for example figure S11). The QMS ion current is calibrated via the desorption integral of a saturation coverage of the Ti-lattice sites with methanol in a TPD experiment.

The turnover frequency (TOF) values are calculated by integrating the baseline corrected signals of the QMS. These are further corrected with the  $m/z$ -dependent transmissions through the QMS, electron impact ionization cross sections (ICS) as well as with a factor considering ion fragmentation which are taken from reference mass spectra. The fragmentation pattern are obtained from recording the mass spectra of the respective molecules. The ICS values and the  $m/z$ -value of the respective fragment used for the quantification are given in table S1.

Table S1: Electron impact ionization cross sensitivity values at 70 eV and m/z-value of the respective fragment used for quantification.

substance	ICS [ $\text{\AA}^2$ ]	m/z fragment
2-butanone	12.9 <sup>S10</sup>	72
2-pentanone	15.2 <sup>S10</sup>	86
propane	11.6 <sup>S10</sup>	29
ethane	8.39 <sup>S10</sup>	30
acetone	10.2 <sup>S10</sup>	58
hydrogen	1.021 <sup>S11</sup>	2
hexane	20.8 <sup>S10</sup>	86

## Evaluation of Mass Spectra

The products are identified by the evaluation the mass scans. Firstly, a mass scan **I** over the whole mass range with potential product masses, is carried out at a certain alcohol background pressure, which is given in the caption of the respective figure. This mass scan **I** includes the fragmentation pattern of the alcohol and possible contaminations from the residual gas in the UHV chamber (mainly H<sub>2</sub>, CO, CO<sub>2</sub> and H<sub>2</sub>O). Secondly, the sample is illuminated and a mass scan **II** under steady-state condition is recorded. This mass scan **II** includes the fragmentation pattern of the alcohol and its photo products. Subtracting mass scan **I** (dark) from mass scan **II** (illuminated) reveals a mass scan of the photocatalytic reaction. These spectra are named as difference spectra and are shown in Figure S2a, S3a and S4a. Positive values indicate that these masses arise from photo products and negative values originate from the consumed alcohol. In order to demonstrate that the resulting mass peaks are due to the presence of the ketones and the respective alkanes, self-recorded mass spectra of the reactant and products are added or subtracted from the difference spectrum

**a).**

In a first step, from spectrum **a)** to **b)**, the mass spectrum of the alcohol is added to the difference spectrum. This results spectrum **b)**, which only includes reaction products (i.e. positive signals). Subsequently, the mass peaks of one product after the other is subtracted from **b)** so that a baseline spectrum **d)** is obtained. Before every addition or subtraction, the mass spectrum is normalized to a unique mass fragment of the respective molecule. All the products can be clearly identified and it can be demonstrated, that no other products result.

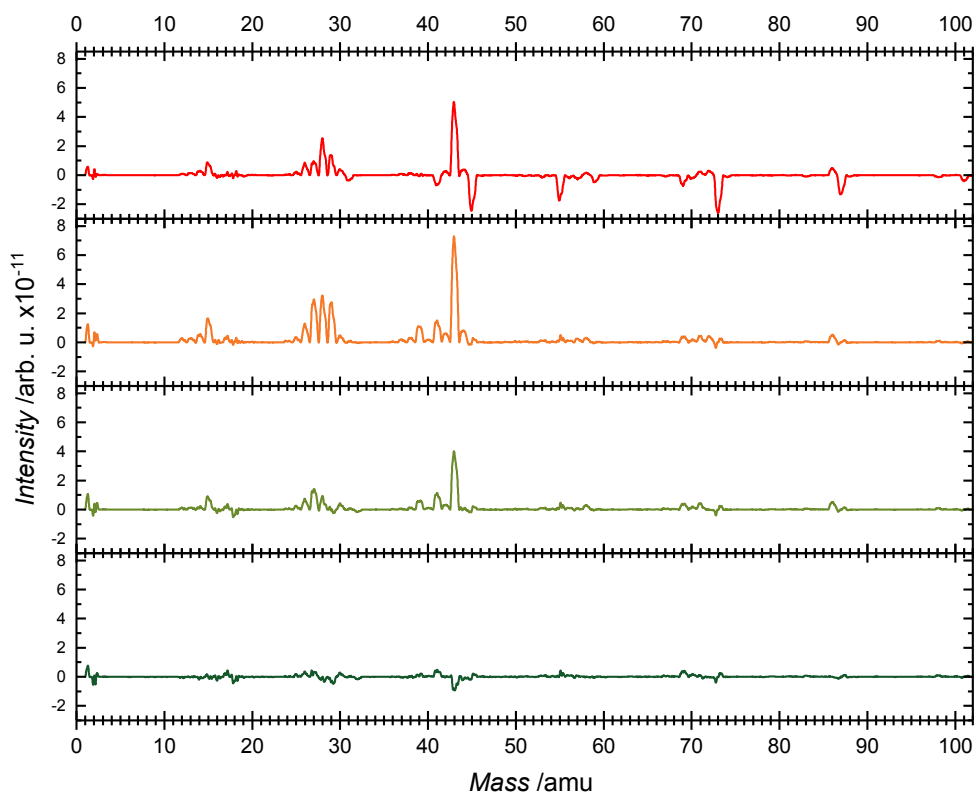


Figure S2: Mass spectra for the product analysis of the photocatalytic reforming of 3-methyl-3-hexanol (0.1% ML Pt<sub>x</sub>/TiO<sub>2</sub>, 300 K, alcohol background pressure  $1.7 \cdot 10^{-7}$  mbar). The difference spectrum is shown in **a**). Positive peaks originate from the products (2-butanone, propane, 2-pentanone and ethane), and the negative peaks stem from consumed 3-methyl-3-hexanol. Spectrum **b**) is obtained by adding the mass spectrum of 3-methyl-3-hexanol to the difference spectrum (both spectra were normalized to  $m/z = 73$  prior to the addition). **c**) depicts the mass spectrum after the subtraction of the spectra of 2-butanone (normalized to  $m/z = 72$ ) and propane (normalized to  $m/z = 44$ ). Spectrum **d**) shows a baseline after subtracting the spectra of 2-pentanone (normalized to  $m/z = 86$ ) and ethane (normalized to  $m/z = 28$ ) from spectrum **c**).

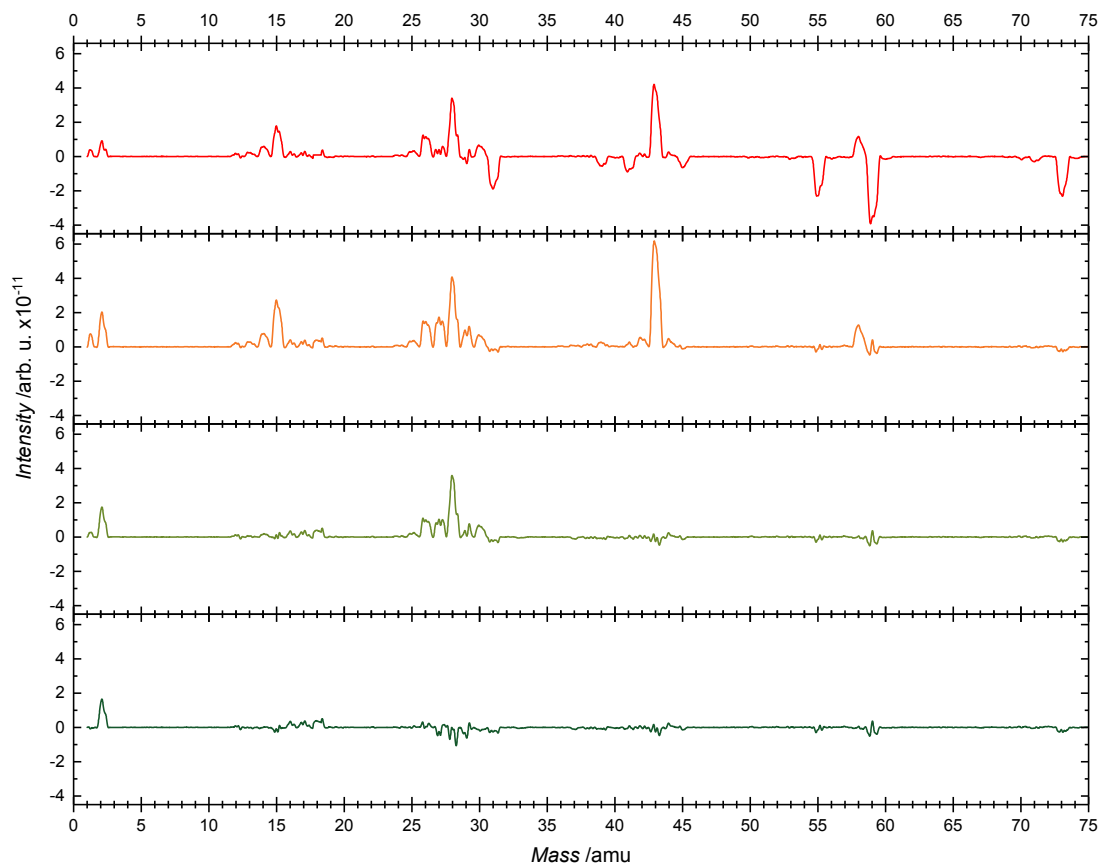


Figure S3: Mass spectra for the product analysis of the photocatalytic reforming of 2-methyl-2-butanol (0.1% ML Pt<sub>x</sub>/TiO<sub>2</sub>, 263 K, alcohol background pressure  $2.0 \cdot 10^{-7}$  mbar). The difference spectrum is shown in **a**). Positive peaks originate from the products (acetone and ethane), and the negative peaks stem from consumed 2-methyl-2-butanol. Spectrum **b**) is obtained by adding the mass spectrum of 2-methyl-2-butanol to the difference spectrum (both spectra were normalized to  $m/z = 59$  prior to the addition). **c**) depicts the mass spectrum after the subtraction of the spectrum of acetone (normalized to  $m/z = 43$ ). Spectrum **d**) shows a baseline after subtracting the spectrum of ethane (normalized to  $m/z = 28$ ) from spectrum **c**).

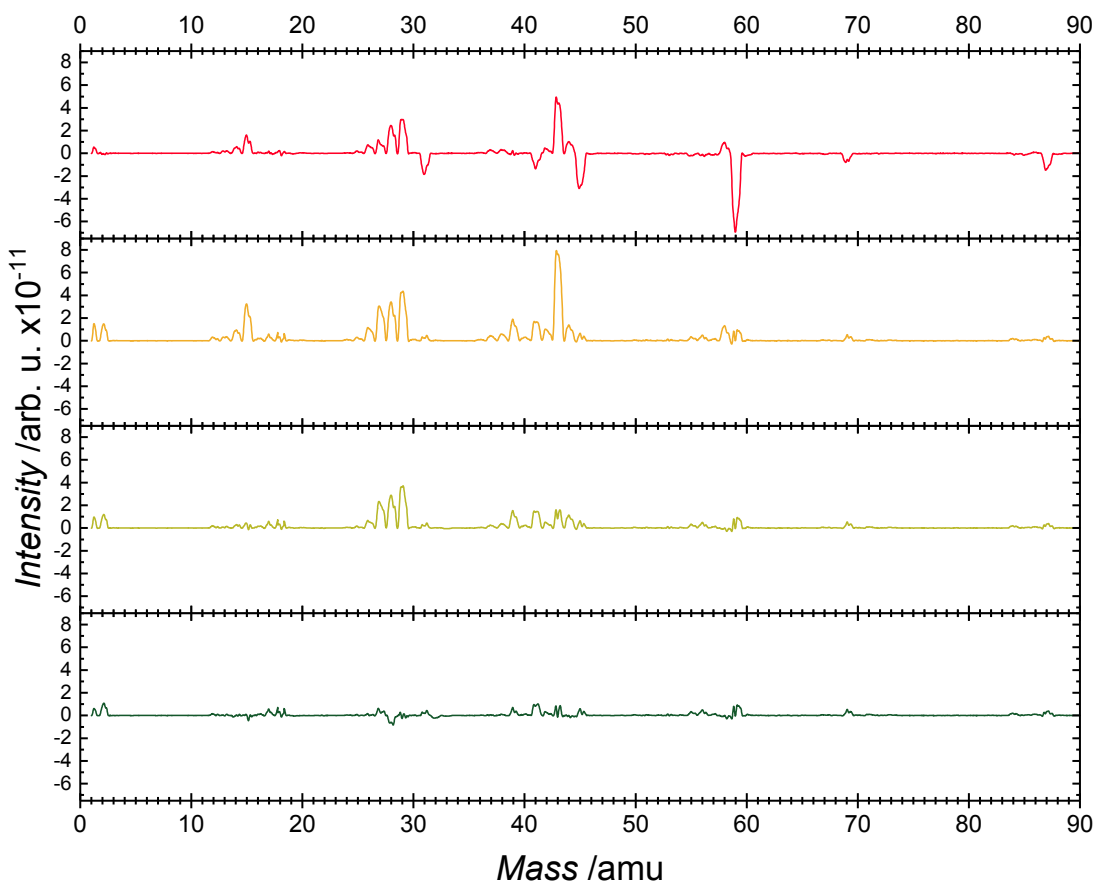


Figure S4: Mass spectra for the product analysis of the photocatalytic reforming of 2-methyl-2-pentanol (0.1% ML Pt<sub>x</sub>/TiO<sub>2</sub>, 321 K, alcohol background pressure  $2.0 \cdot 10^{-7}$  mbar). The difference spectrum is shown in **a**). Positive peaks originate from the products (acetone and propane), and the negative peaks stem from consumed 2-methyl-2-pentanol. Spectrum **b**) is obtained by adding the mass spectrum of 2-methyl-2-pentanol to the difference spectrum (both spectra were normalized to  $m/z = 59$  prior to the addition). **c**) depicts the mass spectrum after the subtraction of the spectrum of acetone (normalized to  $m/z = 58$ ). Spectrum **d**) shows a baseline after subtracting the spectrum of ethane (normalized to  $m/z = 29$ ) from spectrum **c**).

# Turnover Frequencies

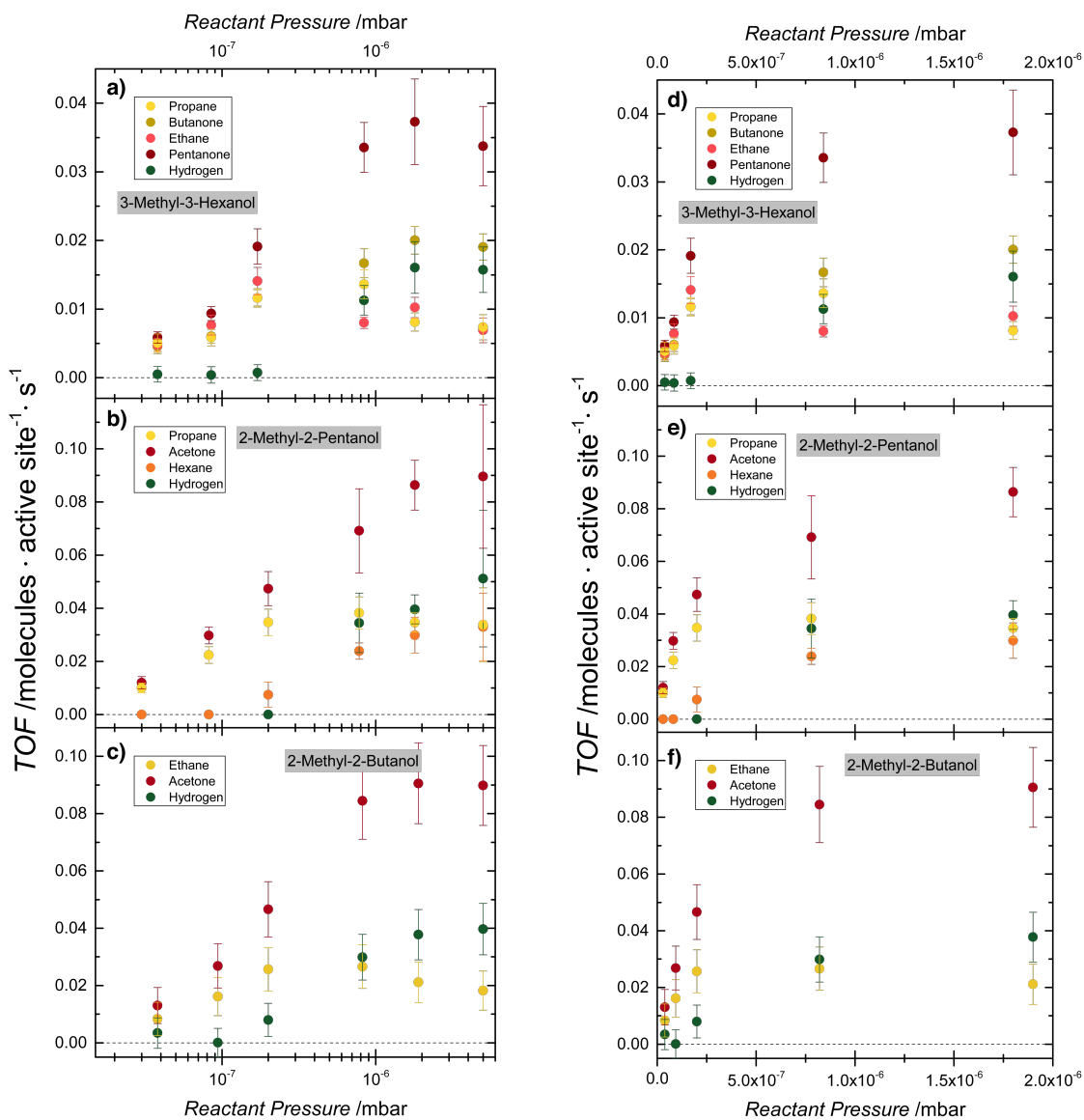


Figure S5: Pressure-dependent Turnover Frequencies (TOFs) for photocatalytic reforming of **a)** and **d)** 3-methyl-3-hexanol, **b)** and **e)** 2-methyl-2-pentanol, **c)** and **f)** 2-methyl-2-butanol over 0.1% ML Pt<sub>x</sub>/TiO<sub>2</sub>. The photocatalytic experiments are performed at 253 K, so that the temperature is above the desorption temperature of the ketones and alkanes and below the desorption temperature of the alcohol. The TOF exhibit a 1<sup>st</sup> order behavior until the regime changes from reactant adsorption to product desorption limitation. The latter results in a 0<sup>st</sup> order behavior. In **a)**, **b)** and **c)**, the pressure-dependent TOFs are plotted on a logarithmic scale and in **d)**, **e)** and **f)**, a section of the TOFs are plotted linearly to demonstrate a linear rise before the saturation behaviour.



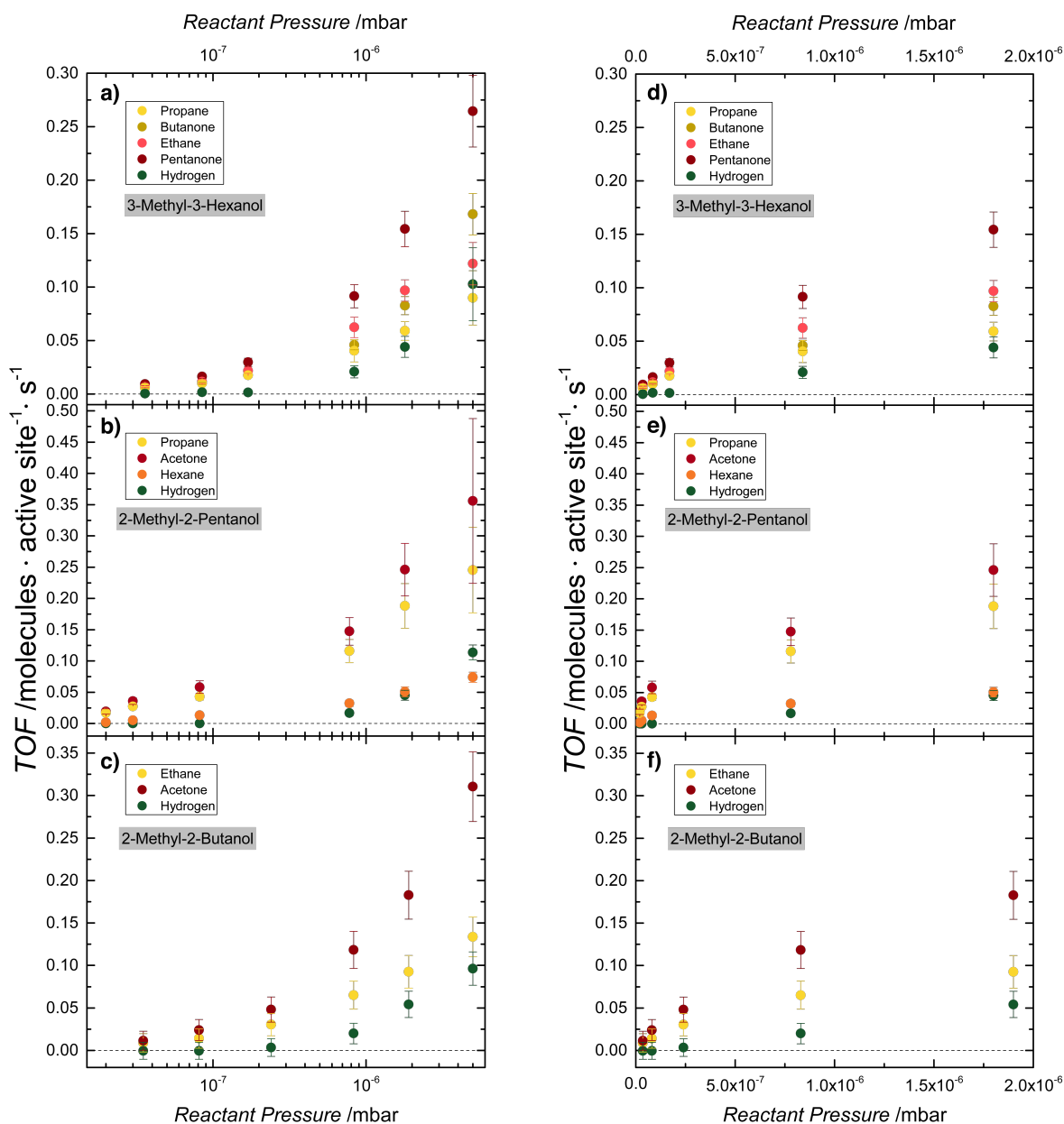


Figure S6: Pressure-dependent TOFs for photocatalytic reforming of **a)** and **d)** 3-methyl-3-hexanol, **b)** and **e)** 2-methyl-2-pentanol, **c)** and **f)** 2-methyl-2-butanol over 0.1% ML  $\text{Pt}_x/\text{TiO}_2$ . The catalytic experiments are performed at 336 K, so that the temperature is above the desorption temperature of the ketones and alkanes and below the desorption temperature of the alcohol. The TOFs exhibit a  $1^{\text{st}}$  order behaviour since the reaction is limited by reactant adsorption at 336 K. Due to higher temperature, a desorption limited regime is not reached, which is different to figure S5. In **a)**, **b)** and **c)**, the pressure-dependent TOFs are plotted on a logarithmic scale and in **d)**, **e)** and **f)**, a section of the TOFs are plotted linearly to demonstrate a linear rise with increasing alcohol pressure.

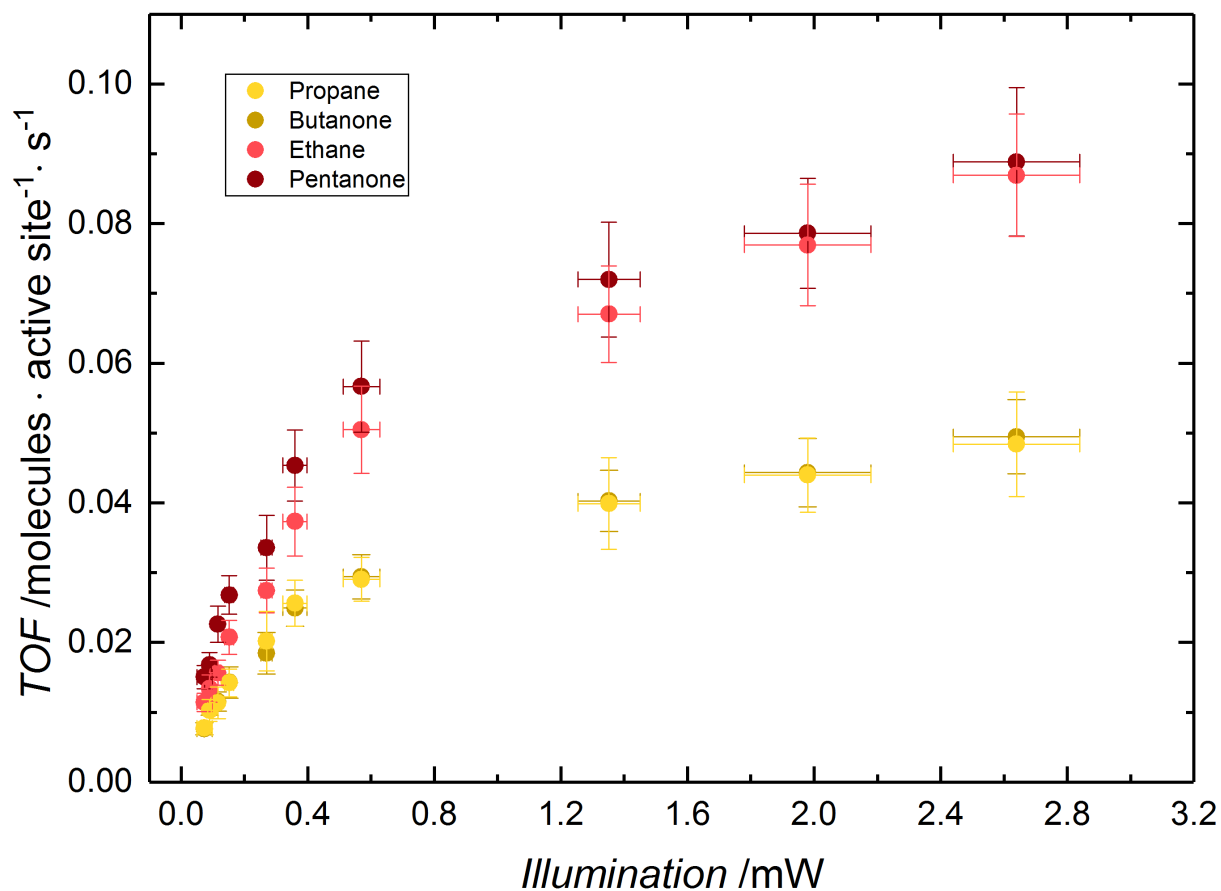


Figure S7: Power-dependent TOFs for photoreforming of 3-methyl-3-hexanol on 0.1% ML  $\text{Pt}_x/\text{TiO}_2(110)$  at 336 K in an alcohol background pressure of  $8.4 \cdot 10^{-7}$  mbar. The reaction exhibits a first-order dependence, which transfers into a zeroth-order regime at higher illumination intensities. This behavior, which is similar to the reaction of other alcohols,<sup>S12</sup> supplies evidence for a one photon process. Note that the overall apparent quantum yield ranges from 0.67% for low illumination intensities ( $0.74 \mu\text{W}$ ) to 0.11% for higher photon fluxes (2.64 mW), when the calculations follow the generally applied procedure via the number of evolved molecules per second with respect to the photon flux<sup>S12-S14</sup> and assuming the usually assumed two-photon process for a direct comparison with literature values.

## Selectivities

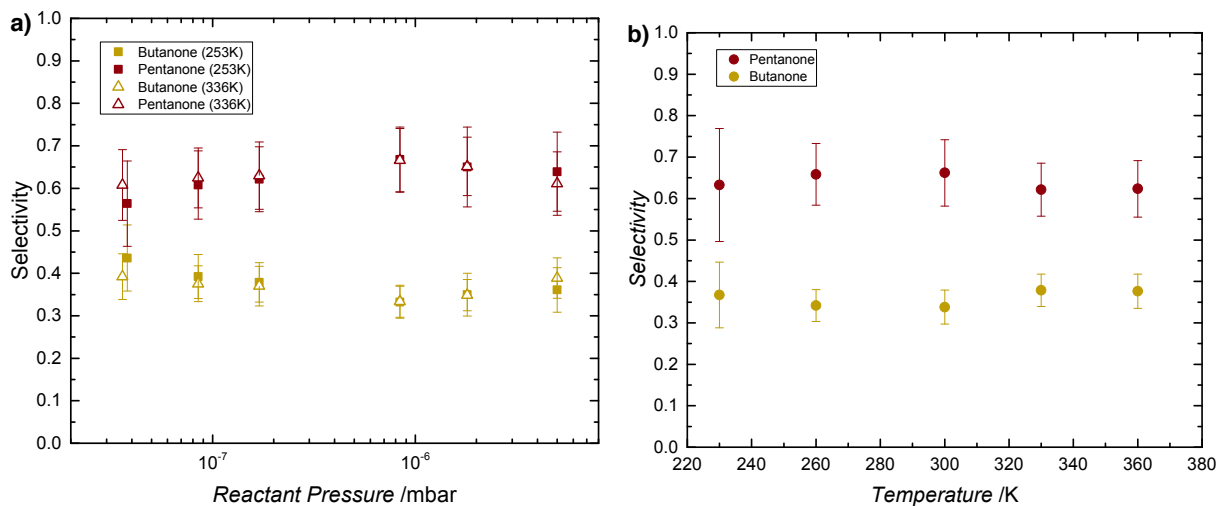


Figure S8: Photocatalytic conversion of 3-methyl-3-hexanol on 0.1% ML Pt<sub>x</sub>/TiO<sub>2</sub>(110). In **a)**, the selectivities for 2-pentanone and 2-butanone based on the TOFs from figure S5 and figure S6 are displayed for different reactant pressures at two different temperatures 253 K and 336 K, respectively. The two temperatures typify the temperature regime limited by product desorption, respectively by reactant adsorption. In **b)**, the selectivities for 2-pentanone and 2-butanone are shown for different temperatures. It is found, that the selectivities are temperature and concentration independent.

## QMS traces

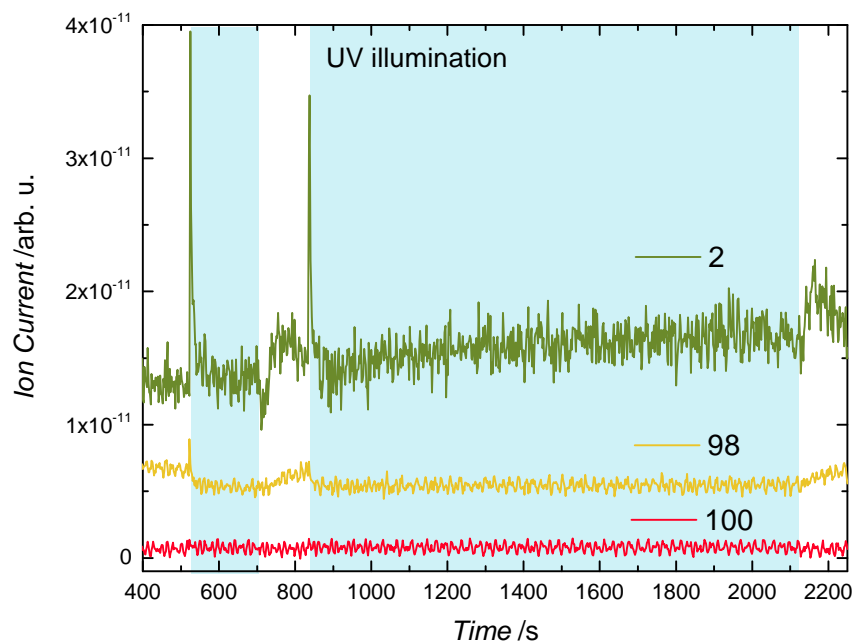


Figure S9: Photocatalytic alcohol reforming of 3-methyl-3-hexanol on  $\text{Pt}_x/\text{TiO}_2(110)$  (0.1% ML cluster coverage). The masses  $m/z = 2$  for hydrogen,  $m/z = 98$  for the dehydration products, hexene and methylene hexane, and  $m/z = 100$  for 3-hexanone are displayed at 340 K under a 3-methyl-3-hexanol pressure of  $1.7 \cdot 10^{-7}$  mbar. The blue region highlights the period of UV irradiation. It can be clearly seen that neither of these products are quantitatively formed. Note that the decrease in the  $m/z = 98$  during illumination is due to the consumption of the alcohol (the substrate), which exhibits a fragment of this particular mass in its fragmentation pattern.

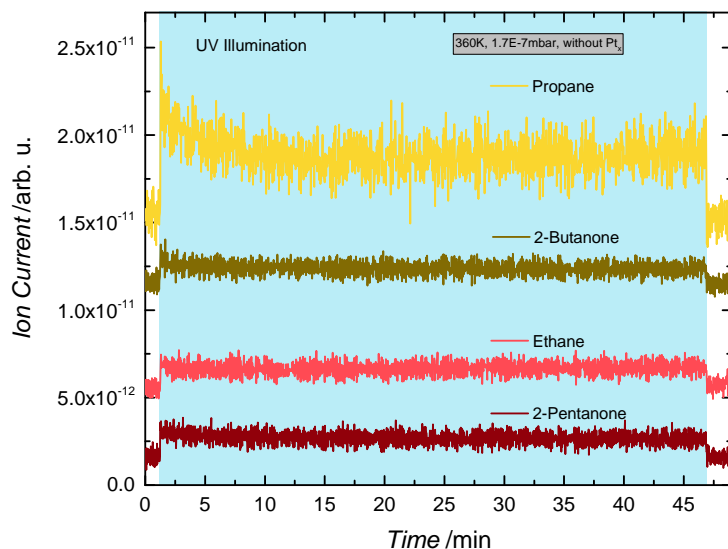


Figure S10: Photocatalytic products of 3-methyl-3-hexanol photoreforming on bare  $r\text{-TiO}_2(110)$ . 3-methyl-3-hexanol ( $m/z=73$ ), propane ( $m/z=29$ ), 2-butanone ( $m/z=72$ ), ethane ( $m/z=30$ ), and 2-pentanone ( $m/z=86$ ) signals are shown at 360 K under a 3-methyl-3-hexanol pressure of  $1.7 \cdot 10^{-7}$  mbar. The blue region highlights the period of UV irradiation. Note that the traces are offset for clarity.

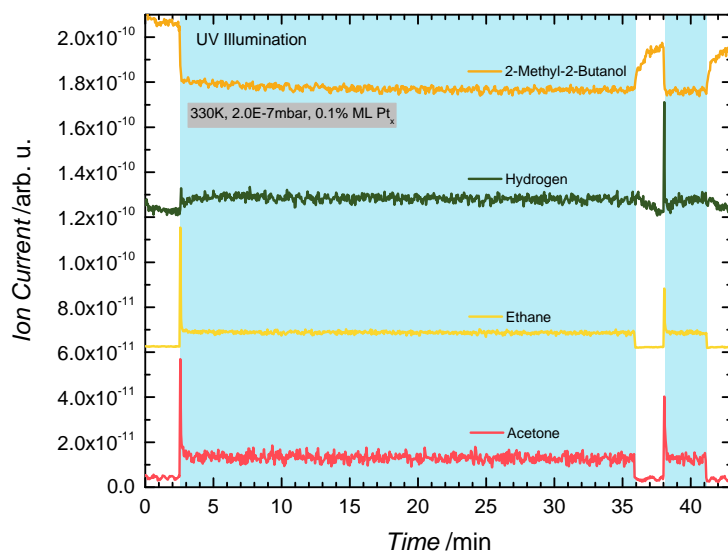


Figure S11: Photocatalytic products of 2-methyl-2-butanol photoreforming on 0.1% ML  $\text{Pt}_x/\text{TiO}_2(110)$ . 2-methyl-2-butanol ( $m/z=73$ ), hydrogen ( $m/z=2$ ), ethane ( $m/z=30$ ), and acetone ( $m/z=58$ ) signals are shown at 330 K under a 2-methyl-2-butanol pressure of  $2.0 \cdot 10^{-7}$  mbar. The blue region highlights the period of UV irradiation. Note that the traces are offset for clarity. Under these reactions conditions, a third reaction product next to acetone and ethane, namely hydrogen is observed.

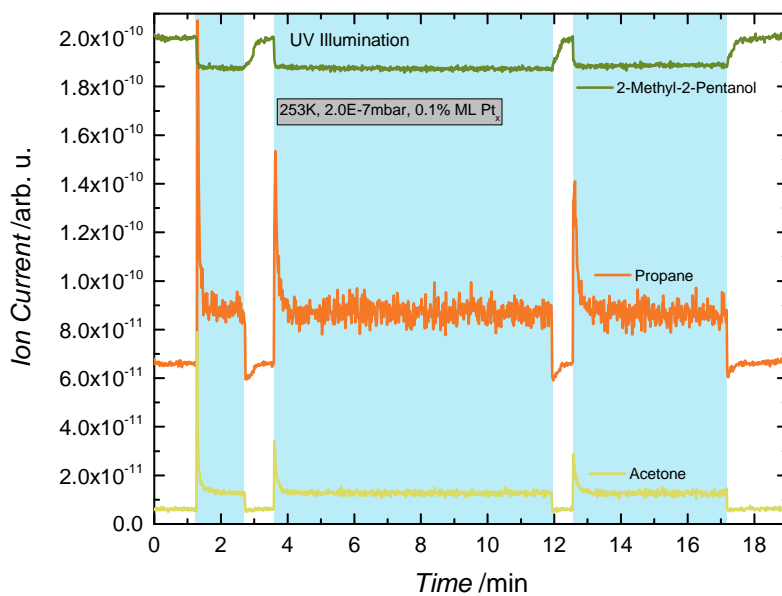


Figure S12: Photocatalytic products of 2-methyl-2-pentanol photoreforming on 0.1% ML  $\text{Pt}_x/\text{TiO}_2(110)$ . 2-methyl-2-pentanol ( $m/z=87$ ), propane ( $m/z=29$ ), and acetone ( $m/z=58$ ) signals are shown at 253 K under a 2-methyl-2-pentanol pressure of  $2.0 \cdot 10^{-7}$  mbar. The blue region highlights the period of UV irradiation. Note that the traces are offset for clarity.

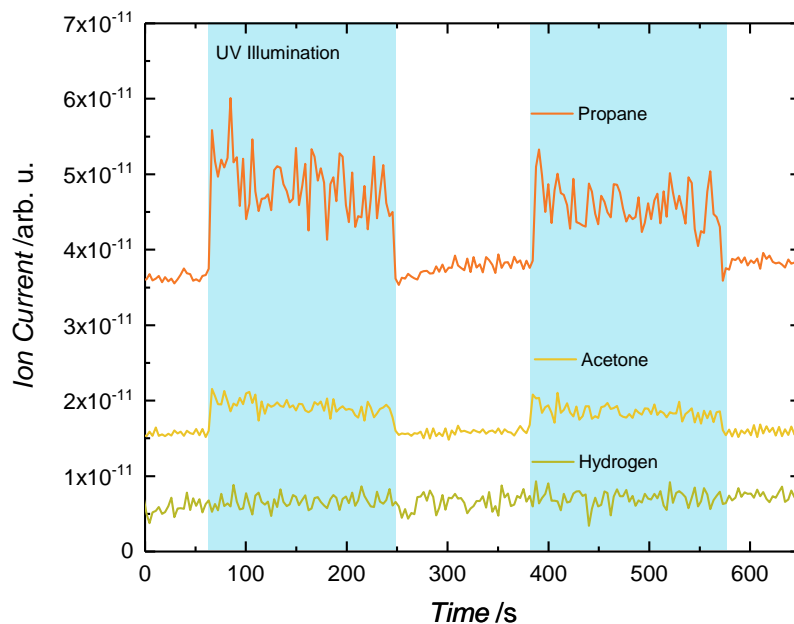


Figure S13: Photocatalytic products of 2-methyl-2-pentanol photoreforming on hydroxylated-TiO<sub>2</sub>(110). Propane ( $m/z=29$ ), acetone ( $m/z=58$ ) and molecular hydrogen ( $m/z=2$ ) signals are shown at 270 K under a 2-methyl-2-pentanol background pressure of  $1.7 \cdot 10^{-7}$  mbar. The hydroxylated-TiO<sub>2</sub>(110) crystal was exposed to water at cryogenic temperatures and annealed to 270 K. This leads to hydroxyl groups on the surface, while residual water molecules are being desorbed.<sup>S15</sup> The photoreaction occurs very similar to that on reduced-TiO<sub>2</sub>(110) (see Fig. 3a) showing that the hydroxylation does not lead to significant changes in the reaction behavior. Note that the traces are offset for clarity.

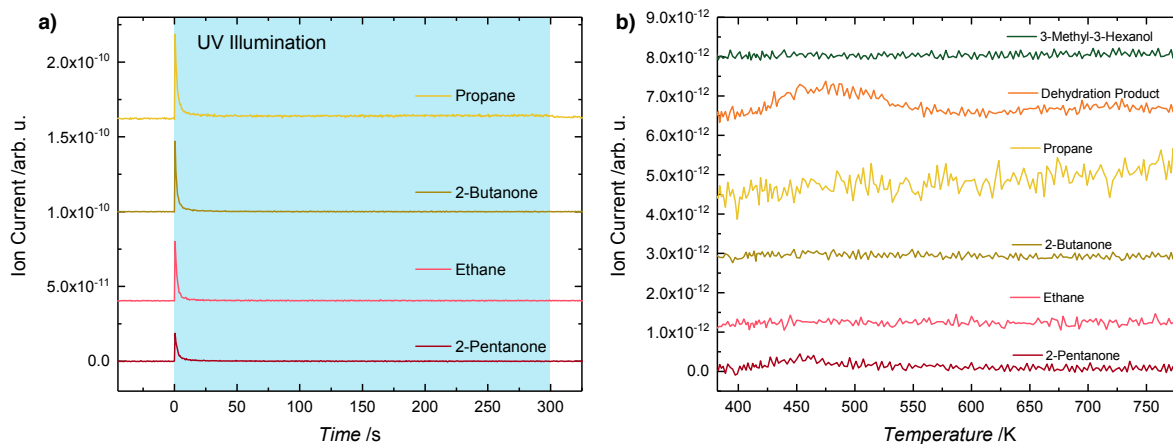


Figure S14: **a)** Isothermal photoreaction experiment of 5 L 3-methyl-3-hexanol on  $r\text{-TiO}_2(110)$  at 340 K. The catalyst is exposed to 3-methyl-3-hexanol at 150 K and then brought to 340 K. Upon illumination (blue region), propane ( $m/z=44$ ), 2-butanone ( $m/z=72$ ), ethane ( $m/z=30$ ), and 2-pentanone ( $m/z=86$ ) are formed.

**b)** Temperature programmed desorption spectroscopy (TPD) experiment after the isothermal photoreaction at 340 K. It is found that no alkanes and ketones appear in the TPD spectrum, which shows that the photoproducts have desorbed completely during illumination. Furthermore, no other photoproducts are detected. Only the formation of small amounts of dehydration products ( $m/z=98$ ) are observed. They originate from the thermal water elimination of alcohol residues, a general property of the thermal reactivity of alcohols,<sup>S16</sup> and may lead to three different structural isomers for which an unambiguous assignment cannot be given by EI-QMS. (Note that in both plots the traces are offset for clarity.)



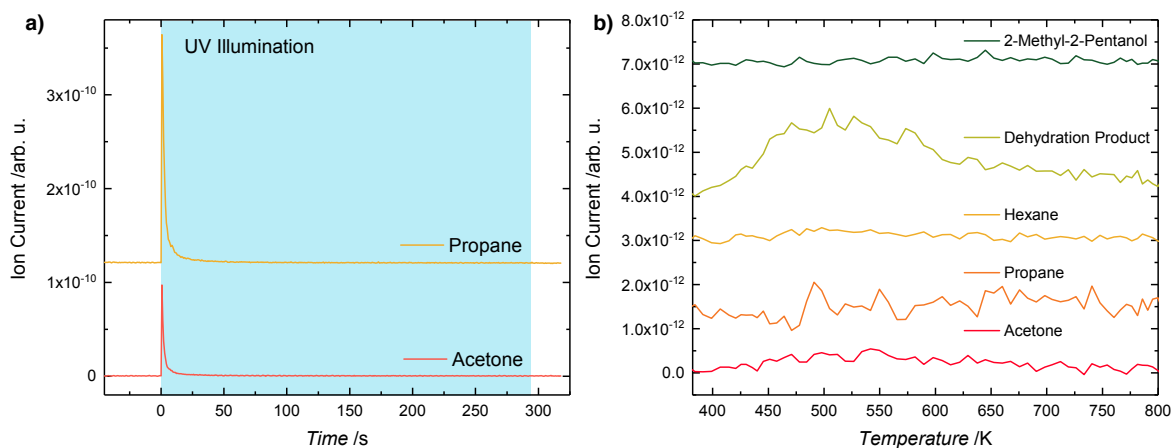


Figure S15: **a)** Isothermal photoreaction experiment of 5 L 2-methyl-2-pentanol on r-TiO<sub>2</sub>(110) at 340 K. The catalyst is exposed to 2-methyl-2-pentanol at 150 K and then brought to 340 K. Upon illumination (blue region), propane ( $m/z=29$ ) and acetone ( $m/z=58$ ) are formed.

**b)** Temperature programmed desorption spectroscopy (TPD) experiment after the isothermal photoreaction at 340 K. It is found that acetone and propane do not appear in the TPD spectrum, which shows that the photoproducts have desorbed completely during illumination. Furthermore, no other photoproducts (e.g. product from alkyl recombination, i.e. hexane ( $m/z=86$ )) are detected. Only the formation of small amounts of dehydration products ( $m/z=84$ ) are observed. They originate from the thermal water elimination of alcohol residues, a general property of the thermal reactivity of alcohols,<sup>S16</sup> and may lead to three different structural isomers for which an unambiguous assignment cannot be given by EI-QMS. (Note that in both plots the traces are offset for clarity.)

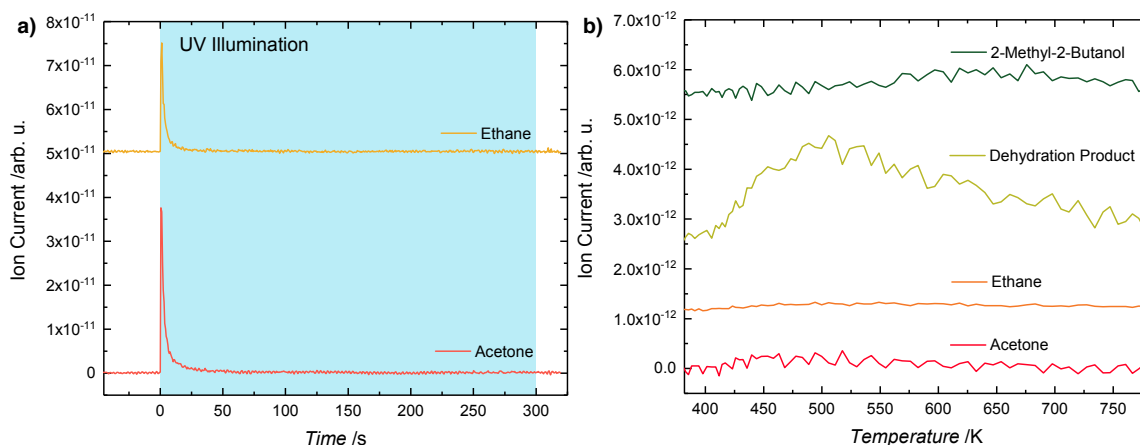


Figure S16: **a)** Isothermal photoreaction experiment of 5 L 2-methyl-2-butanol on r-TiO<sub>2</sub>(110) at 340 K. The catalyst is exposed to 2-methyl-2-butanol at 150 K and then brought to 340 K. Upon illumination (blue region), ethane ( $m/z=30$ ) and acetone ( $m/z=58$ ) are formed.

**b)** Temperature programmed desorption spectroscopy (TPD) experiment after the isothermal photoreaction at 340 K. It is found that acetone and ethane do not appear in the TPD spectrum, which shows that the photoproducts have desorbed completely during illumination. Furthermore, no other photoproducts are detected. Only the formation of small amounts of dehydration products ( $m/z=70$ ) are observed. They originate from the thermal water elimination of alcohol residues, a general property of the thermal reactivity of alcohols,<sup>S16</sup> and may lead to three different structural isomers for which an unambiguous assignment cannot be given by EI-QMS. (Note that in both plots the traces are offset for clarity.)

## Auger Electron Spectroscopy

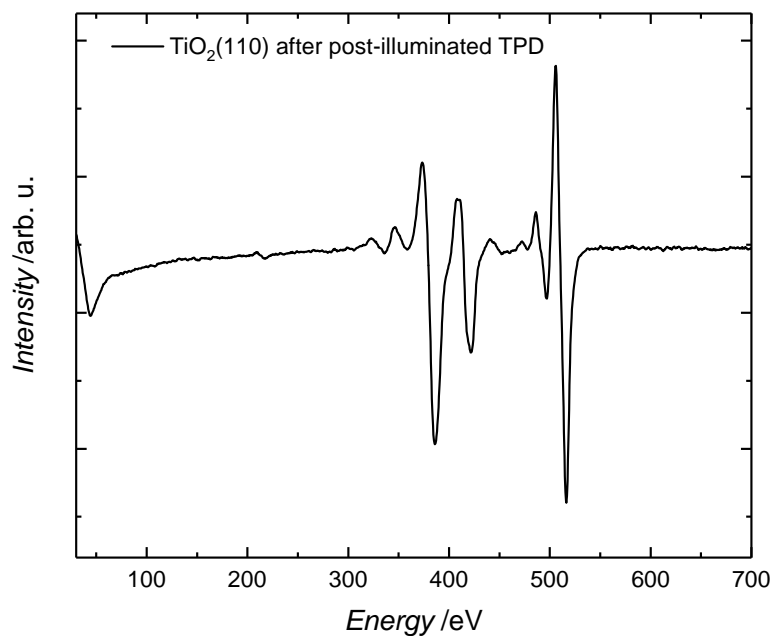


Figure S17: Auger Electron Spectrum of the reduced-TiO<sub>2</sub>(110) after the isothermal photoreaction experiment of 5 L 3-methyl-3-hexanol at 340 K followed by a thermal programmed desorption from 340 – 800 K, shown in S14. No carbon containing species (expected at 272 eV) are detected.

# Thermochemistry

Table S2: Standard enthalpy of formation ( $\Delta H_f^\circ$ ) for molecules, which may be formed in different reactions.

Molecule	$\Delta H_f^\circ$ [kJ/mol]
methane	$-74.6^{S17}$
ethane	$-84.0^{S17}$
propane	$-103.8^{S17}$
butane	$-125.6^{S17}$
pentane	$-146.9^{S17}$
hexane	$-167.1^{S17}$
acetone	$-217.1^{S17}$
2-butanone	$-238.5^{S17}$
2-pentanone	$-259.0^{S17}$
3-hexanone	$-277.6^{S18}$
2-methyl-2-butanol	$-329.3^{S18}$
2-methyl-2-propanol	$-352.1^{S19}$
3-methyl-3-hexanol	$-372.8^{S19}$
atomic hydrogen	$217.998^{S17}$
methyl radical	$146.427^{S20}$
ethyl radical	$119.87^{S21}$
propyl radical	$100.87^{S21}$

Table S3: Standard enthalpy of reaction ( $\Delta H_R^\circ$ ) calculated from the standard enthalpy of formation ( $\Delta H_f^\circ$ ) of the respective reactants and products.

Reaction	$\Delta H_R^\circ$ [kJ/mol]
2-methyl-2-butanol $\longrightarrow$ methane + 2-butanone	16.2
2-methyl-2-butanol $\longrightarrow$ ethane + acetone	28.2
2-methyl-2-butanol $\longrightarrow$ $\frac{1}{2}$ butane + acetone	98.8
2-methyl-2-propanol $\longrightarrow$ methane + 2-pentanone	18.5
2-methyl-2-propanol $\longrightarrow$ propane + acetone	31.2
2-methyl-2-propanol $\longrightarrow$ $\frac{1}{2}$ hexane + acetone	102.9
3-methyl-3-hexanol $\longrightarrow$ methane + 3-hexanone	20.6
3-methyl-3-hexanol $\longrightarrow$ ethane + 2-pentanone	29.8
3-methyl-3-hexanol $\longrightarrow$ propane + 2-butanone	30.5

All potential overall reactions are endothermic and elementary reaction steps are considered to require even more energy due to the cleavage of C-C bonds (see below).

The thermochemistry of three different model reactions is evaluated (see Table S4) in order to relate it to the selectivity of 3-methyl-3-hexanol photoreforming. First, the required energy for a radical formation from the respective alkane via a C-H bond cleavage is calculated. Second, the scission of a C-C bond is addressed by the evaluation of the heat of reaction for the formation of two radicals from the respective alkane. Third, it is assumed that the reaction of the alcohol leads to a ketone, an alkyl radical and atomic hydrogen.

Table S4: Standard Enthalpy of Reaction ( $\Delta H_R^\circ$ ) for three model reactions in order of evaluate the selectivity in 3-methyl-3-hexanol photoreforming (values calculated from Table S2).

Reaction	$\Delta H_R^\circ$ [kJ/mol]
Model Reaction 1	
$\text{CH}_4 \longrightarrow \text{CH}_3\cdot + \text{H}\cdot$	439
$\text{C}_2\text{H}_6 \longrightarrow \text{CH}_3\text{CH}_2\cdot + \text{H}\cdot$	422
$\text{C}_3\text{H}_8 \longrightarrow \text{CH}_3\text{CH}_2\text{CH}_2\cdot + \text{H}\cdot$	423
Model Reaction 2	
$\text{C}_2\text{H}_6 \longrightarrow 2\text{CH}_3\cdot$	377
$\text{C}_4\text{H}_{10} \longrightarrow 2\text{CH}_3\text{CH}_2\cdot$	365
$\text{C}_6\text{H}_{14} \longrightarrow 2\text{CH}_3\text{CH}_2\text{CH}_2\cdot$	369
Model Reaction 3	
3-methyl-3-hexanol $\longrightarrow$ 3-hexanone + $\text{CH}_3\cdot + \text{H}\cdot$	460
3-methyl-3-hexanol $\longrightarrow$ 2-pentanone + $\text{CH}_3\text{CH}_2\cdot + \text{H}\cdot$	452
3-methyl-3-hexanol $\longrightarrow$ 2-butanone + $\text{CH}_3\text{CH}_2\text{CH}_2\cdot + \text{H}\cdot$	453

The reactions yielding a methyl radical require significantly more energy than those for the other two radicals. Reactions for the formation of propyl and ethyl radicals are very similar in energy, but in every case the formation of ethyl is energetically favoured over that of propyl. This is the same trend as for the observed selectivity in 3-methyl-3-hexanol photoreforming.

## References

- (S1) Kollmannsberger, S. L.; Walenta, C. A.; Courtois, C.; Tschurl, M.; Heiz, U. Thermal Control of Selectivity in Photocatalytic, Water-Free Alcohol Photoreforming. *ACS Catal.* **2018**, *8*, 11076 – 11084.
- (S2) Heiz, U.; Vanolli, F.; Trento, L.; Schneider, W.-D. Chemical Reactivity of Size-Selected Supported Clusters: An Experimental Setup. *Review of Scientific Instruments* **1997**, *68*, 1986–1994.
- (S3) Walenta, C. A.; Kollmannsberger, S. L.; Kiermaier, J.; Winbauer, A.; Tschurl, M.; Heiz, U. Ethanol Photocatalysis on Rutile TiO<sub>2</sub>(110): the Role of Defects and Water. *Phys. Chem. Chem. Phys.* **2015**, *17*, 22809–22814.
- (S4) Henderson, M. A. Structural Sensitivity in the Dissociation of Water on TiO<sub>2</sub> Single-Crystal Surfaces. *Langmuir* **1996**, *12*, 5093–5098.
- (S5) Geng, Z.; Jin, X.; Wang, R.; Chen, X.; Guo, Q.; Ma, Z.; Dai, D.; Fan, H.; Yang, X. Low-Temperature Hydrogen Production via Water Conversion on Pt/TiO<sub>2</sub>. *J. Phys. Chem. C* **2018**, *122*, 10956–10962.
- (S6) Isomura, N.; Wu, X.; Hirata, H.; Watanabe, Y. Cluster Size Dependence of Pt Core-Level Shifts for Mass-Selected Pt Clusters on TiO<sub>2</sub>(110) Surfaces. *J. Vac. Sci. Technol., A* **2010**, *28*, 1141–1144.
- (S7) Watanabe, Y.; Isomura, N. A New Experimental Setup for High-Pressure Catalytic Activity Measurements on Surface Deposited Mass-Selected Pt Clusters. *J. Vac. Sci. Technol., A* **2009**, *27*, 1153–1158.
- (S8) Isomura, N.; Wu, X.; Watanabe, Y. Atomic-Resolution Imaging of Size-Selected Platinum Clusters on TiO<sub>2</sub>(110) Surfaces. *J. Chem. Phys.* **2009**, *131*.

- (S9) Bonanni, S.; Aït-Mansour, K.; Harbich, W.; Brune, H. Effect of the TiO<sub>2</sub> Reduction State on the Catalytic CO Oxidation on Deposited Size-Selected Pt Clusters. *J. Am. Chem. Soc.* **2012**, *134*, 3445–3450.
- (S10) Harrison, A. G.; Jones, E. G.; Gupta, S. K.; Nagy, G. P. Total Cross Sections for Ionization by Electron Impact. *Can. J. Chem.* **1966**, *44*, 1967–1973.
- (S11) Kim, Y.-K. et al. Electron-impact ionization cross section for ionization and excitation database. <http://physics.nist.gov/ionxsec>, 2004 version 3.0; 2018, February 12.
- (S12) Walenta, C. A.; Kollmannsberger, S. L.; Courtois, C.; Pereira, R. N.; Stutzmann, M.; Tschurl, M.; Heiz, U. Why Co-Catalyst-Loaded Rutile Facilitates Photocatalytic Hydrogen Evolution. *Phys. Chem. Chem. Phys.* **2019**, *21*, 1491–1496.
- (S13) Kudo, A.; Miseki, Y. Heterogeneous Photocatalyst Materials for Water Splitting. *Chem. Soc. Rev.* **2009**, *38*, 253 – 278.
- (S14) Hisatomi, T.; Kubota, J.; Domen, K. Recent Advances in Semiconductors for Photocatalytic and Photoelectrochemical Water Splitting. *Chem. Soc. Rev.* **2014**,
- (S15) Kim, B.; Li, Z.; Kay, B. D.; Dohnalek, Z.; Kim, Y. K. The Effect of Oxygen Vacancies on the Binding Interactions of NH<sub>3</sub> with Rutile TiO<sub>2</sub>(110)-(1x1). *Phys. Chem. Chem. Phys.* **2012**, *14*, 15060–15065.
- (S16) Kim, Y. K.; Kay, B. D.; White, J. M.; Dohnalek, Z. Alcohol Chemistry on Rutile TiO<sub>2</sub>(110) The Influence of Alkyl Substituents on Reactivity and Selectivity. *J. Phys. Chem. C* **2007**, *111*, 18236–18242.
- (S17) Dean, J. A.; Lange, N. A. *Lange's Handbook of Chemistry, 15th Edition*; New York: McGraw-Hill, 1999.
- (S18) CRC Handbook, In *CRC Handbook of Chemistry and Physics, 85th Edition*; Lide, David R., Ed.; CRC Press, 2004.



- (S19) Alberty, R. A.; Chung, M. B.; Flood, T. M. Standard Chemical Thermodynamic Properties of Alkanol Isomer Groups. *J. Phys. Chem. Ref. Data* **1987**, *16*, 391.
- (S20) Baghal-Vayjooee, M. H.; Colussi, A. J.; Benson, S. W. Very Low Pressure Reactor. A New Technique for Measuring Rates and Equilibria of Radical-Molecule Reactions at Low Temperature. Heat of Formation of the Methyl Radical. *J. Am. Chem. Soc.* **1978**, *100*, 3214–3215.
- (S21) Houle, F. A.; Beauchamp, J. L. Photoelectron Spectroscopy of Methyl, Ethyl, Isopropyl, and *tert*-Butyl Radicals. Implications for the Thermochemistry and Structures of the Radicals and Their Corresponding Carbonium Ions. *J. Am. Chem. Soc.* **1979**, *101*, 4067–4074.

## 4.2 Origin of Poisoning in Methanol Photoreforming on TiO<sub>2</sub>(110): The Importance of Thermal Back-Reaction Steps in Photocatalysis

Alcohols are often used as model substrates for photocatalytic hydrogen evolution.[113, 152] The photo-oxidation process of primary and secondary alcohols on TiO<sub>2</sub>(110) in UHV yields one surface hydrogen (as hydroxyl) with a BBO) upon dissociative adsorption by O-H bond cleavage.[29] The hole-mediated oxidation yields another hydroxyl and the corresponding aldehyde or ketone.[83] While the latter can desorb at room temperature, hydrogen is accumulated on the surface during prolonged photoconversion since H<sub>2</sub> recombination does not occur.[141] In contrast, tertiary alcohols can be photoconverted catalytically on bare TiO<sub>2</sub>(110) since the surface facilitates the recombination and desorption of hydrogen and alkyl surface species at room temperature (see previous section). Related to hydrogen (i.e. hydroxyl) accumulation on titania is the apparent deactivation of the photocatalyst during continuous or repeated methanol photoconversion in UHV.[85] This “poisoning” has mostly been ascribed to electronic effects.[153] For example, hydroxyl species may act as charge carrier traps and promote electron-hole recombination. An alternative explanation was a flattening of the upwards band bending of the n-type semiconductor, which expectedly occurred when the surface hydrogen species are considered to be protons. A blocking of photoactive sites or mutual repulsion of OH groups was also suspected as driving force behind catalyst deactivation.[154]

In this work, the steady state photoconversion of 2-methyl-2-pentanol is observed even if the TiO<sub>2</sub>(110) surface had been poisoned by methanol photoconversion shortly before. In other words, the “poisoned” photocatalyst is actually catalytically active for the conversion of the tertiary alcohol. If methanol is again used as reactant after 2-methyl-2-pentanol photoconversion, formaldehyde formation remains negligibly small, i.e. the surface is still “poisoned”. The physical and electronic effects listed above cannot rationalize these observations. A steric hindrance by surface hydroxyls would prevent hydrogen abstraction from 2-methyl-2-pentanol and inhibit its dissociation and photoconversion. Furthermore, a flattened band or enhanced charge-carrier recombination is not evident due to the steady-state photocatalysis of the tertiary alcohol, putting the representation of surface hydrogen species as protons into perspective.

Instead, we consider the overall process of alcohol photoconversion on TiO<sub>2</sub>(110) in UHV as a set of individual reaction steps. First, the alcohol adsorbs dissociatively to yield one hydrogen as hydroxyl and the photoactive alkoxy species. Subsequently, hole-mediated oxidation occurs, i.e. the abstraction of an alpha-H for primary and secondary alcohols or the homolytic C-C bond cleavage in case of tertiary alcohols. Regarding the latter, this step is not hampered by surface hydroxyls. For primary and secondary alcohols, the thermal back-reaction of this photostep will, however, shift the equilibrium ratio towards the reactants, lowering the yield in photoproducts. Indeed, the thermal reaction of formaldehyde and hydrogen to methoxy has been observed by means of STM by Mao et al. and is exothermic, contrary to the photoreaction.[94]

# Origin of Poisoning in Methanol Photoreforming on TiO<sub>2</sub>(110): The Importance of Thermal Back-Reaction Steps in Photocatalysis

Carla Courtois,<sup>†</sup> Moritz Eder,<sup>†</sup> Sebastian L. Kollmannsberger, Martin Tschurl, Constantin A. Walenta, and Ueli Heiz<sup>\*</sup>



Cite This: *ACS Catal.* 2020, 10, 7747–7752



Read Online

ACCESS |



Metrics & More



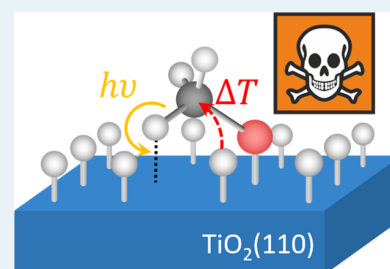
Article Recommendations



Supporting Information

**ABSTRACT:** Alcohol photoreforming on titania represents a perfect model system for elucidating fundamental processes in the heterogeneous photocatalysis of semiconductors. One important but open question is the origin of poisoning during the photoreaction of primary alcohols on a bare, reduced rutile TiO<sub>2</sub>(110) crystal under ultrahigh vacuum conditions. By comparing the photocatalytic properties of methanol and 2-methyl-2-pentanol, it is demonstrated that the fading activity in methanol photoreforming does not originate from the often-assigned increase of trap states for photon-generated charge carriers. Instead, we attribute the apparent catalyst poisoning to an increased rate of thermal back reactions, particularly to that of the photochemical oxidation step. While overall back reactions are generally considered in photocatalysis, back reactions of individual steps are largely neglected so far. Our work shows that their inclusion in the reaction scheme is inevitable for the comprehensive modeling of photocatalytic processes.

**KEYWORDS:** photocatalysis, titania, poisoning, mechanism, alcohol reforming



Rutile titania is one of the most explored (and applied) heterogeneous photocatalysts,<sup>1</sup> but a complete understanding of the fundamental photochemical surface processes is still lacking. Nevertheless, research on titania under ambient<sup>1,2</sup> and vacuum conditions<sup>3,4</sup> has already demonstrated the value of this material not only for application but also as a model system for the elucidation of fundamental effects in photocatalysis. One advantageous property of the model system TiO<sub>2</sub> is its availability as highly defined, single-crystalline material. Because of extensive research, the thermal surface chemistry is already fairly well understood, particularly on rutile TiO<sub>2</sub>(110). For example, the formation of species at different sites and temperatures have been thoroughly elucidated.<sup>5–7</sup> This holds especially for alcohols,<sup>8–11</sup> which are often employed as hole scavengers (i.e., sacrificial agents) in the testing of photocatalysts, with respect to their H<sub>2</sub> evolution performance for photocatalytic water splitting.<sup>12–14</sup> However, the surface chemistry of the materials represents a property often neglected in photocatalysis, and certain phenomena are, in most cases, related solely to charge carrier dynamics. Studies about TiO<sub>2</sub>(110) single crystals in particular highlight the importance of such an understanding.<sup>4</sup> The knowledge about thermal phenomena is crucial for disentangling photocatalytic and thermal reaction steps for a comprehensive understanding of catalytic processes. In this regard, Henderson identified thermally formed methoxy as the photoactive species in methanol photo-oxidation on TiO<sub>2</sub>(110).<sup>15</sup> Consistent with the upward band-bending toward the TiO<sub>2</sub>(110) semiconductor surface, the photo-

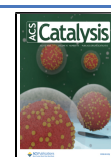
oxidation mechanism of methoxy is driven by a direct hole transfer, leading to a C–H bond cleavage.<sup>15–17</sup> This yields formaldehyde and a hydroxyl group with a bridging oxygen atom (OH<sub>br</sub>) from the lattice. The mechanism mediated by photoholes was further suggested for other alcohols, since it comprehensively explains the formation of all corresponding products.<sup>3,18–22</sup> In the same sense, we have only recently demonstrated that alcohol photoreforming on platinum-loaded TiO<sub>2</sub>(110) occurs through an unexpected (thermal) mechanism for hydrogen formation succeeding the photoreaction<sup>19,23</sup> and not by the usually assumed set of redox reactions. Furthermore, we discovered a similarly unexpected reaction of tertiary alcohols,<sup>22</sup> corroborating our proposed mechanism.

Although the described photo-oxidation pathway seems generally valid for alcohols,<sup>3</sup> important questions still need to be resolved. In this regard, the different photoactivity of methanol and other primary alcohols on bare and co-catalyst-loaded titania over time still remains elusive. Their photo-conversion is truly catalytic on platinum-decorated TiO<sub>2</sub>(110),<sup>19,23</sup> while an upper limit in the conversion of different primary alcohols is observed on the bare semiconductor.<sup>15,18,24</sup> These conversions range between 5% and

Received: April 9, 2020

Revised: May 29, 2020

Published: June 25, 2020



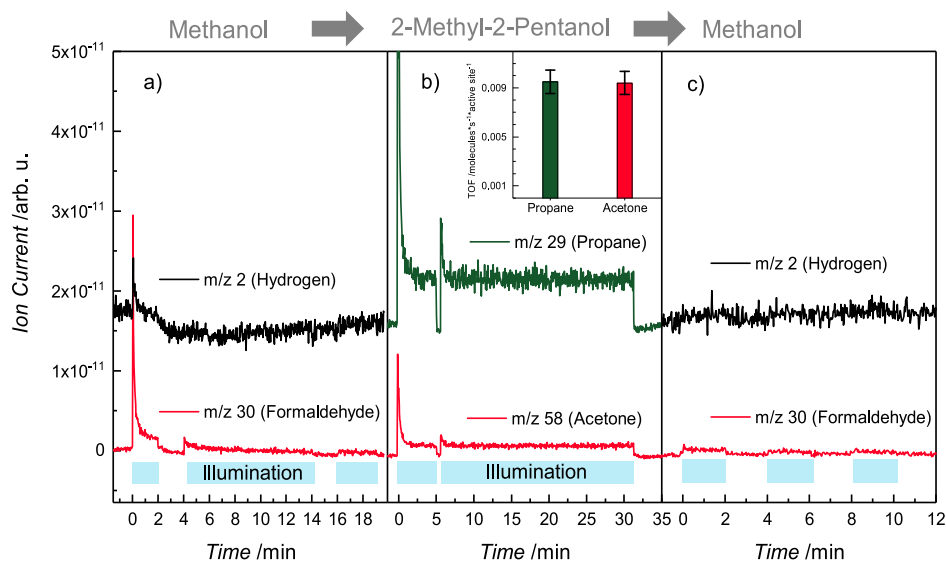


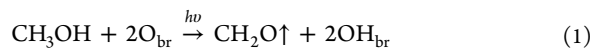
**Figure 1.** Photochemical reaction of methanol and photocatalysis of 2-methyl-2-pentanol on  $r\text{-TiO}_2(110)$  at 300 K in an alcohol background of  $5 \times 10^{-8}$  mbar in consecutive experiments. The blue region highlights the period of UV irradiation. (a) Photochemical product formation of methanol oxidation on a freshly prepared  $r\text{-TiO}_2(110)$ . Upon UV excitation, methoxy species are oxidized to formaldehyde ( $m/z$  30), which thermally desorbs. The amount of formaldehyde decreases continuously as the photoreaction progresses. Note that the small spike in the hydrogen trace is not stoichiometric by 2 orders of magnitude and is attributed to fragmentation in the ionization process.<sup>23</sup> This state of the surface will be referred to as “poisoned”. (b) The consecutive photocatalytic conversion of 2-methyl-2-pentanol on the poisoned  $r\text{-TiO}_2(110)$ . Upon UV illumination, acetone ( $m/z$  58) and propane ( $m/z$  29) are formed catalytically without any deactivation. The initial spike of the signals of the photoproducts is attributed to a saturation of photoactive alkoxy species in darkness. The catalyst is active over the entire illumination time of 30 min. The inset shows the turnover frequencies (TOFs) of the products. (c) Consecutive photo-oxidation of methanol after photocatalysis of the tertiary alcohol. Upon illumination, only very low amounts of formaldehyde are formed, and the activity of the freshly prepared surface has not been restored by the reforming of the tertiary alcohol. Note that the traces are offset for the sake of clarity.

20% of the initial alcohol coverage and are attributed to result from the accompanying hydroxylation of the surface.<sup>15,18,25</sup> So far, it is most commonly believed that surface hydroxyls act as electron traps and promote charge recombination.<sup>26</sup> This seems conceivable, because the photoconversion of methanol amounts to  $\sim 20\%$  at most.<sup>27</sup> At these conversions, by far not all  $\text{O}_{\text{br}}$ -sites are covered by H atoms. Yet, another work only recently ascribed the poisoning during the photoreaction to the mutual repulsion of surface OH-groups, which inhibits the formation of additional surface hydroxyls.<sup>28</sup> Thus, the exact role of  $\text{OH}_{\text{br}}$  in the photochemistry of methanol and other primary alcohols remains unclear and deactivation phenomena are likewise attributed to either a site-blocking or an electronic effect (or both).<sup>3,18,23,26,28,29</sup>

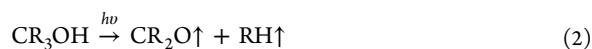
In this Letter, we report strong evidence that thermal backreactions are mainly responsible for the deactivation in alcohol photo-oxidation. Instead of site-blocking or electronic effects, we attribute the thermal back-reactions of carbonyl and surface hydroxyls to cause this deactivation on bare, reduced rutile  $\text{TiO}_2(110)$  ( $r\text{-TiO}_2(110)$ )—an interpretation that is based on the differences in the photochemistry of tertiary (exemplified by 2-methyl-2-pentanol) and primary alcohols (represented by methanol).

The deactivation of the photocatalyst in a steady methanol background on  $r\text{-TiO}_2(110)$  under illumination at room temperature is shown in Figure 1a. While the reactant is continuously replenished, the formation of formaldehyde as the product of the photoreaction step decays over time. The eventual photoinactive state of the catalyst, with respect to methanol conversion, is referred to as “poisoned” in the following. A similar poisoning is also observed for experiments

with a repeated dosage of methanol (see Figure S1 in the Supporting Information), in which the initial conversion decreases to  $\sim 20\%$ , compared to the first photoreaction cycle. The absence of stoichiometric molecular hydrogen desorption (Figure 1a), the second reaction product next to formaldehyde, indicates hydroxylation of the titania surface. This hydroxylation from photo-oxidation of primary alcohols previously was observed directly by means of scanning tunneling microscopy.<sup>27,30,31</sup> Therefore, the removal of this hydroxylation, which is observed on  $\text{TiO}_2(110)$  only, facilitated in the presence of a Pt co-catalyst<sup>23,32</sup> or via the desorption of water from recombining  $\text{OH}_{\text{br}}$  occurring only at higher temperatures, is inhibited at room temperature.<sup>33</sup> Thus, the overall reaction is given as follows:



As shown in Figure 1b, the disproportionation of 2-methyl-2-pentanol to propane and acetone occurs photocatalytically even on the poisoned  $r\text{-TiO}_2(110)$  surface.<sup>22</sup> The abstracted propyl group formed by photo-oxidation recombines with a surface hydrogen (e.g., originating from the dissociative adsorption of the alcohol), which opens up a reaction channel chemically closing the photocatalytic cycle and enables the overall net reaction:<sup>22</sup>



In contrast to the formation of molecular hydrogen from two hydrogen surface species in the photoreaction of methanol, this consecutive thermal reaction (i.e., alkyl and surface hydrogen recombination) occurs at room temperature, averting further

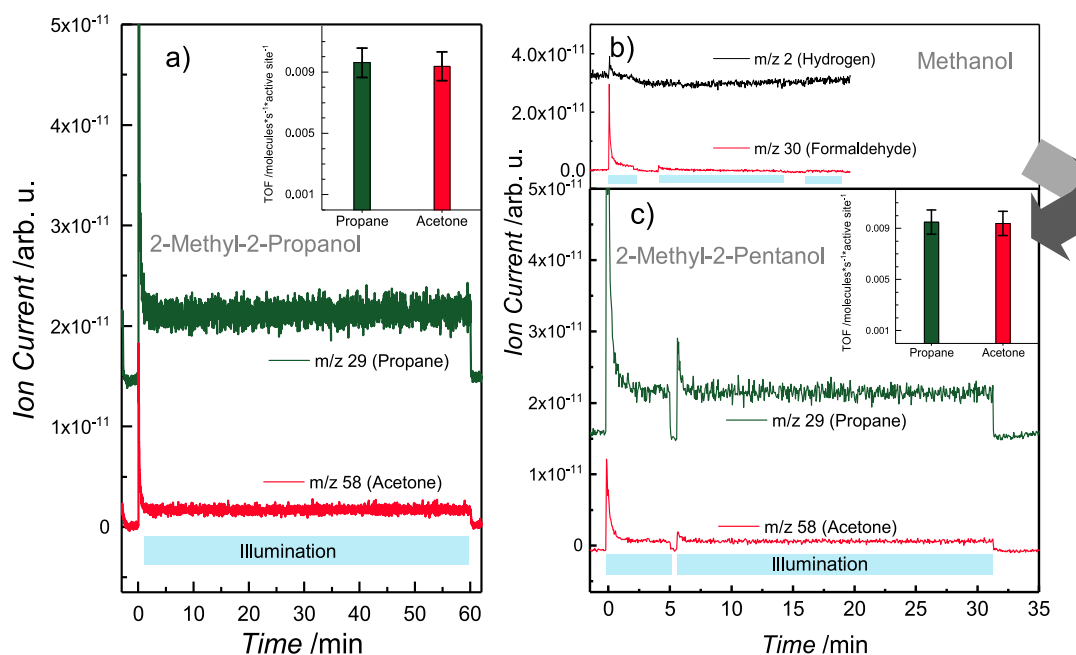


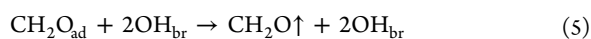
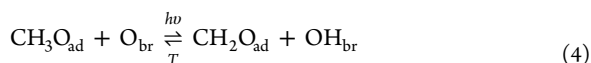
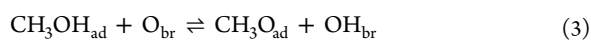
**Figure 2.** Photochemical reaction of 2-methyl-2-pentanol and methanol on  $r\text{-TiO}_2(110)$  at 300 K in an alcohol background of  $5 \times 10^{-8}$  mbar. The blue region highlights the period of UV irradiation. The TOFs of 2M2P photocatalytic conversion are in quantitative agreement on a freshly prepared  $r\text{-TiO}_2(110)$  surface and on one with prior methanol photoconversion. (a) Photocatalytic disproportionation of 2-methyl-2-pentanol on a freshly prepared, bare  $r\text{-TiO}_2(110)$ . Upon UV illumination, acetone ( $m/z$  58) and propane ( $m/z$  29) are formed catalytically. The inset shows the TOFs of the products. (b) Photochemical oxidation of methanol to formaldehyde ( $m/z$  30) leading to a deactivation caused by surface hydroxylation. (c) Consecutive experiment (immediately performed after experiment described in panel (b)) of photocatalytic conversion of 2-methyl-2-pentanol on the poisoned  $r\text{-TiO}_2(110)$ . Upon UV illumination, acetone ( $m/z$  58) and propane ( $m/z$  29) are formed catalytically without any deactivation. The inset shows the TOFs of the products, which remain unchanged from the freshly prepared to the poisoned surface. Note that the traces are offset for the sake of clarity.

accumulation of hydroxyl groups on the surface and rendering the reaction stoichiometric.<sup>22</sup>

While the disproportionation reaction of the tertiary alcohol is not hampered by the hydroxylation of the surface, the crystal remains in its poisoned state for a succeeding methanol photoconversion (Figure 1c). As the photoreforming of the tertiary alcohol proceeds stoichiometrically, neither the concentration of  $\text{OH}_{\text{br}}$  groups on the surface nor the photoactivity toward methanol is altered.

In order to evaluate potential changes in the photocatalytic behavior of the tertiary alcohol quantitatively, the activity of the  $\text{TiO}_2(110)$  crystal in this reaction is expressed by the TOF.<sup>19,22</sup> Clearly, the product formation remains quantitatively unaffected by a preceding methanol photo-oxidation (Figure 2). This demonstrates that  $\text{OH}_{\text{br}}$  groups do not affect the charge-driven process significantly enough to influence the photochemical reaction itself.

Therefore, other effects must be taken into account for the poisoning in photocatalytic methanol oxidation, which we postulate to result mainly from the thermal back reaction of formaldehyde with surface hydroxyls to methoxy. In order to describe the complete reaction sequence occurring on the titania surface thoroughly, at least three different steps must be considered (see eqs 3–5):



First, dissociation of the adsorbed alcohol into a methoxy species and an  $\text{OH}_{\text{br}}$  occurs on  $r\text{-TiO}_2(110)$  (eq 3).<sup>8,34</sup> This represents the first reaction step,<sup>15</sup> which must be considered to be reversible by thermal recombination. Second, the succeeding  $\alpha\text{-H}$  abstraction is a photon-driven reaction, initiated by holes migrating to the surface of the  $n$ -type semiconductor (eq 4). This step embodies the oxidation of methoxy to formaldehyde upon C–H bond cleavage<sup>15,17,23</sup> and the concomitant hydroxyl formation on the titania surface.<sup>29</sup> Third, formaldehyde desorbs into the gas phase at room temperature, whereas hydrogen remains bound to lattice oxygen on the surface (eq 5). Low degrees of hydroxylation by water adsorption (see Figure S7 in the Supporting Information) do not lead to a detectable change in photoactivity (see Figure S3 in the Supporting Information), in excellent agreement with the literature,<sup>29</sup> while continuous alcohol adsorption and photoconversion is instead accompanied by surface hydroxyl accumulation. This favors thermal back-reactions in the reaction network (see eqs 3 and 4). The back-reaction of the  $\alpha\text{-H}$  cleavage (eq 4) was indeed shown to occur thermally<sup>35</sup> and directly observed via STM by Mao and co-workers.<sup>27,30,31</sup> Furthermore, it is considered to be exothermic, because of the overall endergonic (and endothermic) forward reaction ( $\Delta_{\text{R}}G^\circ = +59.8 \text{ kJ/mol} \approx 0.62 \text{ eV}$ ).<sup>36</sup> Only the thermal desorption of formaldehyde may be simplified to a formally irreversible reaction, because of the low readsorption probability of the molecule at the reaction conditions.

The photocatalytic conversion of 2-methyl-2-pentanol still occurs after the hydroxylation of the  $\text{TiO}_2(110)$  crystal

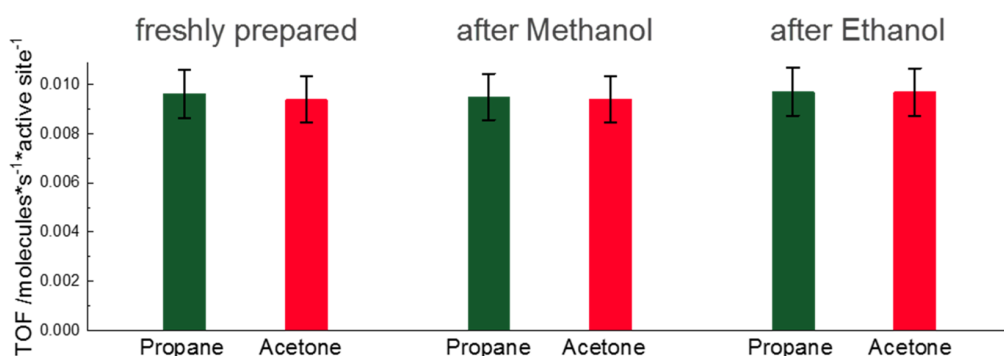
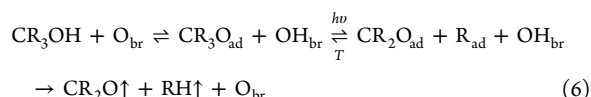


**Figure 3.** Turnover frequencies for the photoreforming of 2-methyl-2-propanol at 300 K on the freshly prepared *r*-TiO<sub>2</sub>(110), after methanol poisoning and ethanol poisoning. It is found that, in each case, the photocatalytic reaction proceeds stoichiometrically and with the same activity.

(through methanol photo-oxidation), in contrast to the photo-oxidation of methanol (Figure 1). This demonstrates that a blocking of photoactive sites by OH<sub>br</sub> is not the main reason for the decline in the photoactivity toward methanol. A mutual repulsion of OH-groups is also unlikely decisive for poisoning,<sup>28</sup> since this would also inhibit the dissociative adsorption of the tertiary alcohol, preventing its photo-oxidation completely. Similarly, the role of surface OH-groups as potential trap and recombination sites for photon-generated charge carriers seems improbable, because the amount of hydroxylation does not have a quantifiable effect on the photoreforming TOF of the tertiary alcohol. Instead, thermal back-reactions should be considered for other photodecomposition reaction (e.g., that of trimethyl acetate<sup>26</sup>) apart from changes in the behavior of the photogenerated charges.

The different surface chemistry of these alcohols under illumination can comprehensively explain their different behavior. However, the adsorption properties of methanol and 2-methyl-2-pentanol are very similar to each other, based on STM work for methanol and longer chain, branched alcohols by Dohnálek and co-workers.<sup>8,37,38</sup> Independent of the nature of the photoactive site, both alkoxy species are expected to occupy the same (photoactive) Ti-sites and undergo a hole-mediated oxidation.<sup>15,22</sup> If dosed successively, the respective alcohol concentration on the titania surface sites is determined by the adsorption strengths of the alcohols and their displacement kinetics (see Figures S4 and S5 in the Supporting Information). Obviously, photoreforming of tertiary alcohols (eq 2) occurs by a photochemical C–C cleavage of the alkoxy (eq 6),<sup>22</sup> in contrast to the photo-oxidation of methanol (eq 4), where a C–H bond is cleaved.<sup>3,15,17,39</sup>



The potential thermal back-reaction of the photo-oxidation of 2-methyl-2-pentanol does not involve hydrogen atoms from hydroxyls, which perfectly agrees with the alcohol's unaffected TOF upon an increasing hydroxylation of the TiO<sub>2</sub>(110) crystal. This unaltered catalytic behavior further points to a similar concentration of photoactive tertiary alkoxy species. This suggests that increasing hydroxylation does not affect the dissociative adsorption of the tertiary alcohol significantly. While a similar thermal chemistry and gas phase acidities<sup>40</sup> are observed, there is a strong difference in the thermal back-

reaction of the photo-oxidation, resulting in their different catalytic behavior.

To generalize the findings, ethanol is investigated as another poisoning agent. The photochemical oxidation occurs analogously to methanol by the conversion of ethoxy to acetaldehyde.<sup>18,20</sup> The dissociative adsorption and the photo-reaction thus lead to an accumulation of hydroxyls on the surface and the TOF of acetaldehyde decreases over time (Figure S6a in the Supporting Information).<sup>18</sup> In a subsequent photocatalytic oxidation of 2-methyl-2-pentanol (Figure S6b in the Supporting Information), the same TOF as in all other photocatalytic experiments of the tertiary alcohol is obtained (see Figure 3). Consequently, charge carriers are not responsible for the poisoning in alcohol photo-oxidation on TiO<sub>2</sub>(110), which may also hold for other photodecomposition reactions.

In conclusion, the presented findings strongly suggest that the limited conversion of primary alcohols on TiO<sub>2</sub>(110) results from the back-reaction of the aldehyde with a surface hydroxyl. The catalytic photoreforming of tertiary alcohols demonstrates that the charge carrier dynamics are not altered significantly enough to account for the poisoning effect. Therefore, surface OH groups as trap states/recombination sites have only a negligible effect on these photoreactions. Instead, the different photo-oxidation chemistry of primary and tertiary alcohols allows the assignment of the deactivation to thermal back reactions. In methanol photo-oxidation, two different thermal back reactions were identified, in which hydrogen atoms from surface hydroxyl groups are involved in the reaction scheme. Based on the differences and similarities in the photoreaction steps of methanol and 2-methyl-2-pentanol, we attribute the back-reaction from formaldehyde to methoxy as being mainly responsible for the vanishing photoactivity of TiO<sub>2</sub>(110) in methanol photoreforming. For tertiary alcohols, the forward reaction represents a photochemical C–C bond cleavage, instead of the splitting of a C–H bond. Consequently, the thermal back-reaction is completely different from that of primary alcohols.

While overall back-reactions are sometimes considered in photocatalysis, as e.g. in the prominent example of Maeda et al. in full water splitting,<sup>41</sup> back-reactions of individual reaction steps are so far largely ignored. Given the abundance of hydroxyls on the titania surface in the liquid phase,<sup>4</sup> the similar photochemical behavior of other TiO<sub>2</sub> surfaces,<sup>42</sup> modifications (i.e., anatase(101))<sup>43,44</sup> and morphologies (i.e., nanowires)<sup>45–47</sup> suggests that similar effects may also play an important role for these systems. Our work demonstrates that



individual back-reaction steps must be included in a comprehensive modeling of photocatalytic systems.

## ■ ASSOCIATED CONTENT

### SI Supporting Information

The Supporting Information is available free of charge at <https://pubs.acs.org/doi/10.1021/acscatal.0c01615>.

Description of experimental procedures, consecutive isothermal photoreaction experiments of methanol, consecutive photochemical reaction data of ethanol and 2-methyl-2-pentanol on r-TiO<sub>2</sub>(110) at 300 K and corresponding TOFs, temperature-programmed desorption of H<sub>2</sub>O on r-TiO<sub>2</sub>(110), general description of TOF calculation (PDF)

## ■ AUTHOR INFORMATION

### Corresponding Author

Ueli Heiz – Chair of Physical Chemistry, Department of Chemistry & Catalysis Research Center, Technische Universität München, 85748 Garching, Germany; [orcid.org/0000-0002-9403-1486](https://orcid.org/0000-0002-9403-1486); Email: [ulrich.heiz@mytum.de](mailto:ulrich.heiz@mytum.de)

### Authors

Carla Courtois – Chair of Physical Chemistry, Department of Chemistry & Catalysis Research Center, Technische Universität München, 85748 Garching, Germany

Moritz Eder – Chair of Physical Chemistry, Department of Chemistry & Catalysis Research Center, Technische Universität München, 85748 Garching, Germany

Sebastian L. Kollmannsberger – Chair of Physical Chemistry, Department of Chemistry & Catalysis Research Center, Technische Universität München, 85748 Garching, Germany

Martin Tschurl – Chair of Physical Chemistry, Department of Chemistry & Catalysis Research Center, Technische Universität München, 85748 Garching, Germany; [orcid.org/0000-0001-6618-7312](https://orcid.org/0000-0001-6618-7312)

Constantin A. Walenta – Chair of Physical Chemistry, Department of Chemistry & Catalysis Research Center, Technische Universität München, 85748 Garching, Germany; [orcid.org/0000-0001-9879-5101](https://orcid.org/0000-0001-9879-5101)

Complete contact information is available at <https://pubs.acs.org/doi/10.1021/acscatal.0c01615>

### Author Contributions

<sup>†</sup>These authors contributed equally to this work.

### Notes

The authors declare no competing financial interest.

## ■ ACKNOWLEDGMENTS

The authors thank the DFG for financial support through the Germany's Excellence Strategy – EXC 2089/1-390776260. C.C. acknowledges the support from the Luxembourg National Research Fund (FNR) (Project Code No. 12531916) and that from the TUM International Graduate School of Science and Engineering (No. TUM-IGSSE).

## ■ REFERENCES

(1) Schneider, J.; Matsuoka, M.; Takeuchi, M.; Zhang, J.; Horiuchi, Y.; Anpo, M.; Bahnemann, D. W. Understanding TiO<sub>2</sub> Photocatalysis: Mechanisms and Materials. *Chem. Rev.* **2014**, *114* (19), 9919–9986.

(2) Nosaka, Y.; Nosaka, A. Y. Generation and Detection of Reactive Oxygen Species in Photocatalysis. *Chem. Rev.* **2017**, *117* (17), 11302–11336.

(3) Walenta, C. A.; Tschurl, M.; Heiz, U. Introducing Catalysis in Photocatalysis: What can be Understood from Surface Science Studies of Alcohol Photoreforming on TiO<sub>2</sub>. *J. Phys.: Condens. Matter* **2019**, *31* (47), 473002.

(4) Henderson, M. A. A Surface Science Perspective on TiO<sub>2</sub> Photocatalysis. *Surf. Sci. Rep.* **2011**, *66* (6), 185–297.

(5) Diebold, U. The Surface Science of Titanium Dioxide. *Surf. Sci. Rep.* **2003**, *48* (5), 53–229.

(6) Lun Pang, C.; Lindsay, R.; Thornton, G. Chemical reactions on rutile TiO<sub>2</sub>(110). *Chem. Soc. Rev.* **2008**, *37* (10), 2328–2353.

(7) Dohnálek, Z.; Lyubimetsky, I.; Rousseau, R. Thermally-Driven Processes on Rutile TiO<sub>2</sub>(110)-(1 × 1): A Direct View at the Atomic Scale. *Prog. Surf. Sci.* **2010**, *85* (5), 161–205.

(8) Zhang, Z.; Bondarchuk, O.; White, J. M.; Kay, B. D.; Dohnálek, Z. Imaging Adsorbate O-H Bond Cleavage: Methanol on TiO<sub>2</sub>(110). *J. Am. Chem. Soc.* **2006**, *128* (13), 4198–4199.

(9) Kim, Y. K.; Kay, B. D.; White, J. M.; Dohnálek, Z. Alcohol Chemistry on Rutile TiO<sub>2</sub>(110): The Influence of Alkyl Substituents on Reactivity and Selectivity. *J. Phys. Chem. C* **2007**, *111* (49), 18236–18242.

(10) Kim, Y. K.; Kay, B. D.; White, J. M.; Dohnálek, Z. Inductive Effect of Alkyl Chains on Alcohol Dehydration at Bridge-bonded Oxygen Vacancies of TiO<sub>2</sub>(110). *Catal. Lett.* **2007**, *119* (1), 1–4.

(11) Li, Z.; Smith, R. S.; Kay, B. D.; Dohnálek, Z. Determination of Absolute Coverages for Small Aliphatic Alcohols on TiO<sub>2</sub>(110). *J. Phys. Chem. C* **2011**, *115* (45), 22534–22539.

(12) Lee, Y. J.; Joo, J. B.; Yin, Y.; Zaera, F. Evaluation of the Effective Photoexcitation Distances in the Photocatalytic Production of H<sub>2</sub> from Water using Au@Void@TiO<sub>2</sub> Yolk–Shell Nanostructures. *ACS Energy Lett.* **2016**, *1* (1), 52–56.

(13) Hainer, A. S.; Hodgins, J. S.; Sandre, V.; Vallieres, M.; Lanterna, A. E.; Scavano, J. C. Photocatalytic Hydrogen Generation Using Metal-Decorated TiO<sub>2</sub>: Sacrificial Donors vs True Water Splitting. *ACS Energy Lett.* **2018**, *3* (3), 542–545.

(14) Joo, J. B.; Dillon, R.; Lee, I.; Yin, Y.; Bardeen, C. J.; Zaera, F. Promotion of atomic hydrogen recombination as an alternative to electron trapping for the role of metals in the photocatalytic production of H<sub>2</sub>. *Proc. Natl. Acad. Sci. U. S. A.* **2014**, *111* (22), 7942.

(15) Shen, M.; Henderson, M. A. Identification of the Active Species in Photochemical Hole Scavenging Reactions of Methanol on TiO<sub>2</sub>. *J. Phys. Chem. Lett.* **2011**, *2* (21), 2707–2710.

(16) Phillips, K. R.; Jensen, S. C.; Baron, M.; Li, S.-C.; Friend, C. M. Sequential Photo-Oxidation of Methanol to Methyl Formate on TiO<sub>2</sub>(110). *J. Am. Chem. Soc.* **2013**, *135* (2), 574–577.

(17) Kolesov, G.; Vinichenko, D.; Tritsarlis, G. A.; Friend, C. M.; Kaxiras, E. Anatomy of the Photochemical Reaction: Excited-State Dynamics Reveals the C–H Acidity Mechanism of Methoxy Photo-oxidation on Titania. *J. Phys. Chem. Lett.* **2015**, *6* (9), 1624–1627.

(18) Walenta, C. A.; Kollmannsberger, S. L.; Kiermaier, J.; Winbauer, A.; Tschurl, M.; Heiz, U. Ethanol Photocatalysis on Rutile TiO<sub>2</sub>(110): the Role of Defects and Water. *Phys. Chem. Chem. Phys.* **2015**, *17* (35), 22809–22814.

(19) Kollmannsberger, S. L.; Walenta, C. A.; Courtois, C.; Tschurl, M.; Heiz, U. Thermal Control of Selectivity in Photocatalytic, Water-Free Alcohol Photoreforming. *ACS Catal.* **2018**, *8*, 11076–11084.

(20) Hansen, J. Ø.; Bebensee, R.; Martinez, U.; Porsgaard, S.; Lira, E.; Wei, Y.; Lammich, L.; Li, Z.; Idriss, H.; Besenbacher, F.; Hammer, B.; Wendt, S. Unravelling Site-Specific Photo-Reactions of Ethanol on Rutile TiO<sub>2</sub>(110). *Sci. Rep.* **2016**, *6*, 21990.

(21) Walenta, C. A.; Kollmannsberger, S. L.; Courtois, C.; Tschurl, M.; Heiz, U. Photocatalytic selectivity switch to C–C scission: 2-methyl ejection of tert-butanol on TiO<sub>2</sub>(110). *Phys. Chem. Chem. Phys.* **2018**, *20* (10), 7105–7111.

(22) Courtois, C.; Eder, M.; Schnabl, K.; Walenta, C. A.; Tschurl, M.; Heiz, U. Reactions in the Photocatalytic Conversion of Tertiary

- Alcohols on Rutile TiO<sub>2</sub>(110). *Angew. Chem., Int. Ed.* **2019**, *58* (ja), 14255.
- (23) Walenta, C. A.; Kollmannsberger, S. L.; Courtois, C.; Pereira, R. N.; Stutzmann, M.; Tschurl, M.; Heiz, U. Why Co-Catalyst-Loaded Rutile Facilitates Photocatalytic Hydrogen Evolution. *Phys. Chem. Chem. Phys.* **2019**, *21* (3), 1491–1496.
- (24) Guo, Q.; Xu, C.; Yang, W.; Ren, Z.; Ma, Z.; Dai, D.; Minton, T. K.; Yang, X. Methyl Formate Production on TiO<sub>2</sub>(110), Initiated by Methanol Photocatalysis at 400 nm. *J. Phys. Chem. C* **2013**, *117* (10), 5293–5300.
- (25) Guo, Q.; Xu, C.; Ren, Z.; Yang, W.; Ma, Z.; Dai, D.; Fan, H.; Minton, T. K.; Yang, X. Stepwise Photocatalytic Dissociation of Methanol and Water on TiO<sub>2</sub>(110). *J. Am. Chem. Soc.* **2012**, *134* (32), 13366–13373.
- (26) Wang, Z.-T.; Henderson, M. A.; Lyubinsky, I. Origin of Coverage Dependence in Photoreactivity of Carboxylate on TiO<sub>2</sub>(110): Hindering by Charged Coadsorbed Hydroxyls. *ACS Catal.* **2015**, *5* (11), 6463–6467.
- (27) Guo, Q.; Zhou, C.; Ma, Z.; Ren, Z.; Fan, H.; Yang, X. Elementary Photocatalytic Chemistry on TiO<sub>2</sub> Surfaces. *Chem. Soc. Rev.* **2016**, *45* (13), 3701–3730.
- (28) Zhang, R.; Wang, H.; Peng, X.; Feng, R.-r.; Liu, A.-a.; Guo, Q.; Zhou, C.; Ma, Z.; Yang, X.; Jiang, Y.; Ren, Z. In Situ Studies on Temperature-Dependent Photocatalytic Reactions of Methanol on TiO<sub>2</sub>(110). *J. Phys. Chem. C* **2019**, *123* (15), 9993–9999.
- (29) Shen, M.; Henderson, M. A. Role of Water in Methanol Photochemistry on Rutile TiO<sub>2</sub>(110). *J. Phys. Chem. C* **2012**, *116* (35), 18788–18795.
- (30) Mao, X.; Wei, D.; Wang, Z.; Jin, X.; Hao, Q.; Ren, Z.; Dai, D.; Ma, Z.; Zhou, C.; Yang, X. Recombination of Formaldehyde and Hydrogen Atoms on TiO<sub>2</sub>(110). *J. Phys. Chem. C* **2015**, *119* (2), 1170–1174.
- (31) Guo, Q.; Ma, Z.; Zhou, C.; Ren, Z.; Yang, X. Single Molecule Photocatalysis on TiO<sub>2</sub> Surfaces. *Chem. Rev.* **2019**, *119* (20), 11020–11041.
- (32) Hao, Q.; Wang, Z.; Wang, T.; Ren, Z.; Zhou, C.; Yang, X. Role of Pt Loading in the Photocatalytic Chemistry of Methanol on Rutile TiO<sub>2</sub>(110). *ACS Catal.* **2019**, *9* (1), 286–294.
- (33) Henderson, M. A. Structural Sensitivity in the Dissociation of Water on TiO<sub>2</sub> Single-Crystal Surfaces. *Langmuir* **1996**, *12* (21), 5093–5098.
- (34) Oviedo, J.; Sánchez-De-Armas, R.; San Miguel, M. Á.; Sanz, J. F. Methanol and Water Dissociation on TiO<sub>2</sub> (110): The Role of Surface Oxygen. *J. Phys. Chem. C* **2008**, *112* (46), 17737–17740.
- (35) Yuan, Q.; Wu, Z.; Jin, Y.; Xiong, F.; Huang, W. Surface Chemistry of Formaldehyde on Rutile TiO<sub>2</sub>(110) Surface: Photocatalysis vs Thermal-Catalysis. *J. Phys. Chem. C* **2014**, *118* (35), 20420–20428.
- (36) Rumble, J. R.; Lide, D. R.; Bruno, T. J. *CRC Handbook of Chemistry and Physics*; CRC Press: Boca Raton, FL, 2017.
- (37) Zhang, Z.; Bondarchuk, O.; Kay, B. D.; White, J. M.; Dohnálek, Z. Direct Visualization of 2-Butanol Adsorption and Dissociation on TiO<sub>2</sub>(110). *J. Phys. Chem. C* **2007**, *111* (7), 3021–3027.
- (38) Zhang, Z.; Rousseau, R.; Gong, J.; Kay, B. D.; Dohnálek, Z. Imaging Hindered Rotations of Alkoxy Species on TiO<sub>2</sub>(110). *J. Am. Chem. Soc.* **2009**, *131* (49), 17926–17932.
- (39) Walenta, C. A.; Courtois, C.; Kollmannsberger, S. L.; Eder, M.; Tschurl, M.; Heiz, U. Surface Species in Photocatalytic Methanol Reforming on Pt/TiO<sub>2</sub>(110): Learning from Surface Science Experiments for Catalytically Relevant Conditions. *ACS Catal.* **2020**, *10*, 4080–4091.
- (40) Lias, S. G.; Bartmess, J. E.; Liebman, J. F.; Holmes, J. L.; Levin, R. D.; Mallard, W. G. Ion Energetics Data. In *NIST Chemistry WebBook, NIST Standard Reference Database*, No. 69; Lindstrom, P. J., Mallard, W. G., Eds.; National Institute of Standards and Technology: Gaithersburg, MD, 2019, DOI: 10.18434/T4D303.
- (41) Maeda, K.; Teramura, K.; Lu, D.; Saito, N.; Inoue, Y.; Domen, K. Noble-Metal/Cr<sub>2</sub>O<sub>3</sub> Core/Shell Nanoparticles as a Cocatalyst for Photocatalytic Overall Water Splitting. *Angew. Chem., Int. Ed.* **2006**, *45* (46), 7806–7809.
- (42) Wilson, J. N.; Idriss, H. Effect of Surface Reconstruction of TiO<sub>2</sub>(001) Single Crystal on the Photoreaction of Acetic Acid. *J. Catal.* **2003**, *214* (1), 46–52.
- (43) Katsiev, K.; Harrison, G.; Alghamdi, H.; Alsalik, Y.; Wilson, A.; Thornton, G.; Idriss, H. Mechanism of Ethanol Photooxidation on Single-Crystal Anatase TiO<sub>2</sub>(101). *J. Phys. Chem. C* **2017**, *121* (5), 2940–2950.
- (44) Setvin, M.; Shi, X.; Hulva, J.; Simschitz, T.; Parkinson, G. S.; Schmid, M.; Di Valentin, C.; Selloni, A.; Diebold, U. Methanol on Anatase TiO<sub>2</sub>(101): Mechanistic Insights into Photocatalysis. *ACS Catal.* **2017**, *7* (10), 7081–7091.
- (45) Crampton, A. S.; Cai, L.; Janvelyan, N.; Zheng, X.; Friend, C. M. Methanol Photo-Oxidation on Rutile TiO<sub>2</sub> Nanowires: Probing Reaction Pathways on Complex Materials. *J. Phys. Chem. C* **2017**, *121* (18), 9910–9919.
- (46) Pepin, P. A.; Diroll, B. T.; Choi, H. J.; Murray, C. B.; Vohs, J. M. Thermal and Photochemical Reactions of Methanol, Acetaldehyde, and Acetic Acid on Brookite TiO<sub>2</sub> Nanorods. *J. Phys. Chem. C* **2017**, *121* (21), 11488–11498.
- (47) Pepin, P. A.; Lee, J. D.; Murray, C. B.; Vohs, J. M. Thermal and Photocatalytic Reactions of Methanol and Acetaldehyde on Pt-Modified Brookite TiO<sub>2</sub> Nanorods. *ACS Catal.* **2018**, *8*, 11834–11846.



**Supporting Information:**  
**Origin of Poisoning in Methanol Photoreforming on  
TiO<sub>2</sub>(110): The Importance of Thermal Back Reaction Steps in  
Photocatalysis**

Carla Courtois<sup>‡,¶</sup>, Moritz Eder<sup>‡,¶</sup>, Sebastian L. Kollmannsberger<sup>¶</sup>,  
Martin Tschurl<sup>¶</sup>, Constantin A. Walenta<sup>¶</sup>, Ueli Heiz<sup>¶,\*</sup>

¶ Chair of Physical Chemistry & Catalysis Research Center, Technical University of  
Munich, Lichtenbergstr. 4, 85748 Garching, Germany

‡ The authors contributed equally.

\*Corresponding Author: ulrich.heiz@mytum.de

## Experimental

The details of the experimental setup are described elsewhere.<sup>1-3</sup> The experiments are performed in an ultra-high vacuum apparatus with a base pressure of  $< 9.8 \times 10^{-11}$  mbar. The quadratic rutile TiO<sub>2</sub>(110) single crystal (SurfaceNet GmbH, 9.95 mm x 9.95 mm x 0.3 mm) is mounted on a sample holder, which is heated by resistive heating and cooled with liquid N<sub>2</sub> to set the sample on a defined temperature. The crystal is prepared by several sputter-annealing cycles, which consist of Ar<sup>+</sup> sputtering (20 min, 1 keV,  $1 \times 10^{-5}$  mbar Ar), oxygen annealing (20 min, 800 K,  $5 \times 10^{-6}$  mbar O<sub>2</sub>) and vacuum annealing (10 min, 800 K), until a clean and flat surface is obtained. The cleanliness is verified by Auger electron spectroscopy (Omicron Nanotechnology). The defect concentration and the flatness of the reduced surface is determined by H<sub>2</sub>O temperature-programmed desorption experiments.<sup>4, 5</sup> The blueish TiO<sub>2</sub>(110) has a bridge-bonded oxygen vacancy concentration of  $6 \pm 1\%$  ML with respect to Ti-lattice sites (Fig. S7). Photochemical experiments are carried out by illuminating the sample with a Nd:YAG-pumped (3<sup>rd</sup> harmonic, Innolas Spitlight HighPower 1200, 7 ns pulse width, 20 Hz repetition rate) frequency-doubled OPO (GWU, premiScan ULD/400) laser beam at a wavelength of 242 nm with a power of  $5.9 \pm 0.3$  mW at the crystal surface. Product evolution, as well as the purity of the alcohol background, are monitored with a line of sight quadrupole mass spectrometer (QMA 430, Pfeiffer Vacuum GmbH). Catalytic experiments are carried out in a defined alcohol background pressure, where the chamber is filled with reactant via a leak valve. Single coverage measurements are conducted via Langmuir dosing at cryogenic temperatures. A representative set of raw data is shown in Fig. S8. 2-methyl-2-pentanol (99%, Sigma Aldrich), ethanol (Chromasolv,  $\geq 99.8\%$ , Sigma-Aldrich) and methanol

(Chromasolv,  $\geq 99.9\%$ , Sigma-Aldrich) are degasified by several freeze-pump-thaw cycles.

## Additional Data

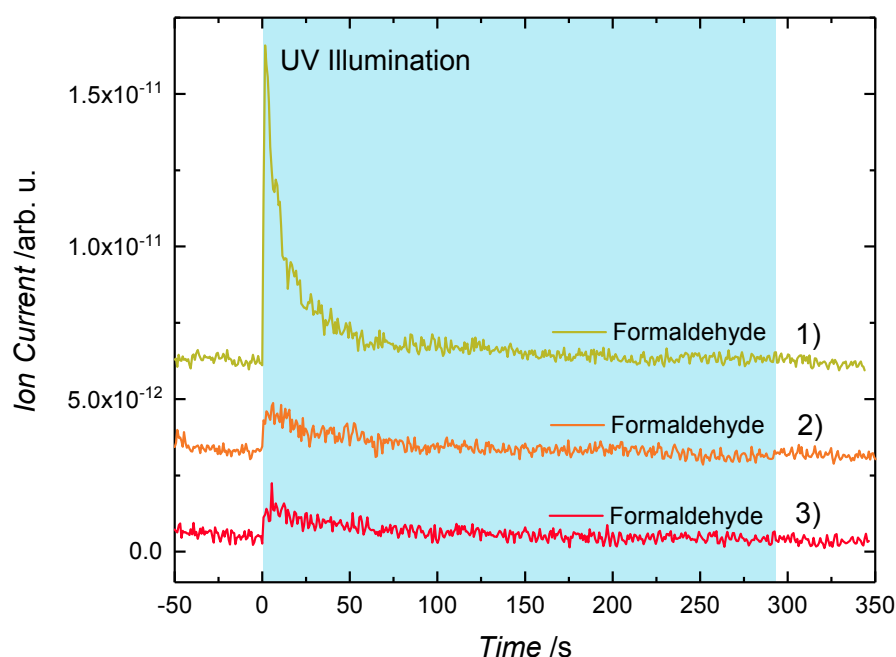


**Figure S1.** Isothermal mass traces ( $m/z$  30) of the photoreaction of 1 L methanol on r-TiO<sub>2</sub>(110) at 300 K for consecutive dosages. In experiment 1), 1 L methanol is adsorbed on the freshly prepared crystal at 130 K, the sample is thermalized to 300 K, and UV illumination starts at  $t=0$  s. Upon excitation, an immediate formation of formaldehyde is observed. The methoxy is oxidized by the photo-hole forming formaldehyde, which is thermally desorbing at the reaction temperature of 300 K. Other photoproducts, as well as water, are not observed during illumination. In experiment 2) and 3), the sample is cooled down to 130 K immediately after experiment 1). 1 L methanol is adsorbed and the sample is thermalized to 300 K. Upon illumination, about 20% of the initial amount of formaldehyde is observed in experiment 2) and 3). 2) and 3) show a poisoning of the catalyst towards formaldehyde production with respect to experiment 1). The blue region shows the time of UV illumination.

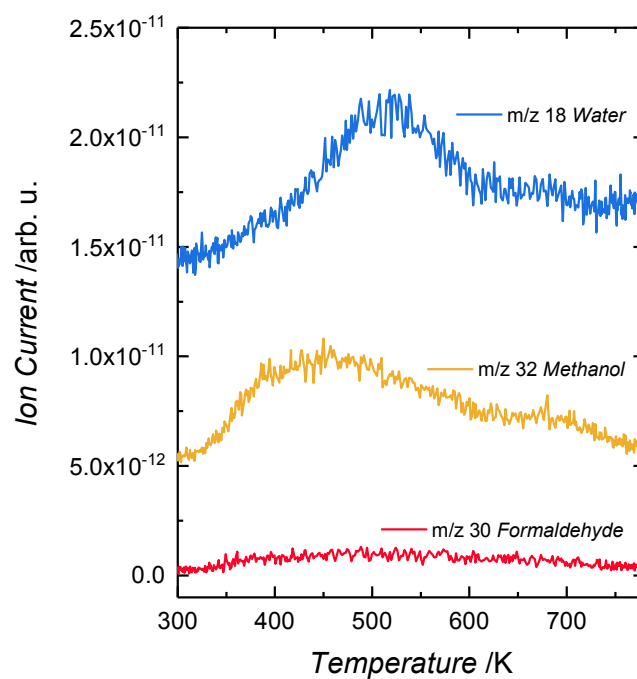


**Figure S2.** Temperature-programmed desorption experiment after isothermal photoreaction of 1 L methanol on r-TiO<sub>2</sub>(110) at 300 K, analogue to Figure S1). 1 L methanol is adsorbed on r-TiO<sub>2</sub>(110) at 130 K, the sample is thermalized to 300 K and illuminated with UV light for 5 min. Subsequently, a temperature-programmed desorption experiment shows remaining methanol and the expected water peak around 530 K resulting from recombinative desorption of OH<sub>br</sub>. No other products were observed in TPD.

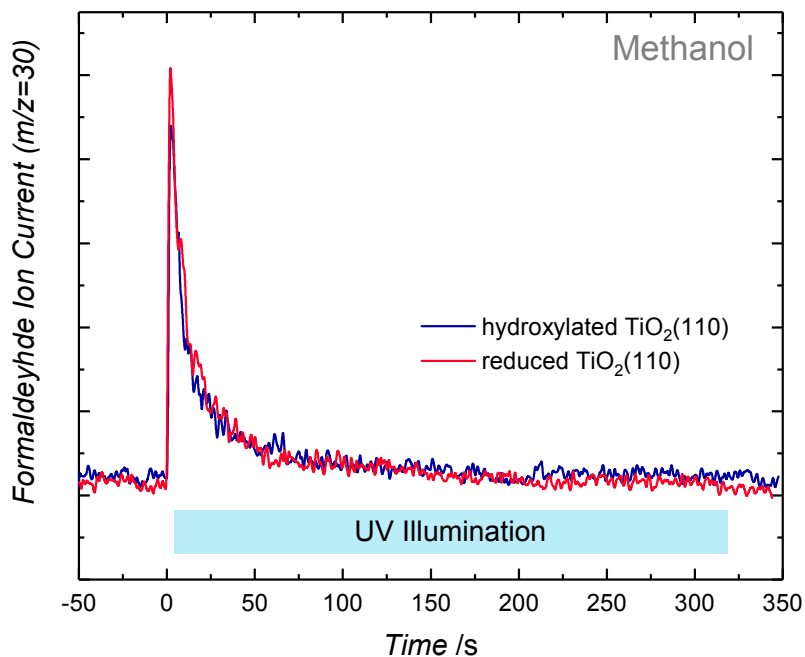


**Figure S3.** Isothermal mass traces of formaldehyde ( $m/z$  30) of the photoreaction of 1L methanol on r-TiO<sub>2</sub>(110) and pre-hydroxylated TiO<sub>2</sub>(110) at 300 K. 1 L methanol is adsorbed on the prepared crystal at 130 K, the sample is thermalized at 300 K, and UV illumination starts at  $t = 0$  s. The hydroxylated TiO<sub>2</sub>(110) is prepared by adsorbing a saturation layer of water, heating the sample to 350 K, so that all molecular water is desorbing, and is cooled down to cryogenic temperatures. For both surfaces, upon excitation, an immediate formation of formaldehyde is observed. The methoxy is oxidized by the photo-hole yielding formaldehyde, which is thermally desorbing at 300 K. Other photo-products, as well as water, are not observed at these conditions. The blue region shows the time of UV illumination.

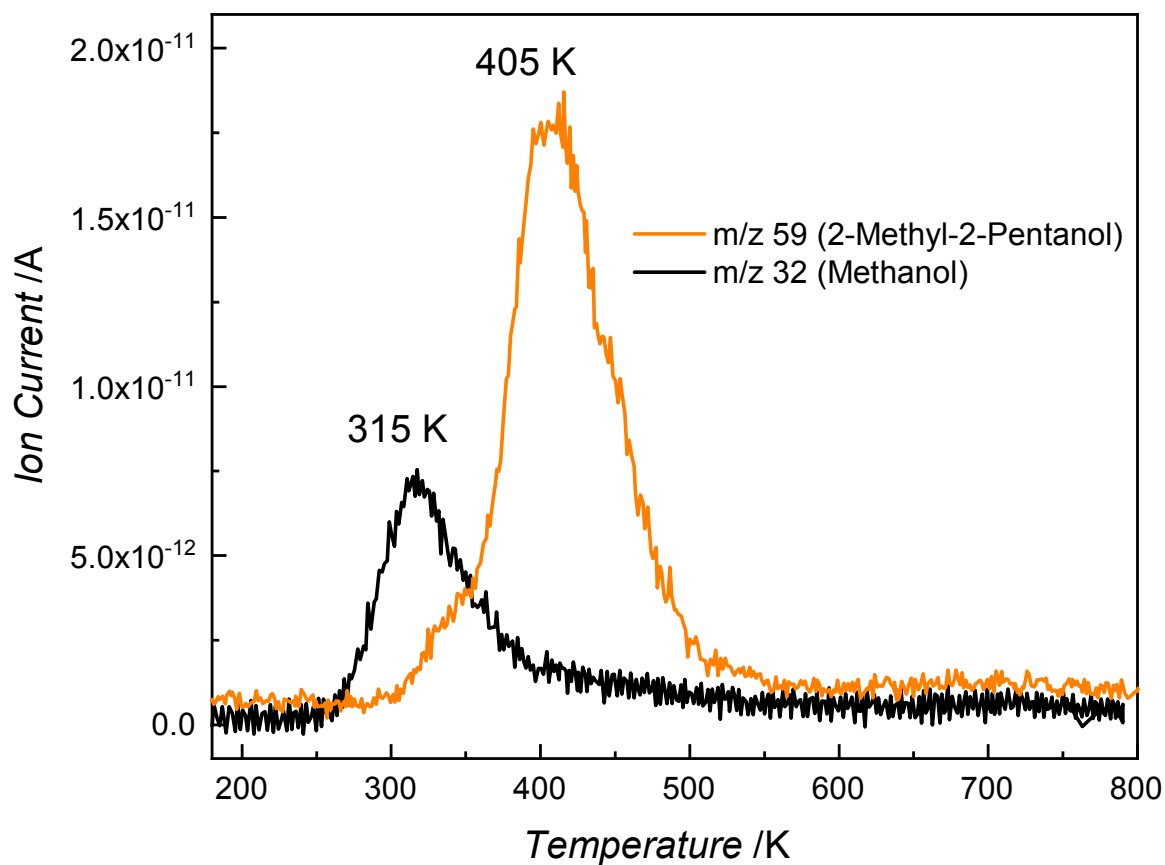


**Figure S4.** Temperature programmed desorption experiments for methanol (black) and 2-methyl-2-pentanol (orange) on a freshly prepared  $r\text{-TiO}_2(110)$ , respectively. Alcohol exposures (1 L for methanol and 5 L for 2M2P) are carried out at 150 K with a heating rate of 1.5 K/s.

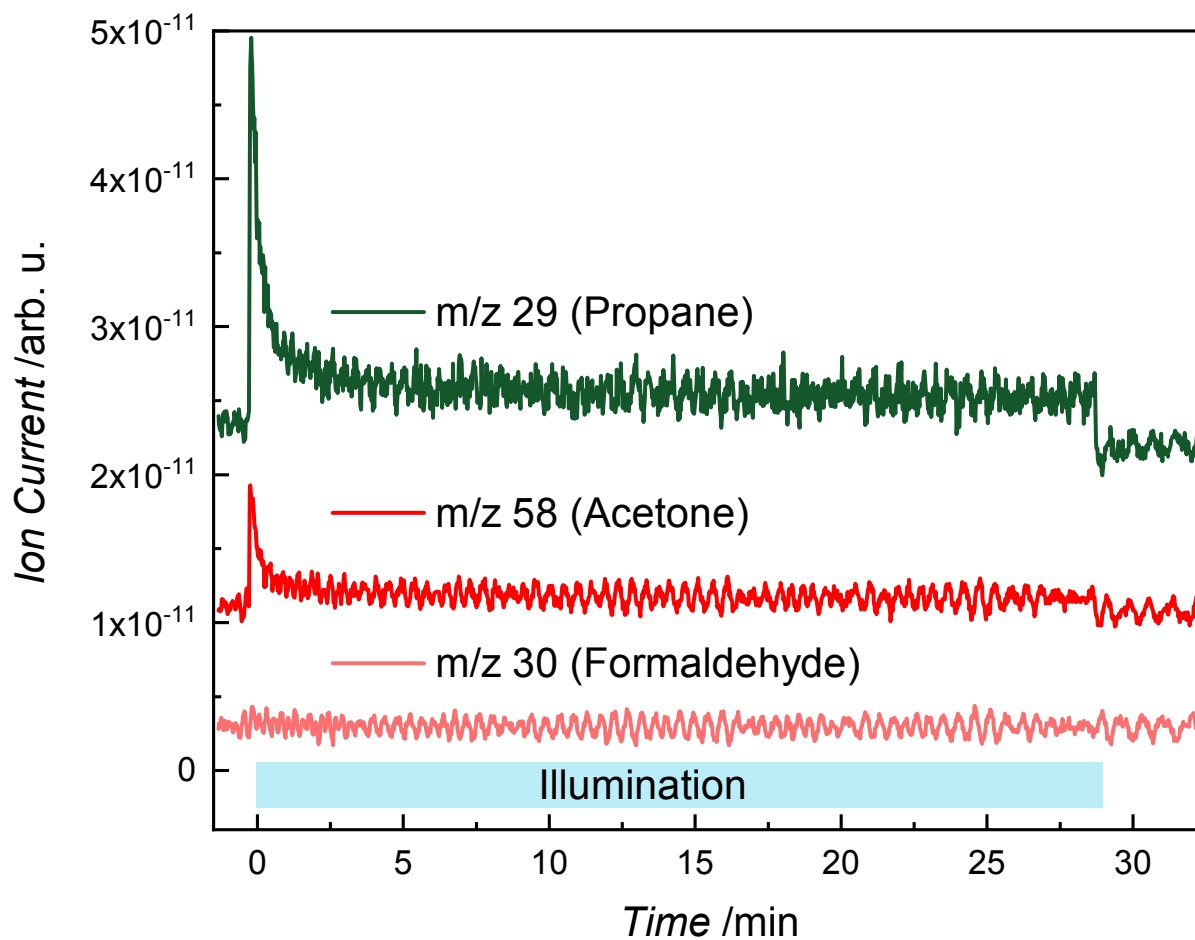


**Figure S5.** Photocatalysis of 2-methyl-2-pentanol on r-TiO<sub>2</sub>(110) at 300 K in an alcohol background of  $5 \times 10^{-8}$  mbar after a dosage of 5 L (i.e.  $5 \times 10^{-8}$  mbar for 133 s) of methanol at 300 K. The blue region highlights the period of UV irradiation. Upon UV illumination, acetone (m/z 58) and propane (m/z 29) are formed catalytically without any deactivation. The catalyst is active over the whole illumination time of 28 min. Upon illumination, significant amounts of formaldehyde from methanol photooxidation are not detected, showing that the tertiary alcohol replaces methanol completely due to its higher binding energy (see Fig. S4). Note that the traces are offset for clarity.

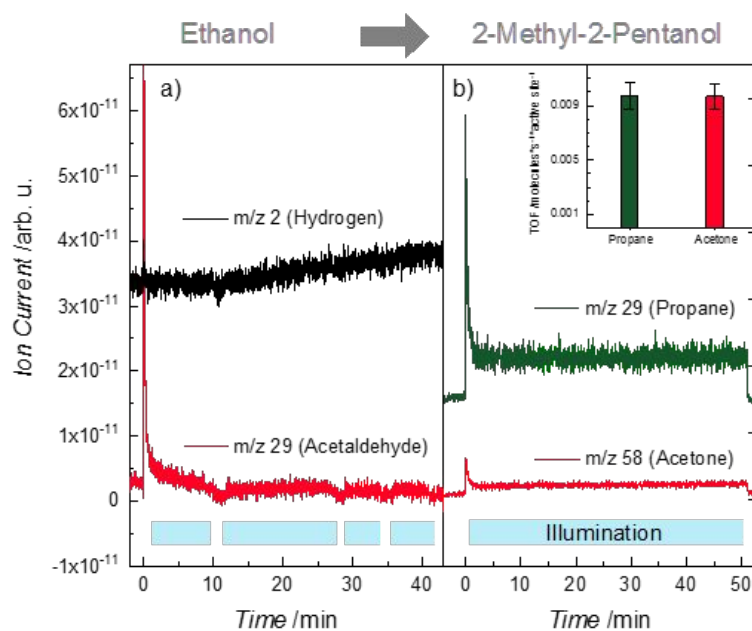


**Figure S6.** Photochemical reaction of ethanol and 2-methyl-2-pentanol on r-TiO<sub>2</sub>(110) at 300 K in an alcohol background of  $5 \times 10^{-8}$  mbar in consecutive experiments. The blue region highlights the period of UV irradiation. a) Photochemical product of ethanol oxidation on a freshly prepared r-TiO<sub>2</sub>(110). Upon UV excitation, ethoxy species are oxidized to acetaldehyde ( $m/z$  29), which thermally desorbs. The amount of acetaldehyde decreases continuously due to the hydroxylation of the titania surface. b) Consecutive experiment of photocatalytic conversion of 2-methyl-2-pentanol on the ethanol-poisoned r-TiO<sub>2</sub>(110). Upon UV illumination, acetone ( $m/z$  58) and propane ( $m/z$  29) are formed catalytically without deactivation. The catalyst is active over the whole illumination time of 50 min towards 2-methyl-2-pentanol conversion. The inset shows the TOFs of acetone and propane. Note that the traces are offset for clarity.

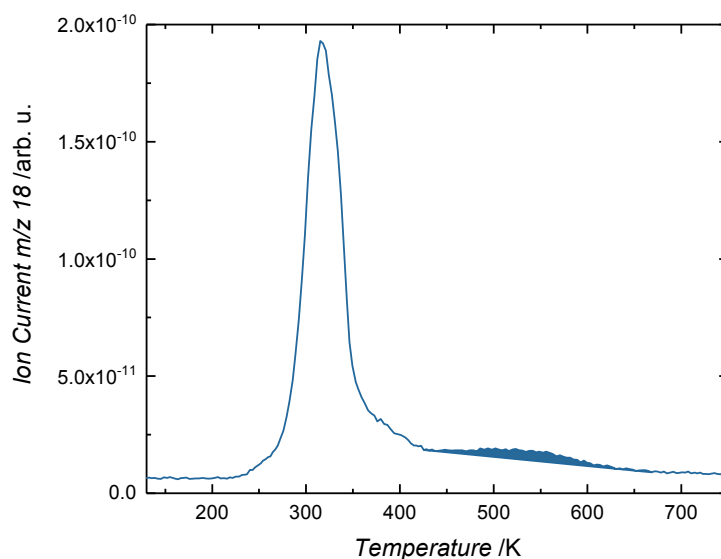


**Figure S7.** Temperature-programmed desorption of 1 ML H<sub>2</sub>O from reduced TiO<sub>2</sub>(110). 1 ML H<sub>2</sub>O is dosed at 145 K with a molecular beam doser. Molecular water is desorbing at 310 K from Ti-lattice sites. The broad feature at 530 K originates from dissociatively adsorbed water in BBO vacancies forming two OH<sub>br</sub> species. The integral of the high temperature feature yields a BBO vacancy concentration of  $6 \pm 1\%$  ML following the titration method established by Henderson.<sup>4</sup>



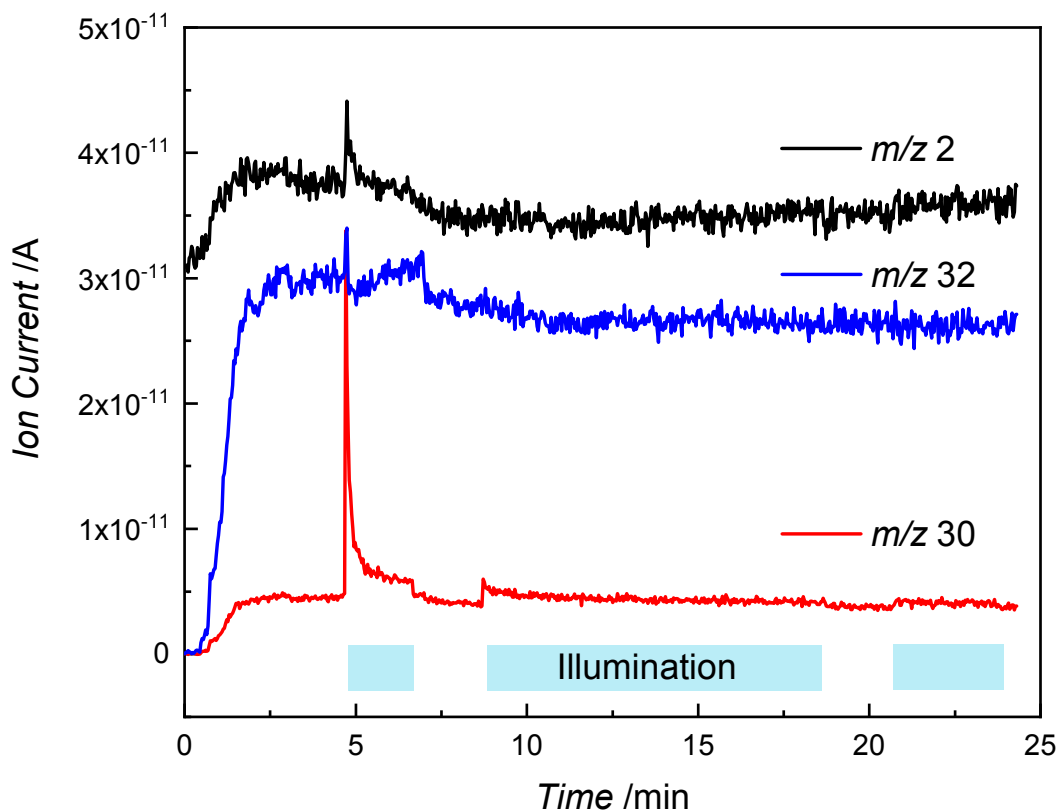


**Figure S8.** Raw data of the isothermal photooxidation experiment with methanol as shown in Fig. 1a.

### Calculation of the turn-over-frequency

The evaluation of the turn-over-frequency allows for a quantification of the product formation with the help of an unequivocal mass fragment. The baseline corrected signal of the QMS is integrated in the steady-state regime. This value is corrected for the  $m/z$ -dependent transmission through the QMS, the electron impact ionization cross section (ICS), as well as with a factor considering the ion fragmentation taken from a reference mass spectrum. The ICS values as well as the  $m/z$ -values are given in table S1.

**Table S1.** Electron impact ionization cross section values at 70 eV and  $m/z$ -value of the respective fragment used for quantification.

Molecule	$m/z$ fragment	ICS [ $\text{\AA}$ ] <sup>6</sup>
Acetone	58	10.2
Propane	29	11.6

## References

1. Walenta, C. A.; Kollmannsberger, S. L.; Courtois, C.; Tschurl, M.; Heiz, U., Photocatalytic Selectivity Switch to C-C scission:  $\alpha$ -Methyl Ejection of tert-Butanol on TiO<sub>2</sub>(110). *Phys. Chem. Chem. Phys.* **2018**, *20* (10), 7105-7111.
2. Kollmannsberger, S. L.; Walenta, C. A.; Courtois, C.; Tschurl, M.; Heiz, U., Thermal Control of Selectivity in Photocatalytic, Water-Free Alcohol Photoreforming. *ACS Catal.* **2018**, 11076-11084.
3. Walenta, C. A.; Kollmannsberger, S. L.; Pereira, R. N.; Tschurl, M.; Stutzmann, M.; Heiz, U., Anhydrous Ethanol Dehydrogenation on Metal–Organic Chemical Vapor Deposition Grown GaN(0001). *J. Phys. Chem. C* **2017**, *121* (30), 16393-16398.
4. Henderson, M. A., Structural Sensitivity in the Dissociation of Water on TiO<sub>2</sub> Single-Crystal Surfaces. *Langmuir* **1996**, *12* (21), 5093-5098.
5. Zehr, R. T.; Henderson, M. A., Influence of O<sub>2</sub>-induced Surface Roughening on the Chemistry of Water on TiO<sub>2</sub>(110). *Surf. Sci.* **2008**, *602* (8), 1507-1516.
6. Harrison, A. G.; Jones, E. G.; Gupta, S. K.; Nagy, G. P., Total Cross Sections for Ionization by Electron Impact. *Can. J. Chem.* **1966**, *44* (16), 1967-1973.

### 4.3 Nickel clusters on TiO<sub>2</sub>(110): thermal chemistry and photocatalytic hydrogen evolution of methanol

For considerable hydrogen evolution on TiO<sub>2</sub>(110) photocatalysts, the presence of a co-catalyst is necessary, as discussed in section 2.5. Most studies employed noble metal transition metals such as Au or Pt.[50, 83, 145, 143, 141] Their implementation on a larger scale is economically problematic due to the metals' prices and abundancies. Therefore, cheaper transition metals are sought which can fulfill the mechanistic role of the co-catalyst equally well. Here, Ni is a promising candidate, being a typical catalyst for hydrogenations in applied catalysis and for hydrogen-evolving reactions in surface science.[155, 156, 157, 158] Furthermore, this metal has been successfully employed as co-catalyst on powder TiO<sub>2</sub> in several studies on applied photocatalysis, and different Ni and Ni oxide compounds were claimed to be the catalytically active species.[159, 160, 161, 162] This work investigated Ni clusters on TiO<sub>2</sub>(110) with respect to their thermal and photochemical reactivity towards methanol.

Methanol TPD experiments on Ni<sub>x</sub>/TiO<sub>2</sub>(110) showed that the alcohol desorbs in part molecularly, but is to an extent also decomposed, yielding CO and molecular hydrogen as desorption products. This proved the capability of Ni clusters to thermally evolve H<sub>2</sub>, which is not possible on the bare TiO<sub>2</sub>(110) surface. The decomposition of methanol and the corresponding desorption products is similar to Pt<sub>x</sub>/TiO<sub>2</sub>(110) systems under comparable conditions. Conducting several TPD experiments successively shows an alteration in the intensities of the desorbing species, with less H<sub>2</sub> and CO being detected for the benefit of molecular methanol until a stable ratio is reached. This suggests a significant alteration of the Ni clusters during the heat treatment, which finally results in a state which is thermodynamically stable against the elevated temperatures.

During methanol photocatalysis on Ni<sub>x</sub>/TiO<sub>2</sub>(110) in a constant alcohol background under UV illumination, formaldehyde and hydrogen are found as reaction products at room temperature. Ni- and Pt-loaded titania hence show a similar selectivity in photocatalytic methanol reforming. Therefore, the mechanism behind the product formation most likely proceeds via the same steps. Apart from that, Ni<sub>x</sub>/TiO<sub>2</sub>(110) slowly deactivates during methanol photoconversion, contrary to Pt<sub>x</sub>/TiO<sub>2</sub>(110), whose activity does not decrease. Exposing the Ni-decorated titania to a methanol background before illumination does not diminish its activity, i.e. the deactivation process takes place during the photoconversion of the alcohol. O<sub>2</sub> PSD experiments show that the presence of Ni clusters does not deteriorate the activity of the photocatalyst.

In Auger spectra of Ni<sub>x</sub>/TiO<sub>2</sub>(110) after methanol photo-oxidation, the formation of carbon is found. The carbon signal decreases after heating, but is persistent against further temperature treatments. This strongly suggests a Ni-C species, which is probably related to the deactivation observed during alcohol photocatalysis.

The results show that Ni clusters are in principle applicable as co-catalysts for photocatalytic hydrogen evolution from methanol on TiO<sub>2</sub>(110). However, the observed deactivation is a drawback for potential applications, which is not the case for e.g. Pt cluster co-catalysts.

Cite this: *Catal. Sci. Technol.*, 2020, 10, 7630

## Nickel clusters on TiO<sub>2</sub>(110): thermal chemistry and photocatalytic hydrogen evolution of methanol†

Moritz Eder,‡<sup>a</sup> Carla Courtois,‡<sup>a</sup> Tim Kratky,<sup>b</sup> Sebastian Günther,<sup>b</sup> <sup>b</sup> Martin Tschurl,<sup>a</sup> <sup>a</sup> and Ueli Heiz\*<sup>a</sup>

In heterogeneous photocatalysis, noble metals such as Au, Pt, or Pd are most commonly used as co-catalysts to facilitate H<sub>2</sub> evolution, yet their costs are problematic for applications on a large scale. In this work, we show that the cheaper, more abundant transition metal nickel as co-catalyst material reacts accordingly, when being deposited as small clusters onto rutile TiO<sub>2</sub>. Different to noble metal systems the photocatalysts undergo photocorrosion, depicted in a declining activity during the photoreforming of methanol. The reaction being performed in an ultra-high vacuum environment allows for a more detailed elucidation of the deactivation processes. Supported by reactivity studies under different conditions, Auger electron spectroscopy reveals that coking of the clusters occurs, while nickel oxide formation is not observed. The study thus shows that nickel co-catalysts are indeed prospective systems for the photocatalytic hydrogen evolution reaction, similar to platinum clusters, but instead may also feature unexpected photon-driven deactivation pathways.

Received 21st July 2020,  
Accepted 9th September 2020

DOI: 10.1039/d0cy01465f

rsc.li/catalysis

### Introduction

Hydrogen is a key element in the intent to decarbonize major sectors of the economy. It is not only an ideal substrate for fuel cells which are used for transportation or for industry energy supply,<sup>1</sup> but its relevance has tremendously increased since the development of hydrogen gas turbines,<sup>2</sup> which may fill the gap of dispatchable generation in the carbon-free energy ecosystem.<sup>3</sup> However, most of the world's hydrogen production (>95%) is based on carbon-emitting processes, such as steam reforming of natural gas.<sup>4</sup> Photocatalytic hydrogen production from alcohols or water under mild conditions is a sustainable approach to guarantee the rising demand for hydrogen. This accounts all the more since the development of bioalcohol generation from renewable sources.<sup>5–7</sup> In addition, photocatalytic alcohol reforming on titania-based systems provides ketones and aldehydes as valuable oxidation side products and even facilitates the selective photocatalytic conversion of tertiary alcohols.<sup>8</sup> TiO<sub>2</sub>

is the most often used and best understood semiconductor in photocatalytic applications,<sup>9</sup> because single-crystalline studies on TiO<sub>2</sub>(110) under highly defined conditions in ultra-high vacuum (UHV) allow the investigation of fundamental mechanisms in photocatalysis and the disentanglement of thermal- and photochemical steps. The highly systematic works by Henderson, Dohnálek and others have provided reliable preparation recipes of the photocatalyst and its surface.<sup>10–14</sup> These procedures provide a defined, reproducible thermal and photochemical reactivity of the TiO<sub>2</sub>(110) surface which is widely established in the field.<sup>8,15–20</sup> Loading the titania photocatalyst with a co-catalyst is indispensable for the system to be able to significantly evolve H<sub>2</sub>.<sup>21,22</sup> For single crystals in UHV, laser-ablation cluster sources have proven to be outstanding tools for the *in situ* deposition of small, size-selected metal clusters.<sup>23</sup> It allows for a more precise size and coverage control than *e.g.* evaporation techniques, since soft-landing of the clusters ensures a destruction-free surface coverage.<sup>24</sup> A very prominent, stable and widely used co-catalyst is platinum. The photocatalytic oxidation of methanol on (Pt-loaded) rutile titania has been identified to be a hole-driven process.<sup>25,26</sup> On the well-investigated TiO<sub>2</sub>(110) model surface, methanol is to a certain extent adsorbed dissociatively by O–H bond cleavage, yielding a photo-active methoxy and a hydrogen species. Upon illumination this photo-active methoxy is oxidized to formaldehyde through a C–H bond cleavage.<sup>25</sup> In a previous study, we demonstrated that Pt facilitates H<sub>2</sub>

<sup>a</sup> Chair of Physical Chemistry & Catalysis Research Center, Technical University of Munich, Lichtenbergstr. 4, 85748 Garching, Germany.

E-mail: [ulrich.heiz@mytum.de](mailto:ulrich.heiz@mytum.de)

<sup>b</sup> Department of Chemistry, Technical University of Munich, Lichtenbergstr. 4, 85748 Garching, Germany

† Electronic supplementary information (ESI) available: Mass scan of Ni clusters, methanol photochemistry on titania, oxygen PSD on titania, AES reference spectra. See DOI: 10.1039/d0cy01465f

‡ The authors contributed equally to this work.

evolution such that both abstracted hydrogen atoms recombine thermally on the metal cluster.<sup>21</sup> Although deviating from the widespread electrochemical 2-photon-process, which includes H<sup>+</sup> reduction by an electron, this pathway even comprehensively explains the photochemical reactivity of tertiary alcohols.<sup>27</sup> However, the high costs and low abundance of Pt hamper its implementation into applied systems on a larger scale. As its only role in the catalytic cycle is the thermal hydrogen recombination, a more abundant metal such as nickel, whose surface is able to thermally desorb hydrogen,<sup>28,29</sup> is a promising candidate for replacing it. Single crystal studies reveal that methanol decomposes thermally to H<sub>2</sub> and CO on nickel as it was observed for methanol on Pt clusters.<sup>30,31</sup>

The photocatalytic activity of Ni-loaded TiO<sub>2</sub> powder mixtures in methanol- or ethanol-water mixtures has been subject in several studies.<sup>32–40</sup> Chen *et al.* report a comparable photocatalytic hydrogen production rate from ethanol-water solutions for Ni/TiO<sub>2</sub> and Au/TiO<sub>2</sub>.<sup>41</sup> In contrast, Bahruji *et al.* present a vanishingly small rate of hydrogen production for Ni/TiO<sub>2</sub> in methanol photoreforming.<sup>33</sup> There is, however, no consensus about whether metallic nickel, nickel hydroxide or nickel oxide is the active phase. In addition, hydrogen production rates are strongly dependent on the various preparation methods. The different conditions and the heterogeneity of the employed catalysts make it difficult to compare the results among each other and to draw systematic conclusions. Apart from titania, NiO<sub>x</sub> is used as co-catalyst on Ga<sub>2</sub>O<sub>3</sub> and various other support materials for overall water splitting, where the nickel-containing phase might act as hydrogen evolution catalyst, although the focus of these works often lies on the support and the exact role of the co-catalyst remains elusive.<sup>42–44</sup> Those studies imply that the key factors limiting the photocatalytic hydrogen evolution remain an open scientific question. As in the case of noble metals, these open questions can be approached from a fundamental level in order to clarify the role of Ni clusters as co-catalysts for heterogeneous photocatalysis.

In this work, we report the photocatalytic hydrogen evolution from methanol reforming on Ni<sub>x</sub>-loaded TiO<sub>2</sub>(110) using size-selected metal clusters in a water-free, anaerobic environment under highly defined conditions in UHV. The absence of a solution underlines the direct hole transfer mechanism without involving any additional intermediate species, which allows to draw a complete picture of methanol photoreforming.

Conventional characterization methods cannot be applied to ideal single crystals in UHV. For example, the TiO<sub>2</sub>(110) sample is too thick for TEM analysis, and the cluster surface concentration is too low for a detection by Raman spectroscopy or X-ray diffraction. Instead, analytic procedures typical for surface science studies are used. We apply temperature programmed desorption (TPD) to investigate the thermal reaction pathways and Auger electron spectroscopy (AES) to characterize surface species. This method is

extremely surface sensitive and in some cases even allows a better disentanglement of Ni and carbon species than *e.g.* X-ray photoelectron spectroscopy (XPS).<sup>45–47</sup> The photocatalytic activity is probed by well-defined reaction conditions to unravel elemental processes on the catalysts surface on a molecular level. The thoughtful choice of defined reaction conditions then allows a disentanglement of elemental thermal- and photochemical processes on a molecular level on the catalysts surface.

## Experimental

All experiments were carried out in a home built ultra-high vacuum setup with a base pressure lower than  $9.9 \times 10^{-11}$  mbar.<sup>8</sup> Briefly, it consisted of a liquid N<sub>2</sub>-cooled ( $x, y, z, \phi$ ) – manipulator (VAB Vakuum GmbH), an Auger spectrometer (CMA 100, Omicron Nanotechnology GmbH), a sputter gun (IQE 11/35, SPECS GmbH), a line-of-sight quadrupole mass spectrometer (QMS) (QMA 430, Pfeiffer Vacuum GmbH), a leak valve (Pfeiffer Vacuum GmbH), and a home-built gasline (base pressure  $5.0 \times 10^{-9}$  mbar). A laser vaporization cluster source, which allowed the generation and *in situ* deposition of metal cluster cations with an atomically precise number of atoms, was connected with the analysis chamber. Generally, the experimental parameters for the cluster deposition were chosen to ensure soft-landing conditions to eventually yield Ni<sup>0</sup> clusters on the reduced titania (Ni<sub>x</sub>/r-TiO<sub>2</sub>(110)) surface, as determined by Aizawa *et al.* by means of X-ray photoelectron spectroscopy (XPS).<sup>24</sup>

For cluster generation, a focused beam of a frequency-doubled Nd:YAG (532 nm, 100 Hz, Spitlight DPSS, Innolas) ablated a rotating Ni target (99.96% purity, ESG Edelmetalle, Germany). The as-generated plasma was cooled down by pulses of He gas (He 6.0, Air Westfalen) synchronized with the laser pulses. This way, the expansion of the cluster beam into the vacuum was facilitated. The cationic cluster beam was orthogonally deflected by a quadrupole bender and guided through a quadrupole mass filter (QMF; Extrel, USA), which enabled either the selection of a particular cluster size or the guidance of the clusters in ion-guide mode. For this study, the latter mode was used and the device was operated as high-pass filter transmitting only ions larger than Ni<sub>10</sub>. The settings resulted in a cluster size distribution with a maximum from Ni<sub>20</sub> to Ni<sub>23</sub> (see Fig. S1†). Cluster loadings were determined by monitoring and integrating the cluster neutralization current during the deposition with a picoammeter (Keithley, 6587). The amount of metal clusters deposited onto the titania surface was 1% of a monolayer (ML) with respect to the total number of TiO<sub>2</sub>(110) surface atoms on the crystal in every experiment if not indicated differently. For experiments with different cluster coverages, the desired amount of nickel, which was specified in the presented data, were deposited by varying the deposition time (in the order of minutes).

The rutile TiO<sub>2</sub>(110) crystal plate (Surface-net GmbH, 0.995 cm × 0.995 cm × 0.3 mm) was mounted in a

molybdenum sample holder, whose temperature was controlled by resistive heating and liquid N<sub>2</sub> cooling and measured by a thermocouple attached to the bottom of the mounting plate. Crystal preparation and cleaning was done by repeated cycles of Ar<sup>+</sup> (100% N60; Air Liquide) sputtering (20 min, 1.0 keV,  $1 \times 10^{-5}$  mbar Ar), O<sub>2</sub> ( $\geq 99\%$ , Westfalen) annealing (20 min, 800 K,  $1.0 \times 10^{-6}$  mbar O<sub>2</sub>), and vacuum annealing (15 min, 800 K). The cleanliness was confirmed by AES. With this procedure a reduced, blue, conductive crystal was obtained containing a constant surface defect density of  $6 \pm 1\%$ , determined by H<sub>2</sub>O TPD.<sup>13,19</sup>

The reactants were dosed by Langmuir dosing at 150 K in the case of TPD, photon-stimulated reaction (PSR) and subsequent post-illumination TPD (PI-TPD) experiments. The TPD and PI-TPD measurements used a heating rate of 1–2 K s<sup>-1</sup>. For the PSR experiment, the reactant-covered crystal was thermalized to 250 K prior to an illumination of 10 min at 250 K. Subsequently a PI-TPD was performed. For catalytic studies, the crystal was illuminated in a constant methanol background pressure of  $5.0 \times 10^{-7}$  mbar at 300 K. Mass signals in the QMS of thermal and photochemically desorbing species were identified by a fragmentation pattern analysis. The ion signals were corrected for the fragmentation contribution taken from reference mass spectra,<sup>48</sup> the transmission through the QMS, and the electron-impact ionization cross section. Methanol (absolute, HPLC grade, 99.8%, Sigma-Aldrich) was purified by several freeze–pump–thaw cycles and repeated flushing of the gasline prior to use. Its purity was confirmed by QMS analysis at a constant methanol background pressure.

The light source for the illumination of the photocatalyst was a frequency-doubled optical parametric oscillator (242 nm, GWU, premiScan ULD/400), pumped by the third harmonic of a Nd:YAG (Innolas Spitlight HighPower 1200, 20 Hz repetition rate, 7 ns pulse width). A pulse energy of  $600 \pm 50$   $\mu$ J of the incident light beam guaranteed the saturation of the absorbing crystal with photons. No laser induced thermal heating effects were observed.

## Results

### Thermal chemistry on Ni-decorated titania

The thermal reactivity of methanol on Ni cluster loaded reduced-titania was investigated by means of TPD. Five consecutive methanol TPD spectra were taken in order to observe possible changes induced by the heat treatment, shown in Fig. 1 in comparison to a methanol TPD spectrum on bare r-TiO<sub>2</sub>(110).

The bare surface (dashed lines) yields only one peak of the methanol fragment *m/z* 31 at  $\sim 340$  K, which corresponds to the desorption of molecular methanol, as expected in this temperature range for an exposure of 1 L.<sup>13</sup> The TPDs on Ni<sub>*x*</sub>/r-TiO<sub>2</sub>(110) (solid lines) show the same peak, whose intensity is initially lower but increases consecutively in the following experiments. Additionally, the cluster-loaded surface shows an H<sub>2</sub> signal ( $\sim 370$  K) as well as a high

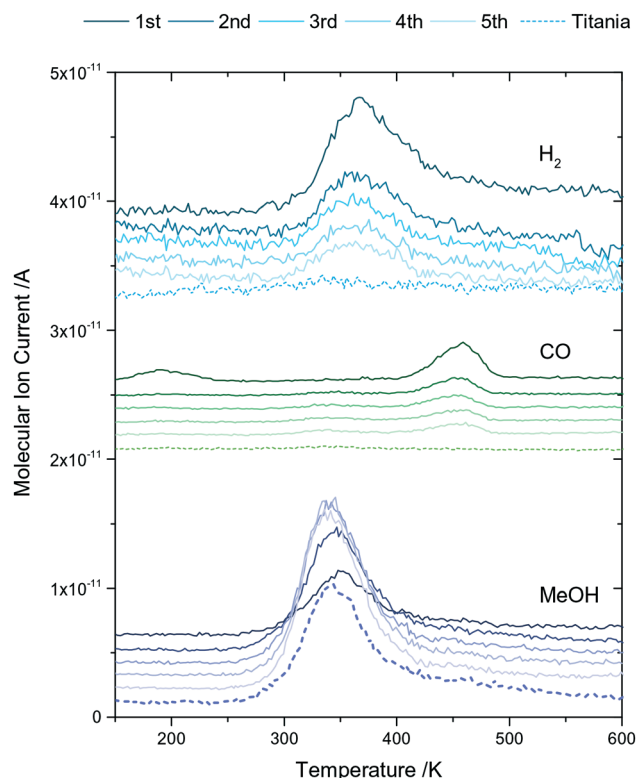


**Fig. 1** Five consecutive TPD experiments with 1 L of methanol from 150 to 600 K on Ni<sub>*x*</sub>/r-TiO<sub>2</sub>(110) (solid lines) and an identical TPD experiment on bare r-TiO<sub>2</sub>(110) (dashed lines) with traces for hydrogen (*m/z* 2), carbon monoxide (*m/z* 28) and methanol (*m/z* 31) are shown. The brightness of the graphs increases in the consecutive running order of the TPD experiments (see top legend). The signals are corrected for ionization cross section, QMS transmission, and cracking contributions by other molecules. After dosing 1 L of methanol onto the surface at 150 K, the catalyst was heated to 600 K at a rate of 1–2 K s<sup>-1</sup>. After cooling to 150 K, the next TPD experiment was started immediately. Note that the traces are offset for sake of clarity.

temperature CO peak ( $\sim 470$  K). These two TPD profiles in Fig. 1 are in accordance with H<sub>2</sub> and CO TPD spectra published by Raupp and Dumesic using Ni evaporated on titania,<sup>49</sup> and with CO TPD studies by the Anderson group on Ni<sub>*x*</sub>/TiO<sub>2</sub> using size-selected clusters.<sup>24</sup> Contrariwise to the methanol feature, their intensities are initially highest but decrease consecutively in the first three experiments. The desorption temperatures of H<sub>2</sub> and CO observed in Fig. 1 are close to literature desorption temperatures of these molecules from Ni nanoparticles.<sup>49,50</sup>

### Photochemistry on Ni-decorated titania

In order to obtain insights into the photochemical properties of Ni<sub>*x*</sub>/TiO<sub>2</sub>(110), methanol photoconversion was investigated at 250 K. Isothermal PSR experiments are shown in the top of Fig. 2.

Upon illumination of the photocatalyst with 1 L of methanol adsorbed, the bare semiconductor surface (dark lines) shows no desorbing species other than formaldehyde



(orange). In contrast, the formaldehyde trace and the  $H_2$  signal (blue) exhibit a sudden increase upon the illumination of the cluster-loaded semiconductor. Since both quantitatively corrected formaldehyde traces are virtually congruent, the molecule is detected in equal amounts in both experiments. Methyl formate, which is a common product upon irradiation at low-temperature, is not at all detected.<sup>15</sup>

Since more strongly bound adsorbates will not desorb at the chosen photoreaction temperature of 250 K, a PI-TPD was conducted subsequently. The PI-TPD spectrum (bottom Fig. 2) shows methanol desorption from both, the bare and the cluster-loaded surface, in similarly high amounts, whereas again no methyl formate and only negligible

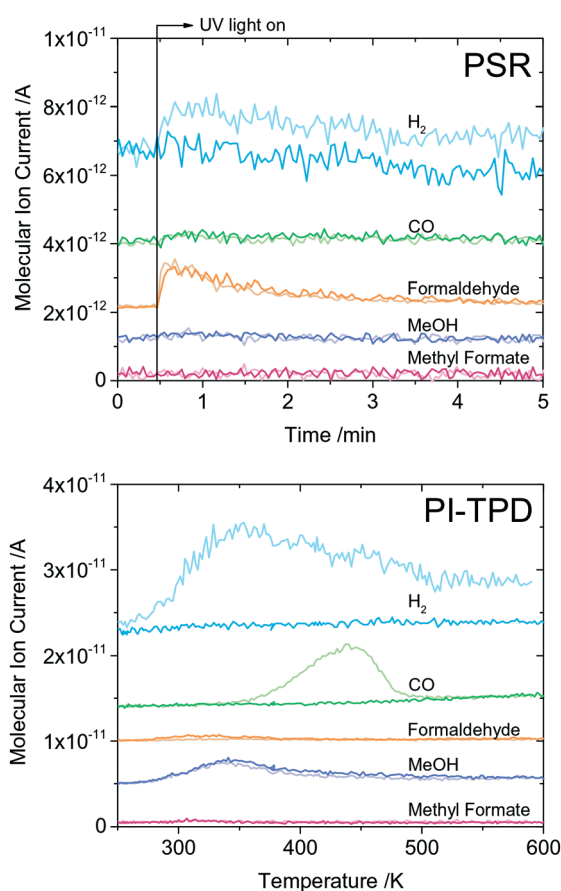


**Fig. 2** Top: Isothermal photon stimulated reaction (PSR) experiments with 1 L of methanol at 250 K on  $Ni_x/r-TiO_2(110)$  (bright graphs) and the bare  $r-TiO_2(110)$  (dark graphs), with traces for hydrogen ( $m/z$  2), water ( $m/z$  18), carbon monoxide ( $m/z$  28), formaldehyde ( $m/z$  30), methanol ( $m/z$  31) and methyl formate ( $m/z$  60) shown. The signals are corrected for ionization cross section, QMS transmission, and cracking contributions by other molecules. Note that the traces are offset for sake of clarity. After dosing 1 L methanol onto the surface at 150 K, the catalyst was heated to 250 K and illuminated for 10 min. Bottom: PI-TPD spectrum taken subsequently to the PSR experiment at a heating rate of at a rate of  $1-2 \text{ K s}^{-1}$ . Contrary to the bare titania, the Ni loaded semiconductor facilitates both, thermal and photochemical hydrogen evolution by methanol (photo) conversion.

amounts of formaldehyde are detected. In contrast to the bare surface,  $Ni_x/r-TiO_2(110)$  PI-TPDs show broad features of molecular hydrogen starting at 300 K as well as carbon monoxide desorption starting at 350 K.

### Photocatalysis on Ni-decorated titania

The photochemical investigations of  $Ni_x/r-TiO_2(110)$  were extended to photocatalytic methanol oxidation under steady-state conditions. The photocatalytic conversion was conducted in a steady methanol background of  $5 \times 10^{-7}$  mbar near room temperature (300 K). The results are shown in Fig. 3.

Upon illumination (yellow background), an increase in both, the  $H_2$  and formaldehyde trace, is observed, which drops back to its former level as the light is turned off (white background). Superimposing the quantitatively corrected traces (see inset in Fig. 3) shows that the molecules are generated in stoichiometrically equal amounts under irradiation. The intensities of formaldehyde and hydrogen traces taper off in parallel during repeated illumination intervals over time, which can be regarded as a deactivation process of the photocatalyst. This deactivation occurs in a non-linear fashion, *i.e.* the intensities of the traces under illumination approach their respective baseline in the dark asymptotically.

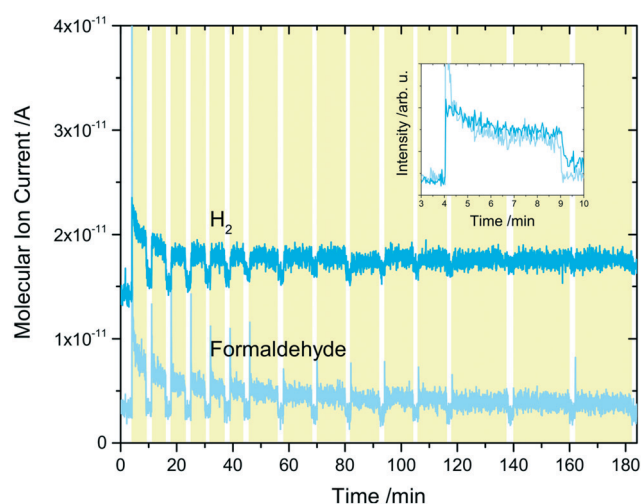


**Fig. 3** Products of methanol photoreforming on  $Ni_x/r-TiO_2(110)$  at  $5 \times 10^{-7}$  mbar alcohol background pressure at 300 K. The traces for hydrogen ( $m/z$  2) and formaldehyde ( $m/z$  30) are shown. The signals are corrected for ionization cross section, QMS transmission, and cracking contributions by other molecules. The yellow background highlights the illumination periods (242 nm), where the initial bursts stem from an enhanced methanol concentration on the surface due to its accumulation in the dark. Note that the traces are offset for sake of clarity. The inset shows both graphs superimposed within the first ten minutes. The equal area under the curves shows a stoichiometric formation of  $H_2$  and formaldehyde as the respective traces have been corrected for their sensitivities. With increasing duration of the experiment, deactivation of the catalyst is evident as hydrogen and formaldehyde formation under illumination declines.

While the photocatalytic activity thus approaches zero, photocatalytic hydrogen and formaldehyde evolution is again feasible after heat treatment of the catalyst as depicted in Fig. 4. Annealing to 800 K recovers its photocatalytic activity to a considerable extent, even though the initial activity after cluster deposition is not reached. As in the case of the fresh catalyst, the traces of hydrogen and formaldehyde are congruent when superimposed as shown by the inset in Fig. 4.

To elucidate a possible change in the elemental surface composition in the course of the experiment, we employed Auger electron spectroscopy (AES) as a very surface-sensitive technique (Fig. 5). A loading of 3% ML of Ni clusters ensured pronounced and visible signals of the metal. For clarity, the insets show excerpts of the C KLL (left) and the Ni LMM peaks (right).

In the Auger spectrum shortly after the deposition of Ni clusters at 150 K (black), only the expected signals for Ti, O, and Ni are detected.<sup>47</sup> In the red spectrum recorded 16 h after catalysis a carbon peak is additionally observed while the intensities of the Ni transitions have decreased. As the carbon peak might originate from residual surface methoxy or carbonyl species, the crystal was treated with two cycles of annealing to 800 K and a spectrum was recorded while cooling (blue and green). While the Ni

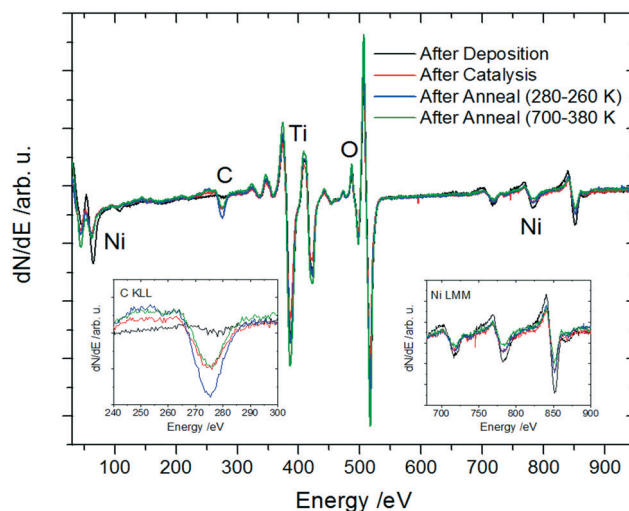


Fig. 5 Auger spectra of  $\text{Ni}_x/\text{r-TiO}_2(110)$  (3% ML cluster coverage) taken consecutively: directly after deposition (black), after two catalytic experiments and storage *in vacuo* for 16 h (red), annealed to 800 K and cooled to 270 K (blue); while cooling down after annealing to 800 K and recording from 700 K on (green). The insets show excerpts of the spectrum with magnified C KLL peak (left) and Ni LMM peaks (right), respectively. The peaks were assigned using ref. 47.

signals barely lose in intensity, the carbon signal persists in the spectra.

While prolonged illumination in the presence of methanol leads to deactivation, the impact of methanol exposure on the catalytic activity was investigated in the absence of illumination. Fig. 6 shows a direct comparison of the hydrogen and formaldehyde traces between two catalytic experiments, which were started either directly after the cluster deposition (blue graphs) or after pre-exposing the catalyst to a steady methanol background for one hour. The congruency of the  $\text{H}_2$  and formaldehyde traces from the two experiments show their formation in quantitatively equal amounts.

## Discussion

### Thermal chemistry on Ni-decorated titania

The TPDs of 1 L of methanol (Fig. 1) represent a direct comparison of the purely thermal chemistry of bare and Ni-decorated  $\text{TiO}_2(110)$ . During five consecutive methanol TPDs on  $\text{Ni}_x/\text{TiO}_2(110)$ , the declining intensity of the molecular alcohol trace and rise of the  $\text{H}_2/\text{CO}$  traces suggest that the alcohol decomposes into the latter. The fact that both decomposition products are absent in TPD spectra on bare titania indicates that the metal clusters on  $\text{Ni}_x/\text{TiO}_2(110)$  are their formation sites. On the other hand, both molecules are more strongly bound to the surface than methanol, which supplies evidence for Ni clusters being also their desorption sites. On bare  $\text{r-TiO}_2(110)$ , surface CO already desorbs below 200 K,<sup>51</sup> while hydrogen does not desorb molecularly but as water from surface hydroxyl

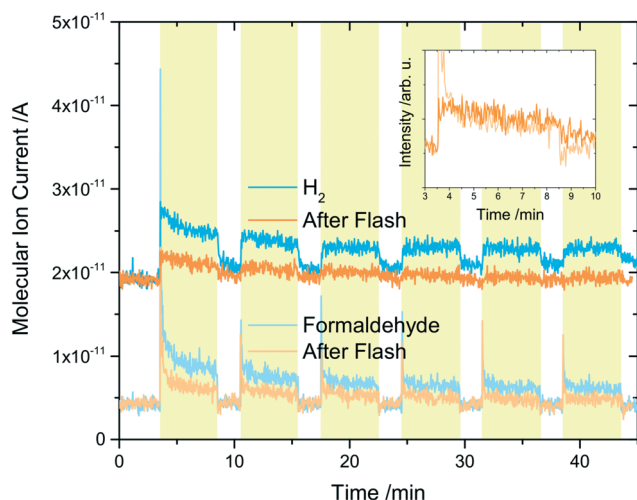
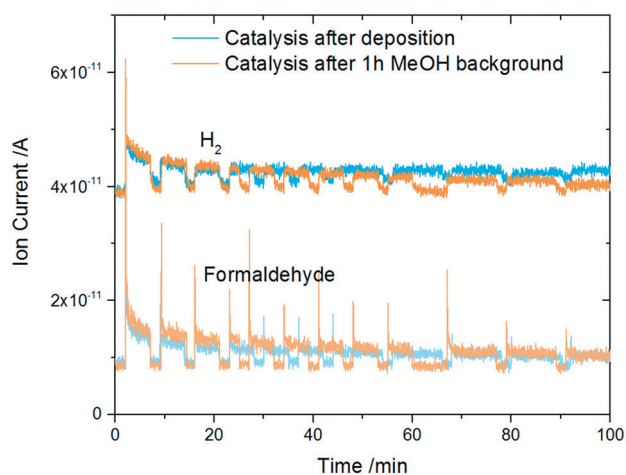


Fig. 4 Products of methanol photoreforming on  $\text{Ni}_x/\text{r-TiO}_2(110)$  at  $5 \times 10^{-7}$  mbar alcohol background pressure at 300 K. The signals are corrected for ionization cross section, QMS transmission, and cracking contributions by other molecules. The  $\text{H}_2$  and formaldehyde trace were recorded during the catalytic experiment after cluster deposition (blue). Subsequently, the catalyst was annealed to 800 K, cooled to room temperature and another catalytic experiment was conducted (orange). The yellow background highlights the illumination periods (242 nm). The initial bursts stem from an enhanced methanol concentration on the surface due to its accumulation in the dark. Note that the traces are offset for sake of clarity. With increasing duration of the experiment, deactivation of the catalyst is evident in all curves as hydrogen and formaldehyde formation under illumination declines. Flashing the catalyst to high temperatures partially regenerates the catalytic activity.



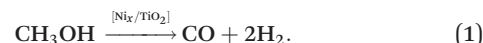


**Fig. 6** Products of methanol photoreforming on  $\text{Ni}_x/\text{r-TiO}_2(110)$  at  $5 \times 10^{-7}$  mbar alcohol background pressure at room temperature, corrected traces for hydrogen ( $m/z$  2, dark colors) and formaldehyde ( $m/z$  30, bright colors) shown. The  $\text{H}_2$  and formaldehyde trace were recorded during the catalytic experiment after cluster deposition (blue) and after cluster deposition followed by a constant MeOH background exposure of  $5 \times 10^{-7}$  mbar before illumination (orange). The initial bursts stem from an initially enhanced methanol concentration on the surface due to its accumulation in the dark. Note that the traces are offset for sake of clarity. With increasing duration of the experiment, deactivation of the catalyst is evident in all curves as hydrogen and formaldehyde formation under illumination declines. As the superimposed traces reach equal heights upon illumination (elevated traces), product formation remains quantitatively unaffected by MeOH pre-exposure.

recombination above 300 K.<sup>18,52</sup> Ni clusters hence induce additional surface reaction pathways to the thermal reactivity of titania to facilitate thermal  $\text{H}_2$  formation. Since the desorption temperatures of  $\text{H}_2$  and CO observed in Fig. 1 are close to literature desorption temperatures of these molecules from Ni nanoparticles,<sup>49,50</sup> decomposition already takes place below the desorption temperature. An impact on the clusters by the heat treatment is evident, too, because the peak intensities change with repeated ramping to 600 K.

Thermal  $\text{H}_2$  evolution and strongly bound CO species during methanol TPD have also been observed on  $\text{Au/TiO}_2$ ,<sup>53</sup>  $\text{Pt/TiO}_2(110)$ <sup>17,31</sup> and other noble metal loaded oxides<sup>54,55</sup> under ideal and applied conditions. The results from Fig. 1 confirm that Ni as co-catalyst can indeed react in the same way. As the methanol peak shows reduced intensity on  $\text{Ni}_x/\text{TiO}_2$  in the first experiments, it is conceivable that the signals of hydrogen and carbon monoxide emerge at the expense of the methanol signal's intensity, *i.e.*,  $\text{H}_2$  and CO are generated thermally by partial dehydrogenation of adsorbed methanol in the presence of Ni. These results agree with findings on transition metal surfaces, which can thermally decompose methanol to CO and molecular hydrogen.<sup>56–60</sup> TPD experiments on Ni single crystals have shown that methanol and intermediate methoxy species are decomposed to  $\text{H}_2$  and CO.<sup>58,61</sup> In the same sense, the results herein show that methanol on Ni cluster-loaded titania

decomposes to  $\text{H}_2$  and CO at the metal clusters (pursuant to eqn (1)), which also serve as the desorption sites of these thermal products.



The change in the peak intensities caused by the heat treatment (Fig. 1), suggests a significant alteration of the Ni clusters in the course of the experiments. A possible scenario could be the diffusion of Ni clusters into the titania bulk. However, this process usually occurs at temperatures above 600 K,<sup>62,63</sup> which is the upper threshold of the TPD experiments in this work and is hence discarded as being relevant herein. While other studies in the literature also report a significantly strong metal-support interaction (SMSI) in Ni/TiO<sub>2</sub> systems at high temperatures,<sup>64</sup> Tanner *et al.* observed the growth of Ni nanoislands on TiO<sub>2</sub>(110) *via* the Volmer–Weber mode between 295 and 400 K.<sup>65</sup> Based on their results, Anderson and coworkers estimated the size of these islands to 30 atoms, which appears to be a stable number based on their own TPD results in a temperature range from 150 to 600 K.<sup>24</sup> The size distribution of the Ni clusters in this work ranges from 12 to 27 atoms, and thus a growth of these clusters to slightly larger sizes seems likely. Since the last TPD spectra differ less strongly in intensity than the first ones, a majority of the clusters has presumably achieved a stable size after few TPD cycles, in excellent agreement with the results from the literature. This suggests a modification of the Ni clusters by the heat treatment until a thermodynamically more stable conformation is reached, which is accompanied by a lower amount of methanol being decomposed to  $\text{H}_2$  and CO.

### Photochemistry on Ni-decorated titania

Generally, the photoactivity of the titania photocatalyst appears unaffected by the presence of Ni clusters, because the formaldehyde peaks in the PSR experiments (orange, top of Fig. 2) and the methanol peaks in the PI-TPD (bottom of Fig. 2) are of equal intensity and shape. The latter stems from remaining alcohol species that have not been photo-converted. Formaldehyde is formed in equal amounts in the PSR spectra, which can be seen from the quantitatively corrected QMS traces. As expected from literature studies, TiO<sub>2</sub>(110) does not show  $\text{H}_2$  evolution under UV light,<sup>21</sup> whereas the Ni cluster-loaded surface leads to a rise of the  $\text{H}_2$  trace upon illumination (top of Fig. 2). This result clearly shows that Ni clusters facilitate photochemical hydrogen evolution on TiO<sub>2</sub>(110) in methanol photo-oxidation. Although this reactivity had been observed with Ni nanoparticles on P25 in aqueous systems,<sup>32,40</sup> in UHV studies using rutile it was hitherto only achieved with Au or Pt metal clusters.<sup>8,17,21,66</sup> As methyl formate is not detected due to the short residence time of formaldehyde on the surface at 250 K,<sup>15,31</sup> the

overall photoreaction exclusively occurs *via* the following equation:



Since the same reaction products are formed in equal amounts in both experiments (depicted in Fig. 2), it can be concluded that the Ni clusters do not affect the photoreactivity and -activity of the reduced titania surface in the photo-oxidation of the alcohol.

The photocatalyst  $\text{Ni}_x/\text{TiO}_2(110)$  shows parallels to  $\text{Pt}_x/\text{TiO}_2(110)$  in UHV as well as to  $\text{Ni}/\text{TiO}_2$  in wet-chemical systems. Despite of the photochemical similarities of metal cluster-loaded titania in wet-chemical and UHV conditions, it must be noted that the presence of a liquid environment and, in particular, molecules other than the alcohol (*e.g.* water or oxygen) may facilitate additional reaction pathways (*e.g.* an indirect hole transfer through the solvent).<sup>9,22,67</sup> Since the photoreaction depicted in eqn (2) occurs analogously on  $\text{Pt}_x/\text{TiO}_2$ , it is likely that the surface mechanism is identical, although the rates of individual reaction steps may differ.<sup>21</sup>

Similar as in the TPD experiments in the absence of illumination (Fig. 1), the TPDs after irradiation of bare and cluster-loaded titania also differ from each other (bottom of Fig. 2). In the PI-TPDs, only the Ni cluster-loaded surface shows  $\text{H}_2$  and CO desorption, in agreement with the results from the TPD series (Fig. 1). Obviously, only a fraction of  $\text{H}_2$  desorbs upon illumination at 250 K on  $\text{Ni}_x/\text{TiO}_2(110)$ , as significant amounts still desorb during the PI-TPD at higher temperature. This indicates that the chosen temperature hampers hydrogen recombination and desorption from Ni sites.

#### Photocatalysis on Ni-decorated titania and auger analysis

$\text{Ni}_x/\text{TiO}_2(110)$  facilitates steady-state hydrogen and formaldehyde formation by photocatalytic methanol conversion at room temperature as shown in Fig. 3. As no further byproducts are detected, methanol photo-oxidation takes place as described in eqn (2), in a manner as it is known from Pt-loaded  $\text{TiO}_2(110)$ .<sup>21</sup> Contrary to the latter (see Fig. S2†), the intensities of both, the formaldehyde and hydrogen trace under illumination, taper off over time. The photocatalytic activity of Ni-loaded titania hence declines during methanol photoreforming. Bare  $\text{TiO}_2(110)$  also deactivates during alcohol photoreforming, but the deactivation pattern compared to  $\text{Ni}_x/\text{r-TiO}_2(110)$  is notably different:  $\text{r-TiO}_2(110)$  does not show any photon-driven hydrogen evolution (see Fig. 2 and S3†) and deactivates more rapidly due to the accumulation of hydrogen on the surface.<sup>18</sup>  $\text{O}_2$  photon-stimulated desorption (PSD) measurements on the bare and nickel-loaded titania surface (see Fig. S4†) indicate that nickel clusters do not block photoactive sites to a significant extent (in parallel to Pt clusters).<sup>21</sup> Thus, the activity of the titania photocatalyst itself is not severely affected by cluster decoration. The number of photo-active sites is hence virtually equal to the bare  $\text{r-TiO}_2(110)$  surface, and deactivation most likely occurs by a decreasing hydrogen recombination activity at the Ni clusters. This might be caused by a chemical change of the metal clusters, which are deposited in the metallic state due to the soft-landing conditions.<sup>24</sup> Apart from deactivation, the reactivity patterns (photochemical as well as thermal) of  $\text{Ni}_x/\text{TiO}_2(110)$  are virtually identical to that of  $\text{Pt}_x/\text{TiO}_2(110)$ .<sup>31</sup>

Possible mechanisms for a chemical change of the clusters are sintering,<sup>24,65</sup> encapsulation underneath the surface,<sup>62–64</sup> the formation of oxide species,<sup>24</sup> carbonaceous deposits blocking the sites for hydrogen recombination or carbide formation.<sup>68–70</sup> In a first instance, encapsulation and sintering can be ruled out as origin of deactivation, as these processes would be significantly enhanced by higher temperatures. However, the catalytic activity can in contrast be restored to a certain degree by annealing (Fig. 5). The decrease in intensity of the Ni peaks in the Auger spectrum from before (black) to after photocatalysis (red) indeed points toward a diminished cluster concentration on the surface. However, the persistence of the Ni signal upon further heat treatment (blue and green) indicates that a certain stable conformation is eventually reached. This is in accordance with the observed thermal chemistry (Fig. 1) and literature results.<sup>24</sup> The fact that the metal clusters are still detectable although the photocatalytic activity for  $\text{H}_2$  evolution has vanished, indicates that the Ni surface concentration and  $\text{H}_2$  formation are not directly correlated. Therefore, a chemical change of the Ni surface species seems the most probable reason for the decline of the product formation rate.

An oxidation of the metallic Ni clusters to an oxide species seems a plausible scenario for deactivation but is contradicted by a more detailed analysis of all four Auger measurements and thermodynamic considerations. Generally, Ni oxidation by reduction of  $\text{TiO}_2$  is unfavorable since the heat of formation of  $\text{NiO}$  ( $-250 \text{ kJ mol}^{-1}$ ) is energetically higher than the change in the standard free energy to form  $\text{Ti}^{3+}$  or  $\text{Ti}^{2+}$  ( $-364 \text{ kJ mol}^{-1}$  and  $-483 \text{ kJ mol}^{-1}$ , respectively).<sup>71</sup> Superimposing the spectra from Fig. 5 with reference spectra of  $\text{Ni}^0$  and  $\text{NiO}$  (Fig. S4†) clearly demonstrates the dominance of metallic species in this series of experiments. This is in excellent agreement with literature results showing that metallic Ni is detected after various oxygen treatments at high temperatures of the  $\text{Ni}_3\text{Al}(111)$  surface in UHV by means of Auger spectroscopy.<sup>46</sup> Furthermore, a recent *operando* XPS study on a bimetallic  $\text{NiCu-TiO}_2$  photocatalyst for  $\text{H}_2$  evolution unequivocally shows the metallic state of both co-catalyst metals.<sup>72</sup> While Prahov *et al.* concluded that  $\text{Ni}^0$  atoms are required to evolve  $\text{H}_2$  in a wet chemical environment, based on comparisons between the freshly reduced catalyst and after its exposure to air,<sup>40</sup> the observed decline in catalytic activity in the present work is not attributed to the oxide formation of the Ni co-catalyst.

On the other hand, the persistence of the carbon signal in the spectra after photocatalysis (orange, bright and dark green) points toward a strongly bound carbon surface compound. Since all common organic species on titania desorb upon heating to 800 K, the formation of strongly

bound carbonaceous species on the Ni clusters seems plausible based on general research on Ni catalysts.<sup>68–70</sup> In contrast, carbon formation is not observed on Pt<sub>x</sub>/TiO<sub>2</sub>(110) after a similarly long period of photocatalytic methanol conversion (see Fig. S6†). As carbon can be removed by heat treatment as CO (Fig. 1), the residues on Ni clusters can be removed thermally, but only to a certain extent. At the same time, the catalytic activity is partially restored. The fact that Ni<sub>x</sub>/TiO<sub>2</sub>(110) is not fully regenerated can thus be ascribed to irremovable carbonaceous surface residues as indicated by the still detectable C signal after repeated annealing (Fig. 5 dark green).

This scenario is supported by kinetic considerations on the declining photoactivity of Ni<sub>x</sub>/TiO<sub>2</sub>(110). TiO<sub>2</sub> is known to show formaldehyde formation but no H<sub>2</sub> evolution in methanol photo-reforming due to the absence of suitable recombination sites. If the rate of hydrogen recombination and desorption is lower than the desorption rate of formaldehyde, hydrogen accumulation on the surface will result. This, in turn, changes the observed steady-state behavior: surface hydrogen and formaldehyde species will be converted back to methanol and methoxy rather than being desorbed from the surface if the hydrogen concentration on the surface becomes sufficiently high.<sup>19</sup> This will occur with an increasing probability as the H<sub>2</sub> recombination activity of Ni decreases, which is likely induced by the formation of a carbonaceous Ni species. The formation of C-species is clearly documented by the Auger spectrum and most likely linked to the declining catalytic activity. Furthermore, Ni clusters are the most plausible site for the formation of carbon species as the observed carbon deposits correlate with the clusters' presence at the TiO<sub>2</sub> crystal. Similarly, the clusters also enable H<sub>2</sub> recombination in the photoreaction, supplying evidence for the two mechanisms being interconnected. Thus, prolonged illumination does not only result in an increase in carbon residues on Ni, but at the same time impedes H<sub>2</sub> formation and deteriorates the photocatalytic activity.

Notably, the deactivation of the photo-catalyst indeed seems to be a purely photon-driven process. In additional experiments, Ni<sub>x</sub>/TiO<sub>2</sub>(110) was exposed to a constant methanol background without illumination for one hour. The photocatalytic formation of H<sub>2</sub> and formaldehyde was found to be unaffected by prolonged methanol pre-exposure (see Fig. 6). Consequently, the presence of molecular methanol in the absence of UV irradiation does thus not lead to the deactivation of the Ni co-catalyst. Hence, the deactivation represents a phenomenon known as photo-corrosion and appears to originate from intermediate species or products rather than from molecularly adsorbed methanol only.

## Conclusion

In summary, the work shows that nickel clusters can indeed facilitate a thermal evolution of H<sub>2</sub> at room temperature and thus enable the photocatalytic hydrogen evolution reaction

on TiO<sub>2</sub>(110), similarly as observed for Pt clusters. However, nickel-loaded titania exhibits deactivation over time for prolonged illumination in a methanol atmosphere, which is different to the alcohol photoreforming with platinum clusters as co-catalysts. The decline in photoactivity is attributed to photocorrosion, as the activity of the photocatalyst is maintained upon exposure with the alcohol in the absence of light. A closer look onto the changes of the photocatalysts after reaction by Auger electron spectroscopy reveals that carbonaceous species are being formed. In contrast, an oxidation of the nickel clusters is not evident and the clusters largely remain in their metallic oxidation state. While the carbonaceous deposits can partially be desorbed as CO at elevated temperature, only a partial restoration of the photoactivity is possible. In general, nickel clusters may thus represent a more benign alternative in comparison to noble metal particles as hydrogen evolution co-catalysts. However, additional reaction pathways leading to the deactivation of the photocatalyst must be considered, in particular in the presence of carbon-containing molecules.

## Conflicts of interest

There are no conflicts to declare.

## Acknowledgements

The authors thank the DFG for financial support through the Germany's Excellence Strategy – EXC 2089/1-390776260. C. C. acknowledges the support from the Luxembourg National Research Fund (FNR), project code 12531916 and that from the TUM International Graduate School of Science and Engineering (TUM-IGSSE). M. E. would like to thank C. C. A. for fruitful discussions.

## References

- I. Staffell, D. Scamman, A. Velazquez Abad, P. Balcombe, P. E. Dodds, P. Ekins, N. Shah and K. R. Ward, *Energy Environ. Sci.*, 2019, **12**, 463–491.
- M. Nose, T. Kawakami, H. Araki, N. Senba and S. Tanimura, *Tech. Rev. - Mitsubishi Heavy Ind.*, 2018, **55**, 1–7.
- T. Bexten, *et al.*, Optimal Operation of a Gas Turbine Cogeneration Unit With Energy Storage for Wind Power System Integration, *Turbo Expo: Power for Land, Sea, and Air*, American Society of Mechanical Engineers, 2018, vol. 51043.
- I. E. A., Technology Roadmap Hydrogen and Fuel Cells [www.iea.org/t&c/](http://www.iea.org/t&c/), 2015, (accessed on 26.03.2020).
- D. S. Thakur and A. Kundu, *J. Am. Oil Chem. Soc.*, 2016, **93**, 1575–1593.
- S. Pugh, R. McKenna, I. Halloum and D. R. Nielsen, *Metab. Eng. Commun.*, 2015, **2**, 39–45.
- A. Demirbaş, *Energy Sources*, 2005, **27**, 327–337.
- S. L. Kollmannsberger, C. A. Walenta, C. Courtois, M. Tschurl and U. Heiz, *ACS Catal.*, 2018, **8**, 11076–11084.
- M. A. Henderson, *Surf. Sci. Rep.*, 2011, **66**, 185–297.

- 10 R. T. Zehr and M. A. Henderson, *Surf. Sci.*, 2008, **602**, 1507–1516.
- 11 Z. Zhang, O. Bondarchuk, J. M. White, B. D. Kay and Z. Dohnálek, *J. Am. Chem. Soc.*, 2006, **128**, 4198–4199.
- 12 M. Shen and M. A. Henderson, *J. Phys. Chem. C*, 2012, **116**, 18788–18795.
- 13 M. A. Henderson, S. Otero-Tapia and M. E. Castro, *Faraday Discuss.*, 1999, **114**, 313–319.
- 14 M. A. Henderson and I. Lyubinetsky, *Chem. Rev.*, 2013, **113**, 4428–4455.
- 15 K. R. Phillips, S. C. Jensen, M. Baron, S.-C. Li and C. M. Friend, *J. Am. Chem. Soc.*, 2013, **135**, 574–577.
- 16 Q. Guo, C. Xu, W. Yang, Z. Ren, Z. Ma, D. Dai, T. K. Minton and X. Yang, *J. Am. Chem. Soc.*, 2013, **117**, 5293–5300.
- 17 Q. Hao, Z. Wang, T. Wang, Z. Ren, C. Zhou and X. Yang, *ACS Catal.*, 2019, **9**, 286–294.
- 18 C. A. Walenta, S. L. Kollmannsberger, J. Kiermaier, A. Winbauer, M. Tschurl and U. Heiz, *Phys. Chem. Chem. Phys.*, 2015, **17**, 22809–22814.
- 19 C. Courtois, M. Eder, S. L. Kollmannsberger, M. Tschurl, C. A. Walenta and U. Heiz, *ACS Catal.*, 2020, **10**, 7747–7752.
- 20 P. M. Clawin, C. M. Friend and K. Al-Shamery, *Chem. – Eur. J.*, 2014, **20**, 7665–7669.
- 21 C. A. Walenta, S. L. Kollmannsberger, C. Courtois, R. N. Pereira, M. Stutzmann, M. Tschurl and U. Heiz, *Phys. Chem. Chem. Phys.*, 2019, **21**, 1491–1496.
- 22 G. L. Chiarello, M. H. Aguirre and E. Selli, *J. Catal.*, 2010, **273**, 182–190.
- 23 U. Heiz, F. Vanolli, L. Trento and W.-D. Schneider, *Rev. Sci. Instrum.*, 1997, **68**, 1986–1994.
- 24 M. Aizawa, S. Lee and S. L. Anderson, *J. Chem. Phys.*, 2002, **117**, 5001–5011.
- 25 M. Shen and M. A. Henderson, *J. Phys. Chem. Lett.*, 2011, **2**, 2707–2710.
- 26 A. Yamakata, T.-a. Ishibashi and H. Onishi, *J. Phys. Chem. B*, 2002, **106**, 9122–9125.
- 27 C. Courtois, M. Eder, K. Schnabl, C. A. Walenta, M. Tschurl and U. Heiz, *Angew. Chem., Int. Ed.*, 2019, **58**, 14255–14259.
- 28 I. Chorkendorff, J. N. Russell and J. T. Yates, *Surf. Sci.*, 1987, **182**, 375–389.
- 29 B. E. Koel, D. E. Peebles and J. M. White, *Surf. Sci.*, 1983, **125**, 709–738.
- 30 J. N. Russell, I. Chorkendorff and J. T. Yates, *Surf. Sci.*, 1987, **183**, 316–330.
- 31 C. A. Walenta, C. Courtois, S. L. Kollmannsberger, M. Eder, M. Tschurl and U. Heiz, *ACS Catal.*, 2020, **10**, 4080–4091.
- 32 W.-T. Chen, A. Chan, D. Sun-Waterhouse, T. Moriga, H. Idriss and G. I. N. Waterhouse, *J. Catal.*, 2015, **326**, 43–53.
- 33 H. Bahruji, M. Bowker, P. R. Davies, J. Kennedy and D. J. Morgan, *Int. J. Hydrogen Energy*, 2015, **40**, 1465–1471.
- 34 E. P. Melián, M. N. Suárez, T. Jardiel, J. M. D. Rodríguez, A. C. Caballero, J. Araña, D. G. Calatayud and O. G. Díaz, *Appl. Catal., B*, 2014, **152–153**, 192–201.
- 35 J. B. Joo, R. Dillon, I. Lee, Y. Yin, C. J. Bardeen and F. Zaera, *Proc. Natl. Acad. Sci. U. S. A.*, 2014, **111**, 7942.
- 36 A. J. Simamora, F.-C. Chang, H. P. Wang, T. C. Yang, Y. L. Wei and W. K. Lin, *Int. J. Photoenergy*, 2013, **2013**, 419182.
- 37 P. D. Tran, L. Xi, S. K. Batabyal, L. H. Wong, J. Barber and J. S. Chye Loo, *Phys. Chem. Chem. Phys.*, 2012, **14**, 11596–11599.
- 38 J. Yu, Y. Hai and B. Cheng, *J. Phys. Chem. C*, 2011, **115**, 4953–4958.
- 39 W. Wang, S. Liu, L. Nie, B. Cheng and J. Yu, *Phys. Chem. Chem. Phys.*, 2013, **15**, 12033–12039.
- 40 L. T. Prahov, J. Disdier, J.-M. Herrmann and P. Pichat, *Int. J. Hydrogen Energy*, 1984, **9**, 397–403.
- 41 W.-T. Chen, A. Chan, D. Sun-Waterhouse, J. Llorca, H. Idriss and G. I. N. Waterhouse, *J. Catal.*, 2018, **367**, 27–42.
- 42 X. Wang, Q. Xu, M. Li, S. Shen, X. Wang, Y. Wang, Z. Feng, J. Shi, H. Han and C. Li, *Angew. Chem., Int. Ed.*, 2012, **51**, 13089–13092.
- 43 Y. Takashi, S. Yoshihisa and I. Hayao, *Chem. Lett.*, 2004, **33**, 726–727.
- 44 Q. Wang and K. Domen, *Chem. Rev.*, 2020, **120**, 919–985.
- 45 C. Ronning, H. Feldermann, R. Merk and H. Hofsäss, *Phys. Rev. B: Condens. Matter Mater. Phys.*, 1998, **58**, 2207–2215.
- 46 X. Ma, T. Kratky and S. Günther, *Nanoscale Adv.*, 2019, **1**, 4501–4512.
- 47 L. E. Davis, N. C. MacDonald, P. W. Palmberg, G. E. Riach and R. E. Weber, *Handbook of Auger Electron Spectroscopy*, Physical Electronics Industries, Inc., 2nd edn, 1976.
- 48 <https://webbook.nist.gov/>, 2020.
- 49 G. B. Raupp and J. A. Dumesic, *J. Catal.*, 1986, **97**, 85–99.
- 50 Y. Yao and D. W. Goodman, *J. Mol. Catal. A: Chem.*, 2014, **383–384**, 239–242.
- 51 A. Linsebigler, G. Lu and J. T. Yates, *J. Chem. Phys.*, 1995, **103**, 9438–9443.
- 52 Y. Du, N. G. Petrik, N. A. Deskins, Z. Wang, M. A. Henderson, G. A. Kimmel and I. Lyubinetsky, *Phys. Chem. Chem. Phys.*, 2012, **14**, 3066–3074.
- 53 S. A. Tenney, B. A. Cagg, M. S. Levine, W. He, K. Manandhar and D. A. Chen, *Surf. Sci.*, 2012, **606**, 1233–1243.
- 54 C. Lee, H.-K. Yoon, S.-H. Moon and K. J. Yoon, *Korean J. Chem. Eng.*, 1998, **15**, 590–595.
- 55 W. Jianxin and L. Laitao, *Catal. Lett.*, 2008, **126**, 325–332.
- 56 L. J. Richter and W. Ho, *J. Chem. Phys.*, 1985, **83**, 2569–2582.
- 57 F. L. Baudais, A. J. Borschke, J. D. Fedyk and M. J. Dignam, *Surf. Sci.*, 1980, **100**, 210–224.
- 58 S. R. Bare, J. A. Stroschio and W. Ho, *Surf. Sci.*, 1985, **150**, 399–418.
- 59 J. A. Gates and L. L. Kesmodel, *J. Catal.*, 1983, **83**, 437–445.
- 60 G. A. Attard, K. Chibane, H. D. Ebert and R. Parsons, *Surf. Sci.*, 1989, **224**, 311–326.
- 61 R. Neubauer, C. M. Whelan, R. Denecke and H.-P. Steinrück, *Surf. Sci.*, 2002, **507–510**, 832–837.
- 62 C. C. Kao, S. C. Tsai, M. K. Bahl, Y. W. Chung and W. J. Lo, *Surf. Sci.*, 1980, **95**, 1–14.
- 63 J. P. Espinós, A. Fernández and A. R. González-Elipe, *Surf. Sci.*, 1993, **295**, 402–410.
- 64 S. Takatani and Y.-W. Chung, *J. Catal.*, 1984, **90**, 75–83.
- 65 R. E. Tanner, I. Goldfarb, M. R. Castell and G. A. D. Briggs, *Surf. Sci.*, 2001, **486**, 167–184.
- 66 K. Katsiev, G. Harrison, Y. Al-Salik, G. Thornton and H. Idriss, *ACS Catal.*, 2019, **9**, 8294–8305.



- 67 G. L. Chiarello, D. Ferri and E. Selli, *J. Catal.*, 2011, **280**, 168–177.
- 68 I. Czekaj, F. Loviat, F. Raimondi, J. Wambach, S. Biollaz and A. Wokaun, *Appl. Catal., A*, 2007, **329**, 68–78.
- 69 P. K. Debokx, A. J. H. M. Kock, E. Boellaard, W. Klop and J. W. Geus, *J. Catal.*, 1985, **96**, 454–467.
- 70 M. Ichihashi, T. Hanmura, R. T. Yadav and T. Kondow, *J. Phys. Chem. A*, 2000, **104**, 11885–11890.
- 71 C. T. Campbell, *Surf. Sci. Rep.*, 1997, **27**, 7–9.
- 72 D. Spanu, A. Minguzzi, S. Recchia, F. Shahvardanfard, O. Tomanec, R. Zboril, P. Schmuki, P. Ghigna and M. Altomare, *ACS Catal.*, 2020, **10**, 8293–8302.

## Supporting Information for Nickel Clusters on TiO<sub>2</sub>(110): Thermal Chemistry and Photocatalytic Hydrogen Evolution of Methanol

Moritz Eder<sup>‡,a</sup>, Carla Courtois<sup>‡,a</sup>, Tim Kratky<sup>b</sup>, Sebastian Günther<sup>b</sup>, Martin Tschurl<sup>a</sup>, and Ueli Heiz<sup>a</sup>.

<sup>a</sup> Chair of Physical Chemistry & Catalysis Research Center, Technical University of Munich, Lichtenbergstr. 4, 85748 Garching, Germany

<sup>b</sup> Department of Chemistry & Catalysis Research Center, Technical University of Munich, Lichtenbergstr. 4, 85748 Garching, Germany

‡ The authors contributed equally.

\*Corresponding Author: [ulrich.heiz@mytum.de](mailto:ulrich.heiz@mytum.de)

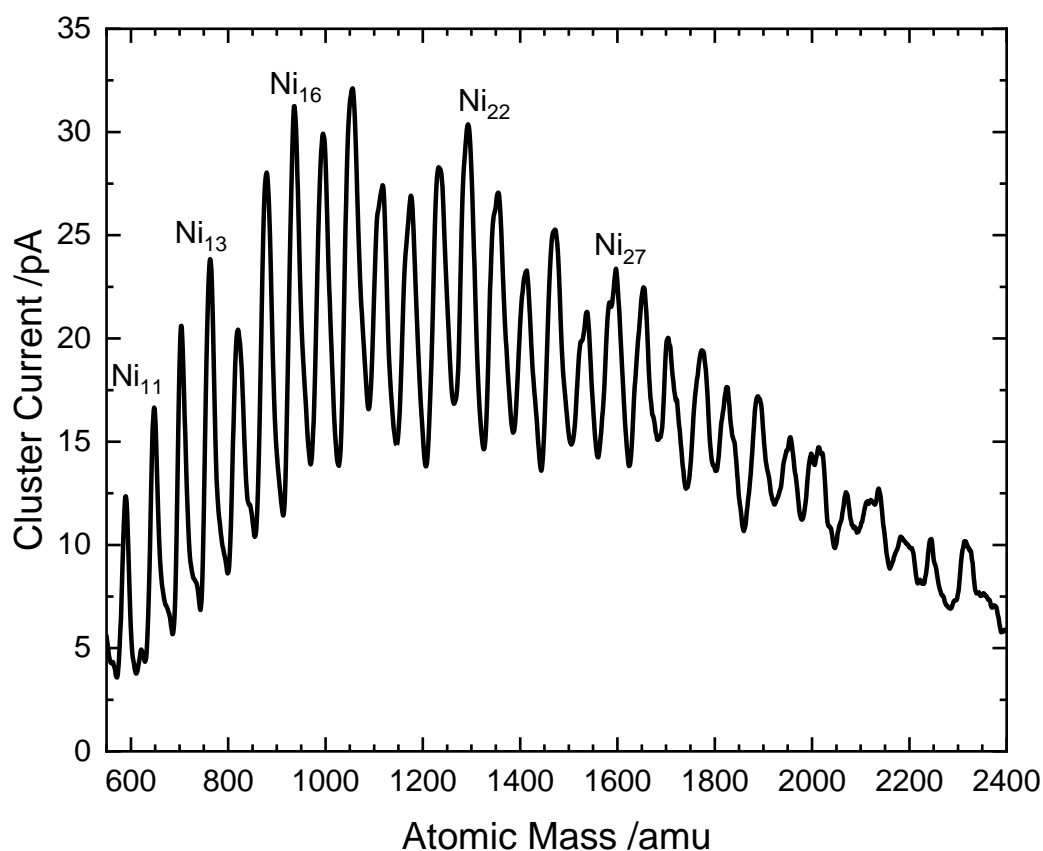


**Figure S1.** Mass spectrum of the cluster size distribution of Ni clusters from the laser vaporization source. The spectrum is taken after the quadrupole mass filter and shows a size-distribution of Ni<sub>10</sub> up to Ni<sub>30</sub>. When depositing in the ion guide mode, all masses lower than Ni<sub>8</sub> are discarded.

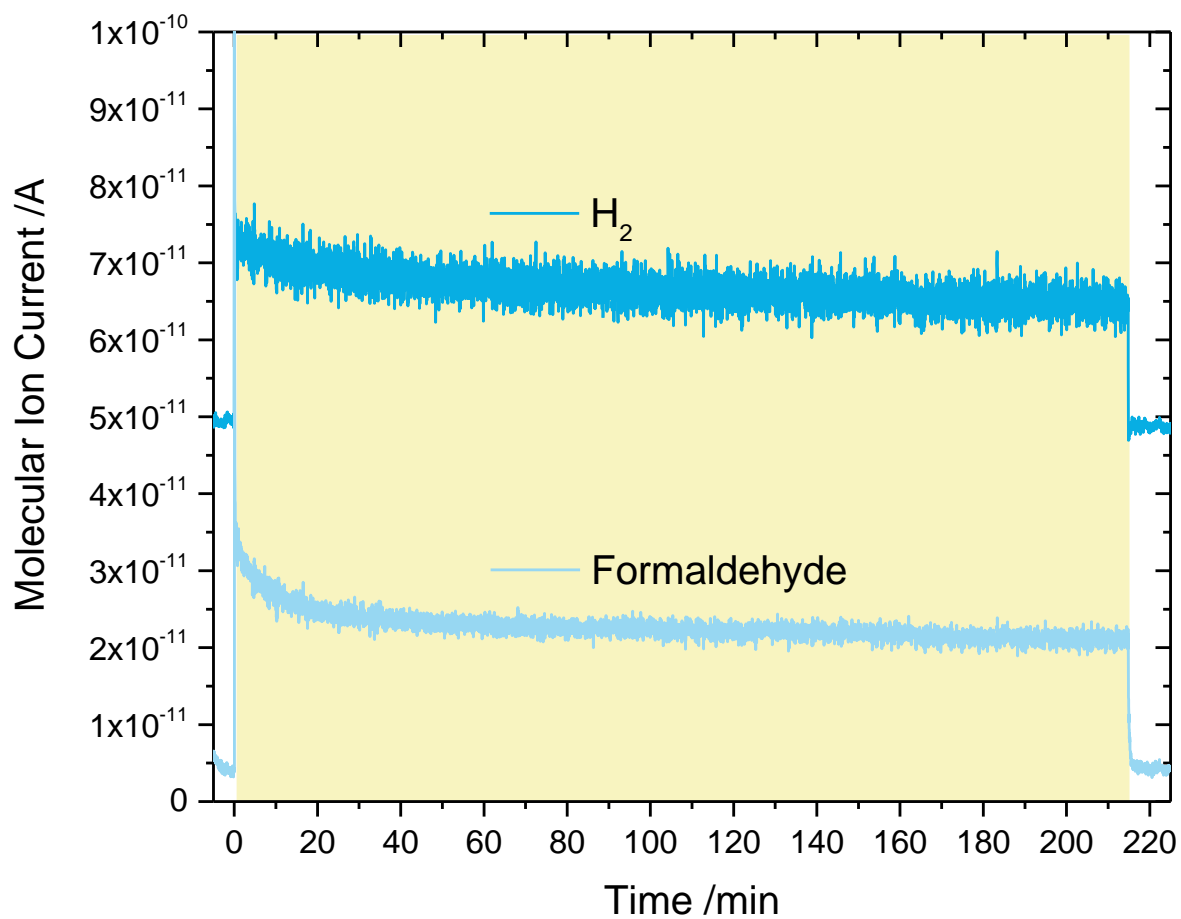


**Figure S2.** Products of methanol photoreforming on Pt<sub>x</sub>/r-TiO<sub>2</sub>(110) at  $7 \times 10^{-8}$  mbar alcohol background pressure at 267 K, corrected traces for hydrogen ( $m/z$  2), and formaldehyde ( $m/z$  30) shown. The colored background highlights the illumination period, where the initial bursts stem from an enhanced methanol concentration on the surface due to its accumulation in the dark. Note that the traces are offset for clarity. With increasing duration of the experiment, no deactivation of the catalyst is evident.

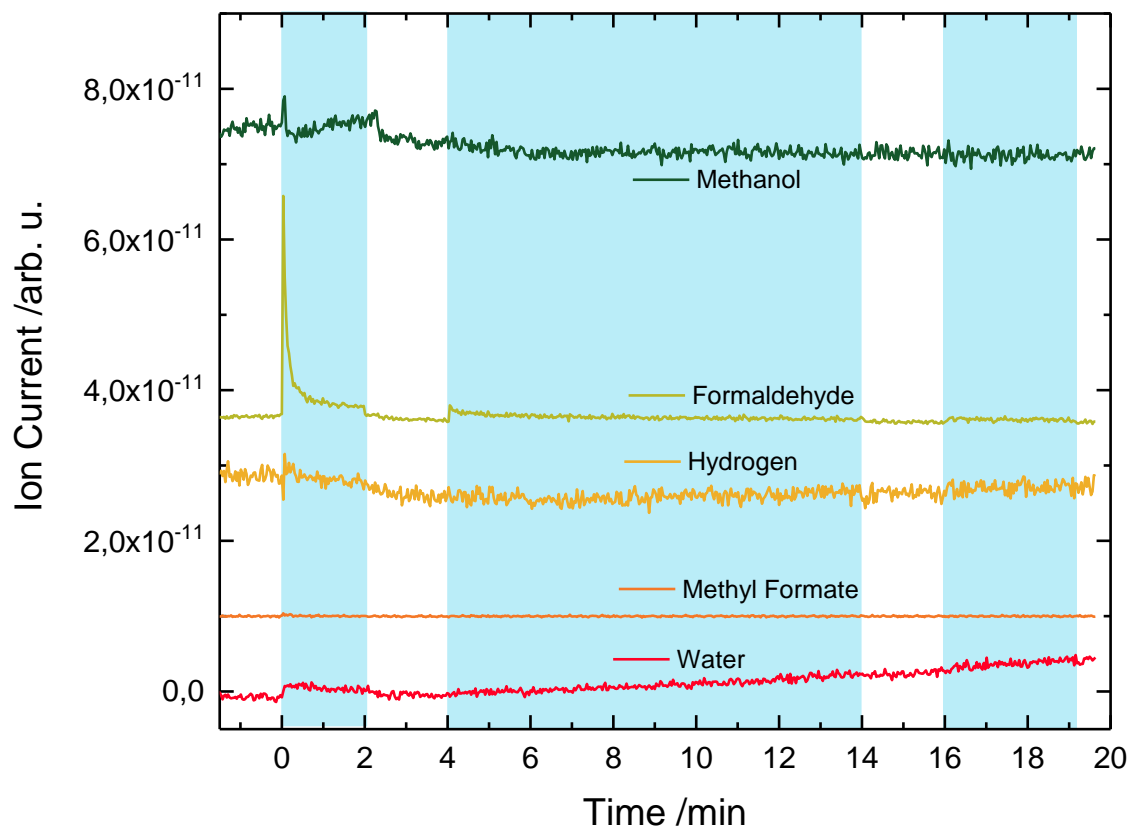


**Figure S3.** Products of methanol photoreforming on r-TiO<sub>2</sub>(110) at  $5 \times 10^{-7}$  mbar alcohol background pressure at room temperature (RT), raw traces for hydrogen ( $m/z$  2), water ( $m/z$  18) formaldehyde ( $m/z$  30), methanol ( $m/z$  31), and methyl formate ( $m/z$  60) shown. The blue background highlights the illumination periods, where the initial bursts stem from an enhanced methanol concentration on the surface due to its accumulation in the dark. Note that the traces are offset for clarity. With increasing duration of the experiment, deactivation of the catalyst is evident as formaldehyde formation under illumination declines.



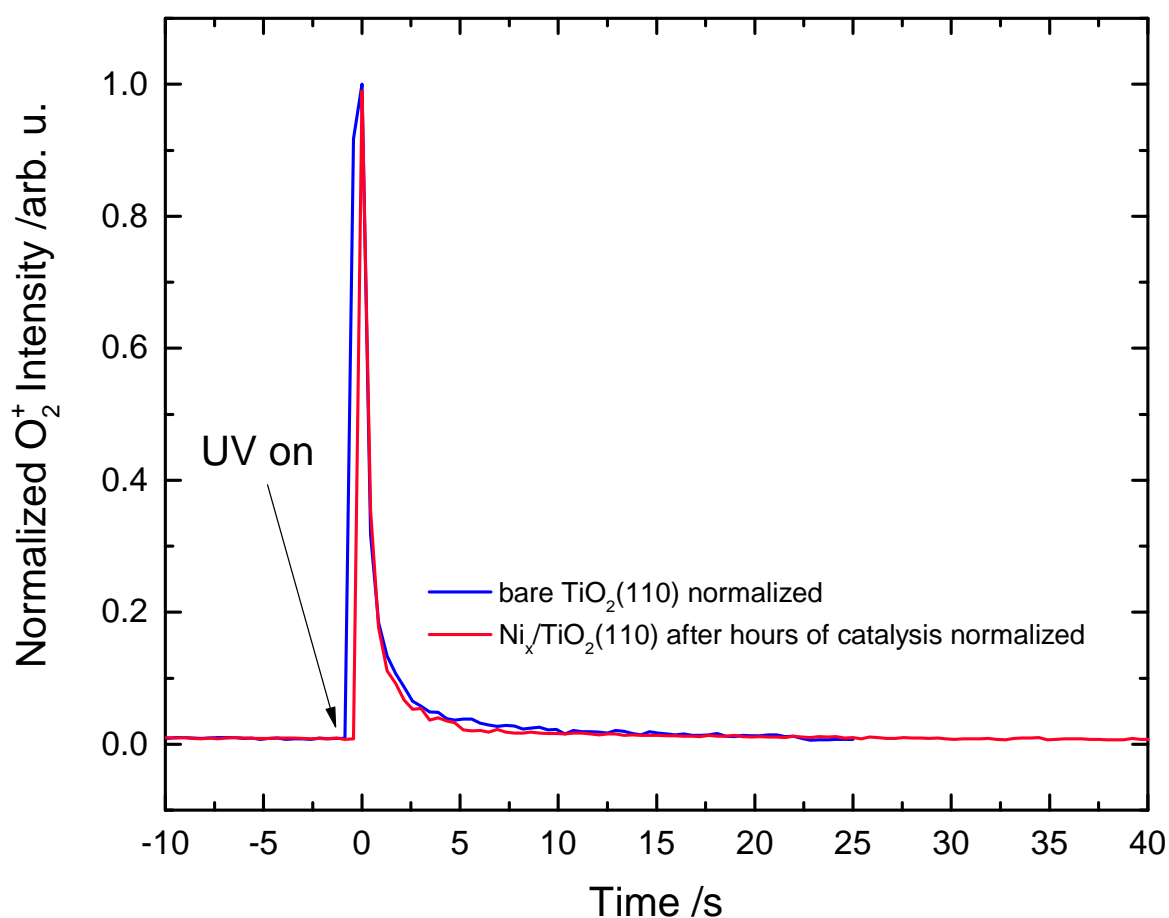


**Figure S4.** Normalized  $O_2$  photon-stimulated desorption (PSD) spectra on  $r\text{-TiO}_2(110)$  and  $Ni_{16-45}/r\text{-TiO}_2(110)$ , trace  $m/z$  32 shown. For  $r\text{-TiO}_2(110)$ , after dosing 20 L of  $O_2$  at cryogenic temperatures, the crystal surface was illuminated at 241.8 nm. For  $Ni_{16-45}/r\text{-TiO}_2(110)$  after the experiment, the methanol background is turned off and the sample was illuminated for another 15 min to deplete all the methanol from the photo-oxidation sites. The illumination is turned off, the sample cooled down to 130 K and exposed to 20 L of oxygen, to saturate the surface. Upon UV illumination, the same intensity and kinetics for the  $O_2$  PSD are observed as for the bare sample, indicating that the number of photoactive sites stays constant and that the methanol at least in the active sites was completely converted. (Note that the signals only slightly deviate in their maximum values from each other. This is caused due to the uncertainty in the starting time of the illumination as well as deviations by the QMS when the recording data points.)

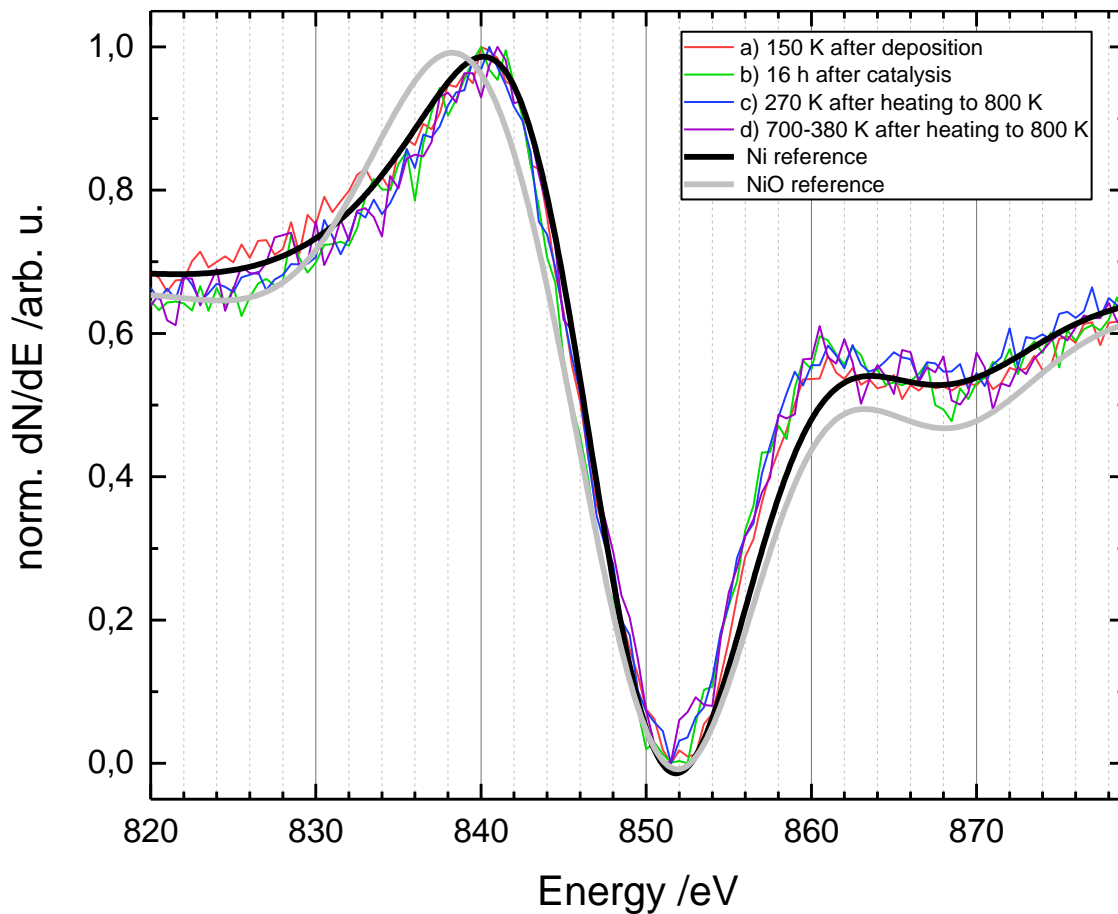


**Figure S5.** Excerpt of the Auger spectra of the Ni/r-TiO<sub>2</sub>(110) surface from **Figure 5** in the manuscript, normalized to the maximum peak intensity between 800 eV and 900 eV (Ni). Two reference curves outline the progression of metallic Ni (black) and NiO (grey) references for comparison. The auger spectra were recorded with a primary electron energy of 3 keV.

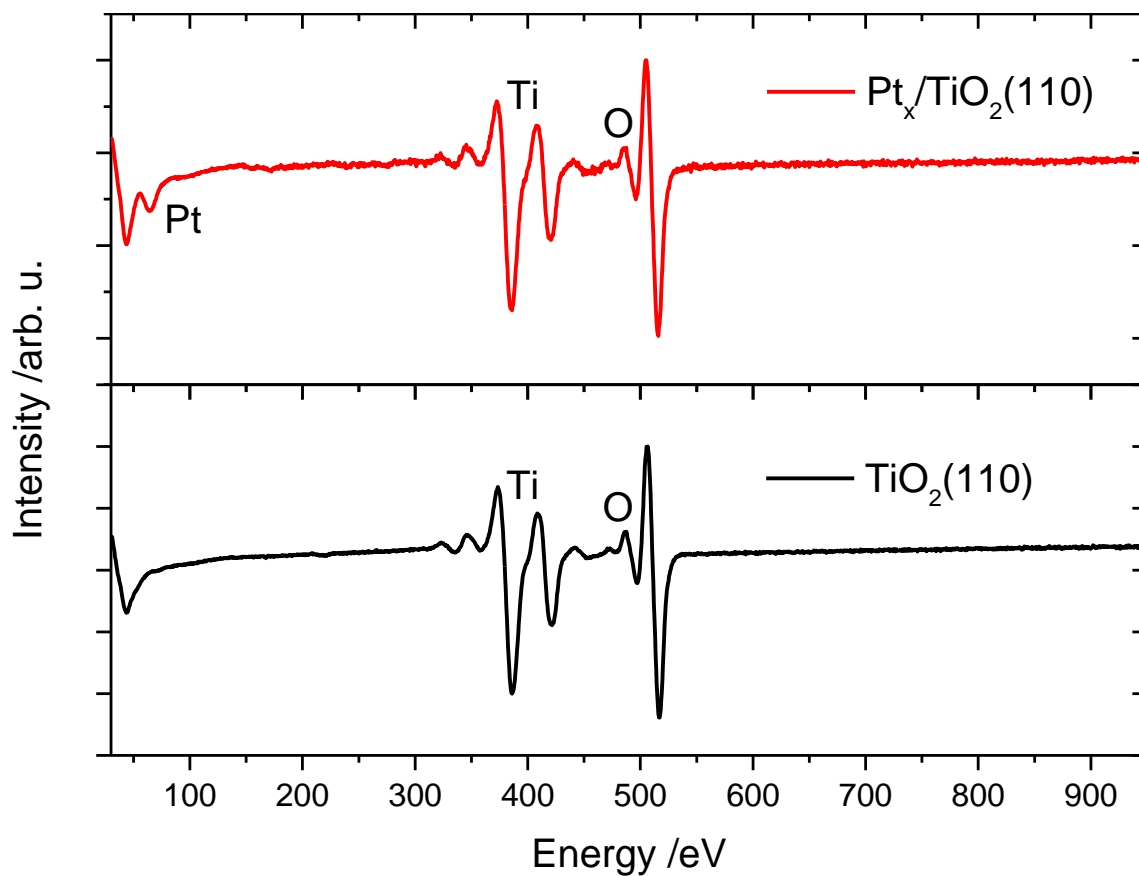


**Figure. S6.** Auger Electron Spectra of the clean  $r-TiO_2(110)$  surface (bottom) and  $Pt_x/r-TiO_2(110)$  after methanol photocatalysis and subsequent annealing to 800 K (top). Only titanium and oxygen are observed for the  $r-TiO_2(110)$  surface, while a small feature of the Pt NOO Peak appears at 64 eV on  $Pt_x/r-TiO_2(110)$ . The coverage is 0.3%  $Pt > 47/ML$ .



# List of Figures

2.1	Ball and stick model of the rutile $\text{TiO}_2(110)-(1 \times 1)$ surface with BBO vacancies and $\text{O}_{ad}$ adatoms. Black spheres represent BBO species, grey spheres in-plane O ions, pink spheres $\text{O}_{ad}$ adatoms and red spheres Ti cations. Adapted from [31]. . . . .	4
2.2	Schematic representation of band bending and charge carrier dynamics in titania upon illumination with light whose energy $h\nu$ is above the band gap $E_g$ . 1: The negatively charged defects at the surface cause an upward band bending, i.e. a repulsive and attractive potential for electrons and holes, respectively. Therefore, electrons travel preferentially towards the bulk and holes towards the surface. 2: When the negative surface states have been extinguished by the holes, the formerly bent bands are flattened. Electrons and holes diffuse towards the surface and the bulk to finally recombine, releasing the absorbed light energy as heat. CBE: Conduction band edge; VBE: Valence band edge. . . . .	6
2.3	TPD spectrum of 1.5 ML methanol on reduced $\text{TiO}_2(110)$ recorded in the course of this thesis. While the multilayer peak is absent due too the low coverage, the four features highlighted by the arrows are in good agreement with the literature.[67, 68] Deviations in the desorption temperature from the literature values can be traced back to experimental differences such as heating rate, heat transfer, or location of the thermocouples. . . .	8
2.4	Schematic illustration of alcohol photochemistry on $\text{TiO}_2(110)$ using methanol as an example based on the literature results discussed in the text. Upon adsorption, the alcohol partially dissociates to form the photoactive alkoxy species. Upon illumination, the alcohol is oxidized by a homolytic $\alpha$ -H bond cleavage. At sufficiently high temperatures (e.g. at room temperature), the aldehyde/ketone desorbs into the gas phase, whereas the hydrogen species remain on the surface. . . . .	10
2.5	Schematic illustration of the surface sites, defects, and methanol adsorbates present on $\text{TiO}_2(110)$ . [23, 24, 25, 26, 27] The ideal $\text{TiO}_2(110)$ surface consists of $\text{Ti}^{4+}$ and BBO sites. Additionally, defects (sub-surface Ti interstitials ( $\text{Ti}_{int}$ ), BBO vacancies, $\text{O}_{ad}$ , hydroxyls (H on BBO)) are present. These defects influence the adsorption states of methanol, leading to methoxy groups on the Ti rows ( $\text{CH}_3\text{O}_{\text{Ti5c}}$ ) and in BBO vacancies ( $\text{CH}_3\text{O}_{\text{BBOvac}}$ ) next to molecular methanol ( $\text{CH}_3\text{OH}_{\text{Ti5c}}$ ). . . . .	13

## LIST OF FIGURES

- 2.6 Photocatalytic reaction mechanism for methanol conversion at a co-catalyst-loaded r-TiO<sub>2</sub>(110) surface as described in the text. Upon adsorption, a methoxy and hydroxyl species [2] is formed thermally. The latter diffuses across the surface at sufficiently high temperature[3]. Upon illumination, methoxy is oxidized by a photohole [4] yielding formaldehyde [5], which eventually desorbs thermally. The thus formed atomic hydrogen diffuses on the surface [6] and recombines with another hydrogen at a co-catalyst, desorbing as H<sub>2</sub> [7]. The negatively charged surface states (e.g. BBO vacancies or Ti<sup>3+</sup> interstitials) of the n-type semiconductor get replenished by the photoelectron [8]. The catalyst remains unchanged after the completion of the cycle [1]. The reaction mechanism facilitates an overall charge-neutral stoichiometric reaction comprising thermal and photochemical steps. Adapted from [141]. . . . . 15
- 2.7 The band bending scheme adapted to the photocatalytic cycle proposed by Walenta *et al.*. The photoactive methoxy group is bound to a negatively charged surface state, which causes an upward band bending. The adsorbate affects the surface density of states, as indicated by the dashed lines and the hemisphere. A photohole created by illumination migrates to the surface state, and by its consumption reduces the electron density there, leading to a C–H bond cleavage. Formaldehyde subsequently desorbs, the reduction of negative surface charge creates a band flattening and enables the diffusion of photoelectrons to the surface, where it regenerates the initial negatively charged surface state. Black dotted line: actual occupation, grey dotted line: previous occupation. . . . . 16
- 3.1 Sketch of the experimental setup used in this work which is divided into two parts: the laser vaporization cluster source for the generation of Pt or Ni clusters as co-catalysts (top) and the analysis chamber for surface preparation, characterization, and reactivity measurements (bottom). Adapted with permission from [83]. Copyright 2018 American Chemical Society. . . . . 19
- 3.2 Principle behind the photocatalytic measurements with the example of methanol photoreforming on Pt-loaded TiO<sub>2</sub>(110). The reaction is started by UV illumination (yellow background) at a certain background pressure of the reactant. Upon light exposure, the traces of the desorbing reaction products are detected in the QMS. . . . . 20

## 5 Bibliographic Details

### 5.1 Reactions in the Photocatalytic Conversion of Tertiary Alcohols on Rutile TiO<sub>2</sub>(110)

C. Courtois,<sup>†</sup> M. Eder,<sup>†</sup> K. Schnabl, C. A. Walenta, M. Tschurl, U. Heiz\*

*Angew. Chem Int. Ed.*, **2019**, *58* (40), 14255-14259.

doi: 10.1002/anie.201907917

Chair of Physical Chemistry, Department of Chemistry and Catalysis Research Center, Technische Universität München, Lichtenbergstr. 4, 85748 Garching, Germany

<sup>†</sup> Contributed equally to this work.

\*Corresponding author, E-mail: ulrich.heiz@mytum.de

*Angew. Chem Int. Ed.*, **2019**, *58* (40), 14255-14259 - Published by Wiley-VCH Verlag GmbH & Co. KGaA .

## 5.2 Origin of Poisoning in Methanol Photoreforming on TiO<sub>2</sub>(110): The Importance of Thermal Back-Reaction Steps in Photocatalysis

C. Courtois,<sup>†</sup> M. Eder,<sup>†</sup> S. L. Kollmannsberger, M. Tschurl, C. A. Walenta, U. Heiz\*

*ACS Catal.*, **2020**, *10* (14), 7747–7752.

doi: 10.1021/acscatal.0c01615

Chair of Physical Chemistry, Department of Chemistry and Catalysis Research Center, Technische Universität München, Lichtenbergstr. 4, 85748 Garching, Germany

<sup>†</sup> Contributed equally to this work.

\*Corresponding author, E-mail: ulrich.heiz@mytum.de

Reprinted with permission from *ACS Catal.*, **2020**, *10* (14), 7747–7752. Copyright 2021 American Chemical Society.



### 5.3 Nickel clusters on $\text{TiO}_2(110)$ : thermal chemistry and photocatalytic hydrogen evolution of methanol

C. Courtois,<sup>†,a</sup> M. Eder,<sup>†,a</sup> T. Kratky,<sup>b</sup> S. Günther,<sup>b</sup> C. M. Tschurl,<sup>a</sup> U. Heiz<sup>\*,a</sup>

*Catal. Sci. Technol.*, **2020**, *10* (22), 7630–7639.

doi: 10.1039/D0CY01465F

<sup>a</sup> Chair of Physical Chemistry & Catalysis Research Center, Technical University of Munich, Lichtenbergstr. 4, 85748 Garching, Germany

<sup>b</sup> Department of Chemistry, Technical University of Munich, Lichtenbergstr. 4, 85748 Garching, Germany

<sup>†</sup> Contributed equally to this work.

\*Corresponding author, E-mail: ulrich.heiz@mytum.de

Reprinted with permission from *Catal. Sci. Technol.*, **2020**, *10* (22), 7630–7639. Copyright 2021 Royal Society of Chemistry.



## 6 Conclusion & Outlook

This work provides novel chemical insights into the photoreforming of alcohols on bare and metal cluster-loaded rutile  $\text{TiO}_2(110)$ . New substrates as well as new co-catalysts were investigated for the first time in  $\text{TiO}_2(110)$  photocatalysis in UHV. In the course of this work, chemical mechanisms and the role of Ni and Pt co-catalysts in the heterogeneous photocatalysis of alcohols on  $\text{TiO}_2(110)$  was elucidated. Tertiary alcohols were photooxidized at high selectivities on both bare and Pt-loaded titania. These results were further used to elucidate deactivation mechanisms which occur during the photoconversion of methanol on bare  $\text{TiO}_2(110)$ . Furthermore, Ni clusters were employed to facilitate hydrogen evolution during methanol photoreforming.

The photoreforming of tertiary alcohols on rutile  $\text{TiO}_2(110)$  was shown to proceed as selective oxidation, which can be described as hole-mediated disproportionation to form an alkane and the respective ketone. The abstraction of methyl groups did not occur at all if longer hydrocarbon chains were present, i.e. only  $\alpha$ -C bonds to ethyl or propyl groups were selectively cleaved. The thermochemistry of radical formation may be suitable to explain the selectivity of the photoreaction. The recombination of the cleaved alkyl radical and surface hydrogen was enabled on bare titania, in contrast to the recombination of two hydrogen atoms which requires a co-catalyst. Therefore, photoreforming tertiary alcohols on bare  $\text{TiO}_2(110)$  proved to be stoichiometric and was conducted catalytically without any metal co-catalyst. Low amounts of Pt clusters on the rutile crystal enhanced the overall reaction rate. Furthermore, they opened another reaction pathway at elevated pressures, which yielded molecular hydrogen and the recombination product of two alkyl radicals.

This study on tertiary alcohols paved the way for the discovery of the mechanism behind catalyst poisoning during the photoreforming of primary and secondary alcohols. On bare  $\text{TiO}_2(110)$ , it was observed that the catalytic activity in methanol photoconversion quickly ceased while that of 2-methyl-2-pentanol remained at a constant TOF. The speculative origins of deactivation found in the literature, such as an alteration of charge carrier dynamics or steric hindrances, fail to explain this behavior. Instead, the results suggested the surface reactions to be reversible. The limited conversion of primary alcohols originated from thermal back-reactions of the aldehyde with an surface hydrogen species (hydroxyls). Hydrogen as reaction product could not leave the surface at room temperature, causing a shift in the chemical equilibria. The initially low concentration of hydroxyls on the surface did not inhibit the photochemical formation of formaldehyde, but their concentration was enhanced by continuing methanol photoreforming. This altered the equilibrium concentrations between photoactive methoxy and the photoproducts formaldehyde/hydroxyl towards the reactant side. Tertiary alcohols were photoconverted to a ketone and an alkyl radical. The latter could thermally recombine

## 6 Conclusion & Outlook

with a surface hydroxyl species, yielding an alkane which desorbed thermally at room temperature, much like the ketone. Since all reaction products were thus removed from the equilibrium, no deactivation was observed. These findings showed that merely considering physical properties of a semiconductor is insufficient to comprehensively explain the behavior of a photocatalyst. Chemical phenomena and equilibria on the surface are equally important when describing heterogeneous photocatalysis on a molecular level. The results as well as those in the literature unambiguously demonstrated the necessity of a co-catalyst for hydrogen evolution on  $\text{TiO}_2(110)$ . [141, 83, 143, 145] To this end, noble metals such as Pt or Au are usually employed, which is problematic from an application point of view due to their high costs. To overcome this drawback, Ni clusters were studied on titania in order to investigate their reactivity on methanol photoreforming. The addition of this co-catalyst clearly facilitated hydrogen evolution at room temperature, in the same way as it was known from Pt clusters. Yet different to Pt, Ni-loaded titania deactivated over time, as evidenced by a steadily decreasing hydrogen and formaldehyde formation. The deactivation was found to be caused by illumination, since a prolonged exposure to a methanol background prior to illumination showed no effect on the catalytic activity. Auger electron spectroscopy revealed the presence of carbon on the surface after methanol photoreforming, although the Ni clusters remained in a metallic state. This suggested the formation of carbonaceous deposits on the clusters. Heating the carbon-contaminated surface *in vacuo* partially restored the catalytic activity. However, a persistent carbon peak remained in the Auger spectra, and the highest initial photoactivity was not achieved again. The results show that Ni clusters are suitable co-catalysts for hydrogen evolution on titania, but their eventual deactivation is a disadvantage over Pt as co-catalyst material.

The studies conducted in the course of this work show on the one hand the importance of co-catalysts and the necessity of a deliberate choice of material for photocatalytic hydrogen evolution. On the other hand, it demonstrates the remarkable practical potential of heterogeneous photocatalysis, which can significantly broaden the possibilities of applied chemistry. To this end, further research has to be conducted on the surface chemistry and mechanisms in heterogeneous photocatalysis.

Regarding alcohol photoreforming in UHV, still little is known about the stability and chemically or physically induced alterations of the co-catalyst. For catalytic applications, a more detailed knowledge in this respect is imperative for a target-oriented catalyst design. Therefore, future work should focus on a deeper chemical understanding of the co-catalyst. For example, photocatalytic reactions are usually conducted at mild conditions, but bringing the catalyst to elevated temperatures and pressures might be a necessity when it comes to regeneration procedures, as demonstrated in the study on  $\text{Ni}_x/\text{TiO}_2(110)$ . Therefore, the co-catalyst stability should be investigated under harsher conditions. Naturally, the impact of compounds whose presence is expected during applied photocatalysis (e.g.  $\text{O}_2$ ,  $\text{CO}$ ,  $\text{H}_2\text{O}$ , etc.) is of interest. Apart from that, it might be worthwhile to conduct studies on possible effects arising from strong metal-support interaction, which is a well-known phenomenon on metal-loaded titania. [163, 164, 165] On the one hand, an encapsulation of the co-catalyst might of course lead to deactivation. On the other hand, even encapsulated clusters may show an effect on the photocatalytic

activity (e.g. by a permanent effect on charge-carrier dynamics) seems conceivable even by encapsulated metal clusters. Thus, the influence of strong metal-support interaction on photochemical reactions is not straightforward and therefore hard to predict. A detailed understanding on this topic is of interest from both a fundamental as well as an application point of view.[166, 167]

In the same manner, further efforts are necessary to identify the nature of intermediates during photocatalytic reactions. This accounts especially for adsorbates on the co-catalyst during photocatalysis. For this purpose, infrared reflection absorption spectroscopy is a powerful tool for providing such insights.[168, 169, 98] For example, the adsorption of methanol could be used to detect changes in the oxidation states of the metal co-catalyst or the number of binding sites. Apart from that, the occurrence and vanishing of certain intermediate species can be detected. Similarly, XPS would yield information about oxidation and encapsulation state of the metal co-catalysts as well as the  $\text{TiO}_2(110)$  surface itself. Especially near ambient pressure XPS is a promising technique in this respect, as it provides a chemical surrounding which is closer to applied conditions than idealistic UHV studies.[170, 171, 172]

From a more general point of view, future studies on heterogeneous photocatalysis in UHV should not be solely based on titania, which is hitherto the only extensively investigated system under ideal conditions.  $\text{TiO}_2$  clearly has its limitations as photocatalyst, which should be understood, accepted, and overcome by employing alternative systems. For example, efficient water splitting has not yet been achieved on titania in UHV, most probably due to its incapability of evolving oxygen. Even in the liquid phase, titania-based photocatalytic water splitting was so far inefficient at best, although numerous co-catalysts and preparation strategies have been tested. With respect to water splitting, alternative systems should be considered.[173, 174, 175, 176]

In this regard, strontium titanate ( $\text{SrTiO}_3$ ) is a very promising candidate to examine for this reaction. It is commercially available as single crystal exposing different facets, and various degrees of doping are obtainable with various cations. Notably, full water splitting has already been achieved on  $\text{SrTiO}_3$ -based powder photocatalysts. While no photochemical experiments have been hitherto conducted in UHV, several thermal studies were performed with different substrate molecules, setting a solid foundation for an understanding of photochemical surface chemistry.[177, 178, 179]



## Bibliography

- [1] World energy balances – analysis [online]. 2021. URL: <https://www.iea.org/reports/world-energy-balances-overview/world> [last checked 2021-08-23].
- [2] Sandia national laboratories - energy overview [online]. 218. URL: [https://www.sandia.gov/news/publications/fact\\_sheets/index.html](https://www.sandia.gov/news/publications/fact_sheets/index.html) [last checked 2021-08-23].
- [3] How much oil is used to make plastic? [online]. 2021. URL: <https://www.eia.gov/tools/faqs/faq.php?id=34&t=6> [last checked 2021-08-23].
- [4] M. Capdevila-Cortada. Electrifying the Haber-Bosch. *Nat. Catal.*, 2(12):1055–1055, 2019.
- [5] X. Chang, T. Wang, and J. Gong. CO<sub>2</sub> photo-reduction: insights into CO<sub>2</sub> activation and reaction on surfaces of photocatalysts. *Energy Environ. Sci.*, 9(7):2177–2196, 2016.
- [6] L. Yuan, C. Han, M.-Q. Yang, and Y.-J. Xu. Photocatalytic water splitting for solar hydrogen generation: fundamentals and recent advancements. *Int. Rev. Phys. Chem.*, 35(1):1–36, 2016.
- [7] A. Kubacka, M. Fernández-García, and G. Colón. Advanced nanoarchitectures for solar photocatalytic applications. *Chem. Rev.*, 112(3):1555–1614, 2012.
- [8] D. Rodríguez-Padrón, A. R. Puente-Santiago, A. M. Balu, M. J. Muñoz-Batista, and R. Luque. Environmental catalysis: Present and future. *ChemCatChem*, 11(1):18–38, 2018.
- [9] Y. Qu and X. Duan. Progress, challenge and perspective of heterogeneous photocatalysts. *Chem. Soc. Rev.*, 42(7):2568–2580, 2013.
- [10] B. A. Pinaud, J. D. Benck, L. C. Seitz, A. J. Forman, Z. Chen, T. G. Deutsch, B. D. James, K. N. Baum, G. N. Baum, S. Ardo, H. Wang, E. Miller, and T. F. Jaramillo. Technical and economic feasibility of centralized facilities for solar hydrogen production via photocatalysis and photoelectrochemistry. *Energy Environ. Sci.*, 6(7):1983–2002, 2013.
- [11] L. Kavan, M. Grätzel, S. E. Gilbert, C. Klemen, and H. J. Scheel. Electrochemical and photoelectrochemical investigation of single-crystal anatase. *J. Am. Chem. Soc.*, 118(28):6716–6723, 1996.

## BIBLIOGRAPHY

- [12] L. Chen, J. Tang, L.-N. Song, P. Chen, J. He, C.-T. Au, and S.-F. Yin. Heterogeneous photocatalysis for selective oxidation of alcohols and hydrocarbons. *Appl. Catal. B*, 242:379–388, 2019.
- [13] M. Dilla, N. G. Moustakas, A. E. Becerikli, T. Peppel, A. Springer, R. Schlögl, J. Strunk, and S. Ristig. Judging the feasibility of TiO<sub>2</sub>(110) as photocatalyst for chemical energy conversion by quantitative reactivity determinants. *Phys. Chem. Chem. Phys.*, 21(24):13144–13150, 2019.
- [14] M. A. Henderson. A surface science perspective on TiO<sub>2</sub>(110) photocatalysis. *Surf. Sci. Rep.*, 66(6):185–297, 2011.
- [15] W. Huang. Oxide nanocrystal model catalysts. *Acc. Chem. Res.*, 49:520–527, 2016.
- [16] B. Ohtani. Revisiting the original works related to titania photocatalysis: A review of papers in the early stage of photocatalysis studies. *Electrochemistry*, 82:414–425, 2014.
- [17] A. Fujishima and K. Honda. Electrochemical photolysis of water at a semiconductor electrode. *Nature*, 82:414–425, 2014.
- [18] J. Schneider, M. Matsuoka, M. Takeuchi, J. Zhang, Y. Horiuchi, M. Anpo, and D. W. Bahnemann. Understanding TiO<sub>2</sub>(110) photocatalysis: Mechanisms and materials. *Chem. Rev.*, 114:9919–9986, 2014.
- [19] J.-M. Herrmann. Fundamentals and misconceptions in photocatalysis. *J. Photochem. Photobiol. A*, 216:85–93, 2010.
- [20] B. Ohtani. Preparing articles on photocatalysis—beyond the illusions, misconceptions, and speculation. *Chem. Lett.*, 37:216–229, 2008.
- [21] B. Ohtani, O. Prieto-Mahaney, D. Li, and R. Abe. What is Degussa (Evonik) P25? crystalline composition analysis, reconstruction from isolated pure particles and photocatalytic activity test. *J. Photochem. Photobiol. A*, 216:179–182, 2010.
- [22] U. Diebold. The surface science of titanium dioxide. *Surf. Sci. Rep.*, 48:53–229, 2003.
- [23] U. Diebold, J. F. Anderson, K.-O. Ng, and D. Vanderbilt. Evidence for the tunneling site on transition-metal oxides: TiO<sub>2</sub>(110). *Phys. Rev. Lett.*, 77:1322–1325, 1996.
- [24] H. Onishi, K.-i. Fukui, and Y. Iwasawa. Atomic-scale surface structures of TiO<sub>2</sub>(110) determined by scanning tunneling microscopy: A new surface-limited phase of titanium oxide. *Bull. Chem. Soc. Jpn.*, 68:2447–2458, 1995.



- [25] T. Minato, Y. Sainoo, Y. Kim, H. S. Kato, K.-i. Aika, M. Kawai, J. Zhao, H. Petek, T. Huang, W. He, B. Wang, Z. Wang, Y. Zhao, J. Yang, and J. G. Hou. The electronic structure of oxygen atom vacancy and hydroxyl impurity defects on titanium dioxide (110) surface. *J. Chem. Phys.*, 130:124502, 2009.
- [26] S. Fischer, A. W. Munz, K.-D. Schierbaum, and W. Göpel. The geometric structure of intrinsic defects at  $\text{TiO}_2(110)$  surfaces: an STM study. *Surf. Sci.*, 337:17–30, 1995.
- [27] K.-i. Fukui, H. Onishi, and Y. Iwasawa. Atom-resolved image of the  $\text{TiO}_2(110)$  surface by noncontact atomic force microscopy. *Phys. Rev. Lett.*, 79:4202–4205, 1997.
- [28] S. Wendt, P. T. Sprunger, E. Lira, G. K. H. Madsen, Z. Li, J. Ø. Hansen, J. Matthiesen, A. Blekinge-Rasmussen, E. Lægsgaard, B. Hammer, and F. Besenbacher. The role of interstitial sites in the  $\text{Ti}3d$  defect state in the band gap of titania. *Science*, 320:1755–1759, 2008.
- [29] Z. Dohnálek, I. Lyubinetzky, and R. Rousseau. Thermally-driven processes on rutile  $\text{TiO}_2(110)-(1 \times 1)$ : A direct view at the atomic scale. *Prog. Surf. Sci.*, 85(5-8):161–205, 2010.
- [30] Y. Du, N. A. Deskins, Z. Zhang, Z. Dohnalek, M. Dupuis, and I. Lyubinetzky. Formation of O adatom pairs and charge transfer upon  $\text{O}_2$  dissociation on reduced  $\text{TiO}_2(110)$ . *Phys. Chem. Chem. Phys.*, 12:6337–6344, 2010.
- [31] E. Lira, J. Ø. Hansen, P. Huo, R. Bechstein, P. Galliker, E. Lægsgaard, B. Hammer, S. Wendt, and F. Besenbacher. Dissociative and molecular oxygen chemisorption channels on reduced rutile  $\text{TiO}_2(110)$ : An STM and TPD study. *Surf. Sci.*, 604(21-22):1945–1960, 2010.
- [32] J. Pan, B. L. Maschhoff, U. Diebold, and T. E. Madey. Interaction of water, oxygen, and hydrogen with  $\text{TiO}_2(110)$  surfaces having different defect densities. *J. Vac. Sci. Technol. A*, 10(4):2470–2476, 1992.
- [33] L.-Q. Wang, D. Baer, and M. Engelhard. Creation of variable concentrations of defects on  $\text{TiO}_2(110)$  using low-density electron beams. *Surf. Sci.*, 320(3):295–306, 1994.
- [34] M. Li, W. Hebenstreit, L. Gross, U. Diebold, M. A. Henderson, D. R. Jennison, P. A. Schultz, and M. P. Sears. Oxygen-induced restructuring of the  $\text{TiO}_2(110)$  surface: a comprehensive study. *Surf. Sci.*, 437(1):173–190, 1999.
- [35] J. Ø. Hansen, J. Matthiesen, E. Lira, L. Lammich, and S. Wendt. A new recipe for preparing oxidized  $\text{TiO}_2(110)$  surfaces: An STM study. *Surf. Sci.*, 666:113–122, 2017.

## BIBLIOGRAPHY

- [36] P. Scheiber, A. Riss, M. Schmid, P. Varga, and U. Diebold. Observation and destruction of an elusive adsorbate with STM: TiO<sub>2</sub>(110). *Phys. Rev. Lett.*, 105:216101, Nov 2010.
- [37] M. A. Henderson. A surface perspective on self-diffusion in rutile TiO<sub>2</sub>(110). *Surf. Sci.*, 419(2):174–187, 1999.
- [38] M. A. Barteau. Site requirements of reactions on oxide surfaces. *J. Vac. Sci. Technol. A*, 11(4):2162–2168, 1993.
- [39] Z. Zhang and J. T. Yates Jr. Band bending in semiconductors: Chemical and physical consequences at surfaces and interfaces. *Chem. Rev.*, 112:5520–5551, 2012.
- [40] E. Cho, S. Han, H.-S. Ahn, K.-R. Lee, S. K. Kim, and C. S. Hwang. First-principles study of point defects in rutile TiO<sub>2-x</sub>. *Phys. Rev. B*, 73:193202–193205, 2006.
- [41] J. Nowotny, M. Radecka, and M. Rekas. Semiconducting properties of undoped TiO<sub>2</sub>(110). *J. Phys. Chem. Solids*, 58:927–937, 1997.
- [42] C. Di Valentin, G. Pacchioni, and A. Selloni. Reduced and n-type doped TiO<sub>2</sub>(110): Nature of Ti<sup>3+</sup> species. *J. Phys. Chem. C*, 113:20543–20552, 2006.
- [43] X. Mao, X. Lang, Z. Wang, Q. Hao, B. Wen, Z. Ren, D. Dai, C. Zhou, L.-M. Liu, and X. Yang. Band-gap states of TiO<sub>2</sub>(110): Major contribution from surface defects. *J. Phys. Chem. Lett.*, 4(22):3839–3844, 2013.
- [44] A. Fujishima, X. Zhang, and D. A. Tryk. TiO<sub>2</sub>(110) photocatalysis and related surface phenomena. *Surf. Sci. Rep.*, 63:515–582, 2008.
- [45] A. Stevanovic and J. T. Yates. Electron hopping through TiO<sub>2</sub>(110) powder: A study by photoluminescence spectroscopy. *J. Phys. Chem. C*, 117(46):24189–24195, 2013.
- [46] J. M. Lantz and R. M. Corn. Electrostatic field measurements and band flattening during electron-transfer processes at single-crystal TiO<sub>2</sub>(110) electrodes by electric field-induced optical second harmonic generation. *J. Phys. Chem.*, 98(18), 1994.
- [47] J. M. Lantz and R. M. Corn. Time-resolved optical second harmonic generation measurements of picosecond band flattening processes at single crystal TiO<sub>2</sub>(110) electrodes. *J. Phys. Chem.*, 98(38):9387–9390, 1994.
- [48] M. J. Berr, P. Wagner, S. Fischbach, A. Vaneski, J. Schneider, A. S. Sussha, A. L. Rogach, F. Jäckel, and J. Feldmann. Hole scavenger redox potentials determine quantum efficiency and stability of Pt-decorated CdS nanorods for photocatalytic hydrogen generation. *Appl. Phys. Lett.*, 100(22):223903, 2012.
- [49] T. Simon, N. Bouchonville, M. J. Berr, A. Vaneski, A. Adrović, D. Volbers, R. Wyrwich, M. Döblinger, A. S. Sussha, A. L. Rogach, et al. Redox shuttle mechanism enhances photocatalytic H<sub>2</sub> generation on Ni-decorated CdS nanorods. *Nat. Mater.*, 13(11):1013–1018, 2014.

- [50] V. Jovic, W.-T. Chen, D. Sun-Waterhouse, M. G. Blackford, H. Idriss, and G. I. Waterhouse. Effect of gold loading and TiO<sub>2</sub>(110) support composition on the activity of Au/ TiO<sub>2</sub> photocatalysts for H<sub>2</sub> production from ethanol–water mixtures. *J. Catal.*, 305:307–317, 2013.
- [51] W.-T. Chen, A. Chan, Z. H. Al-Azri, A. G. Dosado, M. A. Nadeem, D. Sun-Waterhouse, H. Idriss, and G. I. Waterhouse. Effect of TiO<sub>2</sub>(110) polymorph and alcohol sacrificial agent on the activity of Au/ TiO<sub>2</sub> photocatalysts for H<sub>2</sub> production in alcohol–water mixtures. *J. Catal.*, 329:499–513, 2015.
- [52] J. Schneider and D. W. Bahnemann. Undesired role of sacrificial reagents in photocatalysis. *J. Phys. Chem. Lett.*, 4(20):3479–3483, 2013.
- [53] A. S. Hainer, J. S. Hodgins, V. Sandre, M. Vallieres, A. E. Lanterna, and J. C. Scaiano. Photocatalytic hydrogen generation using metal-decorated TiO<sub>2</sub>(110): sacrificial donors vs true water splitting. *ACS Energy Lett.*, 3(3):542–545, 2018.
- [54] P. V. Kamat and S. Jin. Semiconductor photocatalysis: “tell us the complete story!”. *ACS Energy Lett.*, 3(3):622–623, 2018.
- [55] L. I. Granone, F. Sieland, N. Zheng, R. Dillert, and D. W. Bahnemann. Photocatalytic conversion of biomass into valuable products: a meaningful approach? *Green Chem.*, 20:1169–1192, 2018.
- [56] M. Cargnello, A. Gasparotto, V. Gombac, T. Montini, D. Barreca, and P. Fornasiero. Photocatalytic H<sub>2</sub> and added-value by-products - the role of metal oxide systems in their synthesis from oxygenates. *Eur. J. Inorg. Chem.*, 2011(28):4309–4323, 2011.
- [57] C. Y. Toe, C. Tsounis, J. Zhang, H. Masood, D. Gunawan, J. Scott, and R. Amal. Advancing photoreforming of organics: highlights on photocatalyst and system designs for selective oxidation reactions. *Energy Environ. Sci.*, 14:1140–1175, 2021.
- [58] F. Parrino, M. Bellardita, E. I. García-López, G. Marci, V. Loddo, and L. Palmisano. Heterogeneous photocatalysis for selective formation of high-value-added molecules: Some chemical and engineering aspects. *ACS Catal.*, 8(12):11191–11225, 2018.
- [59] S. Kampouri and K. C. Stylianou. Dual-functional photocatalysis for simultaneous hydrogen production and oxidation of organic substances. *ACS Catal.*, 9(5):4247–4270, 2019.
- [60] Z. Zhang, O. Bondarchuk, J. M. White, B. D. Kay, and Z. Dohnálek. Imaging adsorbate O-H bond cleavage: Methanol on TiO<sub>2</sub>(110). *J. Am. Chem. Soc.*, 128(13):4198–4199, 2006.
- [61] S. Wendt, J. Matthiesen, R. Schaub, E. K. Vestergaard, E. Lægsgaard, F. Besenbacher, and B. Hammer. Formation and splitting of paired hydroxyl groups on reduced TiO<sub>2</sub>(110). *Phys. Rev. Lett.*, 96:066107, 2006.

## BIBLIOGRAPHY

- [62] S. P. Bates, M. J. Gillan, and G. Kresse. Adsorption of methanol on  $\text{TiO}_2(110)$ : a first-principles investigation. *J. Phys. Chem. B*, 102(11):2017–2026, 1998.
- [63] R. S. de Armas, J. Oviedo, M. A. San Miguel, and J. F. Sanz. Methanol adsorption and dissociation on  $\text{TiO}_2(110)$  from first principles calculations. *J. Phys. Chem. C*, 111(27):10023–10028, 2007.
- [64] Z. Zhang, O. Bondarchuk, B. D. Kay, J. M. White, and Z. Dohnálek. Direct visualization of 2-butanol adsorption and dissociation on  $\text{TiO}_2(110)$ . *J. Phys. Chem. C*, 111(7):3021–3027, 2007.
- [65] J. O. Hansen, P. Huo, U. Martinez, E. Lira, Y. Y. Wei, R. Streber, E. Lægsgaard, B. Hammer, S. Wendt, and F. Besenbacher. Direct evidence for ethanol dissociation on rutile  $\text{TiO}_2(110)$ . *Phys. Rev. Lett.*, 107:136102, 2011.
- [66] L. Gamble, L. S. Jung, and C. T. Campbell. Decomposition and protonation of surface ethoxys on  $\text{TiO}_2(110)$ . *Surf. Sci.*, 348(1):1–16, 1996.
- [67] M. A. Henderson, S. Otero-Tapia, and M. E. Castro. The chemistry of methanol on the  $\text{TiO}_2(110)$  surface: the influence of vacancies and coadsorbed species. *Faraday Discuss.*, 114:313–329, 1999.
- [68] E. Farfan-Arribas and R. J. Madix. Different binding sites for methanol dehydrogenation and deoxygenation on stoichiometric and defective  $\text{TiO}_2(110)$  surfaces. *Surf. Sci.*, 544(2):241–260, 2003.
- [69] Y. K. Kim, B. D. Kay, J. M. White, and Z. Dohnálek. Alcohol chemistry on rutile  $\text{TiO}_2(110)$ : the influence of alkyl substituents on reactivity and selectivity. *J. Phys. Chem. C*, 111(49):18236–18242, 2007.
- [70] E. Farfan-Arribas and R. J. Madix. Role of defects in the adsorption of aliphatic alcohols on the  $\text{TiO}_2(110)$  surface. *J. Phys. Chem. B*, 106(41):10680–10692, 2002.
- [71] Y. Kim, B. Kay, J. White, and Z. Dohnálek. Inductive effect of alkyl chains on alcohol dehydration at bridge-bonded oxygen vacancies of  $\text{TiO}_2(110)$ . *Catal. Lett.*, 119:1–4, 2007.
- [72] Z. Li, R. S. Smith, B. D. Kay, and Z. Dohnálek. Determination of absolute coverages for small aliphatic alcohols on  $\text{TiO}_2(110)$ . *J. Phys. Chem. C*, 115(45):22534–22539, 2011.
- [73] C. Zhou, Z. Ren, S. Tan, Z. Ma, X. Mao, D. Dai, H. Fan, X. Yang, J. LaRue, R. Cooper, A. M. Wodtke, Z. Wang, Z. Li, B. Wang, J. Yang, and J. Hou. Site-specific photocatalytic splitting of methanol on  $\text{TiO}_2(110)$ . *Chem. Sci.*, 1(5):575–580, 2010.
- [74] C. Zhou, Z. Ma, Z. Ren, X. Mao, and X. Yang. Effect of defects on photocatalytic dissociation of methanol on  $\text{TiO}_2(110)$ . *Chem. Sci.*, 2:1980–1983, 2011.

- [75] W. Chu, W. A. Saidi, Q. Zheng, Y. Xie, Z. Lan, O. V. Prezhdo, H. Petek, and J. Zhao. Ultrafast dynamics of photogenerated holes at a  $\text{CH}_3\text{OH}/\text{TiO}_2$  rutile interface. *J. Am. Chem. Soc.*, 138(41):13740–13749, 2016.
- [76] J. Zhang, C. Peng, H. Wang, and P. Hu. Identifying the role of photogenerated holes in photocatalytic methanol dissociation on rutile  $\text{TiO}_2(110)$ . *ACS Catal.*, 7(4):2374–2380, 2017.
- [77] M. Shen and M. A. Henderson. Identification of the active species in photochemical hole scavenging reactions of methanol on  $\text{TiO}_2(110)$ . *J. Phys. Chem. Lett.*, 2(21):2707–2710, 2011.
- [78] M. Shen and M. A. Henderson. Role of water in methanol photochemistry on rutile  $\text{TiO}_2(110)$ . *J. Phys. Chem. C*, 116(35):18788–18795, 2012.
- [79] M. Shen, D. P. Acharya, Z. Dohnálek, and M. A. Henderson. Importance of diffusion in methanol photochemistry on  $\text{TiO}_2(110)$ . *J. Phys. Chem. C*, 116(48):25465–25469, 2012.
- [80] K. R. Phillips, S. C. Jensen, M. Baron, S.-C. Li, and C. M. Friend. Sequential photo-oxidation of methanol to methyl formate on  $\text{TiO}_2(110)$ . *J. Am. Chem. Soc.*, 135(2):574–577, 2013.
- [81] Q. Guo, C. Xu, W. Yang, Z. Ren, Z. Ma, D. Dai, T. K. Minton, and X. Yang. Methyl formate production on  $\text{TiO}_2(110)$ , initiated by methanol photocatalysis at 400 nm. *J. Phys. Chem. C*, 117(10):5293–5300, 2013.
- [82] X. Lang, B. Wen, C. Zhou, Z. Ren, and L.-M. Liu. First-principles study of methanol oxidation into methyl formate on rutile  $\text{TiO}_2(110)$ . *J. Phys. Chem. C*, 118(34):19859–19868, 2014.
- [83] S. L. Kollmannsberger, C. A. Walenta, C. Courtois, M. Tschurl, and U. Heiz. Thermal control of selectivity in photocatalytic, water-free alcohol photoreforming. *ACS Catal.*, 8(12):11076–11084, 2018.
- [84] H. Kominami, H. Sugahara, and K. Hashimoto. Photocatalytic selective oxidation of methanol to methyl formate in gas phase over titanium(IV) oxide in a flow-type reactor. *Cat. Commun.*, 11(5):426–429, 2010.
- [85] C. A. Walenta, C. Courtois, S. L. Kollmannsberger, M. Eder, M. Tschurl, and U. Heiz. Surface species in photocatalytic methanol reforming on  $\text{Pt}/\text{TiO}_2(110)$ : Learning from surface science experiments for catalytically relevant conditions. *ACS Catal.*, 10(7):4080–4091, 2020.
- [86] Q. Yuan, Z. Wu, Y. Jin, L. Xu, F. Xiong, Y. Ma, and W. Huang. Photocatalytic cross-coupling of methanol and formaldehyde on a rutile  $\text{TiO}_2(110)$  surface. *J. Am. Chem. Soc.*, 135(13):5212–5219, 2013.

## BIBLIOGRAPHY

- [87] T. Wang, Q. Hao, Z. Wang, X. Mao, Z. Ma, Z. Ren, D. Dai, C. Zhou, and X. Yang. Deuterium kinetic isotope effect in the photocatalyzed dissociation of methanol on TiO<sub>2</sub>(110). *J. Phys. Chem. C*, 122(46):26512–26518, 2018.
- [88] S. Dong, J. Hu, S. Xia, B. Wang, Z. Wang, T. Wang, W. Chen, Z. Ren, H. Fan, D. Dai, J. Cheng, X. Yang, and C. Zhou. Origin of the adsorption-state-dependent photoactivity of methanol on TiO<sub>2</sub>(110). *ACS Catal.*, 11(5):2620–2630, 2021.
- [89] X. Peng, R. Zhang, R.-r. Feng, A.-a. Liu, C. Zhou, Q. Guo, X. Yang, Y. Jiang, and Z. Ren. Active species in photocatalytic reactions of methanol on TiO<sub>2</sub>(110) identified by surface sum frequency generation vibrational spectroscopy. *J. Phys. Chem. C*, 123(22):13789–13794, 2019.
- [90] G. Kolesov, D. Vinichenko, G. A. Tritsarlis, C. M. Friend, and E. Kaxiras. Anatomy of the photochemical reaction: Excited-state dynamics reveals the C–H acidity mechanism of methoxy photo-oxidation on titania. *J. Phys. Chem. Lett.*, 6(9):1624–1627, 2015.
- [91] C. M. Friend. Perspectives on heterogeneous photochemistry. *Chem. Rec.*, 14(5):944–951, 2014.
- [92] C. A. Walenta, S. L. Kollmannsberger, J. Kiermaier, A. Winbauer, M. Tschurl, and U. Heiz. Ethanol photocatalysis on rutile TiO<sub>2</sub>(110): the role of defects and water. *Phys. Chem. Chem. Phys.*, 17:22809–22814, 2015.
- [93] S. Liu, A.-a. Liu, B. Wen, R. Zhang, C. Zhou, L.-M. Liu, and Z. Ren. Coverage dependence of methanol dissociation on TiO<sub>2</sub>(110). *J. Phys. Chem. Lett.*, 6(16):3327–3334, 2015.
- [94] X. Mao, D. Wei, Z. Wang, X. Jin, Q. Hao, Z. Ren, D. Dai, Z. Ma, C. Zhou, and X. Yang. Recombination of formaldehyde and hydrogen atoms on TiO<sub>2</sub>(110). *J. Phys. Chem. C*, 119(2):1170–1174, 2015.
- [95] D. Brinkley and T. Engel. Photocatalytic dehydrogenation of 2-propanol on TiO<sub>2</sub>(110). *J. Phys. Chem. B*, 102(39):7596–7605, 1998.
- [96] D. Brinkley and T. Engel. Active site density and reactivity for the photocatalytic dehydrogenation of 2-propanol on TiO<sub>2</sub>(110). *Surf. Sci.*, 415(3):1001–1006, 1998.
- [97] D. Brinkley and T. Engel. Evidence for structure sensitivity in the thermally activated and photocatalytic dehydrogenation of 2-propanol on TiO<sub>2</sub>(110). *J. Phys. Chem. B*, 104(42):9836–9841, 2000.
- [98] J. Kräuter, L. Mohrhusen, F. Waidhas, O. Brummel, J. Libuda, and K. Al-Shamery. Photoconversion of 2-propanol on rutile titania: A combined liquid-phase and surface science study. *J. Phys. Chem. C*, 125(6):3355–3367, 2021.

- [99] M. D. Kershis and M. G. White. Photooxidation of ethanol and 2-propanol on  $\text{TiO}_2(110)$ : evidence for methyl radical ejection. *Phys. Chem. Chem. Phys.*, 15:17976–17982, 2013.
- [100] C. Courtois, C. A. Walenta, M. Tschurl, U. Heiz, and C. M. Friend. Regulating photochemical selectivity with temperature: Isobutanol on  $\text{TiO}_2(110)$ . *J. Am. Chem. Soc.*, 142(30):13072–13080, 2020.
- [101] N. Djeghri, M. Formenti, F. Juillet, and S. Teichner. Photointeraction on the surface of titanium dioxide between oxygen and alkanes. *Faraday Discuss. Chem. Soc.*, 58:185–193, 1974.
- [102] A. Walker, M. Formenti, P. Meriaudeau, and S. Teichner. Heterogeneous photocatalysis: Photo-oxidation of methylbutanols. *J. Catal.*, 50(2):237–243, 1977.
- [103] L. P. Childs and D. F. Ollis. Photoassisted heterogeneous catalysis: Rate equations for oxidation of 2-methyl-2-butyl-alcohol and isobutane. *J. Catal.*, 67(1):35–48, 1981.
- [104] S. Preis and J. Falconer. Gas-phase photocatalytic oxidation of motor fuel oxygenated additives. *Water Sci. Technol.*, 49(4):141–145, 2004.
- [105] S. Preis, J. L. Falconer, R. del Prado Asensio, N. C. Santiago, A. Kachina, and J. Kallas. Photocatalytic oxidation of gas-phase methyl tert-butyl ether and tert-butyl alcohol. *Appl. Catal. B: Environ.*, 64(1):79–87, 2006.
- [106] S. Teichner. The origins of photocatalysis. *J. Porous Mater.*, 15(3):311–314, 2008.
- [107] Z. H. Al-Azri, W.-T. Chen, A. Chan, V. Jovic, T. Ina, H. Idriss, and G. I. Waterhouse. The roles of metal co-catalysts and reaction media in photocatalytic hydrogen production: Performance evaluation of  $\text{M}/\text{TiO}_2$  photocatalysts ( $\text{M}=\text{Pd}$ ,  $\text{Pt}$ ,  $\text{Au}$ ) in different alcohol–water mixtures. *J. Catal.*, 329:355–367, 2015.
- [108] K. Wietzerbin, J. Bernadou, and B. Meunier. Metal-mediated oxidation of tertiary alcohols and related fragmentations. *Eur. J. Inorg. Chem.*, 2000(7):1391–1406, 2000.
- [109] K. Vollhardt, C. Peter, and N. E. Schore. *Organische Chemie*. John Wiley & Sons, 2020.
- [110] C. A. Walenta, S. L. Kollmannsberger, C. Courtois, M. Tschurl, and U. Heiz. Photocatalytic selectivity switch to C-C scission:  $\alpha$ -methyl ejection of tert-butanol on  $\text{TiO}_2(110)$ . *Physical Chemistry Chemical Physics*, 20(10):7105–7111, 2018.
- [111] P. Huo, J. . Hansen, U. Martinez, E. Lira, R. Streber, Y. Wei, E. Lægsgaard, B. Hammer, S. Wendt, and F. Besenbacher. Ethanol diffusion on rutile  $\text{TiO}_2(110)$  mediated by H adatoms. *The Journal of Physical Chemistry Letters*, 3(3):283–288, 2012.

## BIBLIOGRAPHY

- [112] C. Zhou, Z. Ma, Z. Ren, X. Mao, D. Dai, and X. Yang. Effect of defects on photocatalytic dissociation of methanol on TiO<sub>2</sub>. *Chem. Sci.*, 2(10):1980–1983, 2011.
- [113] Q. Guo, C. Zhou, Z. Ma, and X. Yang. Fundamentals of TiO<sub>2</sub> photocatalysis: concepts, mechanisms, and challenges. *Adv. Mater.*, 31(50):1901997, 2019.
- [114] E. Lira, S. Wendt, P. Huo, J. Ø. Hansen, R. Streber, S. Porsgaard, Y. Wei, R. Bechstein, E. Lægsgaard, and F. Besenbacher. The importance of bulk Ti<sup>3+</sup> defects in the oxygen chemistry on titania surfaces. *J. Am. Chem. Soc.*, 133(17):6529–6532, 2011.
- [115] N. A. Deskins, R. Rousseau, and M. Dupuis. Defining the role of excess electrons in the surface chemistry of TiO<sub>2</sub>. *J. Phys. Chem. C*, 114(13):5891–5897, 2010.
- [116] N. A. Deskins, R. Rousseau, and M. Dupuis. Distribution of Ti<sup>3+</sup> surface sites in reduced TiO<sub>2</sub>. *J. Phys. Chem. C*, 115(15):7562–7572, 2011.
- [117] J. Haubrich, E. Kaxiras, and C. M. Friend. The role of surface and subsurface point defects for chemical model studies on TiO<sub>2</sub>: A first-principles theoretical study of formaldehyde bonding on rutile TiO<sub>2</sub>(110). *Chem. Eur. J.*, 17(16):4496–4506, 2011.
- [118] S. C. Jensen and C. M. Friend. The dynamic roles of interstitial and surface defects on oxidation and reduction reactions on titania. *Top. Catal.*, 56(15-17):1377–1388, 2013.
- [119] M. A. Henderson and I. Lyubinetsky. Molecular-level insights into photocatalysis from scanning probe microscopy studies on TiO<sub>2</sub>(110). *Chem. Rev.*, 113(6):4428–4455, 2013.
- [120] J. Ø. Hansen, R. Bebensee, U. Martinez, S. Porsgaard, E. Lira, Y. Wei, L. Lam-mich, Z. Li, H. Idriss, F. Besenbacher, B. Hammer, and S. Wendt. Unravelling site-specific photo-reactions of ethanol on rutile TiO<sub>2</sub>(110). *Sci. Rep.*, 6(1):1–11, 2016.
- [121] Q. Guo, C. Xu, Z. Ren, W. Yang, Z. Ma, D. Dai, H. Fan, T. K. Minton, and X. Yang. Stepwise photocatalytic dissociation of methanol and water on TiO<sub>2</sub>(110). *J. Am. Chem. Soc.*, 134(32):13366–13373, 2012.
- [122] I. Sokolović, M. Reticcioli, M. Čalkovský, M. Wagner, M. Schmid, C. Franchini, U. Diebold, and M. Setvín. Resolving the adsorption of molecular O<sub>2</sub> on the rutile TiO<sub>2</sub>(110) surface by noncontact atomic force microscopy. *Proc. Natl. Acad. Sci.*, 117(26):14827–14837, 2020.
- [123] M. A. Henderson, W. S. Epling, C. H. Peden, and C. L. Perkins. Insights into photoexcited electron scavenging processes on TiO<sub>2</sub> obtained from studies of the reaction of O<sub>2</sub> with OH groups adsorbed at electronic defects on TiO<sub>2</sub>(110). *J. Phys. Chem. B*, 107(2):534–545, 2003.



- [124] M. A. Henderson, J. Szanyi, and C. H. Peden. Conversion of  $\text{N}_2\text{O}$  to  $\text{N}_2$  on  $\text{TiO}_2(110)$ . *Catal. Today*, 85(2-4):251–266, 2003.
- [125] A. C. Papageorgiou, N. S. Beglitis, C. L. Pang, G. Teobaldi, G. Cabailh, Q. Chen, A. J. Fisher, W. A. Hofer, and G. Thornton. Electron traps and their effect on the surface chemistry of  $\text{TiO}_2(110)$ . *Proc. Natl. Acad. Sci.*, 107(6):2391–2396, 2010.
- [126] Z. Zhang, J. Lee, J. T. Yates Jr, R. Bechstein, E. Lira, J. Ø. Hansen, S. Wendt, and F. Besenbacher. Unraveling the diffusion of bulk Ti interstitials in rutile  $\text{TiO}_2(110)$  by monitoring their reaction with O adatoms. *J. Phys. Chem. C*, 114(7):3059–3062, 2010.
- [127] C. Di Valentin, G. Pacchioni, and A. Selloni. Electronic structure of defect states in hydroxylated and reduced rutile  $\text{TiO}_2(110)$  surfaces. *Phys. Rev. Lett.*, 97(16):166803, 2006.
- [128] M. Ménétrey, A. Markovits, and C. Minot. Adsorption of chlorine and oxygen atoms on clean and defective rutile- $\text{TiO}_2(110)$  and  $\text{MgO}(100)$  surfaces. *Journal of Molecular Structure: Theochem*, 808(1-3):71–79, 2007.
- [129] Q. Zhang, Y. J. Li, H. F. Wen, Y. Adachi, M. Miyazaki, Y. Sugawara, R. Xu, Z. H. Cheng, J. Brndiar, L. Kantorovich, et al. Measurement and manipulation of the charge state of an adsorbed oxygen adatom on the rutile  $\text{TiO}_2(110)-1 \times 1$  surface by nc-AFM and KPFM. *J. Am. Chem. Soc.*, 140(46):15668–15674, 2018.
- [130] C. M. Yim, J. Chen, Y. Zhang, B.-J. Shaw, C. L. Pang, D. C. Grinter, H. Bluhm, M. Salmeron, C. A. Muryn, A. Michaelides, et al. Visualization of water-induced surface segregation of polarons on rutile  $\text{TiO}_2(110)$ . *J. Phys. Chem. Lett.*, 9(17):4865–4871, 2018.
- [131] M. Reticcioni, I. Sokolović, M. Schmid, U. Diebold, M. Setvin, and C. Franchini. Interplay between adsorbates and polarons: CO on rutile  $\text{TiO}_2(110)$ . *Phys. Rev. Lett.*, 122(1):016805, 2019.
- [132] S. Dong, J. Hu, S. Xia, B. Wang, Z. Wang, T. Wang, W. Chen, Z. Ren, H. Fan, D. Dai, et al. Origin of the adsorption-state-dependent photoactivity of methanol on  $\text{TiO}_2(110)$ . *ACS Catal.*, 11(5):2620–2630, 2021.
- [133] P. M. Kowalski, M. F. Camellone, N. N. Nair, B. Meyer, and D. Marx. Charge localization dynamics induced by oxygen vacancies on the  $\text{TiO}_2(110)$  surface. *Phys. Rev. Lett.*, 105(14):146405, 2010.
- [134] T. Shibuya, K. Yasuoka, S. Mirbt, and B. Sanyal. Bipolaron formation induced by oxygen vacancy at rutile  $\text{TiO}_2(110)$  surfaces. *J. Phys. Chem. C*, 118(18):9429–9435, 2014.
- [135] P. Moses, A. Janotti, C. Franchini, G. Kresse, and C. Van de Walle. Donor defects and small polarons on the  $\text{TiO}_2(110)$  surface. *J. Appl. Phys.*, 119(18):181503, 2016.

## BIBLIOGRAPHY

- [136] Y. Cao, M. Yu, S. Qi, S. Huang, T. Wang, M. Xu, S. Hu, and S. Yan. Scenarios of polaron-involved molecular adsorption on reduced  $\text{TiO}_2(110)$  surfaces. *Sci. Rep.*, 7(1):1–7, 2017.
- [137] T. Shibuya, K. Yasuoka, S. Mirbt, and B. Sanyal. Subsurface polaron concentration as a factor in the chemistry of reduced  $\text{TiO}_2(110)$  surfaces. *J. Phys. Chem. C*, 121(21):11325–11334, 2017.
- [138] T. Kawai and T. Sakata. Photocatalytic hydrogen production from liquid methanol and water. *Chem. Commun.*, (15):694–695, 1980.
- [139] S. Sato and J. M. White. Photodecomposition of water over Pt/ $\text{TiO}_2$  catalysts. *Chem. Phys. Lett.*, 72(1):83–86, 1980.
- [140] C. Xu, W. Yang, Q. Guo, D. Dai, M. Chen, and X. Yang. Molecular hydrogen formation from photocatalysis of methanol on  $\text{TiO}_2(110)$ . *J. Am. Chem. Soc.*, 135(28):10206–10209, 2013.
- [141] C. A. Walenta, S. L. Kollmannsberger, C. Courtois, R. N. Pereira, M. Stutzmann, M. Tschurl, and U. Heiz. Why co-catalyst-loaded rutile facilitates photocatalytic hydrogen evolution. *Phys. Chem. Chem. Phys.*, 21(3):1491–1496, 2019.
- [142] T. Ohno, S. Izumi, K. Fujihara, Y. Masaki, and M. Matsumura. Vanishing of current-doubling effect in photooxidation of 2-propanol on  $\text{TiO}_2$  in solutions containing Fe(III) ions. *J. Phys. Chem. B*, 104(29):6801–6803, 2000.
- [143] Q. Hao, Zhiqiang Wang, T. Wang, Z. Ren, C. Zhou, and X. Yang. Role of Pt loading in the photocatalytic chemistry of methanol on rutile  $\text{TiO}_2(110)$ . *ACS Catal.*, 9(1):286–294, 2018.
- [144] K. Katsiev, G. Harrison, Y. Al-Salik, G. Thornton, and H. Idriss. Gold cluster coverage effect on  $\text{H}_2$  production over rutile  $\text{TiO}_2(110)$ . *ACS Catal.*, 9(9):8294–8305, 2019.
- [145] F. Li, X. Chen, Q. Guo, and X. Yang. Hydrogen production via methanol photocatalysis on Au/rutile  $\text{TiO}_2(110)$ . *J. Phys. Chem. C*, 124(49):26965–26972, 2020.
- [146] U. Heiz, F. Vanolli, L. Trento, and W.-D. Schneider. Chemical reactivity of size-selected supported clusters: An experimental setup. *Rev. Sci. Inst.*, 68(5):1986–1994, 1997.
- [147] V. N. Popok, I. Barke, E. E. Campbell, and K.-H. Meiwes-Broer. Cluster–surface interaction: From soft landing to implantation. *Surf. Sci. Rep.*, 66(10):347–377, 2011.
- [148] T. Masubuchi, J. F. Eckhard, K. Lange, B. Visser, M. Tschurl, and U. Heiz. An efficient laser vaporization source for chemically modified metal clusters characterized by thermodynamics and kinetics. *Rev. Sci. Inst.*, 89(2):023104, 2018.

- [149] V. Smentkowski and J. Yates Jr. Universal calibration of W5% Re vs W26% Re (type-C) thermocouples in the temperature range 32–2588 K. *J. Vac. Sci. Technol. A*, 14(1):260–265, 1996.
- [150] M. Bozack, L. Muehlhoff, J. Russell Jr., W. Choyke, and J. Yates Jr. Methods in semiconductor surface chemistry. *J. Vac. Sci. Technol. A*, 5(1):1–8, 1987.
- [151] J. T. Yates Jr. Photochemistry on TiO<sub>2</sub>: Mechanisms behind the surface chemistry. *Surf. Sci.*, 603(10-12):1605–1612, 2009.
- [152] C. A. Walenta, M. Tschurl, and U. Heiz. Introducing catalysis in photocatalysis: what can be understood from surface science studies of alcohol photoreforming on tio<sub>2</sub>. *J. Phys.: Condens. Matter*, 31(47):473002, 2019.
- [153] Z.-T. Wang, M. A. Henderson, and I. Lyubinetsky. Origin of coverage dependence in photoreactivity of carboxylate on TiO<sub>2</sub>(110): hindering by charged coadsorbed hydroxyls. *ACS Catal.*, 5(11):6463–6467, 2015.
- [154] R. Zhang, H. Wang, X. Peng, R.-r. Feng, A.-a. Liu, Q. Guo, C. Zhou, Z. Ma, X. Yang, Y. Jiang, et al. In situ studies on temperature-dependent photocatalytic reactions of methanol on TiO<sub>2</sub>(110). *J. Phys. Chem. C*, 123(15):9993–9999, 2019.
- [155] B. Koel, D. Peebles, and J. White. Low temperature coadsorption of hydrogen and carbon monoxide on Ni(100): I. TPD,  $\Delta$ , and UPS studies. *Surf. Sci.*, 125(3):709–738, 1983.
- [156] B. E. Koel, D. Peebles, and J. White. Low temperature coadsorption of hydrogen and carbon monoxide on Ni(100): II. ELS and XPS studies. *Surf. Sci.*, 125(3):739–761, 1983.
- [157] I. Chorkendorff, J. Russell Jr, and J. Yates Jr. Hydrogen implantation in Ni(111) — A study of H<sub>2</sub> desorption dynamics from the bulk. *Surf. Sci.*, 182(3):375–389, 1987.
- [158] J. Yates, J. Russell, I. Chorkendorff, and S. Gates. Isotopic effects in the adsorption and desorption of hydrogen by Ni(111). In *Kinetics of Interface Reactions*, pages 71–88. Springer, 1987.
- [159] A. Kudo, K. Domen, K.-i. Maruya, and T. Onishi. Photocatalytic activities of TiO<sub>2</sub> loaded with NiO. *Chem. Phys. Lett.*, 133(6):517–519, 1987.
- [160] J. Yu, Y. Hai, and B. Cheng. Enhanced photocatalytic H<sub>2</sub>-production activity of TiO<sub>2</sub> by Ni(OH)<sub>2</sub> cluster modification. *J. Phys. Chem. C*, 115(11):4953–4958, 2011.
- [161] W.-T. Chen, A. Chan, D. Sun-Waterhouse, T. Moriga, H. Idriss, and G. I. Waterhouse. Ni/TiO<sub>2</sub>: A promising low-cost photocatalytic system for solar H<sub>2</sub> production from ethanol–water mixtures. *J. Catal.*, 326:43–53, 2015.

## BIBLIOGRAPHY

- [162] H. Bahruji, M. Bowker, P. R. Davies, J. Kennedy, and D. J. Morgan. The importance of metal reducibility for the photo-reforming of methanol on transition metal-TiO<sub>2</sub> photocatalysts and the use of non-precious metals. *Int. J. Hydrogen Energy*, 40(3):1465–1471, 2015.
- [163] F. Pesty, H.-P. Steinrück, and T. E. Madey. Thermal stability of Pt films on TiO<sub>2</sub>(110): evidence for encapsulation. *Surf. Sci.*, 339(1-2):83–95, 1995.
- [164] O. Dulub, W. Hebenstreit, and U. Diebold. Imaging cluster surfaces with atomic resolution: the strong metal-support interaction state of Pt supported on TiO<sub>2</sub>(110). *Phys. Rev. Lett.*, 84(16):3646, 2000.
- [165] S. Bonanni, K. Ait-Mansour, H. Brune, and W. Harbich. Overcoming the strong metal-support interaction state: CO oxidation on TiO<sub>2</sub>(110)-supported Pt nanoclusters. *ACS Catal.*, 1(4):385–389, 2011.
- [166] J. C. Colmenares, A. Magdziarz, M. A. Aramendia, A. Marinas, J. M. Marinas, F. J. Urbano, and J. A. Navio. Influence of the strong metal support interaction effect (SMSI) of Pt/TiO<sub>2</sub>(110) and Pd/TiO<sub>2</sub>(110) systems in the photocatalytic biohydrogen production from glucose solution. *Cat. Commun.*, 16(1):1–6, 2011.
- [167] A. Naldoni, F. Riboni, M. Marelli, F. Bossola, G. Ulisse, A. Di Carlo, I. Píš, S. Nappini, M. Malvestuto, M. V. Dozzi, et al. Influence of TiO<sub>2</sub> electronic structure and strong metal-support interaction on plasmonic Au photocatalytic oxidations. *Catalysis Science & Technology*, 6(9):3220–3229, 2016.
- [168] E. V. Benvenutti, L. Franken, C. C. Moro, and C. U. Davanzo. FTIR study of hydrogen and carbon monoxide adsorption on Pt/TiO<sub>2</sub>, Pt/ZrO<sub>2</sub>, and Pt/Al<sub>2</sub>O<sub>3</sub>. *Langmuir*, 15(23):8140–8146, 1999.
- [169] T. Chen, Z. Feng, G. Wu, J. Shi, G. Ma, P. Ying, and C. Li. Mechanistic studies of photocatalytic reaction of methanol for hydrogen production on Pt/TiO<sub>2</sub> by in situ Fourier transform IR and time-resolved IR spectroscopy. *The Journal of Physical Chemistry C*, 111(22):8005–8014, 2007.
- [170] O. Leiko, Y. Kosto, and K. Mašek. Structural and photoelectron studies of Sn-SnO<sub>x</sub> and SnO<sub>2</sub> nanoparticles on TiO<sub>2</sub>(110) surface. *Surf. Interface Anal.*, 50(11):1116–1121, 2018.
- [171] M. M. Ahmed, R. H. Temperton, and J. N. O’Shea. An in situ exploration of subsurface defect migration to a liquid water-exposed rutile TiO<sub>2</sub>(110) surface by XPS. *Surf. Interface Anal.*, 2020.
- [172] C. Byrne, K. M. Zahra, S. Dhaliwal, D. C. Grinter, K. Roy, W. Q. Garzon, G. Held, G. Thornton, and A. S. Walton. A combined laboratory and synchrotron in-situ photoemission study of the rutile TiO<sub>2</sub>(110)/water interface. *J. Phys. D: Appl. Phys.*, 54(19):194001, 2021.

- [173] M. Ni, M. K. Leung, D. Y. Leung, and K. Sumathy. A review and recent developments in photocatalytic water-splitting using  $\text{TiO}_2$  for hydrogen production. *Renewable Sustainable Energy Rev.*, 11(3):401–425, 2007.
- [174] S. Chen, T. Takata, and K. Domen. Particulate photocatalysts for overall water splitting. *Nat. Rev. Mater.*, 2(10):1–17, 2017.
- [175] A. Miyoshi, S. Nishioka, and K. Maeda. Water splitting on rutile  $\text{TiO}_2$ -based photocatalysts. *Chem. Eur. J.*, 24(69):18204–18219, 2018.
- [176] Y. Li and S. Tsang. Recent progress and strategies for enhancing photocatalytic water splitting. *Mater. Today Sustainability*, 9:100032, 2020.
- [177] K. E. Sanwald, T. F. Berto, A. Jentys, D. M. Camaioni, O. Y. Gutiérrez, and J. A. Lercher. Kinetic coupling of water splitting and photoreforming on  $\text{SrTiO}_3$ -based photocatalysts. *ACS Catal.*, 8(4):2902–2913, 2018.
- [178] T. Hisatomi and K. Domen. Reaction systems for solar hydrogen production via water splitting with particulate semiconductor photocatalysts. *Nat. Catal.*, 2(5):387–399, 2019.
- [179] Y. Fan, Y. Liu, H. Cui, W. Wang, Q. Shang, X. Shi, G. Cui, and B. Tang. Photocatalytic overall water splitting by  $\text{SrTiO}_3$  with surface oxygen vacancies. *Nanomaterials*, 10(12):2572, 2020.



## **A Further Publications**

# Surface Species in Photocatalytic Methanol Reforming on Pt/TiO<sub>2</sub>(110): Learning from Surface Science Experiments for Catalytically Relevant Conditions

Constantin A. Walenta, Carla Courtois, Sebastian L. Kollmannsberger, Moritz Eder, Martin Tschurl, and Ueli Heiz\*

Cite This: *ACS Catal.* 2020, 10, 4080–4091

Read Online

ACCESS |

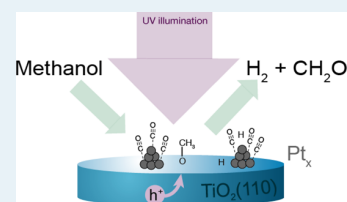
Metrics & More

Article Recommendations

Supporting Information

**ABSTRACT:** Photocatalytic hydrogen evolution from methanol is a standard test reaction for photocatalyst materials. Surprisingly, the exact chemical mechanism is still widely discussed in the literature. In order to disentangle photochemical from thermal reaction steps and gain insights on the atomic level, we use a Pt cluster-loaded TiO<sub>2</sub>(110) photocatalyst in very well-defined environments. Using Auger electron spectroscopy, temperature-programmed desorption/reaction, isotopic labeling, and isothermal photoreactions, it is possible to identify the surface species present on the catalyst under photocatalytic conditions. Furthermore, an initial conditioning of the photocatalyst is observed and attributed to thermal dehydrogenation of methanol to CO species on the cluster. The analysis of the isothermal photoreactions reveals that the photo-oxidation kinetics are not significantly affected by cocatalyst loading. The observed conversion and product distribution of formaldehyde and methyl formate can be rationalized with kinetic parameters gained from the bare TiO<sub>2</sub>(110) crystal. The work leads to a detailed mechanistic understanding of the surface species and paves the way for an educated microkinetic modeling approach, which may be extended to a variety of noble metal cocatalysts and other TiO<sub>2</sub> modifications.

**KEYWORDS:** surface species, photocatalytic conditions, Pt cluster loaded TiO<sub>2</sub>(110)



## INTRODUCTION

Driving catalytic reactions with light has been envisioned for a long time to replace fossil feedstock for hydrogen production,<sup>1</sup> upgrade biomass to chemical feedstock,<sup>2</sup> or decompose waste in an environmentally benign way.<sup>3</sup> In this regard, understanding the key factors limiting the photocatalytic hydrogen evolution and fathoming the selectivity of the corresponding reactions still remain a great scientific challenge, especially because the concomitant oxidation products may influence the hydrogen evolution reaction.<sup>4</sup> This effect has been observed for the photo-electrocatalytic reforming of alcohol already decades ago<sup>5,6</sup> and is commonly known as “current doubling”.<sup>4,7</sup> Thus, a key role for the design of better photocatalysts will be the understanding of the underlying reaction mechanisms and identification of the kinetics of photochemical and thermal reactions. In this regard, the judicious choice of particular reaction conditions (e.g., the temperature and reaction environment) may allow for the disentanglement of the elemental processes on the catalyst surface.

Methanol has been used frequently as a hole scavenger in order to investigate the photocatalytic hydrogen evolution of new catalyst materials.<sup>2,4,8,9</sup> This approach is fostered by the hope to improve the partial reaction of hydrogen evolution separately from the (far more complex) oxidation of water. It is, however, based on the (controversial) assumption that some

of the elementary steps are the same or similar to photocatalytic water splitting.<sup>4,10,11</sup> For widely employed titania-based catalysts, the presence of a cocatalyst on the surface has been found to be inevitable for significant photocatalytic hydrogen evolution under ideal and real conditions.<sup>12</sup> The elucidation of the cocatalysts' properties and their exact role in the photoreaction thus represent important goals in the understanding of photocatalysis in general and for the photocatalytic hydrogen evolution in particular.

Zaera and co-workers deconstructed the mechanism of the photocatalytic hydrogen evolution reaction from a methanol/water mixture and found that the role of the cocatalyst is the promotion of the dimerization of surface hydrogen atoms rather than to act as charge traps.<sup>13–15</sup> Additionally, they showed that a thermodynamic approach, only taking conduction and valence band edges into account, is not sufficient to understand hydrogen evolution from NiO<sub>x</sub> cocatalysts supported on TiO<sub>2</sub>.<sup>16</sup> Further evidence for the

Received: January 16, 2020

Revised: March 3, 2020

Published: March 4, 2020



thermal hydrogen recombination on the cocatalyst has been presented using H/D-exchange experiments on the photocatalyst material without illumination.<sup>16</sup> Nevertheless, similar systems are still often interpreted in a different way, and to obtain stronger evidence for such a reaction mechanism, the study of more defined systems has proven to be advantageous. In this regard, platinum cocatalyst-loaded TiO<sub>2</sub>(110) synthesized under ultrahigh vacuum conditions represents a very well-defined model system to probe photocatalytic reactions. Because rutile TiO<sub>2</sub>(110) is one of the best understood materials under very well-defined conditions,<sup>17,18</sup> the surface physics of the semiconductor and thermal chemistry are very well-known.<sup>17–20</sup> We recently reported the hydrogen evolution from photocatalytic alcohol reforming to occur catalytically under ultrahigh vacuum conditions on Pt<sub>x</sub>/TiO<sub>2</sub>.<sup>21,22</sup> Similar to the studies of Zaera and co-workers,<sup>16</sup> molecular hydrogen is evolved by thermal recombination of surface hydroxyls, but in contrast to those studies, we ruled out the reduction of protons by photoelectrons.<sup>22</sup>

In this study, we further deconstruct the photoreforming of methanol in “snapshots” of the catalytic cycle in order to determine the surface species present under catalytic conditions and their stability. For this purpose, we use Pt-loaded rutile titania (110) because of the advantages of the system mentioned above. We apply Auger electron spectroscopy, temperature-programmed desorption/reaction (TPD/R), isotopic labeling, isothermal photoreactions, and a kinetic analysis to unravel the surface species, their stability, and the driving force for the observed selectivity under photocatalytic conditions. Although only recently photochemical studies have emerged for cocatalyst-loaded rutile TiO<sub>2</sub>(110),<sup>23,24</sup> the present work explicitly addresses the characteristics of the cocatalyst under (photo)catalytic conditions and the resulting material's properties in photocatalysis (i.e., the selectivity and stability).

## EXPERIMENTAL SECTION

**Materials and Methods.** All experiments were carried out under ultrahigh vacuum conditions with a backpressure of <1 × 10<sup>-10</sup> mbar in a home-built setup for studying photocatalytic reactions.<sup>21,25</sup> An overview of the apparatus is shown elsewhere.<sup>21</sup> Briefly, it consists of surface preparation methods, including a sputter gun (SPECS IQE 11/35) and a molecular beam doser,<sup>26</sup> and surface analysis was performed with Auger electron spectroscopy (CMA 100, Omicron Nanotechnology GmbH). It is further equipped with a quadrupole mass spectrometer (QMS, QMA 430, Pfeiffer Vacuum GmbH) and a home-built time-of-flight mass spectrometer<sup>27</sup> for the analysis of reaction products. A load lock enables the transfer of samples and a laser ablation cluster source<sup>28</sup> creates metal clusters from 1 up to 100 atoms, which can be mass-selected and subsequently landed on various support materials.

Methanol (Chromasolv, ≥99.9%, Sigma-Aldrich), ethanol (absolute, HPLC grade, ≥99.8%, Sigma-Aldrich), and H<sub>2</sub>O (Milli-Q, 18.2 MΩ·cm) were extensively degassed and further purified by pump–freeze cycles. D<sub>2</sub> (99% purity, Westfalen, Germany), O<sub>2</sub> (5.0, Westfalen), and CO (4.7, Air Liquide) were used without further purification. All adsorptions were carried out at 100 K sample temperature, unless otherwise indicated. A Pt target (99.95% purity, ESG Edelmetalle, Germany) was used for the generation of the Pt<sub>x</sub> clusters and no contaminants in the clusters were found in the mass spectra before each deposition.

The reactivity measurements were carried out with an electron ionization QMS. The molecules were identified by their respective fragmentation patterns. Quantification with the fragmentation pattern correction, QMS sensitivity, and ionization cross section has been established in previous studies.<sup>21,29</sup> TPD experiments were carried out with a heating rate of 1.2 K/s from 100 K to the indicated temperature. Isothermal photoreaction experiments were performed at chosen temperatures of the photocatalyst, in which illumination was only started after the thermalization of the sample. As a source for this illumination, a laser with a wavelength of 242 nm was used with an intensity of 4.6 mW/cm<sup>2</sup>. As we previously showed, the photoreactivity is independent on the used wavelength (355 or 369 nm was also tested), as long as the photon energy is above the band gap of rutile TiO<sub>2</sub> (3.0 eV).<sup>22</sup> The time resolution in the photoreaction experiments is limited by the detection time of the QMS and the number of mass traces followed in the experiment. Typically, time resolutions of a couple hundred milliseconds are achieved in the experiments presented, as multiple reaction products are recorded at the same time.

**Catalyst Preparation and Characterization.** The rutile TiO<sub>2</sub>(110) single crystal (SurfaceNet GmbH) was cleaned by cycles of sputtering (Ar, 1.0 keV, 1 × 10<sup>-5</sup> mbar, 20 min), oxygen annealing (820 K, 1 × 10<sup>-6</sup> mbar), and annealing in vacuum (820 K), which is known to result in a flat and clean surface as determined by Auger electron spectroscopy (Figure S1) and H<sub>2</sub>O TPD.<sup>30,31</sup> The concentration of bridge-bonded oxygen (BBO) vacancies was determined to be 6 ± 1% with respect to Ti-lattice sites (5.2 × 10<sup>14</sup>/cm<sup>2</sup>) based on the evaluation of H<sub>2</sub>O TPDs.<sup>22,31</sup>

The deposition of the Pt<sub>x</sub> (*x* = 8–32) clusters was facilitated by the operation of the quadrupole in the ion-guide mode, followed by the soft landing of the clusters on the TiO<sub>2</sub>(110) single crystal at 110 K, as described in an earlier study.<sup>22</sup> The catalyst loading is controlled using a picoammeter (Keithley 6587) measuring the neutralization current of the cationic clusters when being deposited on the surface. The total loading is controlled using home-written software, integrating over the current leading to a highly precise cluster coverage determination.<sup>32</sup>

Unless specified differently, the Pt cluster coverage investigated in this work was chosen to be 1% of a monolayer. This value corresponds to a Pt cluster coverage of 1.5 × 10<sup>13</sup> e/cm<sup>2</sup> or 0.15 e/nm<sup>2</sup> for the deposition of singly charged clusters and assumes that every surface site (1.5 × 10<sup>15</sup>/cm<sup>2</sup>) of the single crystal represents an adsorption site. The size distribution was decided to be the same as in our previous studies.<sup>21,22</sup> Furthermore, previous work with scanning probe microscopy<sup>33–37</sup> and X-ray photoelectron spectroscopy<sup>36,37</sup> demonstrated that the clusters are randomly distributed on the surface and do not bind to any specific defect site at room temperature and below. The successful deposition of the platinum cocatalyst is also observed in the Auger electron spectrum at 64 eV (see Figure S1). The complete removal of the Pt clusters from the surface requires an excessive cleaning procedure with multiple sputter–annealing cycles because Pt is very persistent on the surface because of strong metal support interaction.<sup>38,39</sup> The detection of molecular hydrogen from a water TPD proved to be a highly sensitive indicator for the smallest amount of Pt contaminations of the TiO<sub>2</sub>(110) single crystal, which was also demonstrated by Geng et al.<sup>40</sup>

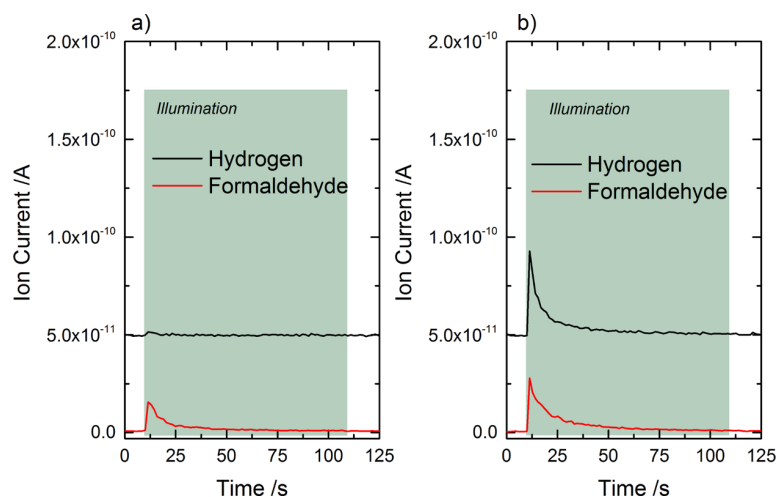


**Figure 1.** Photochemical products of 1 L of  $\text{CH}_3\text{OH}$  on  $\text{r-TiO}_2(110)$  (a) and on  $\text{Pt}_x/\text{TiO}_2(110)$  (b) at 260 K. Upon UV illumination (shown as a gray background), methoxy species are photo-oxidized to formaldehyde, which desorb thermally. In (a), only trace amounts of  $\text{H}_2$  are formed upon illumination, while the catalyst poisoning is observed in subsequent illumination cycles.<sup>22</sup> The Pt-loaded photocatalyst (b) shows formaldehyde desorption accompanied by significant production of  $\text{H}_2$  during illumination. The hydrogen trace is offset to  $5 \times 10^{-11}$  A for clarity. Note that the traces in this figure represent raw data of the masses  $m/z = 2$  for  $\text{H}_2$  and 30 for formaldehyde.

## RESULTS AND DISCUSSION

A side-by-side comparison (Figure 1) of the photochemical reactions of methanol on the same semiconductor single crystal shows almost exclusively formaldehyde production for  $\text{r-TiO}_2(110)$  (Figure 1a). In contrast,  $\text{H}_2$  evolution in addition to formaldehyde formation is observed for Pt-loaded  $\text{TiO}_2(110)$  (Figure 1b). This behavior is known from previous studies on bare  $\text{TiO}_2(110)$ <sup>41,42</sup> and on Pt-loaded  $\text{TiO}_2(110)$ .<sup>21,22</sup> Clearly, the role of the  $\text{Pt}_x$  cocatalyst is to facilitate molecular hydrogen evolution from methanol during illumination. This completes the dehydrogenation reaction of methanol, which is in fact a hole-mediated disproportionation, and makes the reaction truly catalytic.<sup>22</sup> To further investigate the surface chemistry on the Pt cocatalyst, we used isotopically labeled methanol- $d_3$  on the Pt-loaded photocatalyst and monitored the isothermal photoreaction (Figure 2). Upon the first illumination period at 260 K, desorption of formaldehyde (mass 30) and all mass traces of molecular hydrogen (mass 2, 3, and 4) are observed. All traces decay almost to the baseline within an illumination time of 2 min. Consecutive isothermal irradiation experiments on the same surface resaturated with methanol (obtained by again dosing 1 L of  $\text{CD}_3\text{OH}$  after the previous illumination) revealed that the mass trace for formaldehyde remains unchanged in all dosing illumination cycles. All hydrogen mass traces, although persistent, are less intense than those in the first illumination experiment. This observation points to conditioning of the catalyst. As neither the intensity nor the decay kinetics in the mass traces change in consecutive cycles of methanol dosage and illumination, the conditioning of the catalyst seems to be already completed after the first cycle. In the conditioned state, deuterium atoms for  $\text{D}_2$  formation exclusively originate from the photo-oxidation reaction of the alcohol.

Catalyst conditioning proceeds most likely not photochemically but by a thermal mechanism. Initially, a significant amount of hydrogen is on the surface, originating from either the dissociative adsorption of  $\text{CD}_3\text{OH}$  (i.e., hydrogen and methoxy formation) on the  $\text{TiO}_2(110)$  surface or the thermal decomposition of methanol on the  $\text{Pt}_x$  clusters. The second

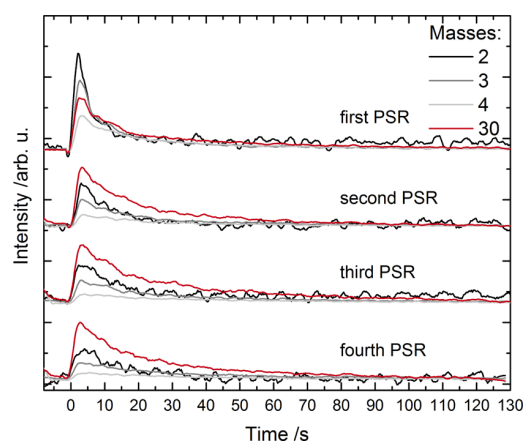


**Figure 2.** Consecutive isothermal irradiation experiments at 260 K on a  $\text{Pt}_x/\text{TiO}_2(110)$  catalyst. The reaction is started by illumination after adsorption of 1 L of  $\text{CD}_3\text{OH}$  at cryogenic temperatures. Between every photochemical experiment, the surface is recovered with 1 L of methanol- $d_3$  at the reaction temperature, which is enough to saturate the surface at 260 K. Upon illumination, formaldehyde (mass 30) and hydrogen desorb (masses 2, 3, and 4). After an initial conditioning of the catalyst, where an increased amount of hydrogen desorbs, further illumination cycles result in stable intensities and decay kinetics for all observed products. Note that the  $\text{Pt}_x$  cluster coverage in this experiment is 0.75% of a monolayer.

pathway yields carbon monoxide and hydrogen species, based on prior work on  $\text{Pt}(111)$ .<sup>43</sup> Both reactions must be considered to give rise to the hydrogen traces in Figure 2. The conditioning is largely finished after the first photochemical reaction cycle, which shows that the time needed for thermalization (in the order of some minutes) is longer than the time scale of the methanol decomposition reaction. In order to analyze the thermal chemistry on the  $\text{Pt}_x$  cocatalyst, a TPR experiment with isotopically labeled methanol  $\text{CD}_3\text{OH}$  on a  $\text{Pt}_x/\text{TiO}_2(110)$  photocatalyst was performed (Figure 3), which is in good agreement with a very recent study of Hao et al.<sup>23</sup> Methanol adsorbed on the semiconductor surface shows

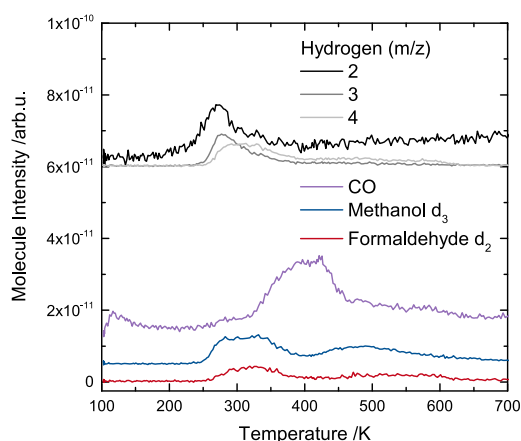


**Figure 3.** TPR experiment from 100 to 700 K on a  $\text{Pt}_x/\text{TiO}_2(110)$  photocatalyst with a  $\text{CD}_3\text{OH}$  coverage of 1 L without illumination. Upon Pt loading of the catalyst, hydrogen evolution around 250 K from methanol dehydrogenation is observed. Additionally, an intense peak of CO around 400 K is observed, which is assigned to CO desorbing from the Pt clusters.<sup>35,48</sup> The traces are offset for clarity, and the hydrogen species represent raw mass traces, while CO ( $m/z = 28$ ), methanol ( $m/z = 35$ ), and formaldehyde ( $m/z = 30$ ) are corrected for fragmentation patterns.

the well-known desorption chemistry of bare  $\text{TiO}_2(110)$ , with the alcohol leaving the surface at mainly around 300 K, as reported before.<sup>44–46</sup> Some methanol, however, is adsorbed on the Pt clusters and undergoes complete dehydrogenation to CO, similar as in the reaction on a  $\text{Pt}(111)$  single crystal.<sup>43,47</sup> In contrast, the TPD of the bare titania surface neither shows a high-temperature CO peak nor thermal hydrogen evolution during methanol desorption. Interestingly, only one broad desorption feature of molecular hydrogen is obtained between 220 and 350 K, while Hao et al. observed an additional feature around 550 K.<sup>23</sup> This difference may originate from different preparation techniques of the Pt cocatalysts, yielding clusters in a different size distribution and of potentially different morphologies, both of which affect their local chemical environment. Based on a careful analysis of all fragmentation

patterns, we rule out the formation of significant amounts of any other products from methanol chemistry such as methyl formate (Figure S2).

The TPR results present evidence that the active hydrogen recombination cocatalysts in the photocatalytic reaction are apparently not the bare Pt clusters. On the conditioned catalyst, the clusters are rather covered by carbon monoxide, which stems from methanol dehydrogenation.

The thermal evolution of molecular hydrogen from methanol, which is not observed on bare  $\text{TiO}_2(110)$ ,<sup>22,45</sup> occurs at around 250 K (Figure 3) in agreement with  $\text{H}_2$  desorption from Pt clusters on other oxide supports (e.g.,  $\text{SiO}_2$ )<sup>49</sup> and the  $\text{D}_2$  desorption from  $\text{Pt}_x/\text{TiO}_2(110)$  (see Figure S3). This indicates that the dehydrogenation chemistry takes place around or below 250 K because the peak temperature also matches the hydrogen desorption feature upon  $\text{D}_2$  adsorption (see Fig. S3). The same desorption temperature is observed for the thermal hydrogen evolution from surface hydroxyl recombination resulting from water adsorption on  $\text{Pt}_x/\text{TiO}_2(110)$  (Figure S3).<sup>40</sup> As mentioned before, molecular water dosed onto the  $\text{Pt}_x/\text{TiO}_2(110)$  surface dissociates in BBO vacancies on the surface and, consequently, two surface hydroxyls are formed.<sup>31</sup> These hydrogen atoms, bound to BBO atoms on the  $\text{TiO}_2(110)$  surface, are able to diffuse<sup>50</sup> and eventually recombine at the Pt clusters, while the oxygen “heals” the surface defects (see also Figure S4). Other than for bare  $\text{TiO}_2(110)$ , water desorption originating from hydroxyl recombination around 450 K is not observed when the cocatalyst is present on the surface (Figure S4).

In order to observe photochemical evolution of molecular hydrogen formed on the Pt cocatalyst, an isothermal photoreaction experiment is carried out at 250 K. It is followed by a TPD run immediately after the illumination to identify the surface species present on the photocatalyst (Figure 4). Upon illumination, all possible isotopomers of molecular hydrogen are observed (Figure 4a) accompanied by formaldehyde desorption. No significant desorption of carbon monoxide, water, or methanol is detected upon illumination. The immediate increase also in the  $\text{D}_2$  signal (mass 4) is indicative for the diffusion of surface hydroxyls and the H atom recombination being fast processes, which is in agreement with

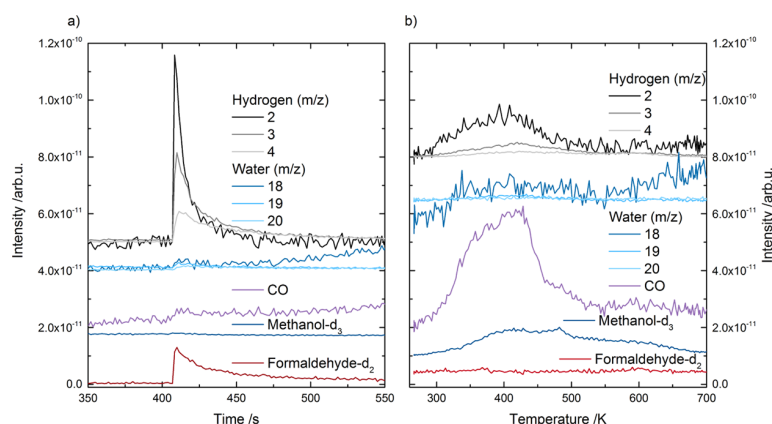


**Figure 4.** (a) Photon-stimulated reaction of 1 L of methanol ( $\text{CD}_3\text{OH}$ ) on a  $\text{Pt}_x/\text{TiO}_2(110)$  catalyst at 250 K. Upon illumination, formaldehyde and hydrogen, which are products from methanol photoreforming, are observed. The traces are offset for clarity. (b) TPR after the isothermal photoreaction (in a) from 250 to 700 K. The traces are again offset for clarity. Mostly, CO is desorbing as a result from thermal methanol dehydrogenation. All the products desorbing are in excellent agreement with the thermal chemistry reported in Figure 3. The photochemical reaction temperature was chosen to be below the onset of methanol desorption.

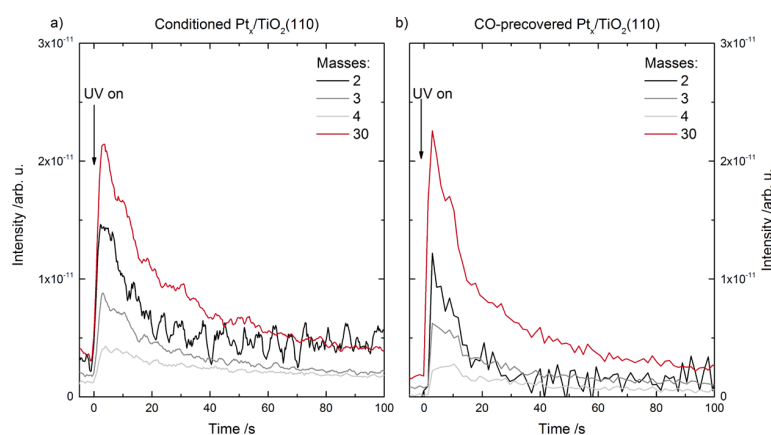


**Figure 5.** Comparison between isothermal photoreaction experiments at 262 K showing that a conditioned  $\text{Pt}_x/\text{TiO}_2$  photocatalyst and an artificially CO-saturated  $\text{Pt}_x/\text{TiO}_2$  lead to very similar desorption characteristics for methanol photocatalysis. (a) Photoreaction of the third cycle (Figure 2) with the photocatalyst prepared without any treatment of the catalyst before the photo-experiments. In (b), the  $\text{Pt}_x/\text{TiO}_2(110)$  catalyst is exposed to 10 L of CO at 110 K and then annealed to 155 K. At this temperature, physisorbed CO on  $\text{TiO}_2(110)$  either desorbs<sup>53</sup> or diffuses to the  $\text{Pt}_x$  clusters, where it chemisorbs and remains strongly bound.<sup>54</sup> Subsequently, 1 L of  $\text{CD}_3\text{OH}$  is dosed onto the surface at 120 K after which the catalyst is set to 262 K, where the photoreaction is carried out. The initial temperature for both experiments was chosen again to ensure the best comparability of the measurements with the different pretreatments of the catalyst. Although the Pt clusters are saturated with carbon monoxide, molecular hydrogen evolution is observed, and the intensities are similar to those on the conditioned catalyst (Molecular hydrogen is indicated by the mass traces 2, 3, and 4, while the  $\text{CDO}^+$  fragment of formaldehyde is identified by  $m/z = 30$ ).

the literature.<sup>51</sup> A TPR measurement of the catalyst after the isothermal photoreaction shows (Figure 4b) that all of the formed formaldehyde is already thermally desorbed and that the majority of the methanol molecules were either photo-oxidized or dehydrogenated on the Pt cluster. The latter pathway is supported by the desorption of CO observed around 400 K.

To gain further insights into the hydrogen evolution and the conditioning of the Pt cocatalyst, we artificially exposed clean  $\text{Pt}_x/\text{TiO}_2(110)$  to a saturation coverage of CO directly after cluster deposition, dosed methanol- $d_3$ , and carried out an isothermal illumination experiment at 262 K (Figure 5). Formaldehyde and all hydrogen species were found to desorb upon illumination, indicating that even a carbon monoxide-saturated platinum cocatalyst is active for molecular hydrogen evolution. The observed intensities and isotope distributions (Figure 5) of the molecular hydrogen evolution are in excellent agreement with the isothermal photoreactions from the conditioned catalyst, as shown in Figure 2. This behavior is similar as in a previous study by Berto et al., in which photocatalytic hydrogen evolution from water was observed from CO-covered noble metal nanoparticles on a nitride-based semiconductor.<sup>52</sup> This result further infers that CO from methanol dehydrogenation is most likely adsorbed onto the Pt cocatalyst during the photoreaction and represents a spectator species on the metal clusters for the photocatalytic hydrogen evolution on a conditioned catalyst.

Although Pt loading clearly changes the reactivity of the semiconductor by enabling hydrogen evolution, it may be suspected that the cocatalyst also affects the photo-oxidation reaction of methanol. To evaluate this potential influence of the clusters in the photo-oxidation mechanism, the formaldehyde traces of the bare and the metal-covered surface are compared in the following. The  $\text{CH}_2\text{O}$  peak exhibits a lower intensity and a smaller integral value on the bare semiconductor with respect to the Pt-decorated one (see Figure 1). The well-known poisoning of the photoreaction of methanol (see Figure 1a) on bare  $\text{TiO}_2(110)$ ,<sup>22,55</sup> which was first

reported for ethanol,<sup>56</sup> makes a kinetic analysis of the peak height gratuitous because it does not represent the amount of active sites directly. It is influenced by the deactivation mechanism (i.e., the hydroxylation of the surface) from the photoreaction on the bare catalyst and the decrease in the coverage of methanol by the initial photoconversion. A complete quantitative microkinetic description is therefore not feasible, as shown by Phillips et al. previously.<sup>42</sup>

On the other hand, both photoreaction products can desorb from  $\text{Pt}_x/\text{TiO}_2(110)$  at the reaction temperature (Figure 1b), leading to a higher observed conversion for formaldehyde. To dissect kinetic information, a qualitative comparison of the rate constants can be performed. The overall photoreforming of methanol can be written in the following kinetic description

$$r = -\frac{d[\text{methanol}]_t}{dt} = \frac{d[\text{formaldehyde}]_t}{dt} = k \times [h\nu] \times [\text{methanol}]_t \quad (1)$$

This expression includes that only the charges created from one photon are needed to oxidize methanol to formaldehyde because the dissociative adsorption of methanol is a thermal process on the semiconductor surface.<sup>41</sup> This is in perfect agreement with our postulated mechanism from catalytic experiments<sup>21,22</sup> and all the current doubling observations in the literature for alcohol photochemistry on titania.<sup>5–7</sup>

Under constant illumination, one can simplify eq 1 further by employing  $k' = k \times [h\nu]$ . Following the reaction mechanism,<sup>21,41,42,57,58</sup> the decay of the product can be assumed in the first approximation to be of first order with the methanol concentration, yielding the typical exponential decay function

$$[\text{methanol}]_t = [\text{methanol}]_0 \times \exp(-k't) \quad (2)$$

with  $[\text{methanol}]_0$  being the initial methanol concentration in photo-active sites.

As



$$[\text{formaldehyde}]_t = [\text{methanol}]_0 - [\text{methanol}]_t \quad (3)$$

this results in the following expression for the integral product yield

$$[\text{formaldehyde}]_t = [\text{methanol}]_0 \times (1 - \exp(-k't)) \quad (4)$$

and its differential form, which represents the signal in the desorption measurements, being

$$\frac{d[\text{formaldehyde}]_t}{dt} = [\text{methanol}]_0 \times k' \times \exp(-k't) \quad (5)$$

Therefore, it is evident that the rate constants ( $k'$  and  $k$  for constant photon fluxes) are reflected in the respective exponential decays, which are very similar for the bare and the cocatalyst-loaded semiconductor (Figure 6).

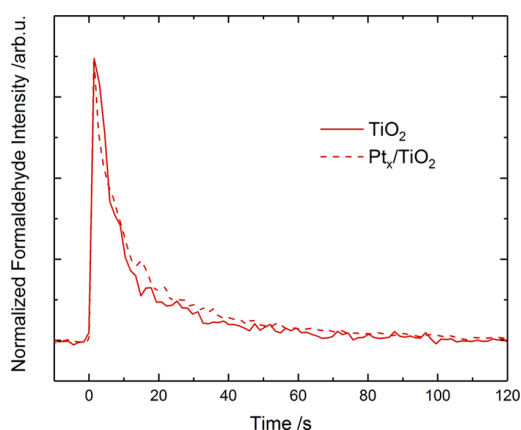


**Figure 6.** Isothermal illumination experiments at 260 K of the  $\text{TiO}_2(110)$  surface and the  $\text{Pt}_x/\text{TiO}_2(110)$  catalyst of 1 L of methanol with normalized intensities to compare the decays. It can be seen that a loading with Pt cocatalysts does not change the exponential decay significantly within the accuracy of the measurements. Illumination is initiated at the time of 0 s.

Because the formaldehyde desorption is a thermal process, it is crucial to keep the sample at the exact temperature of 260 K (with an estimated error of  $\pm 0.5$  K) to avoid temperature-related effects in the exponential decay. This is in particular of importance as the reaction is quite complex with at least the desorption and photoreaction being important reaction steps (more details are given in Phillips et al. in the Supporting Information).<sup>42</sup> The complexity is also reflected in the decay of the formaldehyde signal, which deviates from the simple first-order behavior assumed above. Consequently, the detected decline becomes multi-exponential and the rate constant cannot be directly obtained. Nevertheless, the similarity of the formaldehyde decays of the bare and Pt-loaded titania crystal indicates that the photo-oxidation of methoxy species is the rate-determining step in methanol photocatalysis and that the thermal H-atom recombination is a consecutive thermal reaction, as known from previous studies.<sup>21,22</sup>

Although the Pt cocatalyst is generally known to promote the hydrogen evolution reaction, the qualitative analysis of the apparent kinetics reveals that the photo-oxidation reaction stays largely unaltered. Consequently, at least at this coverage of 1%  $\text{Pt}_x$  on  $\text{TiO}_2(110)$ , an electronic effect induced by the cocatalyst (e.g., the controversial charge accumulation in the metal particles<sup>14,16,24,59,60</sup>) on the photo-oxidation reaction is not observed to play an important role.

The photoreaction of methanol to formaldehyde and molecular  $\text{H}_2$  can be rationalized in a scheme corroborating knowledge from semiconductor physics (Figure 7). Upon

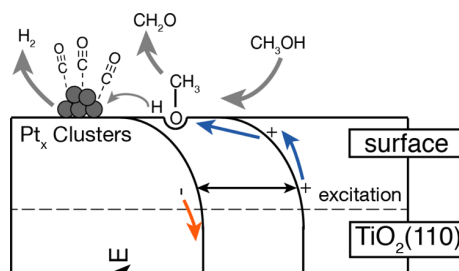


**Figure 7.** Photochemical mechanism upon illumination of the methanol-covered  $\text{Pt}_x/\text{TiO}_2(110)$  catalyst proceeds via a direct hole transfer to the methoxy species on the surface to form formaldehyde and consecutive thermal hydrogen evolution. The cocatalyst for the hydrogen evolution carries adsorbed CO species from the initial thermal methanol dehydrogenation on the Pt cluster. Thermal steps in the reaction mechanism are depicted in gray arrows, while the known pathways for the photogenerated holes and electrons are shown in the respective colors, blue and orange. Note that the position of the Pt cluster does not reflect its position with respect to the band energy diagram but rather a physical location on the surface.

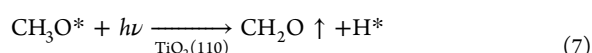
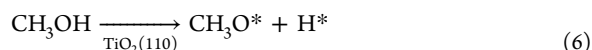
excitation with UV light, an electron–hole pair is formed in the  $\text{TiO}_2(110)$  single crystal. Because the latter is an n-type semiconductor, the holes formed in the space charge region are subject to a driving force from a Coulomb attraction toward the surface, while the electrons preferentially travel toward the bulk. Methoxy species form thermally at a variety of defect sites<sup>41,61</sup> including the negatively charged BBO vacancies.<sup>62–64</sup>

In previous photocatalytic studies on a cocatalyst-loaded  $\text{TiO}_2(110)$  photocatalyst with methanol<sup>21,22</sup> and ethanol,<sup>24</sup> the dependence of the photocatalytic hydrogen evolution with regard to the photon flux was found to be close to 1, meaning that only one absorbed photon leads to the formation of one  $\text{H}_2$  molecule. This observation is in very good agreement with the “current-doubling” effect that has been observed for the same materials.<sup>10,65</sup> Furthermore, methoxy species adsorbed on the  $\text{TiO}_2(110)$  surface were identified in systematic studies as the photo-active intermediate by various groups,<sup>41,42,57,66,67</sup> while a photon-driven O–H dissociation mechanism of molecular methanol remains controversial.<sup>41,58,68–70</sup>

Furthermore, formaldehyde desorption from photo-oxidation is observed at 250 K immediately upon illumination because this molecule desorbs thermally around 240 K.<sup>71</sup> Hydrogen evolution is also observed around that temperature (also see Figures 3 and S3). The methoxy species are directly photo-oxidized by the photohole to form formaldehyde via a split of the C–H bond.<sup>57,66,72</sup> The photoreaction from tertiary alcohols evidences<sup>21,29</sup> that the abstracted H species is most likely a radical (in analogy to  $\cdot\text{CH}_3$  from *tert*-butanol photo-oxidation), while the extinguished charge corresponds to the electron from the carbon atom in a Lewis-type formalism. Although formaldehyde desorbs thermally, the hydrogen atoms on the surface diffuse to the Pt cocatalyst and thermally recombine.<sup>22</sup> The dimerization on the metal cocatalyst of the surface-bound hydrogen species was also suggested to be present in solution.<sup>14,16,73</sup> Some CO is chemisorbed on the cocatalyst from thermal methanol dehydrogenation on the Pt clusters, but the cocatalyst is active for the photocatalytic

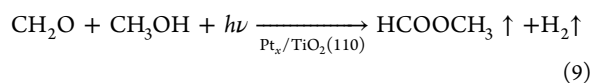
hydrogen evolution nonetheless. The finding that the cocatalyst loading does not alter the photo-oxidation kinetics further corroborates the scheme in Figure 7 because the hydrogen evolution in this picture is a fast, consecutive thermal reaction to the photo-oxidation of the methoxy species.

The chemical catalytic cycle can be closed in this picture because methanol reacts stoichiometrically to molecular hydrogen and formaldehyde. The photocatalytic methanol reforming can be rationalized using the following set of reaction equations (eqs 6–8). Here, methoxy species are photo-oxidized to formaldehyde, while molecular hydrogen desorbs.



The electronic catalytic cycle can be also closed because the methanol predominantly dissociates on the negatively charged surface states and gets subsequently oxidized by the photohole. Closing this electronic cycle and, thus, leaving the catalyst electronically unchanged require the recharging of the surface states.<sup>70</sup>

Below 250 K, another reaction channel opens up under catalytic conditions: formaldehyde gets photo-oxidized and couples with methanol in a consecutive photoreaction to form methyl formate and another H<sub>2</sub> molecule (eq 9)



In order to discriminate between photochemical and thermal reaction steps in the low-temperature methanol photo-oxidation pathway, the photoreaction may be carried out at cryogenic temperatures, and postirradiation temperature-programmed desorption (PI-TPD) experiments may then be used to quantify the conversion of methanol and product formation.<sup>41,42,74</sup> A methanol-covered, bare TiO<sub>2</sub>(110) surface facilitates under such conditions the formation of methyl formate, which was demonstrated by isotopic labeling experiments to occur via a transient formyl species, as evidenced in the literature.<sup>42</sup> The results from such PI-TPDs on bare r-TiO<sub>2</sub>(110) and turnover frequencies (TOFs) from methanol photocatalysis on Pt<sub>x</sub>/TiO<sub>2</sub>(110) are shown in Figure 8. In (a), the PI-TPD from 15 min illumination of 1 L of CD<sub>3</sub>OH at 100 K between 220 and 300 K is displayed. As seen there, methyl formate desorbs around 235 K, formaldehyde desorbs around 245 K, and methanol desorbs around 275 K, which is consistent with the literature.<sup>42,74,75</sup> The full PI-TPD after illumination of methanol on r-TiO<sub>2</sub>(110) is given in Figure S5. The dependence of formaldehyde and methyl formate production as a function of illumination time (Figure S6) is in excellent agreement with a previous study.<sup>74</sup>

The observed photo-oxidation products and their respective desorption temperatures in the PI-TPD of methanol on r-TiO<sub>2</sub>(110) (Figure 8a) are the same as observed under catalytic conditions in the investigated temperature range from 230 to 273 K on the Pt<sub>x</sub>/TiO<sub>2</sub>(110) photocatalyst. This supplies further evidence that the platinum cocatalyst does not open another reaction pathway for photo-oxidation. On the high temperature side, the overall product evolution is

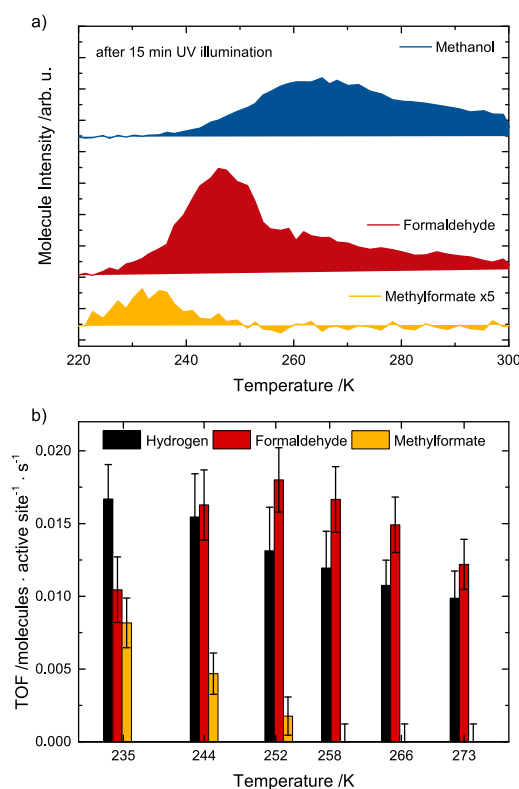


**Figure 8.** (a) Relevant TPD region of 1 L of CD<sub>3</sub>OH on the TiO<sub>2</sub>(110) surface after 15 min of UV illumination at 100 K. The full temperature range of the postirradiation experiment is shown in Figure S5. (b) TOFs of methanol photocatalysis in a methanol background pressure of 1 × 10<sup>-8</sup> mbar on a Pt<sub>x</sub>/TiO<sub>2</sub>(110) photocatalyst as reported in a previous study.<sup>21</sup> A direct correlation between the observed product species under photocatalytic conditions with peaks from postirradiation TPDs is suggested from a joint interpretation of these results.

quantitatively lower because the majority of methanol already desorbs at 275 K. Around 255 K, a peak in the formaldehyde TOF is obtained (Figure 8b). In the PI-TPD (Figure 8a), however, the majority of methanol still remains adsorbed on the surface, while formaldehyde desorption is already facilitated. Photocatalysis at even lower temperatures around 235 K changes the selectivity of the reaction, as methyl formate is obtained from the sequential photo-oxidation of formaldehyde. The selectivity of the photochemical processes clearly depends on available intermediates at the surface and can be altered by the reaction temperature (Figure 8b).<sup>21</sup> In this regard, the PI-TPD can be used to calculate the surface lifetime of adsorbates from their peak in TPD experiments. The surface residence time of an adsorbate can be estimated by the following expression, whose detailed derivation is given in the Supporting Information

$$t_{1/2} = \frac{\ln(2)}{\nu_d \times e^{-\Delta H/RT}} \quad (10)$$

In this regard,  $\Delta H$  is the desorption energy,  $T$  is the temperature,  $\nu_d$  is the pre-exponential factor from the Arrhenius equation, and  $R$  is the gas constant. The residence times for methanol, formaldehyde, and methyl formate are shown in Table 1 along with the observed selectivity of the

methanol photoreforming on cocatalyst-loaded TiO<sub>2</sub>(110) at the reaction temperature obtained from Figure 8b.

**Table 1.** Calculated Surface Residence Times of Methanol, Formaldehyde, and Methyl Formate from PI-TPD Experiments on r-TiO<sub>2</sub>(110) and Observed Selectivities from Methanol Photoreforming on Pt<sub>x</sub>/TiO<sub>2</sub>(110)

temperature/K	surface residence time/s			observed selectivity/%	
	CH <sub>3</sub> OH	CH <sub>2</sub> O	CH <sub>3</sub> OOCH	CH <sub>2</sub> O	CH <sub>3</sub> OOCH
235	497.80	18.48	3.52	56.1	43.9
244	103.93	4.45	0.85	77.7	22.3
252	28.36	1.36	0.26	91.1	8.9
258	11.29	0.59	0.11	99.9	<0.1
265	4.06	0.23	0.04	99.9	<0.1
273	1.35	0.09	0.02	100	

The observed selectivity of photo-oxidation is dependent on the probability of a consecutive photo-oxidation of the formaldehyde intermediate on the surface, which is in competition with thermal formaldehyde desorption.<sup>21</sup> To visualize this dependence, the methyl formate TOF under catalytic conditions on Pt<sub>x</sub>/TiO<sub>2</sub>(110) is shown as a function of the surface residence time of both reactants, methanol and formaldehyde, forming the ester (Figure 9). Because methanol

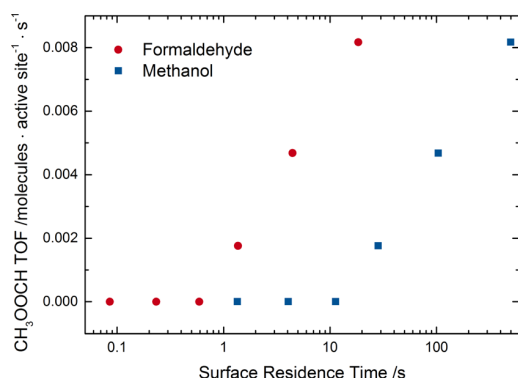


**Figure 9.** Correlation of the calculated surface residence times from Table 1 with the observed TOFs of methanol photoreforming from Figure 8b. Photocoupling to methyl formate is only observed at formaldehyde surface residence times of more than 1 s on the semiconductor surface. By the nature of adsorption properties, methanol has a surface lifetime that is an order of magnitude higher compared to formaldehyde.

is abundant on the surface at the temperatures where photocoupling to methyl formate is observed, formaldehyde photo-oxidation is believed to be the selectivity-determining step (eq 9). Only when formaldehyde is present for longer than 1 s on the surface, significant methyl formate evolution is observed (see Figure 9). This further emphasizes the importance of the chemical reaction kinetics on photoreforming processes because the charge carrier dynamics occur on much faster time scales of picoseconds for single crystals<sup>76</sup> and microseconds for nanoparticles.<sup>77</sup>

The importance of surface residence time on the observed selectivity may reasonably be transferable to gas-phase, water-free methanol reforming under more applied conditions, as similar reaction pathways and products formed are observed under such conditions.<sup>78–80</sup> Furthermore, this may not only

hold true for other rutile surfaces,<sup>81,82</sup> as a very similar thermal and photochemistry for methanol has been observed on anatase<sup>83–89</sup> and brookite modifications.<sup>90,91</sup> The adsorption properties and desorption temperatures for the alcohols and their photo-oxidation products are very similar in general on the investigated TiO<sub>2</sub> surfaces. Especially on anatase, the majority phase<sup>92</sup> in Degussa P25, the same photo-oxidation pathway of methanol to methyl formate has been reported recently.<sup>93</sup>

Stability is one of the major requirements for any future application of photocatalysts.<sup>94</sup> We reported that the Pt<sub>x</sub>/TiO<sub>2</sub>(110) model catalyst is highly stable and demonstrated this for 4 h of methanol photoreforming at a temperature of 262 K, in which no decline in activity was observed.<sup>21</sup> However, while Pt<sub>x</sub>/TiO<sub>2</sub> photocatalysts are generally perceived as stable,<sup>8</sup> recent work from Haselmann et al. reported a deactivation mechanism within the first hour for small platinum loadings.<sup>95</sup> Chung et al. observed a similar deactivation phenomenon after 30 min of photoreforming of methanol on their Pt/TiO<sub>2</sub> catalysts based on Degussa P25, in addition to an induction period lasting a couple of minutes.<sup>96</sup> Therefore, we further investigated the stability under reaction and vacuum conditions. A further sign of the long-term stability of the Pt<sub>x</sub>/TiO<sub>2</sub>(110) photocatalyst under the investigated conditions is demonstrated by the measurements presented in Figure 10. The catalyst is not only stable for more than 200 min as reported previously;<sup>21</sup> there is also no decline in activity in subsequent catalytic experiments (Figure 10a,b). Furthermore, the storage of the photocatalyst in vacuo for 70 h did not lead to any change in the catalytic activity, neither qualitatively as in the formation of products (Figure 10c) nor quantitatively as in the overall TOF (Figure 10d). Furthermore, deactivation by unavoidable adsorption of residual gases such as CO and H<sub>2</sub>O was not observed, which happens because of the long exposure time of 70 h and despite the low pressure of <1 × 10<sup>-10</sup> mbar. This again corroborates the findings summed up in Figure 7 that the Pt cocatalyst gets conditioned quickly and most likely by CO adsorbed on the Pt clusters. These CO species may also contribute to the long-term stability of the particle<sup>52</sup> in a similar way as previously observed for Pt clusters on an iron oxide support.<sup>97</sup>

## CONCLUSIONS

In summary, the extensive analysis of isothermal photo-reactions, TPD, and postirradiation TPDs leads to a complete picture of all the surface species present under photocatalytic conditions in the gas phase. The results supply evidence that the Pt cocatalyst, which acts as a center for thermal hydrogen recombination,<sup>14,16,22,98</sup> is most likely covered by CO under the reaction conditions. Although these spectator species do not inhibit H<sub>2</sub> formation, they may even lead to the protection of the cocatalysts giving rise to high stability, which is observed for the photocatalyst. This observation may not only be important for the interpretation of reactions under applied conditions but also explain or tune the stability of cocatalysts comprising other metals with a strong binding of CO, such as Ni, Pd,<sup>99</sup> and Ru.

Concerning the surface chemistry of the semiconductor, the full understanding of all surface species and the determination of thermal activation barriers and pre-exponentials set the necessary foundation for a meaningful description by microkinetic modeling or ab initio theory investigations. The surface science experiments and their connection to catalytic

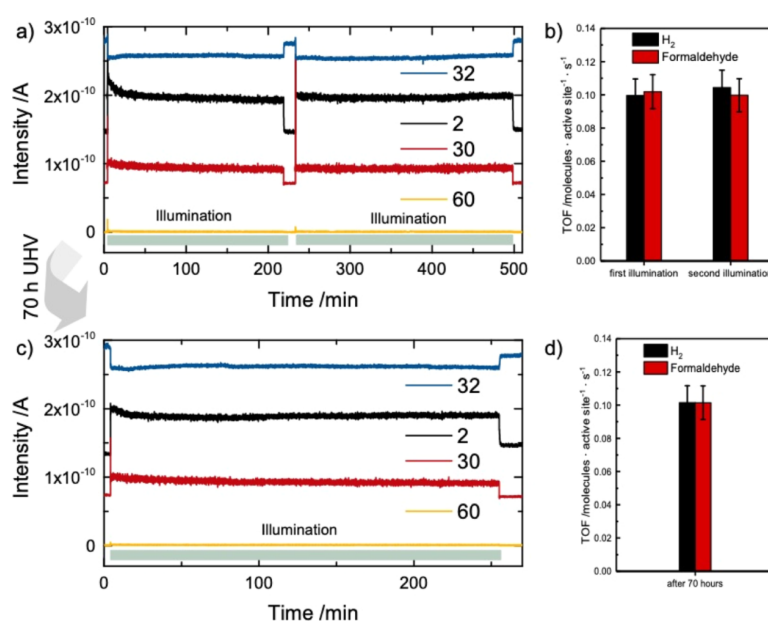


**Figure 10.** Methanol ( $m/z = 32$ ), hydrogen ( $m/z = 2$ ), formaldehyde ( $m/z = 30$ ), and methyl formate ( $m/z = 60$ ) traces at 262 K in a methanol background pressure of  $7 \times 10^{-8}$  mbar (a) and corresponding TOFs (b). The gray bars indicate the period of UV illumination. The presented traces are in quantitative agreement with previous studies.<sup>21</sup> Storing in vacuo at room temperature leads to the same catalytic activity as evidenced in the raw mass traces (c) and the quantitative agreement in the TOFs (d). Note that at this temperature, the mass trace 60 of methyl formate is too low in intensity for the calculation of a meaningful TOF.

conditions offer a new toolbox for photocatalysis research, which can be exploited by chemical reaction dynamics and to estimate selectivities under catalytic conditions. For example, the latter may be governed by the residence time of photoproducts on the surface enabling consecutive photo-reactions, as we demonstrated for methyl formate formation. We were further able to show that under gas-phase reaction conditions, the photo-oxidation of methoxy is not affected by the Pt cocatalyst loading in the 1% range and that the photo-oxidation is the rate-determining step in the photocatalytic hydrogen evolution from methanol.<sup>22</sup> Clearly, the photocatalytic  $H_2$  evolution cannot be analyzed decoupled from the photo-oxidation reaction in this reaction network, where the photogenerated charge is directly involved in the methanol photo-oxidation. However, one may speculate that a strong similarity in the hydrogen evolution mechanism between water and methanol exists because both reactions presumably proceed via the diffusion of hydroxyls and an eventual H dimerization at the Pt cocatalyst.

A complete kinetic understanding of the thermal processes on the catalyst surface will further set a path for a detailed investigation under different illumination conditions and semiconductor doping in very well-defined materials to investigate the influence of charge carrier dynamics on photocatalytic reactions. The kinetic insight from TPD experiments for catalytic conditions shows that the chemical surface reaction kinetics dominate the overall conversion and selectivity in catalysis,<sup>100</sup> which holds true for photocatalytic reactions as well.

## ■ ASSOCIATED CONTENT

### Supporting Information

The Supporting Information is available free of charge at <https://pubs.acs.org/doi/10.1021/acscatal.0c00260>.

Auger electron spectra of the clean  $TiO_2(110)$  sample before and after photocatalysis; TPD data of methanol- $d_3$ ,  $D_2$ , and  $H_2O$  on  $Pt_x/TiO_2(110)$ ; exemplary postillumination TPD data of methanol- $d_3$  after 15 min of UV irradiation and the integrated values of an illumination-dependent TPD series of methanol on bare  $TiO_2(110)$ ; derivation of the surface lifetime values for the different species given along with a table; and summary of the kinetic parameters (PDF)

## ■ AUTHOR INFORMATION

### Corresponding Author

Ueli Heiz – Chair of Physical Chemistry & Catalysis Research Center, Technical University of Munich, Garching 85748, Germany; [orcid.org/0000-0002-9403-1486](https://orcid.org/0000-0002-9403-1486); Email: [ulrich.heiz@mytum.de](mailto:ulrich.heiz@mytum.de)

### Authors

Constantin A. Walenta – Chair of Physical Chemistry & Catalysis Research Center, Technical University of Munich, Garching 85748, Germany; [orcid.org/0000-0001-9879-5101](https://orcid.org/0000-0001-9879-5101)

Carla Courtois – Chair of Physical Chemistry & Catalysis Research Center, Technical University of Munich, Garching 85748, Germany

Sebastian L. Kollmannsberger – Chair of Physical Chemistry & Catalysis Research Center, Technical University of Munich, Garching 85748, Germany

Moritz Eder – Chair of Physical Chemistry & Catalysis Research Center, Technical University of Munich, Garching 85748, Germany

Martin Tschurl – Chair of Physical Chemistry & Catalysis Research Center, Technical University of Munich, Garching 85748, Germany; [orcid.org/0000-0001-6618-7312](https://orcid.org/0000-0001-6618-7312)



Complete contact information is available at:  
<https://pubs.acs.org/10.1021/acscatal.0c00260>

## Notes

The authors declare no competing financial interest.

## ACKNOWLEDGMENTS

The authors thank the DFG for financial support through HE3435/22-1 and under Germany's Excellence Strategy—EXC 2089/1-390776260. C.C. acknowledges the support from the Luxembourg National Research Fund (FNR), project code 12531916 and that from the TUM International Graduate School of Science and Engineering (TUM-IGSSE).

## REFERENCES

- (1) Wang, Q.; Hisatomi, T.; Jia, Q.; Tokudome, H.; Zhong, M.; Wang, C.; Pan, Z.; Takata, T.; Nakabayashi, M.; Shibata, N.; Li, Y.; Sharp, I. D.; Kudo, A.; Yamada, T.; Domen, K. Scalable Water Splitting on Particulate Photocatalyst Sheets with a Solar-to-Hydrogen Energy Conversion Efficiency Exceeding 1%. *Nat. Mater.* **2016**, *15*, 611–615.
- (2) Cargnello, M.; Gasparotto, A.; Gombac, V.; Montini, T.; Barreca, D.; Fornasiero, P. Photocatalytic H<sub>2</sub> and Added-Value By-Products – The Role of Metal Oxide Systems in Their Synthesis from Oxygenates. *Eur. J. Inorg. Chem.* **2011**, 4309–4323.
- (3) Uekert, T.; Kuehnel, M. F.; Wakerley, D. W.; Reisner, E. Plastic Waste as a Feedstock for Solar-driven H<sub>2</sub> Generation. *Energy Environ. Sci.* **2018**, *11*, 2853–2857.
- (4) Hainer, A. S.; Hodgins, J. S.; Sandre, V.; Vallieres, M.; Lanterna, A. E.; Scaiano, J. C. Photocatalytic Hydrogen Generation Using Metal-Decorated TiO<sub>2</sub>: Sacrificial Donors vs True Water Splitting. *ACS Energy Lett.* **2018**, *3*, 542–545.
- (5) Maeda, Y.; Fujishima, A.; Honda, K. The Investigation of Current Doubling Reactions on Semiconductor Photoelectrodes by Temperature Change Measurements. *J. Electrochem. Soc.* **1981**, *128*, 1731–1734.
- (6) Baba, R.; Konda, R.; Fujishima, A.; Honda, K. Photoelectrochemical Deposition of Metals on TiO<sub>2</sub> Powders in the Presence of Alcohols. *Chem. Lett.* **1986**, 1307–1310.
- (7) Yamagata, S.; Nakabayashi, S.; Sancier, K. M.; Fujishima, A. Photocatalytic Oxidation of Alcohols on TiO<sub>2</sub>. *Bull. Chem. Soc. Jpn.* **1988**, *61*, 3429–3434.
- (8) Kandiel, T. A.; Ivanova, I.; Bahnemann, D. W. Long-term Investigation of the Photocatalytic Hydrogen Production on Platinized TiO<sub>2</sub>: an Isotopic Study. *Energy Environ. Sci.* **2014**, *7*, 1420–1425.
- (9) Berr, M. J.; Vaneski, A.; Mauser, C.; Fischbach, S.; Susha, A. S.; Rogach, A. L.; Jäckel, F.; Feldmann, J. Delayed Photoelectron Transfer in Pt-Decorated CdS Nanorods under Hydrogen Generation Conditions. *Small* **2012**, *8*, 291–297.
- (10) Schneider, J.; Bahnemann, D. W. Undesired Role of Sacrificial Reagents in Photocatalysis. *J. Phys. Chem. Lett.* **2013**, *4*, 3479–3483.
- (11) Kamat, P. V.; Jin, S. Semiconductor Photocatalysis: “Tell Us the Complete Story!”. *ACS Energy Lett.* **2018**, *3*, 622–623.
- (12) Liu, N.; Zhou, X.; Nguyen, N. T.; Peters, K.; Zoller, F.; Hwang, I.; Schneider, C.; Miehlich, M. E.; Freitag, D.; Meyer, K.; Fattakhova-Rohlfing, D.; Schmuki, P. Black Magic in Gray Titania: Noble-Metal-Free Photocatalytic H<sub>2</sub> Evolution from Hydrogenated Anatase. *ChemSusChem* **2017**, *10*, 62–67.
- (13) Joo, J. B.; Dillon, R.; Lee, I.; Yin, Y.; Bardeen, C. J.; Zaera, F. Promotion of Atomic Hydrogen Recombination as an Alternative to Electron Trapping for the Role of Metals in the Photocatalytic Production of H<sub>2</sub>. *Proc. Natl. Acad. Sci. U.S.A.* **2014**, *111*, 7942.
- (14) Lee, Y. J.; Joo, J. B.; Yin, Y.; Zaera, F. Evaluation of the Effective Photoexcitation Distances in the Photocatalytic Production of H<sub>2</sub> from Water using Au@Void@TiO<sub>2</sub> Yolk–Shell Nanostructures. *ACS Energy Lett.* **2016**, *1*, 52–56.
- (15) Zaera, F. Gold-Titania Catalysts for Low-Temperature Oxidation and Water Splitting. *Top. Catal.* **2018**, *61*, 336–347.
- (16) Joo, J. B.; Dillon, R.; Lee, I.; Yin, Y.; Bardeen, C. J.; Zaera, F. Promotion of atomic hydrogen recombination as an alternative to electron trapping for the role of metals in the photocatalytic production of H<sub>2</sub>. *Proc. Natl. Acad. Sci. U.S.A.* **2014**, *111*, 7942.
- (17) Diebold, U. The Surface Science of Titanium Dioxide. *Surf. Sci. Rep.* **2003**, *48*, 53–229.
- (18) Henderson, M. A. A surface science perspective on TiO<sub>2</sub> photocatalysis. *Surf. Sci. Rep.* **2011**, *66*, 185–297.
- (19) Thompson, T. L.; Yates, J. T. TiO<sub>2</sub>-based Photocatalysis: Surface Defects, Oxygen and Charge Transfer. *Top. Catal.* **2005**, *35*, 197–210.
- (20) Zhang, Z.; Yates, J. T. Band Bending in Semiconductors: Chemical and Physical Consequences at Surfaces and Interfaces. *Chem. Rev.* **2012**, *112*, 5520–5551.
- (21) Kollmannsberger, S. L.; Walenta, C. A.; Courtois, C.; Tschurl, M.; Heiz, U. Thermal Control of Selectivity in Photocatalytic, Water-Free Alcohol Photoreforming. *ACS Catal.* **2018**, *8*, 11076–11084.
- (22) Walenta, C. A.; Kollmannsberger, S. L.; Courtois, C.; Pereira, R. N.; Stutzmann, M.; Tschurl, M.; Heiz, U. Why Co-catalyst-loaded Rutile Facilitates Photocatalytic Hydrogen Evolution. *Phys. Chem. Chem. Phys.* **2019**, *21*, 1491–1496.
- (23) Hao, Q.; Zhiqiang Wang; Wang, T.; Ren, Z.; Zhou, C.; Yang, X. Role of Pt Loading in the Photocatalytic Chemistry of Methanol on Rutile TiO<sub>2</sub>(110). *ACS Catal.* **2019**, *9*, 286–294.
- (24) Katsiev, K.; Harrison, G.; Al-Salik, Y.; Thornton, G.; Idriss, H. Gold Cluster Coverage Effect on H<sub>2</sub> Production over Rutile TiO<sub>2</sub>(110). *ACS Catal.* **2019**, *9*, 8294–8305.
- (25) Kollmannsberger, S. L.; Walenta, C. A.; Winnerl, A.; Weiszer, S.; Pereira, R. N.; Tschurl, M.; Stutzmann, M.; Heiz, U. Doping-Dependent Adsorption and Photon-Stimulated Desorption of CO on GaN(0001). *J. Phys. Chem. C* **2017**, *121*, 8473–8479.
- (26) Bozack, M. J.; Muehlhoff, L.; Russell, J. N.; Choyke, W. J.; Yates, J. T. Methods in Semiconductor Surface Chemistry. *J. Vac. Sci. Technol. A* **1987**, *5*, 1–8.
- (27) Winbauer, A.; Kollmannsberger, S. L.; Walenta, C. A.; Schreiber, P.; Kiermaier, J.; Tschurl, M.; Heiz, U. Isomer-Selective Detection of Aromatic Molecules in Temperature-Programmed Desorption for Model Catalysis. *Anal. Chem.* **2016**, *88*, 5392–5397.
- (28) Heiz, U.; Vanolli, F.; Trento, L.; Schneider, W.-D. Chemical Reactivity of Size-Selected Supported Clusters: An Experimental Setup. *Rev. Sci. Instrum.* **1997**, *68*, 1986–1994.
- (29) Walenta, C. A.; Kollmannsberger, S. L.; Courtois, C.; Tschurl, M.; Heiz, U. Photocatalytic selectivity switch to C–C scission:  $\alpha$ -Methyl Ejection of tert-Butanol on TiO<sub>2</sub>(110). *Phys. Chem. Chem. Phys.* **2018**, *20*, 7105–7111.
- (30) Zehr, R. T.; Henderson, M. A. Influence of O<sub>2</sub>-Induced Surface Roughening on the Chemistry of Water on TiO<sub>2</sub>(110). *Surf. Sci.* **2008**, *602*, 1507–1516.
- (31) Henderson, M. A. Structural Sensitivity in the Dissociation of Water on TiO<sub>2</sub> Single-Crystal Surfaces. *Langmuir* **1996**, *12*, 5093–5098.
- (32) Crampton, A. S.; Rötzer, M. D.; Landman, U.; Heiz, U. Can Support Acidity Predict Sub-Nanometer Catalyst Activity Trends? *ACS Catal.* **2017**, *7*, 6738–6744.
- (33) Sasahara, A.; Pang, C. L.; Onishi, H. Local Work Function of Pt Clusters Vacuum-Deposited on a TiO<sub>2</sub> Surface. *J. Phys. Chem. B* **2006**, *110*, 17584–17588.
- (34) Bonanni, S.; Ait-Mansour, K.; Brune, H.; Harbich, W. Overcoming the Strong Metal–Support Interaction State: CO Oxidation on TiO<sub>2</sub>(110)-Supported Pt Nanoclusters. *ACS Catal.* **2011**, *1*, 385–389.
- (35) Bonanni, S.; Ait-Mansour, K.; Harbich, W.; Brune, H. Effect of the TiO<sub>2</sub> Reduction State on the Catalytic CO Oxidation on Deposited Size-Selected Pt Clusters. *J. Am. Chem. Soc.* **2012**, *134*, 3445–3450.

- (36) Isomura, N.; Wu, X.; Watanabe, Y. Atomic-Resolution Imaging of Size-Selected Platinum Clusters on TiO<sub>2</sub>(110) Surfaces. *J. Chem. Phys.* **2009**, *131*, 164707.
- (37) Watanabe, Y.; Wu, X.; Hirata, H.; Isomura, N. Size-Dependent Catalytic Activity and Geometries of Size-Selected Pt Clusters on TiO<sub>2</sub>(110) Surfaces. *Catal. Sci. Technol.* **2011**, *1*, 1490–1495.
- (38) Dulub, O.; Hebenstreit, W.; Diebold, U. Imaging Cluster Surfaces with Atomic Resolution: The Strong Metal-Support Interaction State of Pt Supported on TiO<sub>2</sub>(110). *Phys. Rev. Lett.* **2000**, *84*, 3646–3649.
- (39) Pesty, F.; Steinrück, H.-P.; Madey, T. E. Thermal Stability of Pt Films on TiO<sub>2</sub>(110): Evidence for Encapsulation. *Surf. Sci.* **1995**, *339*, 83–95.
- (40) Geng, Z.; Jin, X.; Wang, R.; Chen, X.; Guo, Q.; Ma, Z.; Dai, D.; Fan, H.; Yang, X. Low-Temperature Hydrogen Production via Water Conversion on Pt/TiO<sub>2</sub>. *J. Phys. Chem. C* **2018**, *122*, 10956–10962.
- (41) Shen, M.; Henderson, M. A. Identification of the Active Species in Photochemical Hole Scavenging Reactions of Methanol on TiO<sub>2</sub>. *J. Phys. Chem. Lett.* **2011**, *2*, 2707–2710.
- (42) Phillips, K. R.; Jensen, S. C.; Baron, M.; Li, S.-C.; Friend, C. M. Sequential Photo-oxidation of Methanol to Methyl Formate on TiO<sub>2</sub>(110). *J. Am. Chem. Soc.* **2013**, *135*, 574–577.
- (43) Sexton, B. A. Methanol Decomposition on Platinum (111). *Surf. Sci.* **1981**, *102*, 271–281.
- (44) Osmić, M.; Mohrhusen, L.; Al-Shamery, K. Bulk Defect Dependence of Low-Temperature Partial Oxidation of Methanol and High-Temperature Hydrocarbon Formation on Rutile TiO<sub>2</sub>(110). *J. Phys. Chem. C* **2019**, *123*, 7615.
- (45) Henderson, M. A.; Otero-Tapia, S.; Castro, M. E. The Chemistry of Methanol on the TiO<sub>2</sub>(110) Surface: the Influence of Vacancies and Coadsorbed Species. *Faraday Discuss.* **1999**, *114*, 313–329.
- (46) Guo, Q.; Xu, C.; Ren, Z.; Yang, W.; Ma, Z.; Dai, D.; Fan, H.; Minton, T. K.; Yang, X. Stepwise Photocatalytic Dissociation of Methanol and Water on TiO<sub>2</sub>(110). *J. Am. Chem. Soc.* **2012**, *134*, 13366–13373.
- (47) Gibson, K. D.; Dubois, L. H. Step Effects in the Thermal Decomposition of Methanol on Pt(111). *Surf. Sci.* **1990**, *233*, 59–64.
- (48) Heiz, U.; Sherwood, R.; Cox, D. M.; Kaldor, A.; Yates, J. T. CO Chemisorption on Monodispersed Platinum Clusters on SiO<sub>2</sub>: Detection of CO Chemisorption on Single Platinum Atoms. *J. Phys. Chem.* **1995**, *99*, 8730–8735.
- (49) Crampton, A. S.; Rötzer, M. D.; Ridge, C. J.; Schweinberger, F. F.; Heiz, U.; Yoon, B.; Landman, U. Structure Sensitivity in the Nonscalable Regime Explored via Catalyzed Ethylene Hydrogenation on Supported Platinum Nanoclusters. *Nat. Commun.* **2016**, *7*, 10389.
- (50) Dohnálek, Z.; Lyubintsky, I.; Rousseau, R. Thermally-Driven Processes on Rutile TiO<sub>2</sub>(110)-(1×1): A Direct View at the Atomic Scale. *Prog. Surf. Sci.* **2010**, *85*, 161–205.
- (51) Karim, W.; Spreafico, C.; Kleibert, A.; Gobrecht, J.; VandeVondele, J.; Ekinici, Y.; van Bokhoven, J. A. Catalyst Support Effects on Hydrogen Spillover. *Nature* **2017**, *541*, 68–71.
- (52) Berto, T. F.; Sanwald, K. E.; Byers, J. P.; Browning, N. D.; Gutiérrez, O. Y.; Lercher, J. A. Enabling Overall Water Splitting on Photocatalysts by CO-Covered Noble Metal Co-Catalysts. *J. Phys. Chem. Lett.* **2016**, *7*, 4358–4362.
- (53) Dohnálek, Z.; Kim, J.; Bondarchuk, O.; White, J. M.; Kay, B. D. Physisorption of N<sub>2</sub>, O<sub>2</sub>, and CO on Fully Oxidized TiO<sub>2</sub>(110). *J. Phys. Chem. B* **2006**, *110*, 6229–6235.
- (54) Bonanni, S.; Ait-Mansour, K.; Hugentobler, M.; Brune, H.; Harbich, W. An Experimental Setup Combining a Highly Sensitive Detector for Reaction Products with a Mass-Selected Cluster Source and a Low-Temperature STM for Advanced Nanocatalysis Measurements. *Eur. Phys. J. D* **2011**, *63*, 241–249.
- (55) Zhang, R.; Wang, H.; Peng, X.; Feng, R.-r.; Liu, A.-a.; Guo, Q.; Zhou, C.; Ma, Z.; Yang, X.; Jiang, Y.; Ren, Z. In Situ Studies on Temperature-Dependent Photocatalytic Reactions of Methanol on TiO<sub>2</sub>(110). *J. Phys. Chem. C* **2019**, *123*, 9993–9999.
- (56) Walenta, C. A.; Kollmannsberger, S. L.; Kiermaier, J.; Winbauer, A.; Tschurl, M.; Heiz, U. Ethanol Photocatalysis on Rutile TiO<sub>2</sub>(110): the Role of Defects and Water. *Phys. Chem. Chem. Phys.* **2015**, *17*, 22809–22814.
- (57) Kolesov, G.; Vinichenko, D.; Tritsarlis, G. A.; Friend, C. M.; Kaxiras, E. Anatomy of the Photochemical Reaction: Excited-State Dynamics Reveals the C–H Acidity Mechanism of Methoxy Photo-oxidation on Titania. *J. Phys. Chem. Lett.* **2015**, *6*, 1624–1627.
- (58) Shen, M.; Henderson, M. A. Role of Water in Methanol Photochemistry on Rutile TiO<sub>2</sub>(110). *J. Phys. Chem. C* **2012**, *116*, 18788–18795.
- (59) Takanabe, K. Photocatalytic Water Splitting: Quantitative Approaches toward Photocatalyst by Design. *ACS Catal.* **2017**, *7*, 8006–8022.
- (60) Subramanian, V.; Wolf, E. E.; Kamat, P. V. Catalysis with TiO<sub>2</sub>/Gold Nanocomposites. Effect of Metal Particle Size on the Fermi Level Equilibration. *J. Am. Chem. Soc.* **2004**, *126*, 4943–4950.
- (61) Zhang, Z.; Bondarchuk, O.; White, J. M.; Kay, B. D.; Dohnálek, Z. Imaging Adsorbate O–H Bond Cleavage: Methanol on TiO<sub>2</sub>(110). *J. Am. Chem. Soc.* **2006**, *128*, 4198–4199.
- (62) Henderson, M. A.; Epling, W. S.; Peden, C. H. F.; Perkins, C. L. Insights into Photoexcited Electron Scavenging Processes on TiO<sub>2</sub> Obtained from Studies of the Reaction of O<sub>2</sub> with OH Groups Adsorbed at Electronic Defects on TiO<sub>2</sub>(110). *J. Phys. Chem. B* **2003**, *107*, 534–545.
- (63) Henderson, M. A.; Szanyi, J.; Peden, C. H. F. Conversion of N<sub>2</sub>O to N<sub>2</sub> on TiO<sub>2</sub>(110). *Catal. Today* **2003**, *85*, 251–266.
- (64) Papageorgiou, A. C.; Beglitis, N. S.; Pang, C. L.; Teobaldi, G.; Cabailh, G.; Chen, Q.; Fisher, A. J.; Hofer, W. A.; Thornton, G. Electron Traps and Their Effect on the Surface Chemistry of TiO<sub>2</sub>(110). *Proc. Natl. Acad. Sci. U.S.A.* **2010**, *107*, 2391.
- (65) Bingham, M.; Mills, A. Photonic Efficiency and Selectivity Study of M (M=Pt, Pd, Au and Ag)/TiO<sub>2</sub> Photocatalysts for Methanol Reforming in the Gas Phase. *J. Photochem. Photobiol., A* **2020**, *389*, 112257.
- (66) Chu, W.; Saidi, W. A.; Zheng, Q.; Xie, Y.; Lan, Z.; Prezhdo, O. V.; Petek, H.; Zhao, J. Ultrafast Dynamics of Photogenerated Holes at a CH<sub>3</sub>OH/TiO<sub>2</sub> Rutile Interface. *J. Am. Chem. Soc.* **2016**, *138*, 13740–13749.
- (67) Jensen, S. C.; Friend, C. M. The Dynamic Roles of Interstitial and Surface Defects on Oxidation and Reduction Reactions on Titania. *Top. Catal.* **2013**, *56*, 1377–1388.
- (68) Guo, Q.; Zhou, C.; Ma, Z.; Ren, Z.; Fan, H.; Yang, X. Elementary photocatalytic chemistry on TiO<sub>2</sub> surfaces. *Chem. Soc. Rev.* **2016**, *45*, 3701–3730.
- (69) Guo, Q.; Zhou, C.; Ma, Z.; Ren, Z.; Fan, H.; Yang, X. Elementary Chemical Reactions in Surface Photocatalysis. *Annu. Rev. Phys. Chem.* **2018**, *69*, 451–472.
- (70) Walenta, C. A.; Tschurl, M.; Heiz, U. Introducing Catalysis in Photocatalysis: What Can Be Understood from Surface Science Studies of Alcohol Photoreforming on TiO<sub>2</sub>. *J. Phys.: Condens. Matter* **2019**, *31*, 473002.
- (71) Cremer, T.; Jensen, S. C.; Friend, C. M. Enhanced Photo-Oxidation of Formaldehyde on Highly Reduced o-TiO<sub>2</sub>(110). *J. Phys. Chem. C* **2014**, *118*, 29242–29251.
- (72) Shen, M.; Henderson, M. A. Impact of Solvent on Photocatalytic Mechanisms: Reactions of Photodesorption Products with Ice Overlayers on the TiO<sub>2</sub>(110) Surface. *J. Phys. Chem. C* **2011**, *115*, 5886–5893.
- (73) Méndez-Medrano, M. G.; Kowalska, E.; Lehoux, A.; Herissan, A.; Ohtani, B.; Rau, S.; Colbeau-Justin, C.; Rodríguez-López, J. L.; Remita, H. Surface Modification of TiO<sub>2</sub> with Au Nanoclusters for Efficient Water Treatment and Hydrogen Generation under Visible Light. *J. Phys. Chem. C* **2016**, *120*, 25010–25022.
- (74) Guo, Q.; Xu, C.; Yang, W.; Ren, Z.; Ma, Z.; Dai, D.; Minton, T. K.; Yang, X. Methyl Formate Production on TiO<sub>2</sub>(110), Initiated by Methanol Photocatalysis at 400 nm. *J. Phys. Chem. C* **2013**, *117*, 5293–5300.

- (75) Yuan, Q.; Wu, Z.; Jin, Y.; Xu, L.; Xiong, F.; Ma, Y.; Huang, W. Photocatalytic Cross-Coupling of Methanol and Formaldehyde on a Rutile TiO<sub>2</sub>(110) Surface. *J. Am. Chem. Soc.* **2013**, *135*, 5212–5219.
- (76) Maity, P.; Mohammed, O. F.; Katsiev, K.; Idriss, H. Study of the Bulk Charge Carrier Dynamics in Anatase and Rutile TiO<sub>2</sub> Single Crystals by Femtosecond Time-Resolved Spectroscopy. *J. Phys. Chem. C* **2018**, *122*, 8925–8932.
- (77) Bahnemann, D. W.; Hilgendorff, M.; Memming, R. Charge Carrier Dynamics at TiO<sub>2</sub> Particles: Reactivity of Free and Trapped Holes. *J. Phys. Chem. B* **1997**, *101*, 4265–4275.
- (78) Chiarello, G. L.; Aguirre, M. H.; Selli, E. Hydrogen Production by Photocatalytic Steam Reforming of Methanol on Noble Metal-Modified TiO<sub>2</sub>. *J. Catal.* **2010**, *273*, 182–190.
- (79) Chiarello, G. L.; Ferri, D.; Selli, E. Effect of the CH<sub>3</sub>OH/H<sub>2</sub>O Ratio on the Mechanism of the Gas-Phase Photocatalytic Reforming of Methanol on Noble Metal-Modified TiO<sub>2</sub>. *J. Catal.* **2011**, *280*, 168–177.
- (80) Kominami, H.; Sugahara, H.; Hashimoto, K. Photocatalytic Selective Oxidation of Methanol to Methyl Formate in Gas Phase over Titanium(IV) Oxide in a Flow-type Reactor. *Catal. Commun.* **2010**, *11*, 426–429.
- (81) Kim, K. S.; Barteau, M. A. Reactions of Methanol on TiO<sub>2</sub>(001) Single Crystal Surfaces. *Surf. Sci.* **1989**, *223*, 13–32.
- (82) Idriss, H.; Kim, K. S.; Barteau, M. A. Surface-Dependent Pathways for Formaldehyde Oxidation and Reduction on TiO<sub>2</sub>(001). *Surf. Sci.* **1992**, *262*, 113–127.
- (83) Setvin, M.; Shi, X.; Hulva, J.; Simschitz, T.; Parkinson, G. S.; Schmid, M.; Di Valentin, C.; Selloni, A.; Diebold, U. Methanol on Anatase TiO<sub>2</sub>(101): Mechanistic Insights into Photocatalysis. *ACS Catal.* **2017**, *7*, 7081–7091.
- (84) Setvin, M.; Hulva, J.; Wang, H.; Simschitz, T.; Schmid, M.; Parkinson, G. S.; Di Valentin, C.; Selloni, A.; Diebold, U. Formaldehyde Adsorption on the Anatase TiO<sub>2</sub>(101) Surface: Experimental and Theoretical Investigation. *J. Phys. Chem. C* **2017**, *121*, 8914–8922.
- (85) Xu, C.; Yang, W.; Guo, Q.; Dai, D.; Chen, M.; Yang, X. Molecular Hydrogen Formation from Photocatalysis of Methanol on Anatase-TiO<sub>2</sub>(101). *J. Am. Chem. Soc.* **2014**, *136*, 602–605.
- (86) Xiong, F.; Yu, Y.-Y.; Wu, Z.; Sun, G.; Ding, L.; Jin, Y.; Gong, X.-Q.; Huang, W. Methanol Conversion into Dimethyl Ether on the Anatase TiO<sub>2</sub>(001) Surface. *Angew. Chem., Int. Ed.* **2016**, *55*, 623–628.
- (87) Xiong, F.; Yin, L.-L.; Wang, Z.; Jin, Y.; Sun, G.; Gong, X.-Q.; Huang, W. Surface Reconstruction-Induced Site-Specific Charge Separation and Photocatalytic Reaction on Anatase TiO<sub>2</sub>(001) Surface. *J. Phys. Chem. C* **2017**, *121*, 9991–9999.
- (88) Bennett, D. A.; Cargnello, M.; Diroll, B. T.; Murray, C. B.; Vohs, J. M. Shape-Dependence of the Thermal and Photochemical Reactions of Methanol on Nanocrystalline Anatase TiO<sub>2</sub>. *Surf. Sci.* **2016**, *654*, 1–7.
- (89) Pepin, P. A.; Lee, J. D.; Foucher, A. C.; Murray, C. B.; Stach, E. A.; Vohs, J. M. The Influence of Surface Platinum Deposits on the Photocatalytic Activity of Anatase TiO<sub>2</sub> Nanocrystals. *J. Phys. Chem. C* **2019**, *123*, 10477–10486.
- (90) Pepin, P. A.; Diroll, B. T.; Choi, H. J.; Murray, C. B.; Vohs, J. M. Thermal and Photochemical Reactions of Methanol, Acetaldehyde, and Acetic Acid on Brookite TiO<sub>2</sub> Nanorods. *J. Phys. Chem. C* **2017**, *121*, 11488–11498.
- (91) Pepin, P. A.; Lee, J. D.; Murray, C. B.; Vohs, J. M. Thermal and Photocatalytic Reactions of Methanol and Acetaldehyde on Pt-Modified Brookite TiO<sub>2</sub> Nanorods. *ACS Catal.* **2018**, *8*, 11834–11846.
- (92) Ohtani, B.; Prieto-Mahaney, O. O.; Li, D.; Abe, R. What is Degussa (Evonik) P25? Crystalline Composition Analysis, Reconstruction from Isolated Pure Particles and Photocatalytic Activity Test. *J. Photochem. Photobiol., A* **2010**, *216*, 179–182.
- (93) Setvin, M.; Shi, X.; Hulva, J.; Simschitz, T.; Parkinson, G. S.; Schmid, M.; Di Valentin, C.; Selloni, A.; Diebold, U. Methanol on Anatase TiO<sub>2</sub> (101): Mechanistic Insights into Photocatalysis. *ACS Catal.* **2017**, *7*, 7081–7091.
- (94) Bae, D.; Seger, B.; Hansen, O.; Vesborg, P. C. K.; Chorkendorff, I. Durability Testing of Photoelectrochemical Hydrogen Production under Day/Night Light Cycled Conditions. *ChemElectroChem* **2019**, *6*, 106–109.
- (95) Haselmann, G. M.; Eder, D. Early-Stage Deactivation of Platinum-Loaded TiO<sub>2</sub> Using in Situ Photodeposition During Photocatalytic Hydrogen Evolution. *ACS Catal.* **2017**, *7*, 4668–4675.
- (96) Chung, Y.-H.; Han, K.; Lin, C.-Y.; O'Neill, D.; Mul, G.; Mei, B.; Yang, C.-M.; Photocatalytic Hydrogen Production by Photo-Reforming of Methanol with One-Pot Synthesized Pt-Containing TiO<sub>2</sub> Photocatalysts. *Catal. Today* **2019**.
- (97) Bliem, R.; van der Hoeven, J. E. S.; Hulva, J.; Pavelec, J.; Gamba, O.; de Jongh, P. E.; Schmid, M.; Blaha, P.; Diebold, U.; Parkinson, G. S. Dual Role of CO in the Stability of Subnano Pt Clusters at the Fe<sub>3</sub>O<sub>4</sub>(001) Surface. *Proc. Natl. Acad. Sci. U.S.A.* **2016**, *113*, 8921.
- (98) Luna, A. L.; Drago, D.; Wang, K.; Beauvier, P.; Kowalska, E.; Ohtani, B.; Bahena Uribe, D.; Valenzuela, M. A.; Remita, H.; Colbeau-Justin, C. Photocatalytic Hydrogen Evolution Using Ni–Pd/TiO<sub>2</sub>: Correlation of Light Absorption, Charge-Carrier Dynamics, and Quantum Efficiency. *J. Phys. Chem. C* **2017**, *121*, 14302–14311.
- (99) Al-Mazroai, L. S.; Bowker, M.; Davies, P.; Dickinson, A.; Greaves, J.; James, D.; Millard, L. The Photocatalytic Reforming of Methanol. *Catal. Today* **2007**, *122*, 46–50.
- (100) Reece, C.; Redekop, E. A.; Karakalos, S.; Friend, C. M.; Madix, R. J. Crossing the Great Divide Between Single-Crystal Reactivity and Actual Catalyst Selectivity with Pressure Transients. *Nat. Catal.* **2018**, *1*, 852–859.

**Supporting Information for:  
Surface Species in Photocatalytic Methanol Reforming on Pt/TiO<sub>2</sub>(110):  
Learning from Surface Science Experiments for Catalytically Relevant  
Conditions**

Constantin A. Walenta<sup>¶</sup>, Carla Courtois<sup>¶</sup>, Sebastian L. Kollmannsberger<sup>¶</sup>,  
Moritz Eder<sup>¶</sup>, Martin Tschurl<sup>¶</sup>, Ueli Heiz<sup>¶,\*</sup>

<sup>¶</sup> Chair of Physical Chemistry & Catalysis Research Center, Technical University of  
Munich, Lichtenbergstr. 4, 85748 Garching, Germany

\*Corresponding Author: [ulrich.heiz@mytum.de](mailto:ulrich.heiz@mytum.de)

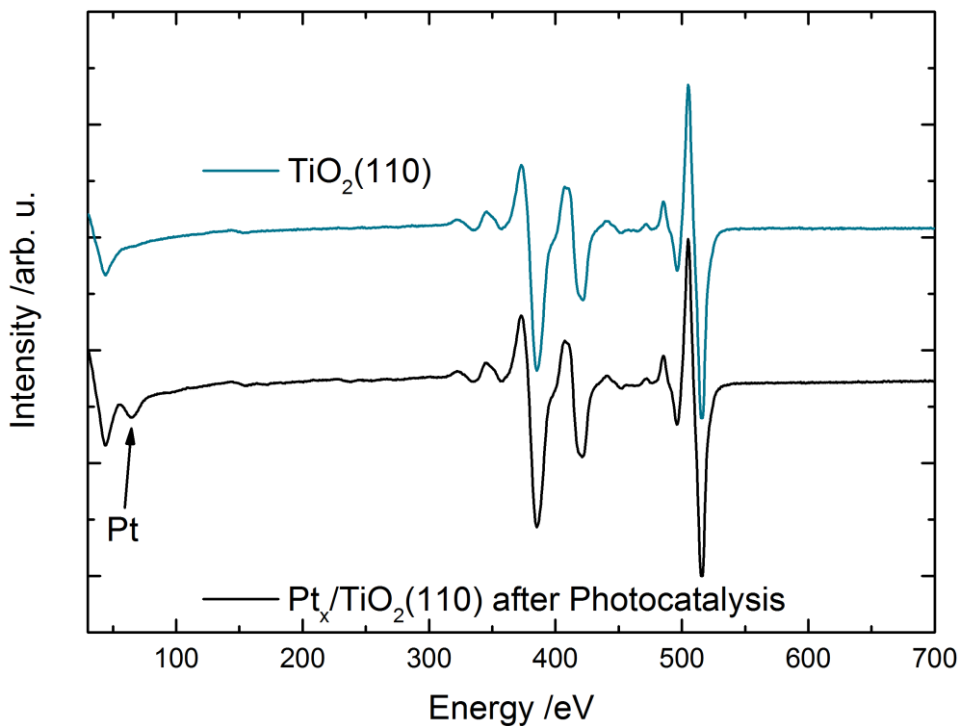


Fig. S1: Auger electron spectrum of the freshly prepared TiO<sub>2</sub>(110) semiconductor (blue) and the Pt<sub>x</sub>/TiO<sub>2</sub>(110) catalyst (black) after photocatalytic experiments for 2 h and 15 min of additional illumination at the reaction temperature without reactant atmosphere. Within the detection limit, no significant carbon containing species (expected at 272 eV) are detected on the surface. Platinum is detected around 64 eV, while the characteristic peaks for titanium and oxygen are located between 350 and 525 eV.



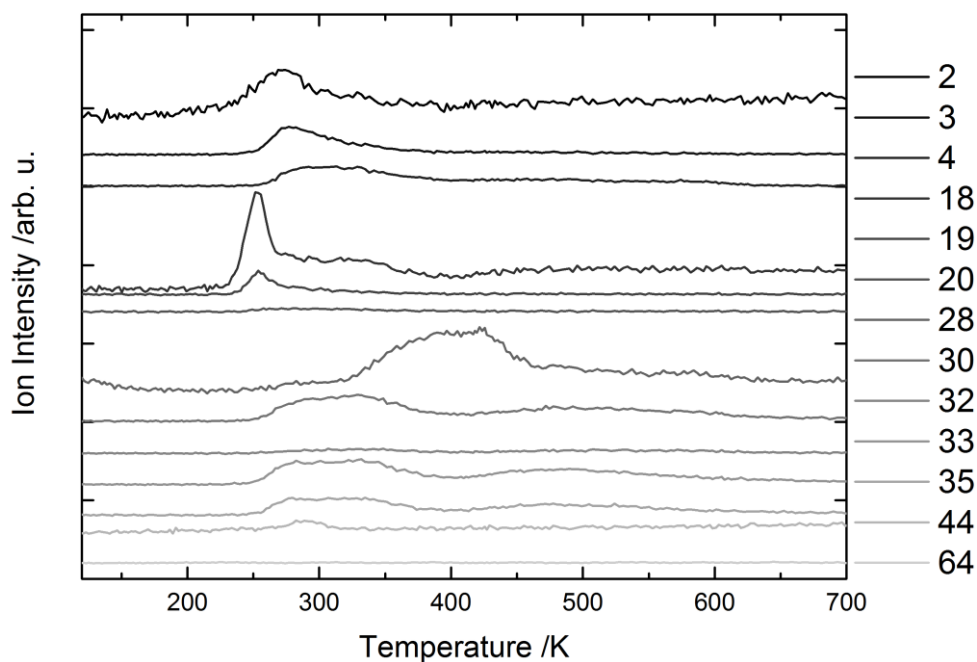


Fig S2: Temperature-programmed desorption of 1 L of methanol- $d_3$  on Pt $_x$ /TiO $_2$ (110). The traces represent raw data and are not corrected. The observations are in excellent agreement in all mass traces with the work of Hao *et al.*<sup>1</sup>, with the exception of the absence of hydrogen at higher temperatures. We relate this difference in the desorption of H $_2$  to the co-catalyst due to different cluster loadings, cluster size and treatment procedure, further supporting the role of the platinum clusters as recombination sites for H $_2$ .<sup>2-3</sup> In both works, potential molecules such as methyl formate- $d_6$  (mass 64), methane- $d_3$  (mass 19) and methane- $d_4$  (mass 20) are not observed. Mass 35 (methanol- $d_3$ ) and mass 32 (formaldehyde- $d_2$ ) follow the trend observed in Fig. 3, corroborated by the joint mass fragment 30 of methanol- $d_3$  and formaldehyde- $d_2$ . Mass 18 is mainly attributed to water as an impurity in the methanol source and mass 19 is attributed to the scrambling products, since methanol decomposition already sets in below the observed temperature of 275 K, evident by the hydrogen signals (2, 3 and 4).

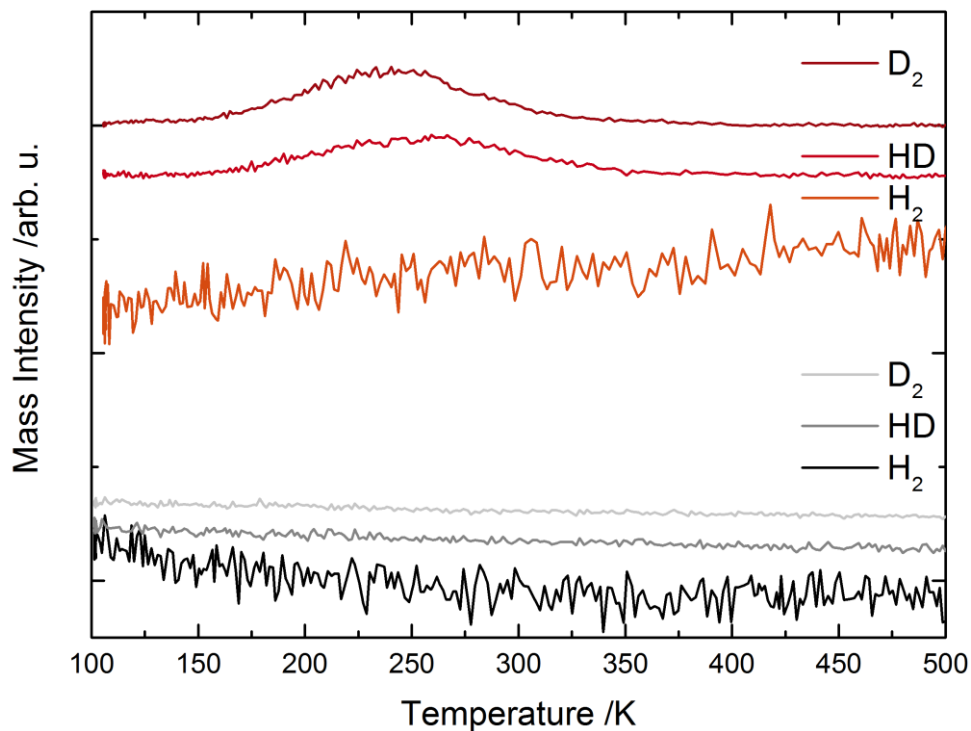


Fig. S3: Temperature programmed desorption of 1 L of D<sub>2</sub> on the TiO<sub>2</sub>(110) surface (grey traces) and the Pt<sub>x</sub>/TiO<sub>2</sub>(110) photocatalyst (red traces). On bare TiO<sub>2</sub>(110), Deuterium does not adsorb on the surface at 100 K in agreement with literature.<sup>4-5</sup> On the Pt cluster-loaded TiO<sub>2</sub>(110), Deuterium does adsorb on the Pt clusters and desorbs in a broad feature around 240 K. A similar peak is observed for the HD trace, indicating some HD scrambling in agreement with literature.<sup>6-7</sup>

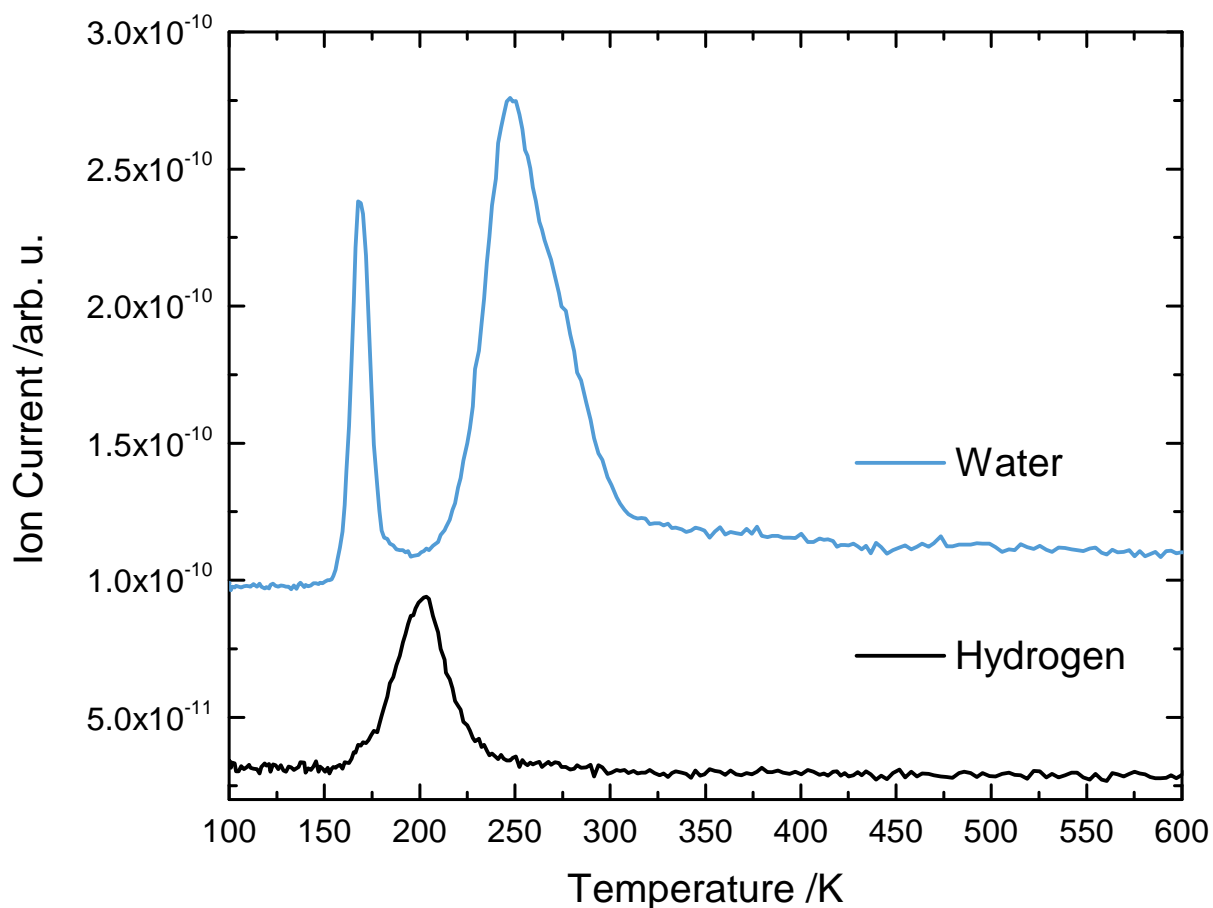


Fig. S4: Temperature programmed desorption measurement of 1.31 ML of H<sub>2</sub>O adsorbed at 100 K on Pt<sub>x</sub>/TiO<sub>2</sub>(110). Water from the O-lattice sites desorbs around 160 K, while H<sub>2</sub>O from the Ti-lattice sites desorbs around 255 K. Hydrogen desorbs between 180 K and 250 K in a peak centered around 210 K in very good agreement with a previous report.<sup>3</sup>



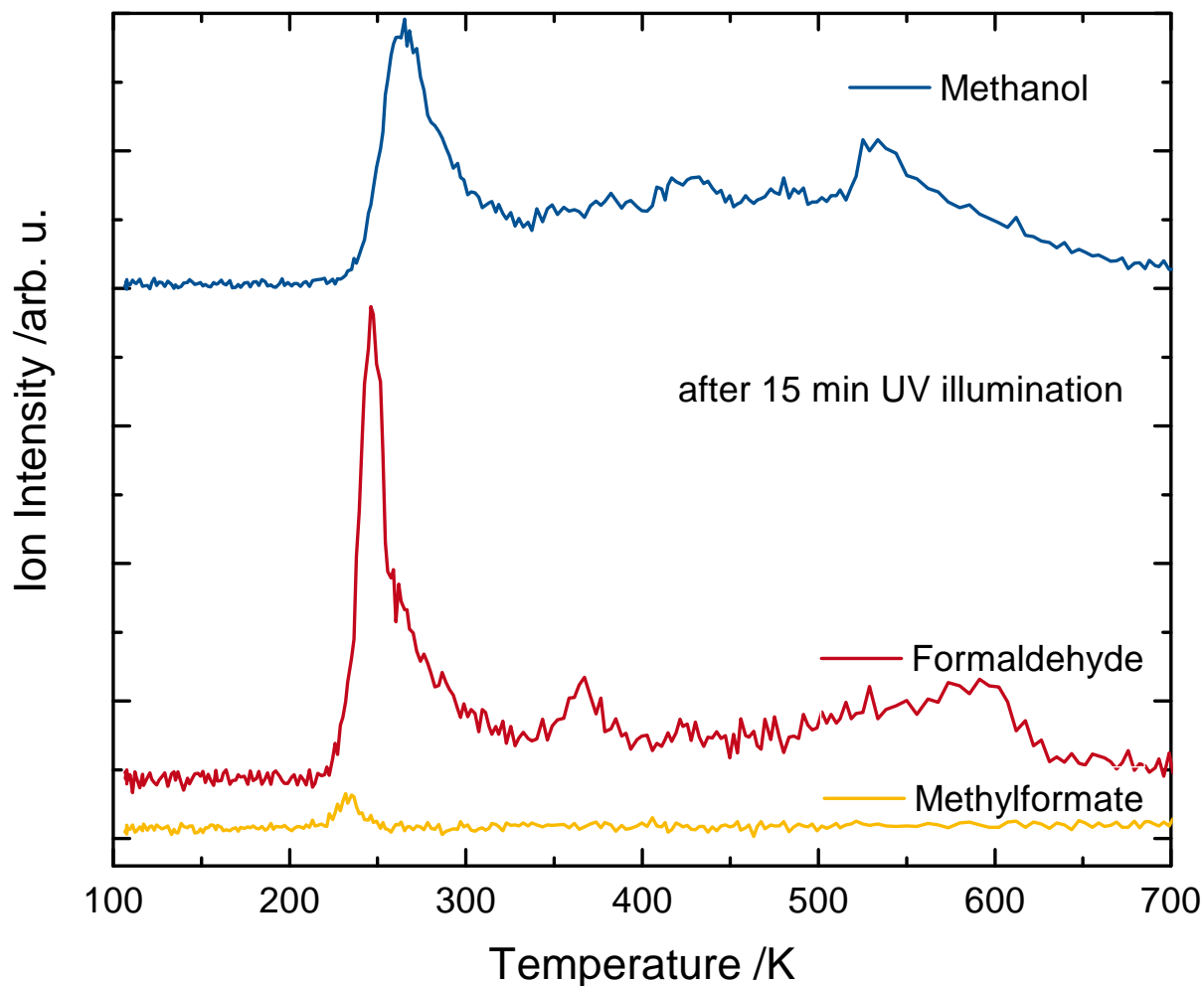


Fig. S5: Post-Irradiation TPD of 1 L of  $\text{CD}_3\text{OH}$  on  $\text{r-TiO}_2(110)$  after 15 min of UV illumination at 110 K. Note, that methanol is oxidized to formaldehyde and in a second photo-oxidation to methyl formate, in excellent agreement with a previous report.<sup>8</sup> Methanol is identified by mass 35, formaldehyde by mass 30 and methyl formate by mass 64. All traces are corrected for the fragmentation patterns.<sup>8-10</sup>

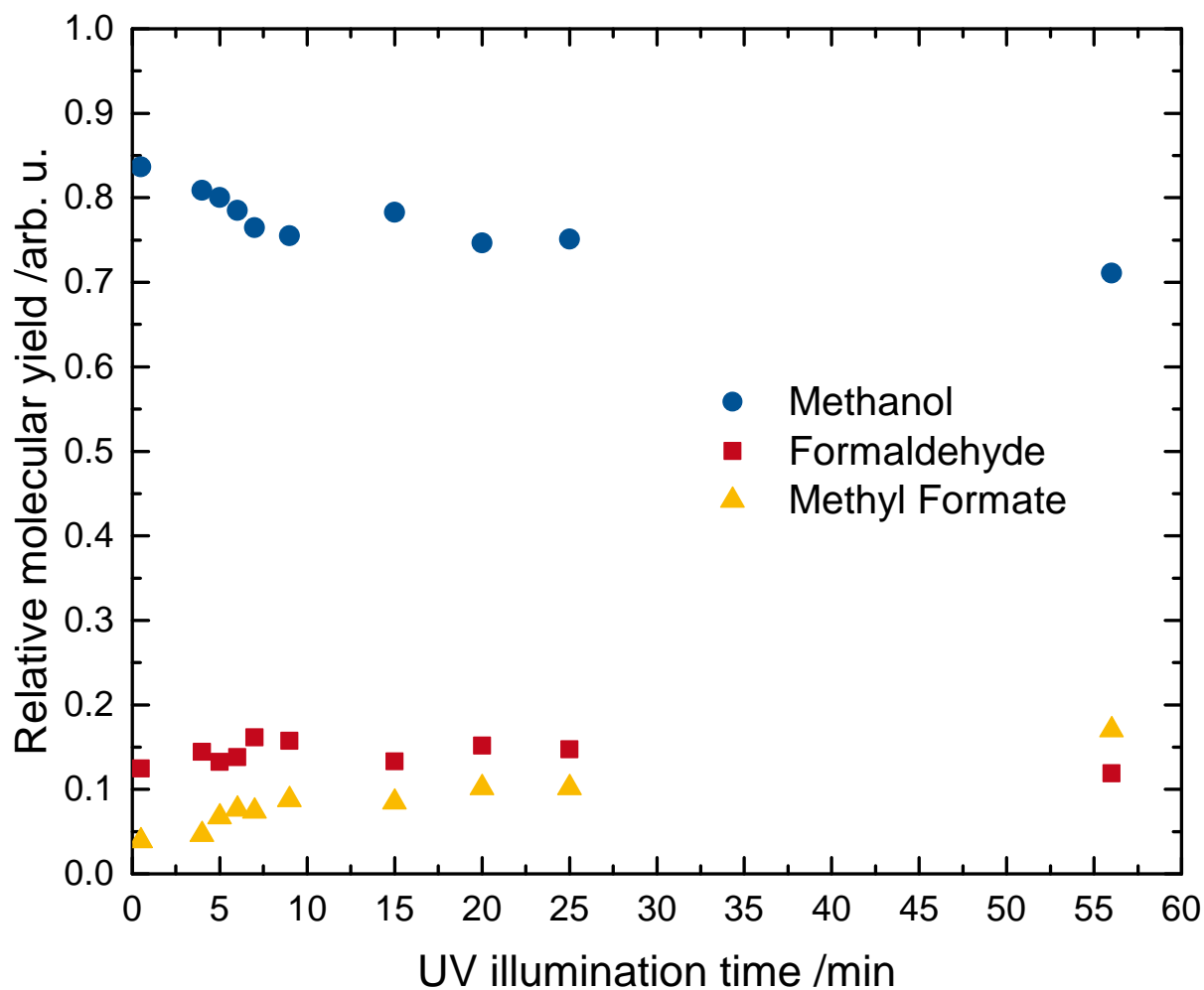


Fig. S6: Product evolution of the PI-TPDs with varied illumination time at 110 K. Methanol is adsorbed on the bare  $r\text{-TiO}_2(110)$  surface and illuminated for a certain time period with UV light. PI-TPD is used to quantify the photoreaction products. Formaldehyde forms even at the shortest illumination times, while the consecutive photocoupling reaction becomes more dominant at larger illumination times in very good agreement with literature.<sup>8</sup> Note, that not all methanol can be converted in these experiments, indicating a poisoning of the reaction at cryogenic temperatures.

The surface lifetime of a species can be estimated from an evaluation of the rate of desorption from a surface. The rate of desorption is given by:

$$-\frac{d\theta}{dt} = v_d \times f(\theta) \times \exp\left(-\frac{\Delta H}{RT}\right) \quad (\text{Eq. S1})$$

While the exponential term (with the desorption energy  $\Delta H$ ) together with pre-exponential factor  $v_d$  reflects the temperature-dependent rate constant,  $f(\theta)$  considers the concentration-dependence of the rate. Assuming a first desorption process and that the desorption is coverage-independent, one can rewrite the formula to:

$$-\frac{d\theta}{dt} = v_d \times \theta \times \exp\left(-\frac{\Delta H}{RT}\right) \quad (\text{Eq. S2})$$

$$-\int_{\theta_i}^{\theta_f} \frac{d\theta}{\theta} = \int_0^{t_f} v_d \times \exp\left(-\frac{\Delta H}{RT}\right) dt \quad (\text{Eq. S3})$$

$$t = \ln\left(\frac{\theta_i}{\theta_f}\right) \times \frac{1}{v_d \times \exp\left(-\frac{\Delta H}{RT}\right)} \quad (\text{Eq. S4})$$

Using the  $\left(\frac{\theta_f}{\theta_i}\right) = 2$  by definition, the surface lifetime is then given by:

$$t_{1/2} = \frac{\ln(2)}{v_d \times e^{-\frac{\Delta H}{RT}}} \quad (\text{Eq. S5})$$

The pre-exponential factors are determined by a method established by Campbell *et al.* and can be obtained from the gas-phase entropies of the molecules.<sup>11-12</sup> These pre-exponential factors can be used in a Redhead formalism<sup>13</sup> to calculate and apparent desorption enthalpy. All of these values are given in Table S1 and set the foundation to calculate the surface residence time at a given temperature.

Table S1: Tabulated values for the gas phase entropy and the resulting pre-exponential factors as well as the activation barriers.

Molecule	Gasphase Entropy $S_0$ [ J/mol $\times$ K]	Reference	Pre-exponential Factor $v_d$ [ $s^{-1}$ ]	Desorption Enthalpy $\Delta H$ [kJ/mol]
Methanol	236.12	14	3.8771E+15	82.9786
Formaldehyde	219.00	15	2.2297E+15	75.4629
Methyl Formate	282.31	15	1.1253E+16	75.3847

## References

1. Hao, Q.; Zhiqiang, W.; Wang, T.; Ren, Z.; Zhou, C.; Yang, X., Role of Pt Loading in the Photocatalytic Chemistry of Methanol on Rutile TiO<sub>2</sub>(110). *ACS Catal.* **2019**, *9*, 286-294.
2. Walenta, C. A.; Kollmannsberger, S. L.; Courtois, C.; Pereira, R. N.; Stutzmann, M.; Tschurl, M.; Heiz, U., Why Co-Catalyst-loaded Rutile Facilitates Photocatalytic Hydrogen Evolution. *Phys. Chem. Chem. Phys.* **2019**, *21*, 1491-1496.
3. Geng, Z.; Jin, X.; Wang, R.; Chen, X.; Guo, Q.; Ma, Z.; Dai, D.; Fan, H.; Yang, X., Low-Temperature Hydrogen Production via Water Conversion on Pt/TiO<sub>2</sub>. *J. Phys. Chem. C* **2018**, *122*, 10956-10962.
4. Chen, L.; Li, Z.; Smith, R. S.; Kay, B. D.; Dohnálek, Z., Molecular Hydrogen Formation from Proximal Glycol Pairs on TiO<sub>2</sub>(110). *J. Am. Chem. Soc.* **2014**, *136*, 5559-5562.
5. Zhang, Z.; Yates, J. T., A New Form of Chemisorbed Photo- and Electro-Active Atomic H Species on the TiO<sub>2</sub>(110) surface. *Surf. Sci.* **2016**, *652*, 195-199.
6. Riedel, J. N.; Rötzer, M. D.; Jørgensen, M.; Vej-Hansen, U. G.; Pedersen, T.; Sebok, B.; Schweinberger, F. F.; Vesborg, P. C. K.; Hansen, O.; Schiøtz, J.; Heiz, U.; Chorkendorff, I., H<sub>2</sub>/D<sub>2</sub> Exchange Reaction on Mono-Disperse Pt Clusters: Enhanced Activity from Minute O<sub>2</sub> Concentrations. *Catal. Sci. Technol.* **2016**, *6*, 6893-6900.
7. Joo, J. B.; Dillon, R.; Lee, I.; Yin, Y.; Bardeen, C. J.; Zaera, F., Promotion of Atomic Hydrogen Recombination as an Alternative to Electron Trapping for the Role of Metals in the Photocatalytic Production of H<sub>2</sub>O. *Proc. Natl. Acad. Sci.* **2014**, *111*, 7942.
8. Guo, Q.; Xu, C.; Yang, W.; Ren, Z.; Ma, Z.; Dai, D.; Minton, T. K.; Yang, X., Methyl Formate Production on TiO<sub>2</sub>(110), Initiated by Methanol Photocatalysis at 400 nm. *J. Phys. Chem. C* **2013**, *117*, 5293-5300.
9. Phillips, K. R.; Jensen, S. C.; Baron, M.; Li, S.-C.; Friend, C. M., Sequential Photo-Oxidation of Methanol to Methyl Formate on TiO<sub>2</sub>(110). *J. Am. Chem. Soc.* **2013**, *135*, 574-577.
10. Yuan, Q.; Wu, Z.; Jin, Y.; Xu, L.; Xiong, F.; Ma, Y.; Huang, W., Photocatalytic Cross-Coupling of Methanol and Formaldehyde on a Rutile TiO<sub>2</sub>(110) Surface. *J. Am. Chem. Soc.* **2013**, *135*, 5212-5219.
11. Campbell, C. T.; Sellers, J. R. V., The Entropies of Adsorbed Molecules. *J. Am. Chem. Soc.* **2012**, *134*, 18109-18115.
12. Campbell Charles, T.; Árnadóttir, L.; Sellers Jason, R. V., Kinetic Prefactors of Reactions on Solid Surfaces. In *Z. Phys. Chem.*, 2013, *227*, p 1435.
13. Redhead, P. A., Thermal Desorption of Gases. *Vacuum* **1962**, *12*, 203-211.
14. Chao, J.; Hall, K. R.; Marsh, K. N.; Wilhoit, R. C., Thermodynamic Properties of Key Organic Oxygen Compounds in the Carbon Range C1 to C4. Part 2. Ideal Gas Properties. *J. Phys. Chem. Ref. Data* **1986**, *15*, 1369-1436.
15. NIST Chemistry WebBook, NIST Standard Reference Database Number 69. Mallard, P. J. L. a. W. G., Ed. National Institute of Standards and Technology, Gaithersburg MD, 20899. (accessed retrieved June 5, 2018).

# Surface Reduction State Determines Stabilization and Incorporation of Rh on $\alpha$ -Fe<sub>2</sub>O<sub>3</sub>(1 $\bar{1}$ 02)

Florian Kraushofer, Nikolaus Resch, Moritz Eder, Ali Rafsanjani-Abbasi, Sarah Tobisch, Zdenek Jakub, Giada Franceschi, Michele Riva, Matthias Meier, Michael Schmid, Ulrike Diebold, and Gareth S. Parkinson\*

Iron oxides (FeO<sub>x</sub>) are among the most common support materials utilized in single atom catalysis. The support is nominally Fe<sub>2</sub>O<sub>3</sub>, but strongly reductive treatments are usually applied to activate the as-synthesized catalyst prior to use. Here, Rh adsorption and incorporation on the (1 $\bar{1}$ 02) surface of hematite ( $\alpha$ -Fe<sub>2</sub>O<sub>3</sub>) are studied, which switches from a stoichiometric (1 × 1) termination to a reduced (2 × 1) reconstruction in reducing conditions. Rh atoms form clusters at room temperature on both surface terminations, but Rh atoms incorporate into the support lattice as isolated atoms upon annealing above 400 °C. Under mildly oxidizing conditions, the incorporation process is so strongly favored that even large Rh clusters containing hundreds of atoms dissolve into the surface. Based on a combination of low-energy ion scattering (LEIS), X-ray photoelectron spectroscopy (XPS) and scanning tunneling microscopy (STM) data, as well as density functional theory (DFT), it is concluded that the Rh atoms are stabilized in the immediate subsurface, rather than the surface layer.

form chemical bonds with the support, which affects their electronic structure and catalytic properties. To accurately model such a system requires the atomic-scale structure of the active site to be known. This information is extremely difficult to ascertain using current experimental methods, particularly under reaction conditions, and most theoretical calculations assume a high-symmetry site on an idealized periodic surface.<sup>[1,8–11]</sup> Transmission electron microscopy (TEM) images usually suggest that isolated adatoms are located in cation-like sites relative to the bulk structure,<sup>[1,12–17]</sup> but it is important to realize that, with this technique, neither the termination of the support nor the binding coordination of the adatom can be unambiguously determined.

## 1. Introduction

Stabilizing ever smaller metallic clusters on inexpensive metal oxide supports has been a long-standing goal of catalysis research. So-called “single-atom” catalysts (SACs) represent the ultimate limit of this endeavor, but stabilizing single atoms against agglomeration under reaction conditions is challenging.<sup>[1–7]</sup> To be stable, the metal atoms must

Some information is often inferred from ex situ X-ray absorption spectroscopy (XAS) measurements, but these area-averaging methods do not necessarily probe the active sites on inhomogeneous samples, and rely on comparison of the SAC sample to standard samples such as a metal oxide, which may have very different coordination environments. In any case, the reactive environment almost certainly changes the state of the support surface, and with it the coordination environment of the single-atom sites. In situ TEM and XAS are possible for such systems,<sup>[18]</sup> but are not commonly applied.<sup>[19]</sup>

F. Kraushofer, N. Resch, A. Rafsanjani-Abbasi, S. Tobisch, Dr. Z. Jakub, Dr. G. Franceschi, Dr. M. Riva, Dr. M. Meier, Prof. M. Schmid, Prof. U. Diebold, Prof. G. S. Parkinson  
Institute of Applied Physics  
TU Wien

Wiedner Hauptstraße 8–10/E134, 1040 Wien, Austria  
E-mail: parkinson@iap.tuwien.ac.at

M. Eder  
Chair of Physical Chemistry, Department of Chemistry & Catalysis  
Research Center  
TU München  
Lichtenbergstraße 4, 85748 Garching, Germany

Dr. M. Meier  
Faculty of Physics and Center for Computational Materials Science  
University of Vienna  
Kolingasse 14–16, 1090 Wien, Austria

 The ORCID identification number(s) for the author(s) of this article can be found under <https://doi.org/10.1002/admi.202001908>.

© 2021 The Authors. Advanced Materials Interfaces published by Wiley-VCH GmbH. This is an open access article under the terms of the Creative Commons Attribution License, which permits use, distribution and reproduction in any medium, provided the original work is properly cited.

DOI: 10.1002/admi.202001908

Iron oxides (FeO<sub>x</sub>) are popular support materials in heterogeneous catalysis because they are inexpensive and chemically robust. In SAC studies, the as-synthesized support is nominally hematite ( $\alpha$ -Fe<sub>2</sub>O<sub>3</sub>). Consequently, the  $\alpha$ -Fe<sub>2</sub>O<sub>3</sub>(0001) surface with or without point oxygen vacancies is often chosen to represent the FeO<sub>x</sub> support in SAC studies.<sup>[1,8–11]</sup> However, the atomic-scale structure of  $\alpha$ -Fe<sub>2</sub>O<sub>3</sub>(0001) remains particularly controversial, even under highly controlled ultrahigh vacuum (UHV) conditions.<sup>[20]</sup> There is evidence for a ferryl termination in oxidizing conditions,<sup>[21,22]</sup> and a whole host of long-range Moiré reconstructions occur when the surface becomes reduced.<sup>[20,23]</sup> Eventually, when reduced more, the surface transforms to Fe<sub>3</sub>O<sub>4</sub>(111),<sup>[24]</sup> Recently, we have studied the  $\alpha$ -Fe<sub>2</sub>O<sub>3</sub>(1 $\bar{1}$ 02) surface, which is non-polar and similarly prevalent as the (0001) orientation on nanomaterial.<sup>[20,25]</sup> This surface exhibits two terminations: a simple, stoichiometric (1 × 1) termination, and a reduced (2 × 1) reconstruction containing surface Fe<sup>2+</sup>.<sup>[26,27]</sup>

In this paper, we explore how Rh adsorbs on these surface terminations, and if stabilization is affected by oxidation and

reduction of the iron oxide support surface. Using scanning tunneling microscopy (STM), XPS, and He<sup>+</sup> LEIS, we find that Rh forms small clusters on both surface terminations upon vapor-deposition at room temperature (RT), indicative of a low surface diffusion barrier. Upon annealing, however, Rh atoms are accommodated in the subsurface on both surfaces. On the stoichiometric (1 × 1) termination, Rh is stabilized as single atoms in the second cation layer when the sample is heated to 400 °C, and does not diffuse further into the bulk. On the reduced (2 × 1) termination, higher coverages of Rh initially sinter to nanometer-sized clusters upon annealing in UHV, and these then dissolve into the hematite lattice with mild oxidation at 520 °C. These observations imply a strong driving force for Rh incorporation into the immediate subsurface of hematite, indicating a potential route for redispersion of sintered particles.

## 2. Experimental Results

First, we investigated the stability of small amounts of Rh on  $\alpha$ -Fe<sub>2</sub>O<sub>3</sub>( $\bar{1}\bar{1}02$ )-(1 × 1) by depositing 0.025 ML Rh on the freshly prepared surface at RT. In STM [Figure 1a], we clearly observe small Rh clusters on an otherwise pristine surface. Based on the expected number of Rh atoms per unit area after deposition, we can estimate that, on average, a cluster consists of 3–4 atoms. Figure 2a shows XPS results for the Rh 3d region after deposition, and after consecutive heating steps at elevated temperatures. The samples were cooled to RT to acquire XPS

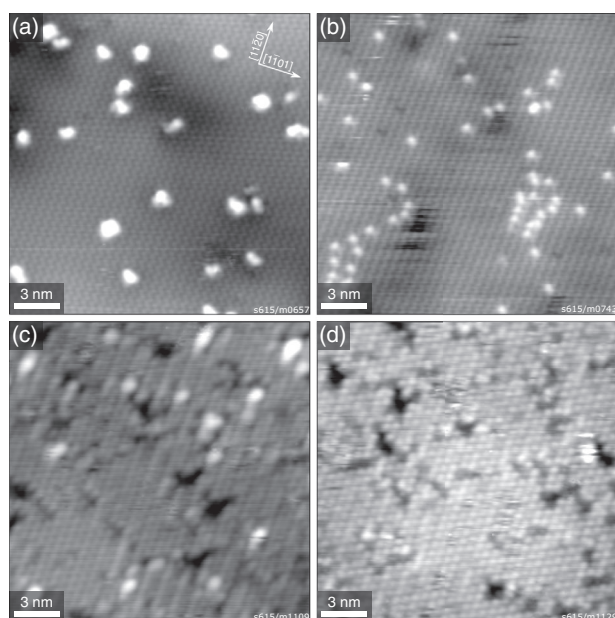


**Figure 1.** STM images of 0.025 ML Rh on  $\alpha$ -Fe<sub>2</sub>O<sub>3</sub>( $\bar{1}\bar{1}02$ ). a) 0.025 ML Rh as deposited on the clean  $\alpha$ -Fe<sub>2</sub>O<sub>3</sub>( $\bar{1}\bar{1}02$ )-(1 × 1) surface at room temperature ( $U_{\text{sample}} = +3$  V,  $I_{\text{tunnel}} = 0.3$  nA) and b) after annealing at 500 °C for 15 min in UHV ( $U_{\text{sample}} = -2.8$  V,  $I_{\text{tunnel}} = 0.1$  nA). c) 0.025 ML Rh as deposited on the clean  $\alpha$ -Fe<sub>2</sub>O<sub>3</sub>( $\bar{1}\bar{1}02$ )-(2 × 1) surface ( $U_{\text{sample}} = -3$  V,  $I_{\text{tunnel}} = 0.1$  nA) and d) after annealing at 300 °C for 10 min in UHV ( $U_{\text{sample}} = -2.8$  V,  $I_{\text{tunnel}} = 0.1$  nA). The images are from the same measurement series as the XPS results shown in Figure 2.

and STM data between the heating steps. Additional STM images from the annealing series are shown in Figure S1, Supporting Information. Immediately after deposition, the Rh 3d peak is relatively broad, with a maximum at  $\approx 307.8$  eV [black line in Figure 2a]. Since the Rh 3d<sub>5/2</sub> peak always exactly mirrors the 3d<sub>3/2</sub> peak with a shift of 4.8 eV and two thirds of the intensity, we will only discuss the 3d<sub>5/2</sub> peak from here on. When fitting the Rh 3d region, appropriate additional components, fully constrained in position, area, and FWHM, were added for the 3d<sub>3/2</sub> peak.

After heating to 200 °C, the Rh 3d<sub>5/2</sub> peak sharpens and shifts to lower binding energies [yellow line in Figure 2a]. This correlates with the formation of larger clusters in STM [Figure S1b, Supporting Information]. At higher temperatures, the peak splits into a component at the position associated with the larger clusters at  $\approx 307.5$  eV, close to that of metallic bulk Rh,<sup>[28]</sup> and a component at higher binding energy. The evolution of the area ratio between these two components is shown in Figure 2c (black). For simplicity, we refer to the second component as the “oxidized” contribution, though it should be noted that for the small clusters found initially, the shift could also be explained at least in part by final state effects related to the cluster size.<sup>[29,30]</sup> Taking a possible asymmetry of the metallic peak into account, with a tail toward higher binding energy, would further reduce the fraction of oxidized Rh, so the percentages of metallic Rh shown in Figure 2c should be taken as a lower limit. After annealing to 550 °C, the metallic component disappears and the Rh 3d<sub>5/2</sub> peak sharpens significantly [red line in Figure 2a]. In this state, the peak contains a single component at 309.3 eV, which can be assigned to an oxidized Rh species. This binding energy is significantly higher than the  $\approx 308.6$  eV that were previously reported for bulk Rh<sub>2</sub>O<sub>3</sub>,<sup>[28,31,32]</sup> and is closer to that reported for RhO<sub>2</sub>.<sup>[31]</sup> In STM, this development corresponds to a disappearance of the clusters, and single bright features are instead observed at negative sample bias [Figure 1b]. A few of these bright features coexisting with clusters are observed in STM starting at 300 °C [Figure S1c–f, Supporting Information], in good agreement with the appearance of the oxidized peak at 309.3 eV in XPS [Figure 2a]. We attribute this to Rh being liberated from the clusters and substituted into Fe sites in the hematite surface. Some of these features are still grouped together locally after annealing to 500 °C, suggesting that the incorporated Rh remains in the vicinity of the original cluster due to slow diffusion within the hematite lattice. However, after annealing for longer times, a random distribution can also be achieved, as shown in Figure S2, Supporting Information. Interestingly, we found no further decrease in the XPS peak intensity even after annealing for 2 h at 520 °C in  $2 \times 10^{-6}$  mbar O<sub>2</sub>, which indicates that Rh does not diffuse further into the bulk under these conditions.

In the annealing series shown in Figure 1 and Figure S2a–h, Supporting Information, the consecutive heating steps were all performed in UHV, which results in the surface being mostly reduced to the (2 × 1) termination after heating to 550 °C. Patches of the (1 × 1) structure remain only at step edges [Figure S1h, Supporting Information]. This is the expected behavior, as annealing in UHV at these temperatures is the normal preparation procedure for the (2 × 1) termination.<sup>[26]</sup>



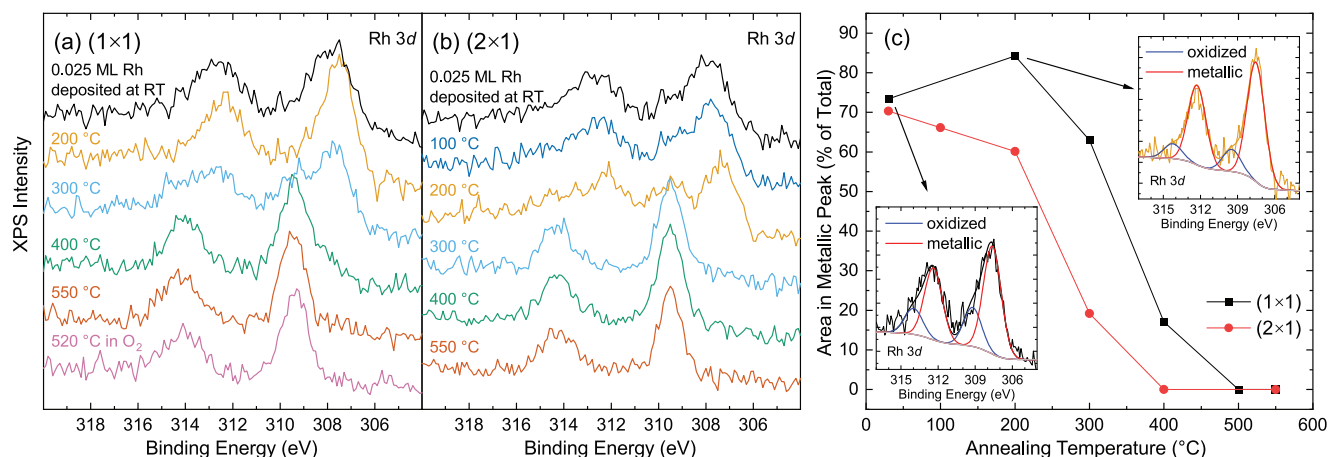


**Figure 2.** Analyzing the thermal stability using the Rh 3d region in XPS. a,b) XPS spectra (Al K $\alpha$ , 70° grazing emission, pass energy 16 eV, offset vertically for clarity) of the Rh 3d core-level peaks for 0.025 ML Rh on the  $\alpha$ -Fe<sub>2</sub>O<sub>3</sub>( $\bar{1}\bar{1}02$ )-(1  $\times$  1) and (2  $\times$  1) surfaces, respectively, as deposited at room temperature and after successive annealing steps in UHV at different temperatures (at least 10 min per step). The spectra were acquired after cooling back to room temperature. For the bottom-most spectrum in (a), the sample was annealed for 30 min at 520 °C in a background of  $2 \times 10^{-6}$  mbar O<sub>2</sub>. c) Area percentages for peak fits to the spectra in (a) and (b) using two components for Rh 3d<sub>5/2</sub>. Fit results for the first two curves in (a) are shown in the insets to (c).

In the presence of Rh, however, small patches of the reduced (2  $\times$  1) termination were found at step edges already after heating to 400 °C [Figure S1e,f, Supporting Information], which is insufficient to form the (2  $\times$  1) termination in the absence of Rh. The (1  $\times$  1) termination could be restored everywhere by the final heating step at 520 °C in  $2 \times 10^{-6}$  mbar O<sub>2</sub> [Figure S1i, Supporting Information] without loss of Rh signal in XPS [Figure 2a, pink]. Qualitatively, this is the same end result as was obtained when heating in  $2 \times 10^{-6}$  mbar O<sub>2</sub> directly after Rh deposition [Figure S2, Supporting Information], which prevents the surface from being reduced in the first place.

On the  $\alpha$ -Fe<sub>2</sub>O<sub>3</sub>( $\bar{1}\bar{1}02$ )-(2  $\times$  1) termination, the initial state immediately after Rh deposition is similar as on the (1  $\times$  1) termination, with small clusters observed in STM [Figure 1c]. The behavior of the Rh 3d peak in XPS with increasing temperature also qualitatively resembles the trends observed on the (1  $\times$  1) termination. The peaks were again fitted by a metallic and an oxidized contribution. However, analysis of the peak intensity ratios [Figure 2c] highlights some differences between the two cases: On the (1  $\times$  1) surface, the metallic contribution initially increases up to 200 °C, corresponding to sintering without incorporation. On the (2  $\times$  1) termination, the metallic component decreases from the very beginning, and disappears completely at 400 °C, at a lower temperature than on the (1  $\times$  1) termination (500 °C). In STM, images taken after annealing to 300 °C [Figure 1d] resemble those of the pristine surface, with no visible signature of the Rh, although it remains present in XPS. Additional STM data from this annealing series is shown in Figure S3, Supporting Information.

As the Rh 3d peak in XPS does not weaken significantly even at high annealing temperatures on either surface termination, and since Rh-related protrusions remain clearly visible in STM on the (1  $\times$  1) surface, the obvious question is whether the Rh is located directly in the surface layer. To answer this, we performed LEIS with 1 keV He<sup>+</sup> ions on both terminations, an exquisitely surface-sensitive technique. The spectra (Figure 3)

clearly show a Rh peak directly following Rh deposition, but no trace of Rh is found in LEIS after annealing. This strongly suggests that incorporated rhodium is situated in the subsurface, rather than the surface layer, for both the (1  $\times$  1) and (2  $\times$  1) termination.

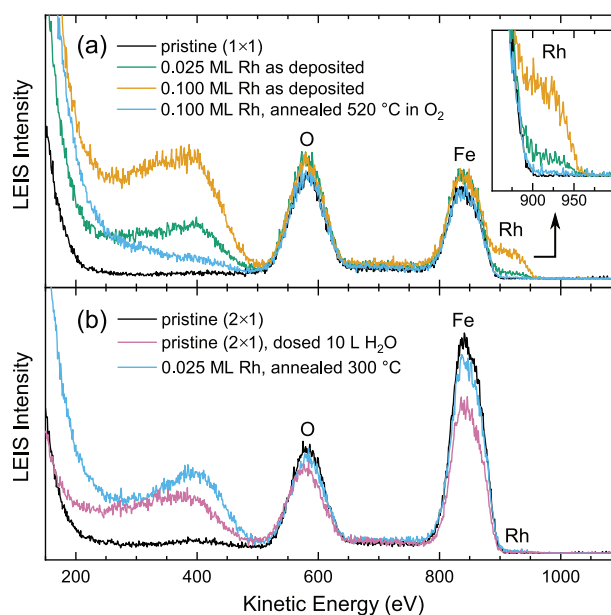


**Figure 3.** He<sup>+</sup> LEIS of as-deposited and incorporated Rh. LEIS measurements (1 keV He<sup>+</sup>, 90° scattering angle) of a) Rh on the  $\alpha$ -Fe<sub>2</sub>O<sub>3</sub>( $\bar{1}\bar{1}02$ )-(1  $\times$  1) surface and b) on the (2  $\times$  1) termination. In panel (a), as-deposited Rh is clearly visible as a peak at  $\approx$ 920 eV for both the 0.025 and 0.1 ML coverage. A magnified view of the Rh region is shown in the inset. The broad peak below 500 eV is correlated with adsorbed water, as demonstrated by the spectrum acquired after dosing 10 L H<sub>2</sub>O (1 L =  $1.33 \times 10^{-6}$  mbar  $\times$  s) on the clean (2  $\times$  1) surface (b, pink). We attribute this peak to fast hydrogen recoils (at 90° scattering angle, these must be either H<sup>+</sup> recoils deflected at surface atoms or H<sup>+</sup> recoils created by He deflected at surface atoms).

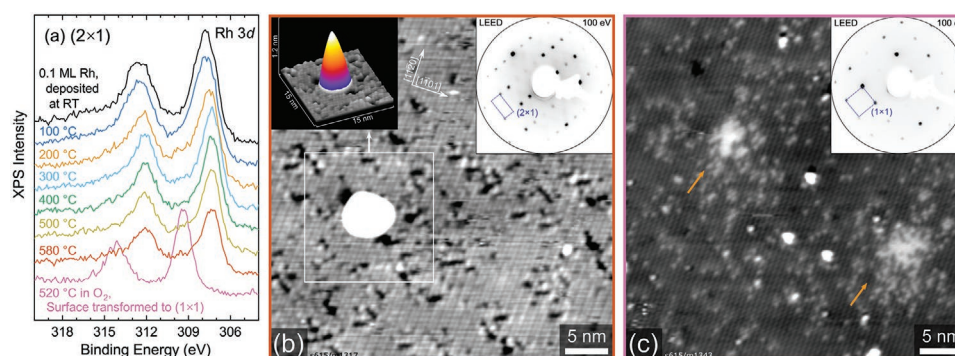


**Figure 4.** 0.1 ML Rh on  $\alpha$ -Fe<sub>2</sub>O<sub>3</sub>( $\bar{1}\bar{1}02$ )-(2 × 1). a) The Rh 3d region in XPS (Al K $\alpha$ , 70° grazing emission, pass energy 16 eV) after depositing 0.1 ML Rh on the  $\alpha$ -Fe<sub>2</sub>O<sub>3</sub>( $\bar{1}\bar{1}02$ )-(2 × 1) surface, then successively annealed in UHV for 10 min at different temperatures. For the last spectrum (pink), the sample was annealed for 1 h at 520 °C in a background of  $2 \times 10^{-6}$  mbar O<sub>2</sub>. All spectra were acquired after cooling the sample to room temperature. b) 40 × 40 nm<sup>2</sup> STM image ( $U_{\text{sample}} = -2.5$  V,  $I_{\text{tunnel}} = 0.1$  nA) taken after heating the sample to 580 °C [red line in (a)]. Large clusters are found on the surface, one of which is plotted in 3D as an inset ( $\approx 1.1$  nm apparent height). A LEED pattern of the surface with (2 × 1) periodicity is shown in the top right. c) 40 × 40 nm<sup>2</sup> STM image ( $U_{\text{sample}} = -3$  V,  $I_{\text{tunnel}} = 0.1$  nA) taken after annealing the sample at 520 °C in  $2 \times 10^{-6}$  mbar O<sub>2</sub> for 1 h. The surface periodicity has changed to (1 × 1), as also seen in the LEED pattern (inset). Orange arrows indicate local agglomerations of brighter features in the surface.

Finally, we explored how the findings for 0.025 ML of Rh extend to a higher coverage (0.1 ML). On the stoichiometric (1 × 1) surface, the results are essentially the same as for 0.025 ML, with all Rh atoms ultimately being incorporated into the surface. An STM image and the corresponding XPS data of 0.1 ML of Rh incorporated in the (1 × 1) surface is shown in Figure S2, Supporting Information. On the reduced, (2 × 1)-reconstructed surface, however, we find a decidedly different behavior for 0.1 ML Rh (Figure 4). In XPS [Figure 4a], the Rh 3d<sub>5/2</sub> peak progressively shifts to 307.3 eV upon heating and remains there, in good agreement with literature values for metallic Rh.<sup>[28]</sup> Fits of the Rh 3d data are shown in Figure S4, Supporting Information, using the same fitting procedure as described above for the low-coverage case. The metallic component dominates at all times, but an oxidized component is also present, most strongly after heating to 200 °C. In STM, this corresponds to sintering of Rh into large clusters, as shown in Figure 4b after annealing to 580 °C in UHV. The increased cluster height also explains the decrease of the overall Rh intensity to 49% of the value after deposition, since the photoelectron signal from Rh in deeper layers of the clusters is attenuated by the layers above. Additional STM images for the entire annealing series are shown in Figure S5, Supporting Information. Assuming a spherical cap shape, we estimate that the cluster visible in Figure 4b contains  $\approx 1200$  Rh atoms. This is an upper bound for the actual number of atoms, as the cluster shape is always convoluted with the tip shape in STM. Interestingly, even for these very large clusters, Rh atoms can still be completely dissolved and incorporated into the surface upon annealing in oxygen, as seen in the STM image in Figure 4c. Again, bright features within the lattice are visible, and these are often agglomerated locally [orange arrows in Figure 4c]. Both STM and LEED [inset to Figure 4c] show that the surface itself is transformed from the reduced (2 × 1) reconstruction to the stoichiometric (1 × 1) termination, as expected after oxygen annealing. In XPS, the Rh 3d peak [pink line in Figure 4a] again shifts to 309.3 eV, as observed whenever Rh is incorporated into the hematite lattice [Figure 2a,b].

### 3. Density Functional Theory Calculations

To rationalize the stabilization of Rh in the subsurface, we performed DFT calculations for the (1 × 1) termination, with one Fe atom substituted by Rh in a (2 × 2) supercell. The substitution was tested for the first eight cation layers, and relative energies are shown in Figure 5. We find the first subsurface layer (C2) to be energetically most favorable, with an energy gain of  $-0.49$  eV compared to the immediate surface layer. The second subsurface layer (C3) is 0.14 eV worse than C2, and below that, the substitution energy is already converged to a bulk value (0.12 eV worse than C2). These energies explain why extended annealing of the system does not lead to the diffusion of much Rh into the bulk of the sample at the temperatures used in this work.

Substitution of multiple Fe atoms in layer C2 by Rh was tested in a (3 × 3) supercell. The substitution energy per Rh atom stayed the same when a second Rh atom was placed in either of the nearest-neighbor sites in the subsurface layer. This means that there is neither repulsive nor attractive interaction between neighboring Rh atoms in these sites, and thus no enthalpic preference to accumulate or disperse them, consistent with the observation of areas with high Rh concentration in Figure 4c. However, random dispersion is favored to maximize entropy.

In all tested configurations, the calculated spin magnetic moments for Fe suggest that all iron remained Fe<sup>3+</sup> ( $4 \mu_B$ ), with no evidence of Fe<sup>2+</sup> ( $3.5 \mu_B$ ).<sup>[26]</sup> No direct conclusions about the Rh charge state can be drawn from the spin magnetic moment of Rh, which we always found to be close to zero. However, the Rh ion in the preferred C2 configuration exhibits a Bader charge of only +1.15 e, lower than in RhO<sub>2</sub> (+1.45 e) and in Rh<sub>2</sub>O<sub>3</sub> (+1.22 e), which suggests a formal charge state of 3+ or less. Based on the known overall charge of the slab and the fact that no iron appears to be reduced, we therefore assign the rhodium as Rh<sup>3+</sup>.



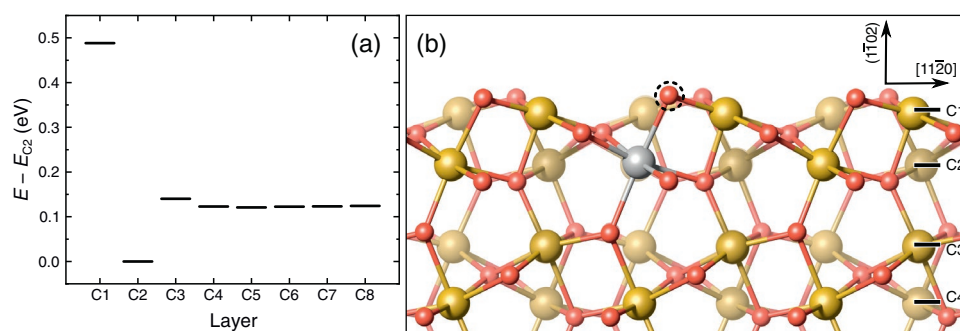


**Figure 5.** DFT results for Rh substitution in the  $\alpha\text{-Fe}_2\text{O}_3(1\bar{1}02)-(1 \times 1)$  surface. a) Substitution energies of one Rh atom replacing one Fe atom in a given layer, referenced to the substitution energy in the first subsurface layer (C2). b) Side view (looking along the  $[\bar{1}101]$  direction) of the  $\alpha\text{-Fe}_2\text{O}_3(1\bar{1}02)-(1 \times 1)$  surface, as in ref. [26]. Cation layers C1–C4 are labeled on the right. Iron is drawn as brown (large), oxygen as red (small) spheres. One iron atom in the first subsurface cation layer is replaced by Rh (grey), which corresponds to the most favorable substitution site according to panel (a). The surface oxygen atom bound directly to Rh is marked by a dashed circle. The direction perpendicular to the surface is labeled as  $(1\bar{1}02)$  in round brackets because there is no integer-index vector corresponding to that direction for the  $(1\bar{1}02)$  plane.

## 4. Discussion

Our results show that, in contrast to  $\text{Fe}_3\text{O}_4(001)$ ,<sup>[33]</sup> neither the stoichiometric  $(1 \times 1)$  surface nor the reduced  $(2 \times 1)$  reconstruction of  $\alpha\text{-Fe}_2\text{O}_3(1\bar{1}02)$  stabilizes Rh adatoms at RT. However, on the  $(1 \times 1)$  termination at least, single atoms can incorporate into the hematite lattice via a thermally activated process. This makes sense, because  $\text{Rh}_2\text{O}_3$ , the most stable Rh oxide, is isostructural with  $\alpha\text{-Fe}_2\text{O}_3$ . Interestingly, our results show that even large clusters can be re-dispersed by very mild oxidation, and these atoms remain visible in STM [Figure 2b]. However, the fact that no Rh signal remains in LEIS after incorporation (Figure 3) strongly suggests that the Rh atoms are in fact not situated in the topmost cation layer, but rather in the subsurface, in agreement with our DFT results. Since the presence of the incorporated Rh atoms is most clearly visible in filled-states images, where oxygen atoms are imaged,<sup>[26]</sup> we conclude that we observe a modified density of states for the surface oxygen atom that is bound directly to an Rh atom in the immediate subsurface layer, marked by a dashed circle in Figure 5b. The dopants are also visible at some positive bias values, as shown in Figure S6, Supporting Information. This indicates that the electronic structure of surface Fe atoms in the vicinity of subsurface Rh is also modified, since we have shown previously that empty-states images show the surface iron atoms.<sup>[26]</sup>

The preference of Rh to assume a subsurface instead of a surface site can be understood in terms of its preferred oxidation state and its lower tolerance for undercoordinated environments compared to Fe. In its native oxides, Rh is always sixfold coordinated, either as Rh(III) in  $\text{Rh}_2\text{O}_3$  or as Rh(IV) in  $\text{RhO}_2$ . Fe, on the other hand, appears as Fe(II) in both  $\text{Fe}_3\text{O}_4$  and  $\text{FeO}$ , and has tetrahedral coordination to oxygen in the former. Crucially, the Rh octahedra in  $\text{Rh}_2\text{O}_3$  have different preferred bond lengths than Fe,<sup>[34]</sup> which they can achieve more easily near the surface in the  $\text{Fe}_2\text{O}_3$  lattice, as the lattice strain induced by substitution can be mitigated by surface relaxations. The Fe octahedra in bulk hematite are trigonally distorted to a  $C_{3v}$  symmetry<sup>[25,35]</sup> with two different bond lengths. However, in our DFT calculations, Rh in the first subsurface layer can realize its preferred, relatively uniform bond lengths of 2.05–2.08 Å,<sup>[34]</sup> as

opposed to the hematite bulk Fe–O bond lengths of 1.97 Å and 2.12 Å, respectively. Together, these two effects favor the closest cation site to the surface in which a sixfold bonding environment can be achieved, which is in the first subsurface layer.

As to how the Rh is oxidized, there are two possible routes: When annealing in a background of oxygen, displaced iron likely diffuses to form more hematite at step edges or as new islands, as we have observed previously when depositing Ti (which also replaces Fe in layer C2).<sup>[36]</sup> When no gas-phase oxygen is available, small amounts of excess cations may be compensated without major reduction of the surface by diffusion of Fe into the bulk, as has been documented for  $\text{Fe}_3\text{O}_4$ .<sup>[20]</sup> However, it is worth noting that when depositing Rh on the  $(1 \times 1)$  termination and annealing in UHV, we found small patches of the  $(2 \times 1)$  termination sooner than expected, after heating to only 400 °C (Figure S1, Supporting Information). This may be a compensation mechanism to help accommodate reduced Fe that has been displaced by Rh incorporation.

Concerning the oxidation state of incorporated Rh, the very high binding energy of 309.3 eV observed in XPS (Figures 2 and 4) may indicate an  $\text{Rh}^{4+}$  state, as the peak position for bulk  $\text{Rh}_2\text{O}_3$  is usually given as  $\approx 308.6$  eV.<sup>[28,32]</sup> However, in the absence of compensating O vacancies, this would require the reduction of iron to  $\text{Fe}^{2+}$ . We have shown previously that introducing  $\text{Ti}^{4+}$  dopants into the surface induces a localized, oxidized restructuring of the surface, which allows all iron to remain  $\text{Fe}^{3+}$ .<sup>[36]</sup> Rh induces no such restructuring, and when annealing in oxygen to prevent partial reduction to the  $(2 \times 1)$  termination, we do not observe any signature of  $\text{Fe}^{2+}$  cations in grazing-emission XPS, even for 0.1 ML Rh [Figure S2b, Supporting Information]. Furthermore, our DFT calculations show no evidence for reduction of  $\text{Fe}^{3+}$  to  $\text{Fe}^{2+}$  in the presence of Rh, and Bader charge analysis indicates a Rh charge state closer to that of Rh in  $\text{Rh}_2\text{O}_3$ . Based on these results, we assign the incorporated rhodium as  $\text{Rh}^{3+}$ , despite the unusually high binding energy in XPS.

The incorporation of Rh in a sixfold coordinated environment in the subsurface means that it would likely be catalytically inactive. Similar behavior has been observed following the calcination of Rh on anatase  $\text{TiO}_2$  particles.<sup>[37]</sup> One can

therefore see why reductive treatment is required to activate the catalysts following calcination.<sup>[37]</sup> However, the fact that lattice incorporation is favorable enough to abstract Rh even from very large clusters may hold interesting possibilities for regenerating SACs. Typical deactivation mechanisms involve sintering and poisoning; both can be reversed if the catalyst is redispersed by an oxidation step (which also burns off carbonaceous species). Note, however, that we could not recover the Rh to the surface by reducing the  $(1 \times 1)$ -terminated surface by UHV annealing, because Rh is also accommodated in the subsurface on the  $(2 \times 1)$ -terminated surface. We have shown previously that Rh atoms are stabilized on  $\text{Fe}_3\text{O}_4(001)$ ,<sup>[33]</sup> so perhaps an even stronger reduction of the surface could recover surface Rh species.

The behavior of Rh on the reduced  $(2 \times 1)$  surface is different from that on the stoichiometric  $(1 \times 1)$  termination. If we start from a 0.1 ML deposition, the reduced  $(2 \times 1)$  termination retains large Rh clusters at temperatures where the stoichiometric surface has already taken all of the metal into the lattice (Figures S2 and S5, Supporting Information). This suggests that there is less energy gain for Rh incorporation on the  $(2 \times 1)$  termination, and that the energy gained by incorporation of Rh is smaller than the cohesive energy in large, bulk-like Rh clusters. This also indicates that reduction should help with re-exposing the Rh atoms and activating them for catalysis. On the other hand, the incorporation of small amounts of Rh appears to be more facile on the  $(2 \times 1)$  surface, as the process begins at lower temperatures [Figure 2c]. Taking the apparently lower thermodynamic driving force into account, this suggests that the faster incorporation of low coverages on the  $(2 \times 1)$  termination [Figure 2c] is due to lower diffusion barriers, perhaps due to the different, more open structure of the  $\alpha\text{-Fe}_2\text{O}_3(1\bar{1}02)$ - $(2 \times 1)$  reconstruction.

The qualitative difference between the low and high Rh coverage on the  $(2 \times 1)$  termination can be explained by two different effects. On the one hand, since incorporating Rh requires it to be oxidized, Fe needs to be reduced simultaneously. Rh is more electronegative than Fe, so it is clear that Rh can only reduce Fe from 3+ to 2+ (which are both common oxidation states of Fe), not any further. Thus, for each incorporated Rh, three Fe atoms have to be reduced to  $\text{Fe}^{2+}$ . Unlike the stoichiometric  $(1 \times 1)$  surface, the  $(2 \times 1)$  reconstruction already contains large amounts of  $\text{Fe}^{2+}$ .<sup>[26]</sup> Rh incorporation will therefore be unfavorable unless diffusion of oxygen from the bulk to the surface, or of excess Fe to the bulk, is fast. If bulk diffusion is slow, displacing Fe upon Rh incorporation becomes increasingly harder. This would offset the energy gained by Rh incorporation, and would lead to a saturation behavior. On the other hand, clusters may never reach a critical size in the low-coverage case (Figure S3, Supporting Information), and thus never become thermodynamically stable against incorporation. Most likely, both effects need to be taken into account to correctly describe the behavior of Rh during the annealing series performed here. However, insufficient bulk diffusion should become less relevant at higher temperatures. We can therefore conclude that once very large clusters are formed, as was the case for our experiments with 0.1 ML Rh, an equilibrium state is reached in which the clusters are indeed thermodynamically stable against incorporation.

These findings illustrate that it is important to account for the reconstructions formed under reducing conditions, instead of simply modeling the reduction by assuming that oxygen vacancies are introduced. In prior DFT studies, the  $\alpha\text{-Fe}_2\text{O}_3(0001)$  surface was usually modeled using the  $\text{O}_3$ -termination capped with a layer of the catalyst atoms (equivalent to an Fe-termination with the terminating Fe layer completely substituted by the metal in question).<sup>[1,8–11]</sup> In modeling CO oxidation, it has been assumed that an oxygen vacancy can be formed next to the SAC site, which can react with  $\text{O}_2$  and CO, forming  $\text{CO}_2$  and repairing the vacancy. To complete the cycle, another CO molecule reacts with a surface oxygen, forming a second  $\text{CO}_2$  molecule and recovering the oxygen vacancy.<sup>[1,8–11]</sup> However, the reduced  $\alpha\text{-Fe}_2\text{O}_3(0001)$  surface exhibits an abundance of reconstructions,<sup>[20,23]</sup> and removing O from an already reduced surface likely costs more energy. Of course, assuming a somewhat simplified model for the surface structure is necessary to make calculations tractable, but it seems unlikely that the real surface activated in reducing conditions would exhibit the bulk-truncated termination with easily available oxygen.

Furthermore, stabilization of single adatoms will depend strongly on both the oxidation state and the structure of the actual surface. Adatom stabilization depends more strongly on diffusion barriers than on pure binding energies, but generally, oxidized surfaces tend to bind cations more strongly, as we have seen on  $\text{Fe}_3\text{O}_4(001)$ .<sup>[38]</sup> While defects can certainly act as trap sites for metal adatoms, oxygen vacancies have been reported to be ineffective at stabilizing metals such as Pt or Rh on  $\text{TiO}_2$ .<sup>[39–41]</sup> For covalently bound cations, this is not surprising, since the adatom loses a potential bond to the support, and bonding may be weakened further if charge transfer is inhibited by the presence of other reduced cations. A recent screening study of a wide range of different transition metals on  $\alpha\text{-Fe}_2\text{O}_3(0001)$  reports strongly covalent binding for all of them.<sup>[10]</sup> Therefore, there is reason to assume that our finding of metal clusters forming on the reduced, but not on the oxidized surface may also be more generally applicable to  $\text{FeO}_x$  surfaces.

Finally, for Rh specifically, it seems likely that the driving forces of preferred sixfold coordination on one hand and lattice strain on the other hand can be generalized to other hematite surfaces, as well as to step defects. This may be helpful for stabilizing and re-dispersing catalyst atoms. A similar route has been demonstrated for Pt on ceria, where Pt can be abstracted from clusters into highly coordinated, but catalytically inactive sites under oxidizing conditions.<sup>[42]</sup> However, whether an atom is situated on the surface or in the first subsurface layer can be extremely hard to distinguish in imaging techniques such as STM [as seen in Figure 1b] or TEM, which is commonly used to identify atom positions in nanoparticle studies.<sup>[1,12–17]</sup> Special care should therefore be taken to avoid erroneous identification of catalyst activity if the preparation leaves the single atom in an inactive subsurface site, or if it moves there under reaction conditions.

## 5. Conclusion

We have studied the interaction of Rh with  $\alpha\text{-Fe}_2\text{O}_3(1\bar{1}02)$  both on the stoichiometric  $(1 \times 1)$  and the reduced  $(2 \times 1)$  termination. Neither surface stabilizes single Rh adatoms, and small

Rh clusters are found after deposition at RT. Low coverages of Rh are incorporated in the substrate below 400 °C in both cases and are stabilized in the subsurface. Larger coverages of Rh sinter into clusters consisting of hundreds of atoms on the reduced ( $2 \times 1$ ) termination, but can be dissolved and re-dispersed by annealing in oxygen, which also transforms the surface back to the ( $1 \times 1$ ) termination. The incorporated oxidized Rh species substitute Fe in the first subsurface layer. We assign the features imaged with increased apparent height in STM as surface O atoms bound to the subsurface Rh.

## 6. Experimental and Computational Methods

All results presented in this work were collected in a UHV setup consisting of a preparation chamber (base pressure  $<10^{-10}$  mbar) and an analysis chamber (base pressure  $<5 \times 10^{-11}$  mbar). The system was equipped with a commercial low-energy electron diffraction (LEED) apparatus (VSI), a nonmonochromatic Al K $\alpha$  X-ray source (VG), an ion gun (He<sup>+</sup>) used for LEIS, a SPECS Phoibos 100 analyzer for XPS and LEIS, and an Omicron  $\mu$ -STM. The STM was operated in constant-current mode using electrochemically etched W tips. STM images were corrected for distortion and creep of the piezo scanner, as described in ref. [43]. Rh was deposited from an electron-beam evaporator (Omicron) in the preparation chamber. A quartz-crystal microbalance was used to calibrate the amount of deposited material, with deposition times of  $\approx 30$ – $120$  s for 0.025–0.1 monolayers (ML) of rhodium. Throughout this paper, a monolayer is defined as the number of Fe atoms in the surface layer. 1 ML of Rh is therefore defined as two Rh atoms per  $\alpha$ -Fe<sub>2</sub>O<sub>3</sub>( $\bar{1}\bar{1}02$ )-( $1 \times 1$ ) unit cell, which corresponds to a density of  $7.3 \times 10^{14}$  atoms cm<sup>-2</sup>.

The experiments were conducted on a single-crystalline, 0.03 at% Ti-doped hematite film grown homoepitaxially by pulsed laser deposition on a natural  $\alpha$ -Fe<sub>2</sub>O<sub>3</sub>( $\bar{1}\bar{1}02$ ) sample (SurfaceNet GmbH,  $10 \times 10 \times 0.5$  mm<sup>3</sup>,  $<0.3^\circ$  miscut) in  $2 \times 10^{-2}$  mbar O<sub>2</sub>, as described previously.<sup>[36]</sup> Doping was achieved by alternating deposition from an Fe<sub>3</sub>O<sub>4</sub> single crystal target and a 1 at% Ti-doped hematite target, home-synthesized from commercial TiO<sub>2</sub> and Fe<sub>2</sub>O<sub>3</sub> powders (99.995% purity, Alfa Aesar). The mixed powders were pressed in an isostatic press at 400 MPa and RT in a cylindrical silicone mold, and sintered in an alumina-tube furnace (6 h at 1200 °C, 1 bar of flowing O<sub>2</sub>, 5 °C min<sup>-1</sup> ramp rates), as described in detail elsewhere.<sup>[44]</sup> The resulting hematite film was sufficiently conductive for STM at RT, with large atomically flat terraces. The surface appeared identical to the undoped samples studied previously.<sup>[26]</sup> Before each experiment, the sample was re-prepared by sputtering (1 keV Ar<sup>+</sup> ions,  $\approx 2$   $\mu$ A) and annealing in oxygen ( $2 \times 10^{-6}$  mbar, 520 °C) for 30 min, which yields the stoichiometric ( $1 \times 1$ ) termination. For experiments on the reduced ( $2 \times 1$ ) reconstruction, the sample was then annealed in UHV at 580 °C for 15 min.

DFT calculations were performed using the Vienna ab initio simulation package<sup>[45,46]</sup> with the projector augmented wave method.<sup>[47,48]</sup> The Perdew, Burke, and Ernzerhof exchange-correlation functional<sup>[49]</sup> was used together with a Hubbard  $U$  ( $U_{\text{eff}} = 4.0$ ) to treat the highly correlated Fe 3d electrons.<sup>[50]</sup> The same  $U$  was applied for Rh atoms to avoid artificially biasing 3d electron occupations among the different transition metal cations.<sup>[51]</sup> Rh substitution was tested in ( $2 \times 2$ ) supercells on asymmetric slabs consisting of 30 atomic layers, with the bottom five layers kept fixed, and using a  $4 \times 4 \times 1$   $\Gamma$ -centred k-mesh. Coverage dependencies of substituting two Rh atoms in the same sublayer were tested in a larger ( $3 \times 3$ ) supercell, with an adjusted k-mesh of  $3 \times 3 \times 1$ . The plane-wave basis-set cut-off energy was set to 450 eV, and convergence was achieved when residual forces acting on ions were smaller than 0.02 eV  $\text{\AA}^{-1}$ . The charge states of Rh ions were evaluated using the Bader approach,<sup>[52–54]</sup> and benchmarked to calculations of bulk RhO<sub>2</sub> and Rh<sub>2</sub>O<sub>3</sub> using the same computational setup.

## Supporting Information

Supporting Information is available from the Wiley Online Library or from the author.

## Acknowledgements

F.K., A.R.-A., M.M., and G.S.P. acknowledge funding from the European Research Council (ERC) under the European Union's Horizon 2020 research and innovation program grant agreement No. 864628. F.K., M.R., and U.D. acknowledge support by the Austrian Science Fund (FWF, Z-250, Wittgenstein Prize). N.R. and Z.J. were supported by the Austrian Science Fund (FWF, Y847-N20, START Prize). G.F. acknowledges support from the TU-D doctoral school of the TU Wien. M.E. acknowledges support from the TUM-GS of the TU Munich. The computational results presented were achieved using the Vienna Scientific Cluster (VSC 3).

## Conflict of Interest

The authors declare no conflict of interest.

## Data Availability Statement

The data that support the findings of this study are available from the corresponding author upon reasonable request.

## Keywords

catalyst deactivation, incorporation, iron oxides, redispersion, single atom catalysis

Received: October 30, 2020  
Revised: December 23, 2020  
Published online: February 4, 2021

- [1] B. Qiao, A. Wang, X. Yang, L. F. Allard, Z. Jiang, Y. Cui, J. Liu, J. Li, T. Zhang, *Nat. Chem.* **2011**, *3*, 634.
- [2] X.-F. Yang, A. Wang, B. Qiao, J. Li, J. Liu, T. Zhang, *Acc. Chem. Res.* **2013**, *46*, 1740.
- [3] S. Liang, C. Hao, Y. Shi, *ChemCatChem* **2015**, *7*, 2559.
- [4] B. C. Gates, M. Flytzani-Stephanopoulos, D. A. Dixon, A. Katz, *Catal. Sci. Technol.* **2017**, *7*, 4259.
- [5] X. Cui, W. Li, P. Ryabchuk, K. Junge, M. Beller, *Nat. Catal.* **2018**, *1*, 385.
- [6] A. Wang, J. Li, T. Zhang, *Nat. Rev. Chem.* **2018**, *2*, 65.
- [7] H. Zhang, G. Liu, L. Shi, J. Ye, *Adv. Energy Mater.* **2018**, *8*, 1701343.
- [8] F. Li, Y. Li, X. C. Zeng, Z. Chen, *ACS Catal.* **2015**, *5*, 544.
- [9] B. Qiao, J.-X. Liang, A. Wang, C.-Q. Xu, J. Li, T. Zhang, J. J. Liu, *Nano Res.* **2015**, *8*, 2913.
- [10] J. Liang, Q. Yu, X. Yang, T. Zhang, J. Li, *Nano Res.* **2018**, *11*, 1599.
- [11] J.-X. Liang, J. Lin, J. Liu, X. Wang, T. Zhang, J. Li, *Angew. Chem., Int. Ed.* **2020**, *59*, 12868.
- [12] J.-X. Liang, J. Lin, X.-F. Yang, A.-Q. Wang, B.-T. Qiao, J. Liu, T. Zhang, J. Li, *J. Phys. Chem. C* **2014**, *118*, 21945.
- [13] Y. Shi, C. Zhao, H. Wei, J. Guo, S. Liang, A. Wang, T. Zhang, J. Liu, T. Ma, *Adv. Mater.* **2014**, *26*, 8147.
- [14] H. Wei, X. Liu, A. Wang, L. Zhang, B. Qiao, X. Yang, Y. Huang, S. Miao, J. Liu, T. Zhang, *Nat. Commun.* **2014**, *5*, 5634.
- [15] M. D. Rossell, F. J. Caparrós, I. Angurell, G. Müller, J. Llorca, M. Seco, O. Rossell, *Catal. Sci. Technol.* **2016**, *6*, 4081.

- [16] J. Liu, *ACS Catal.* **2017**, *7*, 34.
- [17] Y. Zhao, K. R. Yang, Z. Wang, X. Yan, S. Cao, Y. Ye, Q. Dong, X. Zhang, J. E. Thorne, L. Jin, K. L. Materna, A. Trimpalis, H. Bai, S. C. Fakra, X. Zhong, P. Wang, X. Pan, J. Guo, M. Flytzani-Stephanopoulos, G. W. Brudvig, V. S. Batista, D. Wang, *Proc. Natl. Acad. Sci. USA* **2018**, *115*, 2902.
- [18] G. Malta, S. A. Kondrat, S. J. Freakley, C. J. Davies, L. Lu, S. Dawson, A. Thetford, E. K. Gibson, D. J. Morgan, W. Jones, P. P. Wells, P. Johnston, C. R. A. Catlow, C. J. Kiely, G. J. Hutchings, *Science* **2017**, *355*, 1399.
- [19] M. J. Hülsey, B. Zhang, Z. Ma, H. Asakura, D. A. Do, W. Chen, T. Tanaka, P. Zhang, Z. Wu, N. Yan, *Nat. Commun.* **2019**, *10*, 1330.
- [20] G. S. Parkinson, *Surf. Sci. Rep.* **2016**, *71*, 272.
- [21] C. Lemire, S. Bertarione, A. Zecchina, D. Scarano, A. Chaka, S. Shaikhutdinov, H.-J. Freund, *Phys. Rev. Lett.* **2005**, *94*, 166101.
- [22] A. Barbier, A. Stierle, N. Kasper, M.-J. Guittet, J. Jupille, *Phys. Rev. B* **2007**, *75*, 233406.
- [23] H. Kuhlenbeck, S. Shaikhutdinov, H.-J. Freund, *Chem. Rev.* **2013**, *113*, 3986.
- [24] F. Genuzio, A. Sala, T. Schmidt, D. Menzel, H. J. Freund, *Surf. Sci.* **2016**, *648*, 177.
- [25] R. M. Cornell, U. Schwertmann, *The Iron Oxides: Structure, Properties, Reactions, Occurrences and Uses*, Wiley, New York **2003**.
- [26] F. Kraushofer, Z. Jakub, M. Bichler, J. Hulva, P. Drmota, M. Weinold, M. Schmid, M. Setvin, U. Diebold, P. Blaha, G. S. Parkinson, *J. Phys. Chem. C* **2018**, *122*, 1657.
- [27] Z. Jakub, F. Kraushofer, M. Bichler, J. Balajka, J. Hulva, J. Pavelec, I. Sokolovic, M. Mullner, M. Setvin, M. Schmid, U. Diebold, P. Blaha, G. S. Parkinson, *ACS Energy Lett.* **2019**, *4*, 390.
- [28] A. A. Tolia, R. J. Smiley, W. N. Delgass, C. G. Takoudis, M. J. Weaver, *J. Catal.* **1994**, *150*, 56.
- [29] A. Howard, D. Clark, C. Mitchell, R. Egdell, V. Dhanak, *Surf. Sci.* **2002**, *518*, 210.
- [30] C. J. Weststrate, A. Resta, R. Westerström, E. Lundgren, A. Mikkelsen, J. N. Andersen, *J. Phys. Chem. C* **2008**, *112*, 6900.
- [31] Z. Weng-Sieh, R. Gronsky, A. T. Bell, *J. Catal.* **1997**, *170*, 62.
- [32] S. Blomberg, E. Lundgren, R. Westerström, E. Erdogan, N. M. Martin, A. Mikkelsen, J. N. Andersen, F. Mittendorfer, J. Gustafson, *Surf. Sci.* **2012**, *606*, 1416.
- [33] Z. Jakub, J. Hulva, P. T. Ryan, D. A. Duncan, D. J. Payne, R. Bliem, M. Ulreich, P. Hofegger, F. Kraushofer, M. Meier, *Nanoscale* **2020**, *12*, 5866.
- [34] J. Coey, *Acta Crystallogr. B* **1970**, *26*, 1876.
- [35] K. Sivula, F. Le Formal, M. Grätzel, *ChemSusChem* **2011**, *4*, 432.
- [36] G. Franceschi, F. Kraushofer, M. Meier, G. S. Parkinson, M. Schmid, U. Diebold, M. Riva, *Chem. Mater.* **2020**, *32*, 3753.
- [37] C. Asokan, H. V. Thang, G. Pacchioni, P. Christopher, *Catal. Sci. Technol.* **2020**, *10*, 1597.
- [38] R. Bliem, E. McDermott, P. Ferstl, M. Setvin, O. Gamba, J. Pavelec, M. Schneider, M. Schmid, U. Diebold, P. Blaha, *Science* **2014**, *346*, 1215.
- [39] X.-Q. Gong, A. Selloni, O. Dulub, P. Jacobson, U. Diebold, *J. Am. Chem. Soc.* **2008**, *130*, 370.
- [40] H. V. Thang, G. Pacchioni, L. DeRita, P. Christopher, *J. Catal.* **2018**, *367*, 104.
- [41] Y. Tang, C. Asokan, M. Xu, G. W. Graham, X. Pan, P. Christopher, J. Li, P. Sautet, *Nat. Commun.* **2019**, *10*, 4488.
- [42] Y. Lykhach, A. Bruix, S. Fabris, V. Potin, I. Matolínová, V. Matolín, J. Libuda, K. M. Neyman, *Catal. Sci. Technol.* **2017**, *7*, 4315.
- [43] J. Choi, W. Mayr-Schmölzer, F. Mittendorfer, J. Redinger, U. Diebold, M. Schmid, *J. Phys.: Condens. Matter* **2014**, *26*, 225003.
- [44] G. Franceschi, M. Schmid, U. Diebold, M. Riva, *J. Mater. Chem. A* **2020**, *8*, 22947.
- [45] G. Kresse, J. Hafner, *Phys. Rev. B* **1993**, *48*, 13115.
- [46] G. Kresse, J. Furthmüller, *Comput. Mater. Sci.* **1996**, *6*, 15.
- [47] P. E. Blöchl, *Phys. Rev. B* **1994**, *50*, 17953.
- [48] G. Kresse, D. Joubert, *Phys. Rev. B* **1999**, *59*, 1758.
- [49] J. P. Perdew, K. Burke, M. Ernzerhof, *Phys. Rev. Lett.* **1996**, *77*, 3865.
- [50] V. I. Anisimov, J. Zaanen, O. K. Andersen, *Phys. Rev. B* **1991**, *44*, 943.
- [51] P. Liao, J. A. Keith, E. A. Carter, *J. Am. Chem. Soc.* **2012**, *134*, 13296.
- [52] G. Henkelman, A. Arnaldsson, H. Jónsson, *Comput. Mater. Sci.* **2006**, *36*, 354.
- [53] W. Tang, E. Sanville, G. Henkelman, *J. Phys.: Condens. Matter* **2009**, *21*, 084204.
- [54] M. Yu, D. R. Trinkle, *J. Chem. Phys.* **2011**, *134*, 064111.

**ADVANCED  
MATERIALS**  
INTERFACES

Supporting Information

for *Adv. Mater. Interfaces*, DOI: 10.1002/admi.202001908

Surface Reduction State Determines Stabilization and  
Incorporation of Rh on #-Fe<sub>2</sub>O<sub>3</sub>(11 $\bar{0}$ 2)

*Florian Kraushofer, Nikolaus Resch, Moritz Eder, Ali  
Rafsanjani-Abbasi, Sarah Tobisch, Zdenek Jakub, Giada  
Franceschi, Michele Riva, Matthias Meier, Michael Schmid,  
Ulrike Diebold, and Gareth S. Parkinson\**

Supporting Information

**Surface Reduction State Determines Stabilization and Incorporation of Rh on  $\alpha$ - $\text{Fe}_2\text{O}_3(1\bar{1}02)$**

*Florian Kraushofer, Nikolaus Resch, Moritz Eder, Ali Rafsanjani-Abbasi, Sarah Tobisch, Zdenek Jakub, Giada Franceschi, Michele Riva, Matthias Meier, Michael Schmid, Ulrike Diebold, Gareth S. Parkinson\**

*\*Corresponding author: [parkinson@iap.tuwien.ac.at](mailto:parkinson@iap.tuwien.ac.at)*



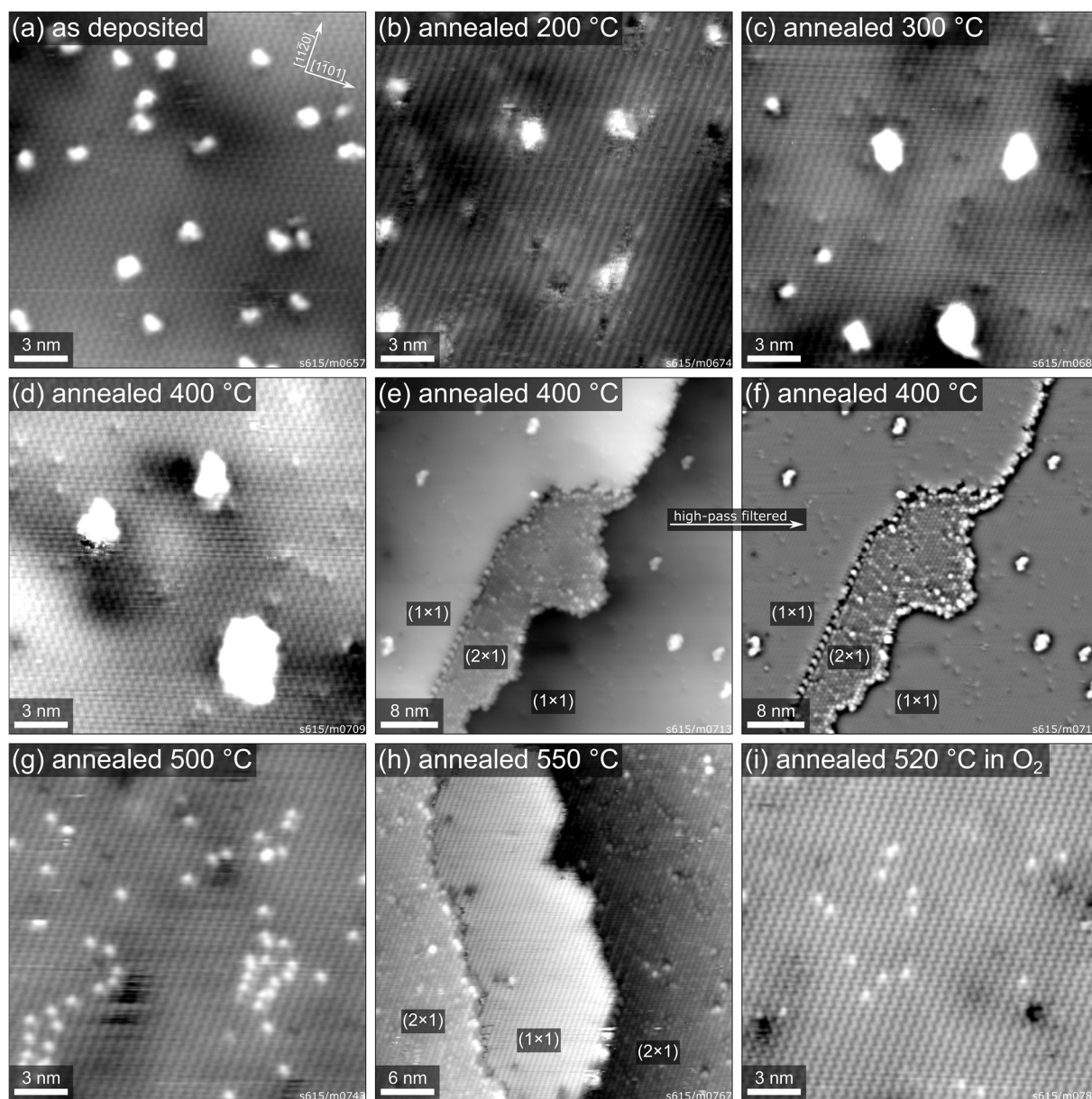


**Figure S1:** STM images corresponding to the XPS data in Figure 2a of 0.025 ML Rh on  $\alpha$ - $\text{Fe}_2\text{O}_3(1\bar{1}02)-(1 \times 1)$ . Apart from panel (i), all annealing steps were performed in UHV. Panels (a) and (g) are the same as in Figure 1a,b. Panel (e) shows a region of interest in which a small patch of the reduced  $(2 \times 1)$  termination was formed at a step edge after annealing to 400 °C. Panel (f) is the same image as (e), high-pass filtered for better visibility of the surface structure. In panel (h), the majority of the surface is  $(2 \times 1)$ -terminated after annealing to 550 °C in UHV, with only small patches of  $(1 \times 1)$  termination remaining at step edges. Note that panels (e), (f) and (h) show larger areas in order to display the termination change at steps. Sample biases and tunnelling currents are: (a)  $U = +3$  V,  $I = 0.3$  nA; (b)  $U = +3$  V,  $I = 0.1$  nA; (c)  $U = +2$  V,  $I = 0.2$  nA; (d)  $U = +2.5$  V,  $I = 0.1$  nA; (e, f)  $U = +2.5$  V,  $I = 0.25$  nA; (g)  $U = -2.8$  V,  $I = 0.1$  nA; (h)  $U = +2.8$  V,  $I = 0.1$  nA; (i)  $U = -2.8$  V,  $I = 0.1$  nA.

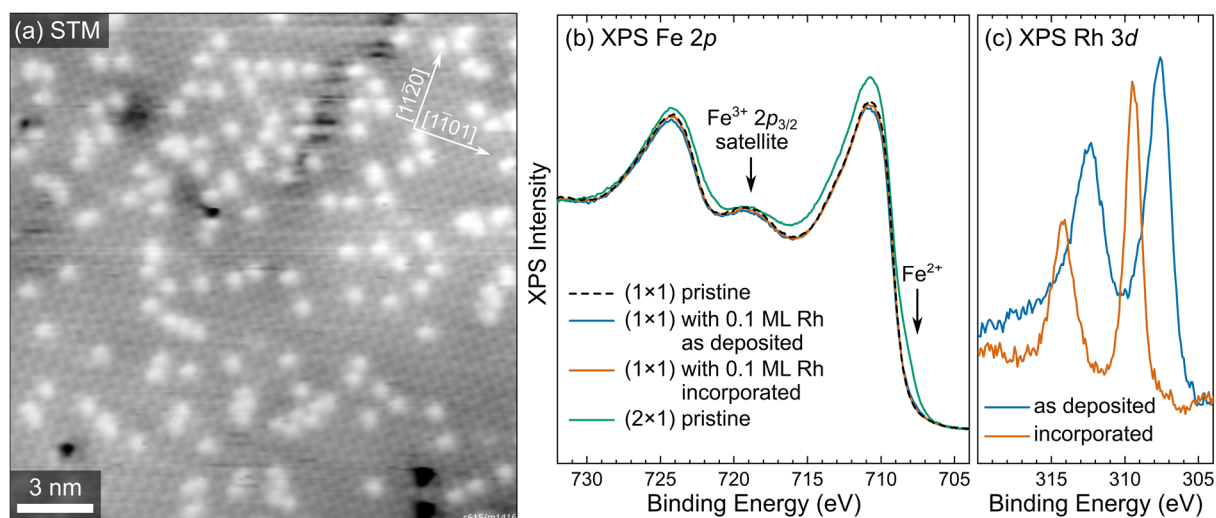


**Figure S2:** 0.1 ML Rh incorporated in  $\alpha$ -Fe<sub>2</sub>O<sub>3</sub>( $1\bar{1}02$ )-(1 × 1). (a) 20 × 20 nm<sup>2</sup> STM image ( $U_{\text{sample}} = -2.8$  V,  $I_{\text{tunnel}} = 0.1$  nA) of the  $\alpha$ -Fe<sub>2</sub>O<sub>3</sub>( $1\bar{1}02$ )-(1 × 1) surface after depositing 0.1 ML Rh, then annealing the sample at 520 °C in  $2 \times 10^{-6}$  mbar O<sub>2</sub> for 30 min. In contrast to Figure 4 of the main text, no UHV annealing (leading to large, metallic clusters) has been applied. (b,c) The Fe 2p and Rh 3d regions in XPS (Al K $\alpha$ , 70° grazing emission) for the pristine (1 × 1) surface before Rh deposition (black, dashed), after deposition of 0.1 ML Rh (blue), and corresponding to the STM image in panel (a) (orange). The Fe 2p peak of the as-prepared (2 × 1)-terminated surface is shown for comparison (green). On the (2 × 1) surface, the shoulder at  $\approx 708$  eV and the less pronounced Fe 2p<sub>3/2</sub> satellite at 719 eV indicate the presence of Fe<sup>2+</sup>.<sup>[1, 2]</sup> These changes are not observed on the (1 × 1) surface even when 0.1 ML Rh are incorporated in the presence of oxygen, suggesting that all iron remains as Fe<sup>3+</sup>.



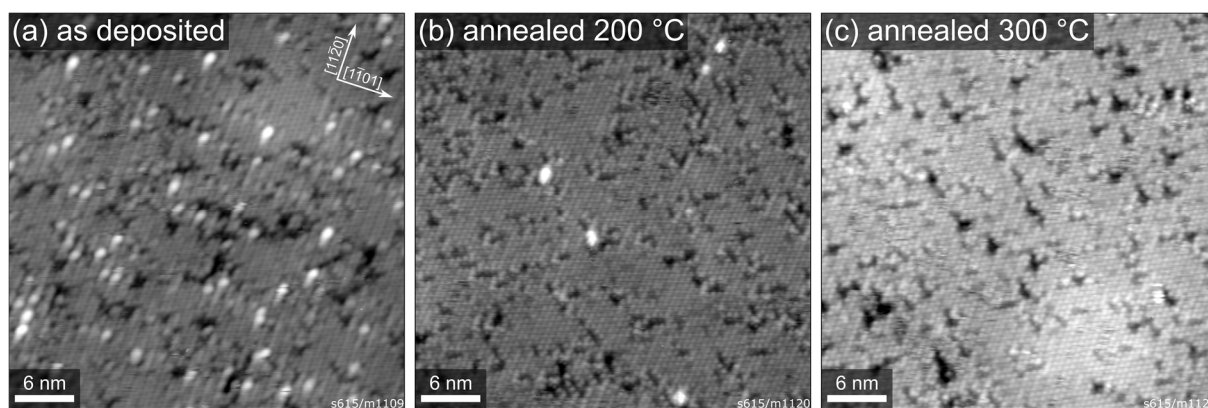


**Figure S3:** STM images corresponding to the XPS data in Figure 2b of 0.025 ML Rh on  $\alpha$ - $\text{Fe}_2\text{O}_3(1\bar{1}02)-(2 \times 1)$ . Panels (a) and (c) show the same STM images as Figure 1c,d at lower magnification. Sample biases and tunnelling currents are: (a)  $U = -3$  V,  $I = 0.1$  nA; (b)  $U = -2$  V,  $I = 0.1$  nA; (c)  $U = -2.8$  V,  $I = 0.1$  nA.

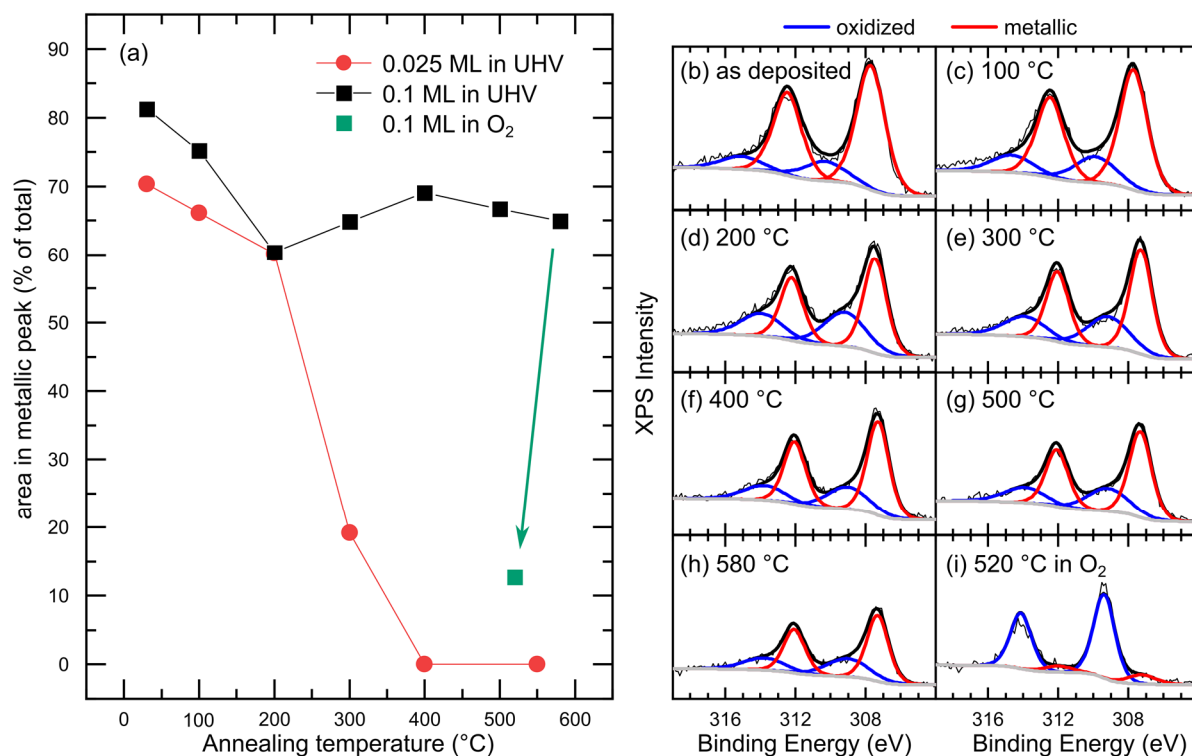


**Figure S4:** Fits of XPS results (Al K $\alpha$ , 70° grazing emission, pass energy 16 eV) for 0.1 ML Rh on  $\alpha$ -Fe<sub>2</sub>O<sub>3</sub>(1 $\bar{1}$ 02)-(2  $\times$  1), using the data shown in Figure 4. (a) Area percentages for peak fits to the spectra in Figure 4a. Black data points correspond to successive heating steps in UHV, while the green data point corresponds to the final annealing step in oxygen, yielding the STM image in Figure 4c. For reference, the data for 0.025 ML Rh from Figure 2c are shown again here (red). Note that in the 0.1 ML case, the peak areas are not good descriptors of the actual ratios between metallic and oxidic Rh because for large clusters, the buried atoms contribute much less signal to XPS. (b-i) Peak fits to the data shown in Figure 4a, using two components for Rh 3d<sub>5/2</sub> as described for Figure 2 in the main text. For the final spectrum in panel (i), the sample was annealed for 1 h at 520 °C in a background of 2  $\times$  10<sup>-6</sup> mbar O<sub>2</sub>.

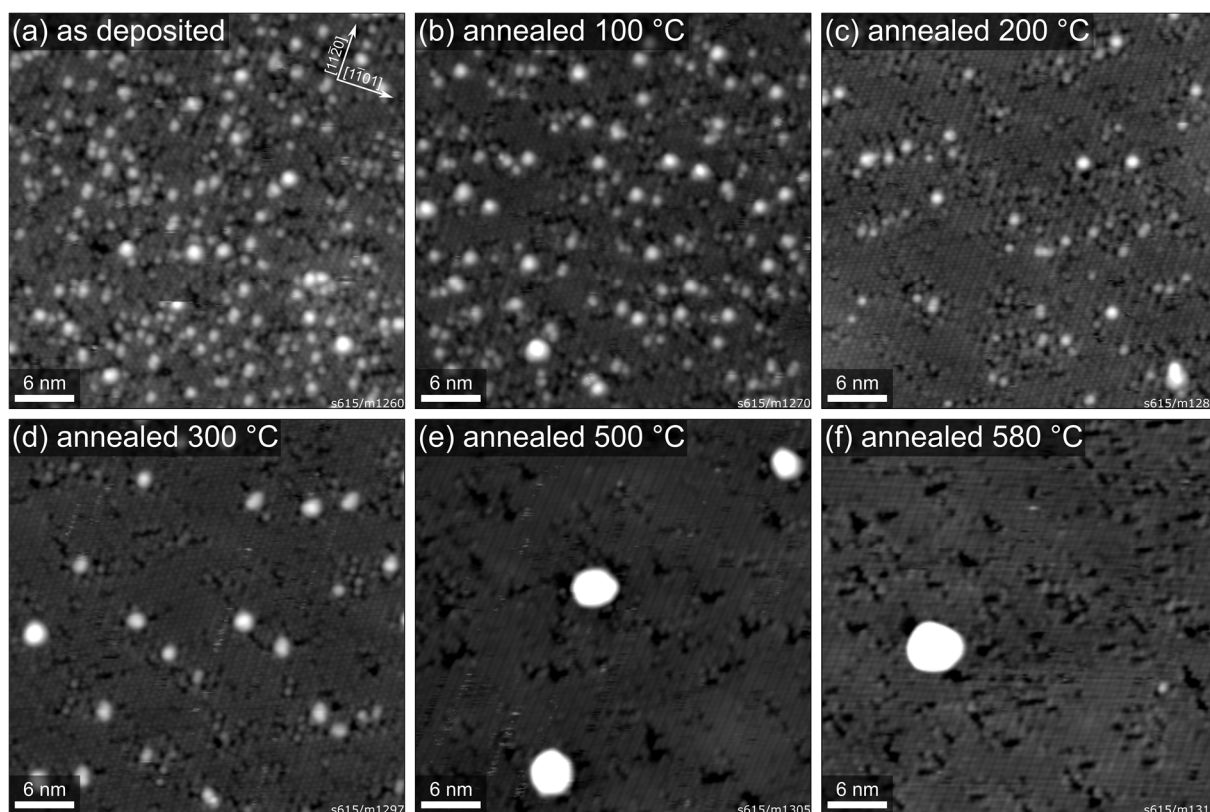


**Figure S5:** STM images corresponding to the XPS data in Figure 4a of 0.1 ML Rh on  $\alpha$ -Fe<sub>2</sub>O<sub>3</sub>(1 $\bar{1}$ 02)-(2 × 1), with annealing steps performed in UHV. Panel (f) is the same image as shown in Figure 4b. Sample biases and tunnelling currents are: (a)  $U = -3$  V,  $I = 0.1$  nA; (b)  $U = -3$  V,  $I = 0.1$  nA; (c)  $U = -2.5$  V,  $I = 0.1$  nA; (d)  $U = -3$  V,  $I = 0.1$  nA; (e)  $U = -3$  V,  $I = 0.1$  nA; (f)  $U = -2.5$  V,  $I = 0.1$  nA.

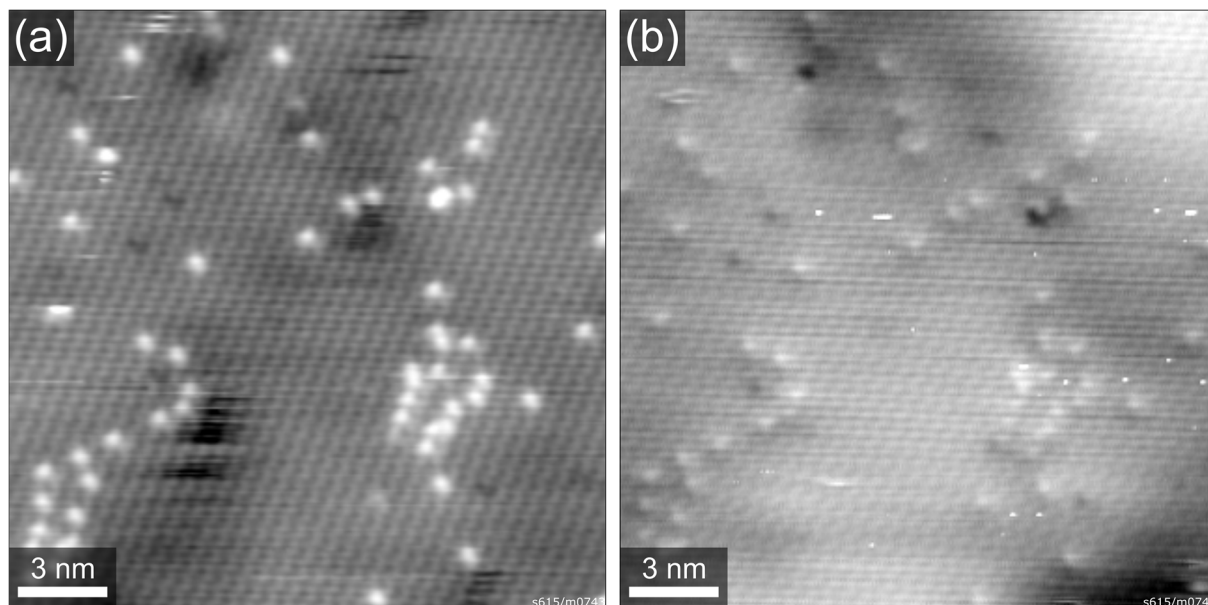


**Figure S6:** STM images of 0.025 ML Rh on  $\alpha\text{-Fe}_2\text{O}_3(1\bar{1}02)-(1 \times 1)$ . Both images were taken after depositing 0.025 ML Rh on the pristine  $\alpha\text{-Fe}_2\text{O}_3(1\bar{1}02)-(1 \times 1)$  surface, followed by annealing at 500 °C for 15 min. The image in panel (a) is the same as shown in the main manuscript in Figure 1b ( $U_{\text{sample}} = -2.8$  V,  $I_{\text{tunnel}} = 0.1$  nA). (b) shows the same area with positive sample bias ( $U_{\text{sample}} = +2.8$  V,  $I_{\text{tunnel}} = 0.1$  nA).

### References

- [1] F. Kraushofer, Z. Jakub, M. Bichler, J. Hulva, P. Drmota, M. Weinold, M. Schmid, M. Setvin, U. Diebold, P. Blaha, G. S. Parkinson, *J. Phys. Chem. C* **2018**, *122*, 1657.
- [2] W. Weiss, W. Ranke, *Prog. Surf. Sci.* **2002**, *70*, 1.

## B Contributions to the Publications

Article	Reference	Contribution
Reactions in the Photocatalytic Conversion of Tertiary Alcohols on Rutile TiO <sub>2</sub> (110)	C. Courtois, <sup>†</sup> <b>M. Eder</b> , <sup>†</sup> K. Schnabl, C. A. Walenta, M. Tschurl, U. Heiz* <i>Angew. Chem Int. Ed.</i> , <b>2019</b> , <i>58</i> (40), 14255-14259.	Performance and evaluation of experiments in a team of two, preparation of figures, discussion and interpretation of results, co-writing of manuscript and SI
Origin of Poisoning in Methanol Photoreforming on TiO <sub>2</sub> (110): The Importance of Thermal Back-Reaction Steps in Photocatalysis	C. Courtois, <sup>†</sup> <b>M. Eder</b> , <sup>†</sup> S. L. Kollmannsberger, M. Tschurl, C. A. Walenta, U. Heiz* <i>ACS Catal.</i> , <b>2020</b> , <i>10</i> (14), 7747-7752.	Performance and evaluation of experiments in a team of two, preparation of figures, discussion and interpretation of results, co-writing of manuscript and SI
Nickel clusters on TiO <sub>2</sub> (110): thermal chemistry and photocatalytic hydrogen evolution of methanol	C. Courtois, <sup>†,a</sup> <b>M. Eder</b> , <sup>†,a</sup> T. Kratky, <sup>b</sup> S. Günther, <sup>b</sup> C. M. Tschurl, <sup>a</sup> U. Heiz*, <sup>a</sup> <i>Catal. Sci. Technol.</i> , <b>2020</b> , <i>10</i> (22), 7630-7639.	Performance and evaluation of experiments in a team of two, preparation of figures, discussion and interpretation of results, writing of manuscript and SI
Surface Species in Photocatalytic Methanol Reforming on Pt/TiO <sub>2</sub> (110): Learning from Surface Science Experiments for Catalytically Relevant Conditions	C. A. Walenta, C. Courtois, M. Eder, S. L. Kollmannsberger, M. Tschurl, U. Heiz*	Discussion and interpretation of results, evaluation of experiments, co-writing of manuscript
Surface Reduction State Determines Stabilization and Incorporation of Rh on $\alpha$ -Fe <sub>2</sub> O <sub>3</sub> (11 $\bar{0}2$ )	F. Kraushofer, N. Resch, M. Eder, A. Rafsanjani-Abbasi, S. Tobisch, Z. Jakub, G. Franceschi, M. Riva, M. Meier, M. Schmid, U. Diebold, G. S. Parkinson*	Performance of experiments in a team of two, evaluation of experiments, discussion and interpretation of results



## **C Reprint Permissions**



## Reactions in the Photocatalytic Conversion of Tertiary Alcohols on Rutile TiO<sub>2</sub>(110)

**Author:** Carla Courtois, Moritz Eder, Kordula Schnabl, et al

**Publication:** Angewandte Chemie International Edition

**Publisher:** John Wiley and Sons

**Date:** Aug 28, 2019

© 2019 The Authors. Published by Wiley-VCH Verlag GmbH & Co. KGaA

### Open Access Article

This is an open access article distributed under the terms of the [Creative Commons CC BY](#) license, which permits unrestricted use, distribution, and reproduction in any medium, provided the original work is properly cited.

You are not required to obtain permission to reuse this article.

For an understanding of what is meant by the terms of the Creative Commons License, please refer to [Wiley's Open Access Terms and Conditions](#).

Permission is not required for this type of reuse.

Wiley offers a professional reprint service for high quality reproduction of articles from over 1400 scientific and medical journals. Wiley's reprint service offers:

- Peer reviewed research or reviews
- Tailored collections of articles
- A professional high quality finish
- Glossy journal style color covers
- Company or brand customisation
- Language translations
- Prompt turnaround times and delivery directly to your office, warehouse or congress.

Please contact our Reprints department for a quotation. Email [corporatesaleseurope@wiley.com](mailto:corporatesaleseurope@wiley.com) or [corporatesalesusa@wiley.com](mailto:corporatesalesusa@wiley.com) or [corporatesalesDE@wiley.com](mailto:corporatesalesDE@wiley.com).



### Origin of Poisoning in Methanol Photoreforming on TiO<sub>2</sub>(110): The Importance of Thermal Back-Reaction Steps in Photocatalysis



**Author:** Carla Courtois, Moritz Eder, Sebastian L. Kollmannsberger, et al

**Publication:** ACS Catalysis

**Publisher:** American Chemical Society

**Date:** Jul 1, 2020

*Copyright © 2020, American Chemical Society*

#### PERMISSION/LICENSE IS GRANTED FOR YOUR ORDER AT NO CHARGE

This type of permission/license, instead of the standard Terms and Conditions, is sent to you because no fee is being charged for your order. Please note the following:

- Permission is granted for your request in both print and electronic formats, and translations.
- If figures and/or tables were requested, they may be adapted or used in part.
- Please print this page for your records and send a copy of it to your publisher/graduate school.
- Appropriate credit for the requested material should be given as follows: "Reprinted (adapted) with permission from {COMPLETE REFERENCE CITATION}. Copyright {YEAR} American Chemical Society." Insert appropriate information in place of the capitalized words.
- One-time permission is granted only for the use specified in your RightsLink request. No additional uses are granted (such as derivative works or other editions). For any uses, please submit a new request.

If credit is given to another source for the material you requested from RightsLink, permission must be obtained from that source.

[BACK](#)

[CLOSE WINDOW](#)

† Electronic supplementary information (ESI) available: Mass scan of Ni clusters, methanol photochemistry on titania, oxygen PSD on titania, AES reference spectra. See DOI: [10.1039/d0cy01465f](https://doi.org/10.1039/d0cy01465f)

‡ The authors contributed equally to this work.

This journal is © The Royal Society of Chemistry 2020

About

Cited by

Related



## Nickel clusters on TiO<sub>2</sub>(110): thermal chemistry and photocatalytic hydrogen evolution of methanol

M. Eder, C. Courtois, T. Kratky, S. Günther, M. Tschurl and U. Heiz, *Catal. Sci. Technol.*, 2020, **10**, 7630  
**DOI:** 10.1039/D0CY01465F

To request permission to reproduce material from this article, please go to the [Copyright Clearance Center request page](#).

If you are **an author contributing to an RSC publication, you do not need to request permission** provided correct acknowledgement is given.

If you are **the author of this article, you do not need to request permission to reproduce figures and diagrams** provided correct acknowledgement is given. If you want to reproduce the whole article in a third-party publication (excluding your thesis/dissertation for which permission is not required) please go to the [Copyright Clearance Center request page](#).

Read more about [how to correctly acknowledge RSC content](#).



### Surface Species in Photocatalytic Methanol Reforming on Pt/TiO<sub>2</sub>(110): Learning from Surface Science Experiments for Catalytically Relevant Conditions



**Author:** Constantin A. Walenta, Carla Courtois, Sebastian L. Kollmannsberger, et al

**Publication:** ACS Catalysis

**Publisher:** American Chemical Society

**Date:** Apr 1, 2020

*Copyright © 2020, American Chemical Society*

#### PERMISSION/LICENSE IS GRANTED FOR YOUR ORDER AT NO CHARGE

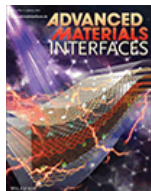
This type of permission/license, instead of the standard Terms and Conditions, is sent to you because no fee is being charged for your order. Please note the following:

- Permission is granted for your request in both print and electronic formats, and translations.
- If figures and/or tables were requested, they may be adapted or used in part.
- Please print this page for your records and send a copy of it to your publisher/graduate school.
- Appropriate credit for the requested material should be given as follows: "Reprinted (adapted) with permission from {COMPLETE REFERENCE CITATION}. Copyright {YEAR} American Chemical Society." Insert appropriate information in place of the capitalized words.
- One-time permission is granted only for the use specified in your RightsLink request. No additional uses are granted (such as derivative works or other editions). For any uses, please submit a new request.

If credit is given to another source for the material you requested from RightsLink, permission must be obtained from that source.

[BACK](#)

[CLOSE WINDOW](#)



### Surface Reduction State Determines Stabilization and Incorporation of Rh on $\alpha$ -Fe<sub>2</sub>O<sub>3</sub>(11 $\bar{0}$ 2)

**Author:** Florian Kraushofer, Nikolaus Resch, Moritz Eder, et al

**Publication:** Advanced Materials Interfaces

**Publisher:** John Wiley and Sons

**Date:** Feb 4, 2021

© 2021 The Authors. Advanced Materials Interfaces published by Wiley-VCH GmbH

#### Open Access Article

This is an open access article distributed under the terms of the [Creative Commons CC BY](#) license, which permits unrestricted use, distribution, and reproduction in any medium, provided the original work is properly cited.

You are not required to obtain permission to reuse this article.

For an understanding of what is meant by the terms of the Creative Commons License, please refer to [Wiley's Open Access Terms and Conditions](#).

Permission is not required for this type of reuse.

Wiley offers a professional reprint service for high quality reproduction of articles from over 1400 scientific and medical journals. Wiley's reprint service offers:

- Peer reviewed research or reviews
- Tailored collections of articles
- A professional high quality finish
- Glossy journal style color covers
- Company or brand customisation
- Language translations
- Prompt turnaround times and delivery directly to your office, warehouse or congress.

Please contact our Reprints department for a quotation. Email [corporatesaleseurope@wiley.com](mailto:corporatesaleseurope@wiley.com) or [corporatesalesusa@wiley.com](mailto:corporatesalesusa@wiley.com) or [corporatesalesDE@wiley.com](mailto:corporatesalesDE@wiley.com).

## **D Prepared Manuscripts**

# Size and Coverage Effects of Ni and Pt Co-catalysts in the Photocatalytic Hydrogen Evolution from Methanol on TiO<sub>2</sub>(110)

Moritz Eder<sup>‡</sup>, Carla Courtois<sup>‡</sup>, Philip Petzoldt, Sonia Mackewicz, Martin Tschurl, and Ueli Heiz\*

Chair of Physical Chemistry & Catalysis Research Center, Technical University of Munich, Lichtenbergstr. 4, 85748 Garching, Germany

<sup>‡</sup> The authors contributed equally.

\*Corresponding Author: ulrich.heiz@mytum.de

## Abstract

In the past decade, hydrogen evolution from photocatalytic alcohol oxidation on noble metal loaded TiO<sub>2</sub> has emerged as a large research field. While the presence of a metal cluster co-catalyst is crucial as H<sub>2</sub> recombination center, respective size and coverage effects on the overall catalyst performance are not yet comprehensively understood. To some extent, this is due to the fact that common deposition methods based on wet chemistry do not allow for independently changing size and coverage. Thus the disentanglement of the role of both properties on the catalytic performance remains remote. This drawback can be overcome by the use of cluster sources and the deposition of size-selected clusters, where cluster size and coverage can be changed deliberately. This study concentrates on the comparison of size-selected Ni and Pt clusters as co-catalyst materials on a TiO<sub>2</sub>(110) single crystal and the resulting size- and coverage-dependent effects in the photocatalytic hydrogen evolution from alcohols in the ultra-high vacuum (UHV). We show that larger clusters and higher coverages of Ni directly enhance the product formation rate, although deactivation over time occurs. This is not the case for Pt co-catalysts, which exhibit a stable and higher photocatalytic activity. Contrary to Ni clusters, size-specific effects have to be taken into account for Pt. While H<sub>2</sub> evolution is improved by a higher concentration of Pt clusters, a simple increase in the metal content by the deposition of larger particles may even be detrimental to the performance of the photocatalyst. Furthermore, the acquired overall mechanistic picture is corroborated by H<sub>2</sub> formation kinetics evaluated from mass spectrometric data by a novel approach. Our study shows that for some metals, size effects are relevant for improving the catalytic performance, while for other co-catalyst materials merely the coverage is decisive. The elucidation of different size- and coverage dependencies is an important step towards a rational catalyst design for photocatalytic hydrogen evolution.

## Introduction

In the recent years, numerous studies have proven the outstanding possibilities that heterogeneous photocatalysis offers, e.g. with respect to H<sub>2</sub> generation from water or other surplus chemicals such as alcohols.<sup>1-3</sup> Considering the economic aspects of applied chemical technology, the photocatalytic production of H<sub>2</sub> would be a cost-effective method.<sup>4</sup> However, state-of-the-art photocatalysts are still generally too inefficient for profitable large-scale applications. For H<sub>2</sub> evolving reactions, the photocatalytic system usually consists of a light-absorbing semiconductor with (noble) metal particles as co-catalysts on the surface. It is hardly predictable which metals are suitable as co-catalyst material. Noble metals such as Pt have shown the most efficient performance in the H<sub>2</sub> evolution. However, since systematic studies are scarce, it is not clear whether cheaper and more abundant metals could be used equally well under suitable conditions.

Apart from the choice of co-catalyst material, the optimization of functional photocatalytic metal-semiconductor systems is challenging. Key parameters such as co-catalyst particle size and coverage are often interconnected and cannot be optimized independently from each other by most conventional deposition methods. More crucially, the majority of experimental studies neglect the normalization of their results to certain photocatalytic activity descriptors, making literature values hardly comparable among each other.<sup>5</sup> These points are most likely the main reasons why literature results often neither agree on the quality of different co-catalyst materials (e.g. Pt, Au, or Ni) nor on their optimum particle size and coverage.<sup>6</sup> For example, experimental results from H<sub>2</sub> evolution on metal-loaded TiO<sub>2</sub> differ with respect to the ideal co-catalyst particle size,<sup>7, 8</sup> which can also not be controlled very precisely using conventional synthetic methods such as impregnation or photodeposition.<sup>9</sup> Nevertheless, there is general consensus that the co-catalyst is crucial for H<sub>2</sub> evolution, and a fundamental understanding is therefore imperative. Hence, studies on ideal model systems, such as semiconductor single crystals in ultra-high vacuum (UHV), can be of great importance for a systematic, rational design of photocatalysts. The use of cluster sources, such as laser ablation cluster sources, allows overcoming this restriction. They facilitate the deposition of metal clusters (which contain a precise number of atoms) at exact coverages with the possibility to control and investigate both parameters independently.<sup>10</sup> Laser ablation cluster sources have already shown their value in many thermal catalytic studies by revealing crucial effects of cluster size, coverages, and material properties.<sup>11,12</sup> In photocatalysis, however, similar studies are scarce and cluster size effects remain largely unexplored, even though there is evidence for a significant impact.<sup>13</sup>

Co-catalyst loaded TiO<sub>2</sub>(110) is one of the most commonly employed photocatalytic

model systems, especially for H<sub>2</sub> evolution.<sup>14-19</sup> In the last decade, several groups have contributed to a fundamental insight into the surface chemistry of titania single crystals,<sup>20, 21</sup> the material's charge carrier dynamics,<sup>22-24</sup> and the role of the co-catalyst in alcohol photo-oxidation.<sup>14, 15, 17, 18, 25-27</sup> It has been shown that Pt, Ni, and other metal clusters serve as co-catalyst to facilitate thermal H<sub>2</sub> evolution during photocatalytic methanol reforming on TiO<sub>2</sub>(110). These metal clusters all fulfill the same purpose as recombination and desorption centers for surface hydrogen species, apparently following the same mechanistic steps.<sup>15, 18, 19, 26</sup> In principle, this allows for their quantitative comparison as co-catalysts in the thermal hydrogen formation during methanol photoreforming. While different metals are evidently suitable for H<sub>2</sub> evolution from alcohols on titania, there is, to the best of our knowledge, no systematic investigation of the relationship between H<sub>2</sub> evolution activity and co-catalyst material, size, and coverage. As these parameters are of decisive impact in thermal catalysis, they are also expected to play a role in photocatalysis, since surface mechanisms are comprised of thermal and photocatalytic steps.

This study investigates the photocatalytic activity of Ni and Pt-loaded TiO<sub>2</sub>(110) in order to address these fundamental questions and elucidate the effects of cluster sizes and coverages. Using Auger electron spectroscopy (AES), photocatalytic experiments at different conditions and catalyst preparations, and a detailed kinetic analysis of hydrogen evolution, we determine and quantify the impact of reaction parameters on photocatalytic hydrogen evolution from methanol.

## Experimental

All experiments are carried out under highly defined conditions in a home built ultra-high vacuum (UHV) apparatus with a background pressure of  $< 9.9 \cdot 10^{-11}$  mbar.<sup>28, 29</sup> The rutile TiO<sub>2</sub>(110) single crystal (SurfaceNet GmbH, 9.95 mm · 9.95 mm · 0.3 mm) is mounted on a tantalum sample holder. Its temperature, which is measured with a type C thermocouple attached to the bottom of the mounting plate, is controlled by resistive heating and liquid N<sub>2</sub> cooling.

Methanol (Chromasolv,  $\geq 99.9\%$ , Sigma-Aldrich) and H<sub>2</sub>O (Milli-Q, 18.2 M $\Omega$  · cm) are degassed and purified by several freeze-pump-thaw cycles. Methanol is fed into the chamber via a leak valve (Pfeiffer Vacuum GmbH) attached to a home-built gas line (base pressure  $5.0 \cdot 10^{-9}$  mbar). H<sub>2</sub>O is brought directly onto the crystal surface with a molecular beam doser (4 minutes exposure time, 420 mbar back pressure at the micro-capillary plate).

Reactants and reaction products are analyzed with a quadrupole mass spectrometer (QMS) (QMA 430, Pfeiffer Vacuum GmbH), which is mounted in a line-of-sight geometry with respect to the desorbing molecules. The ion signals are corrected for the fragmentation contribution taken from reference mass spectra,<sup>30</sup> the transmission



through the QMS, and the electron-impact ionization cross section.<sup>29</sup> Temperature-programmed desorption measurements (TPD) are performed with a heating rate of  $0.8 \text{ K} \cdot \text{s}^{-1}$ .

For photocatalytic studies, the sample is placed directly under the skimmer of the QMS, and illuminated with a UV laser beam at an angle of about  $30^\circ$  with respect to the surface normal. The UV irradiation is generated with an optical parametric oscillator with frequency doubling unit (GWU, premiScan ULD/400), which is pumped by the third harmonic of a Nd:YAG laser (Innolas Spitlight HighPower 1200, 20 Hz repetition rate, 7 ns pulse width) to yield 242 nm photons. A pulse energy of  $200 \mu\text{J}$  of the incident light beam guarantees an illumination power of 4.0 mW at the crystal surface. No laser induced thermal heating effects are observed at such conditions. Prior to illumination, the sample is set to a temperature of 300 K and a constant methanol background pressure of  $5.0 \cdot 10^{-8}$  mbar or  $5.0 \cdot 10^{-7}$  mbar, respectively, is applied. Turnover frequencies (TOFs) are calculated by averaging the steady state ion current and normalizing to the amount of bridge-bonding oxygen (BBO) vacancies, which are assigned as photoactive sites. Their number is determined by means of  $\text{H}_2\text{O}$  TPDs.<sup>31</sup> A detailed description of the TOF and the mass spectrometric analysis can be found in our previous works.<sup>25, 29</sup>

Prior to any thermal or photocatalytic experiments, the crystal is prepared by several cycles of  $\text{Ar}^+$  (Ar 6.0; Air Liquide) sputtering (20 min, 1.0 keV,  $1 \cdot 10^{-5}$  mbar Ar),  $\text{O}_2$  ( $\geq 99\%$ , Westfalen) annealing (20 min, 800 K,  $1.0 \cdot 10^{-6}$  mbar  $\text{O}_2$ ), and vacuum annealing (15 min, 800 K) to obtain a reduced crystal surface. The BBO vacancy density is determined by  $\text{H}_2\text{O}$  TPD experiments.<sup>32</sup> The surface purity is regularly evaluated by Auger Electron Spectroscopy (AES) using a respective spectrometer (CMA 100, Omicron Nanotechnology GmbH).

A laser ablation source, attached to the main analysis chamber, enables the generation of metal clusters with an atomically precise number of atoms. The cluster size distribution is determined with mass scans as shown in our previous works.<sup>15, 25, 26, 29</sup> Size selected  $\text{Pt}_x$  ( $x = 1, 5, 10, \text{ or } >47$  atoms) or  $\text{Ni}_x$  ( $x = 1, 10, \text{ or } >47$  atoms) clusters are deposited *in situ* onto the  $\text{TiO}_2$  crystal under soft-landing conditions ( $<1 \text{ eV/atom}$  in kinetic energy).<sup>15</sup> For their synthesis, a plasma is created by a focused (lens' focal length about 1 m) beam of a frequency-doubled Nd:YAG (532 nm, 100 Hz, Spitlight DPSS, Innolas) that ablates a rotating Pt or Ni target. The plasma cools down through collisional cooling with He gas pulses (He 6.0, Air Westfalen) from a piezo valve, which is synchronized with the laser pulses, and the adiabatic expansion into the vacuum. The resulting cluster beam is guided through the vacuum chamber using ion optics. A quadrupole bender deflects the charged particles orthogonally so that the cationic clusters are separated from the neutral ones. A quadrupole mass filter (QMF; Extrel, USA) either enables the selection of a particular cluster size up to masses of 16000 amu or operates in the radio frequency mode, serving as high pass filter to obtain only

clusters with more than 47 atoms ( $\text{Pt}_{>47}$  or  $\text{Ni}_{>47}$ ). The cluster coverages are given in % ML respective to  $1.5 \cdot 10^{15}$  surface atoms of the  $\text{TiO}_2(110)$  sample surface.<sup>33</sup> They are determined by the neutralization current of the cationic clusters, which is measured with a picoammeter (Keithley 6587) during their deposition onto the titania crystal. The desired cluster coverages are obtained only by varying the deposition time of the size-selected clusters.

## Experimental Results

### Photoactivity of Ni- and Pt-Loaded $\text{TiO}_2(110)$

The product formation rate on cluster-loaded  $\text{TiO}_2(110)$  was quantified by determining the TOFs of formaldehyde and  $\text{H}_2$  during photocatalytic methanol oxidation. This allows to identify cluster size and coverage effects and enables a direct comparison of the performance as co-catalyst for both metals. For Ni, single atoms and clusters with sizes of 10 and  $>47$  atoms were deposited with different coverages. For the atom, coverages of 1%, and 3% of a ML  $\text{TiO}_2(110)$  surface atoms were chosen. The product formation rates of the two products for the respective photocatalytic experiments are shown in **Figure 1**. Ni clusters were deposited at a loading of 0.3% ML. As single atoms of Ni did not lead to detectable amounts of  $\text{H}_2$  during methanol photooxidation a coverage of 0.3% ML (data not shown), higher loadings of 1% ML and 3% ML  $\text{Ni}_1$  were also studied.

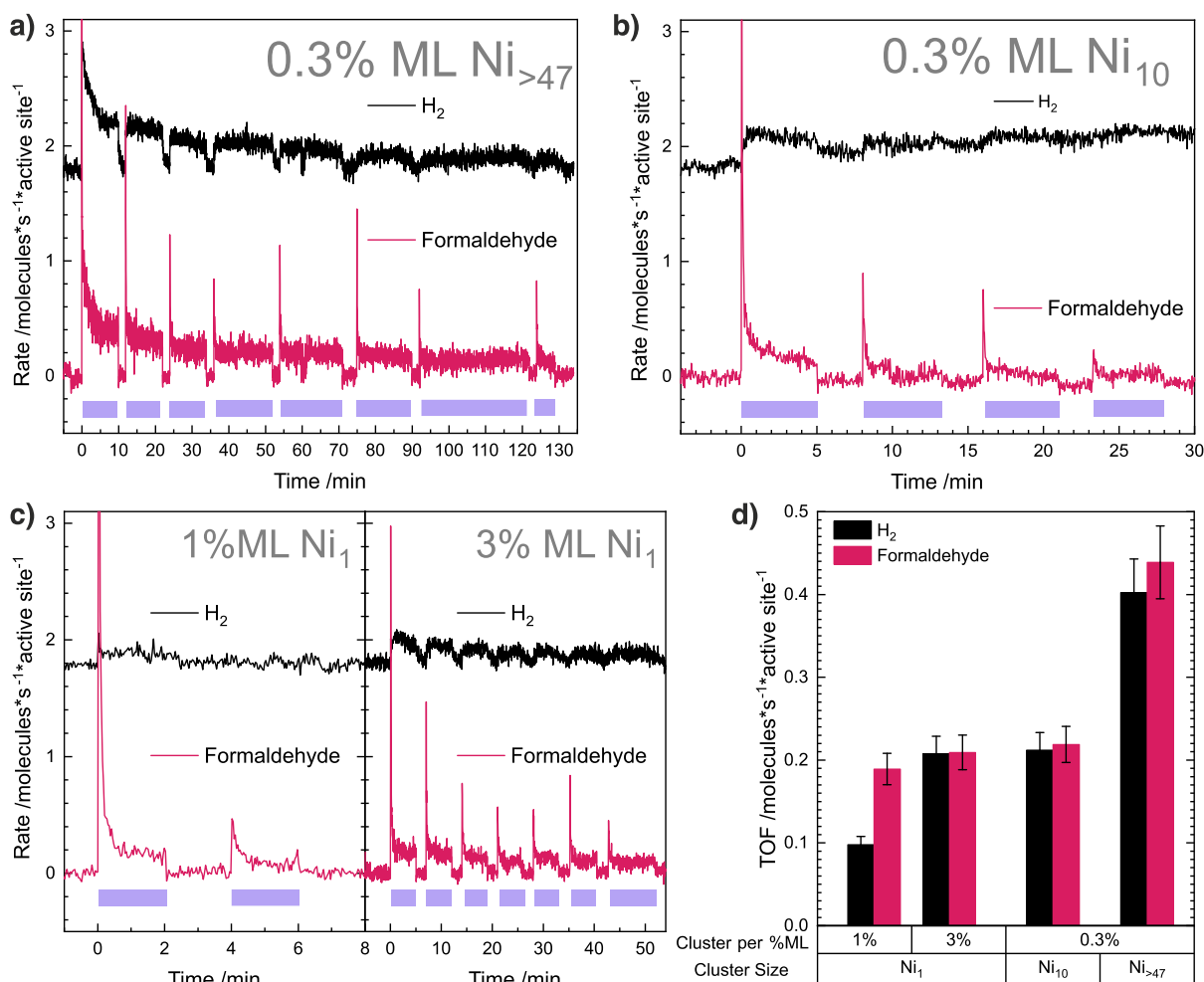


**Figure 1.** Product formation rates of hydrogen ( $m/z$  2, black) and formaldehyde ( $m/z$  30, red) from photocatalytic methanol oxidation on  $\text{Ni}_x/\text{TiO}_2(110)$  with  $x=1, 10, >47$  at 300 K in a methanol background pressure of  $5 \cdot 10^{-7}$  mbar. The signals were corrected for ionization cross section, QMS transmission, and their fragmentation pattern. The traces were offset for clarity. Violet bars indicate periods of illumination. The experiment was conducted for a) 0.3% ML  $\text{Ni}_{>47}$ , b) 0.3% ML  $\text{Ni}_{10}$ , and c) 1% as well as 3% ML atomic Ni. The TOFs for hydrogen and formaldehyde after one minute in the first illumination period were used in d). Larger clusters and higher coverages showed enhanced TOFs and longer overall lifetimes of the photocatalyst.

Independent of cluster size and coverage, the behavior of all mass traces in the photoexperiments (**Figure 1 a), b) and c)** is qualitatively the same. Upon illumination (violet bars), the formaldehyde trace shows a prompt increase of high intensity, but subsequently tapers off to lower values, which are still above the baseline in the dark. This behavior stems from an accumulation of reactant before illumination (SI Eq. 1), leading to a higher surface concentration during the first seconds of light exposure (SI Eq. 2). This phenomenon similarly occurs in this reaction with Pt-loaded  $\text{TiO}_2(110)$  (see below and in our previous works).<sup>14-16, 25, 26, 29</sup> After the initial burst, a catalytic steady state is observed under continuous light exposure. By blocking the light flux, the traces drop back to the baseline level in the dark.

Over the whole time range of the Ni experiments, the steady-state ion signal of the products decreases slightly but constantly during illumination. Each TOF for  $\text{Ni}_x/\text{TiO}_2(110)$  (d) was thus determined after one minute of the first illumination period.

While for example the formaldehyde trace on Ni<sub>>47</sub>/TiO<sub>2</sub>(110) (**Figure 1 a**) exhibits an average steady-state at roughly 0.2 molecules · (active site · s)<sup>-1</sup> during the first illumination period, the rate amounts to only 0.1 molecules · (active site · s)<sup>-1</sup> on average in the last cycle. This photocorrosion phenomenon on Ni<sub>x</sub>/TiO<sub>2</sub>(110) has been described recently by us and was attributed to catalyst deactivation by carbonaceous deposits.<sup>26</sup> These deposits block the Ni clusters so that H<sub>2</sub> recombination and desorption sites become inaccessible for hydrogen (SI Eq. 3). This leads to the accumulation of surface hydrogen species and thus increases the thermal back-reaction of adsorbed formaldehyde to methoxy (SI Eq. 2), reducing the overall reaction rate.<sup>16</sup>

Since Pt and Ni play the same mechanistic role in alcohol photooxidation on TiO<sub>2</sub>(110),<sup>15, 26</sup> their performances can be directly compared quantitatively with each other. **Figure 2** shows the product formation rates obtained from methanol photoreforming using Pt<sub>10</sub> and Ni<sub>10</sub> as co-catalyst, respectively, with a coverage of 0.3% ML.

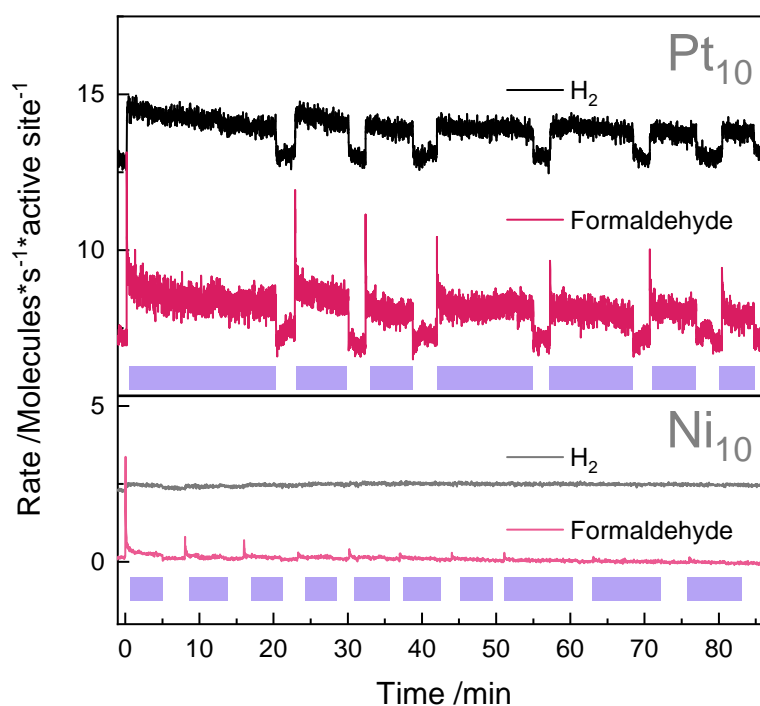


**Figure 2.** Product formation rates for hydrogen ( $m/z$  2, black) and formaldehyde ( $m/z$  30, red) from photocatalytic methanol oxidation on 0.3% ML Pt<sub>10</sub>/TiO<sub>2</sub>(110) and 0.3% ML Ni<sub>10</sub>TiO<sub>2</sub>(110) at 300 K in a methanol background pressure of  $5 \cdot 10^{-7}$  mbar. The signals were corrected for ionization cross section, QMS transmission, and their fragmentation pattern. Violet bars indicate periods of illumination. The traces were offset for clarity. The activity of platinum clusters was more than an order of magnitude higher than that for nickel clusters.

It is found that the activity of the platinum clusters exceeds that of the nickel clusters by more than an order of magnitude. This is in good agreement with observations made in alcohol photoconversion experiments under ambient conditions using Ni and Pt as co-catalysts on TiO<sub>2</sub>.<sup>34</sup> Moreover, a similar deactivation as it occurs for Ni clusters

is not observed on Pt-loaded titania, consistent with previous results on  $\text{Pt}_x/\text{TiO}_2(110)$  with size-distributed clusters.<sup>14, 15, 25, 29</sup>

To further determine the impact of Pt cluster size and loading on its activity in methanol photoreforming, Pt atoms and clusters of 5, 10, and >47 atoms were deposited with coverages ranging between 0.1% and 2% ML on  $\text{TiO}_2(110)$ . The corresponding  $\text{H}_2$  and formaldehyde TOFs are shown in **Figure 3**. A green, yellow and brown background color denotes equal amounts of Pt atoms on the surface among different size-coverage combinations.

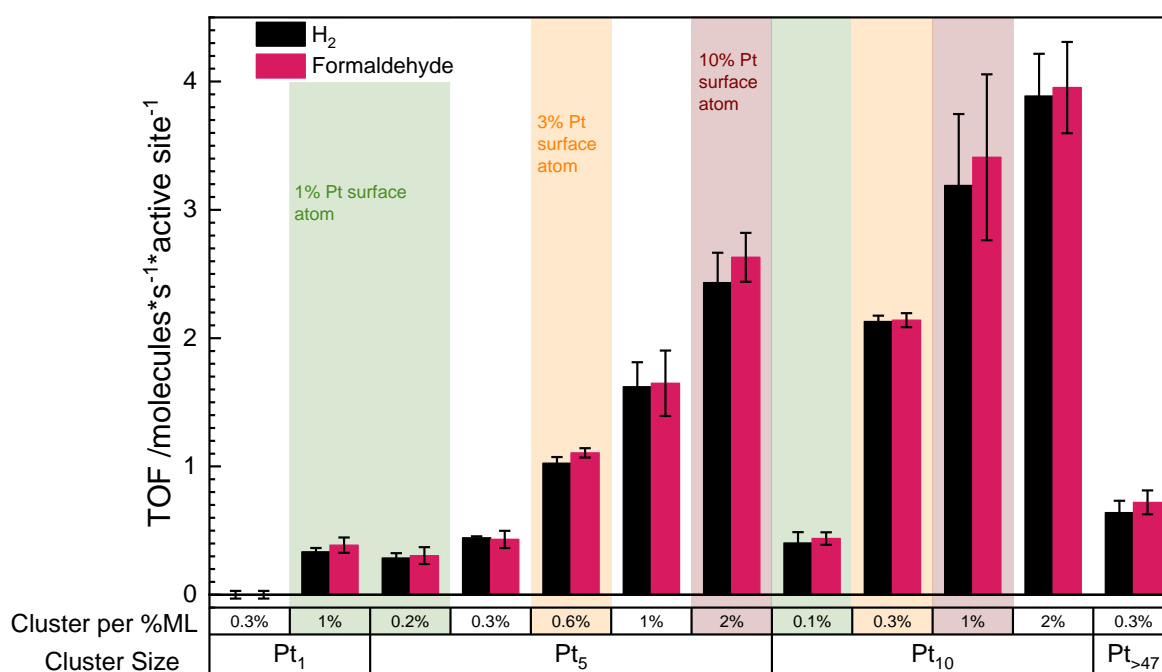


**Figure 3.** TOFs for  $\text{H}_2$  (black bars) and formaldehyde (red bars) from photocatalytic methanol oxidation on  $\text{Pt}_x/\text{TiO}_2(110)$  at 300 K in a methanol background pressure of  $5 \cdot 10^{-7}$  mbar after one hour. A background colored in green, yellow and brown indicates the same total amount of Pt atoms among different coverage-size combinations.

As a general trend, higher coverages lead to higher TOFs within a given cluster size, in agreement with a study by Hao *et al.*<sup>17</sup> In this sense, coverages of 0.3% ML and below show rather small TOFs. In this regime, the catalytic activity is dominated by the number of clusters rather than the total amount of Pt on the surface. This holds also true for samples with a coverage of 0.3% ML of  $\text{Pt}_{>47}$ , which shows relatively low TOFs albeit the total amount of Pt is the highest of all examples shown. In some cases, different coverages with equal amounts of Pt atoms (colored bars) do not yield equally high TOFs (e.g. 0.6% ML  $\text{Pt}_5$  and 0.3% ML  $\text{Pt}_{10}$ ). The TOF of 0.3% ML  $\text{Pt}_{10}$  exceeds the one of 0.6% ML  $\text{Pt}_5$  two-fold, which is completely different to the behavior of Ni clusters described above (**Figure 1d**). Among all Pt cluster sizes,  $\text{Pt}_{10}$  generally shows

very high activities and facilitates significant product evolution already at a low coverage of 0.3% ML. Nevertheless, the activity of Pt<sub>10</sub>/TiO<sub>2</sub>(110) cannot be arbitrarily enhanced by higher loadings. The three-fold increase in loading from 0.3% ML to 1% ML Pt<sub>10</sub> only leads to a roughly doubled product formation rate, while another two-fold increase from 1% ML to 2% ML hardly affects the TOF at all.

When plotting the TOF versus cluster loading (**Figure 4 a**) or the total amount of Pt atoms (**Figure 4 b**), the curve's progression follows a logarithmic behavior for each cluster size. As a result, the product formation rate increases initially fast, then abates and asymptotically approaches an upper value. For example, in the case of Pt<sub>10</sub>, the H<sub>2</sub> and formaldehyde TOFs seem to approach a value of four molecules per active site and s. Notably, the curve progressions of Pt<sub>5</sub> and Pt<sub>10</sub> of **Figure 4 a**) and **b**) are similar but differ in the overall slope and height. For an equal amount of Pt surface atoms (**Figure 4 b**), the curve of Pt<sub>5</sub> runs slightly, but systematically below the curve of Pt<sub>10</sub>. Thus, TOFs for samples with Pt<sub>10</sub> clusters are even higher if the total amount of Pt is the same as for samples with Pt<sub>5</sub>. Furthermore, although TiO<sub>2</sub>(110) loaded with Pt<sub>>47</sub> has a similarly high amount of Pt atoms as 2% ML Pt<sub>10</sub>, its TOF is only one fourth of the latter.

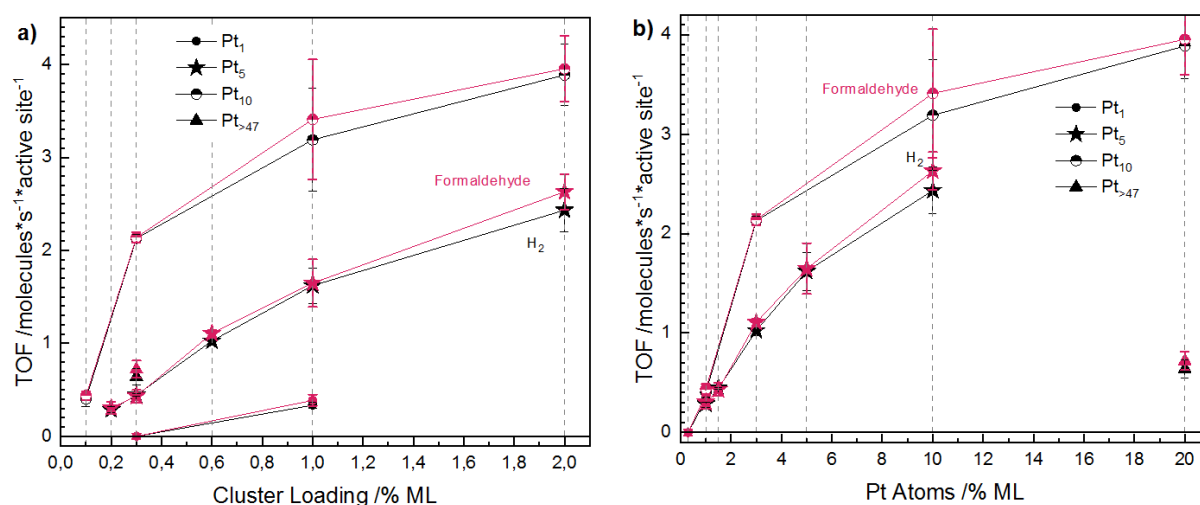


**Figure 4.** TOFs for hydrogen (black) and formaldehyde (red) from photocatalytic methanol oxidation on Pt<sub>x</sub>/TiO<sub>2</sub>(110) at 300 K in a methanol background pressure of  $5 \cdot 10^{-7}$  mbar after one hour. a) TOF for different Pt cluster sizes as a function of loading (i.e. the number of clusters on the surface). b) TOF for different Pt cluster sizes as a function of total amount of Pt atoms.

### Kinetics of H<sub>2</sub> Desorption from Pt-loaded Titania

Throughout the experiments, the formaldehyde trace constantly shows an intensive burst when illumination begins, irrespective of the overall catalyst activity (see **Figure 1**). Similarly, the trace drops immediately back to the baseline level in the dark when stopping the illumination. This is not the case for the H<sub>2</sub> trace, indicating different formation and desorption kinetics of these two photoproducts. As the formation of H<sub>2</sub>

is achieved by a consecutive reaction step on the metal clusters, it exhibits a different behavior than the preceding photoreaction yielding formaldehyde. Therefore, it can be regarded as a separate reaction step.<sup>16</sup> Consequently, a more detailed evaluation of the H<sub>2</sub> trace may provide further information about the formation and desorption kinetics of this molecule. **Figure 5** shows excerpts from photocatalytic experiments on 1% ML Pt<sub>10</sub> (left) and 0.3% ML Ni<sub>>47</sub> (right) on TiO<sub>2</sub>(110) at 300 K in a methanol background of  $5 \cdot 10^{-7}$  mbar to illustrate the resulting effect.

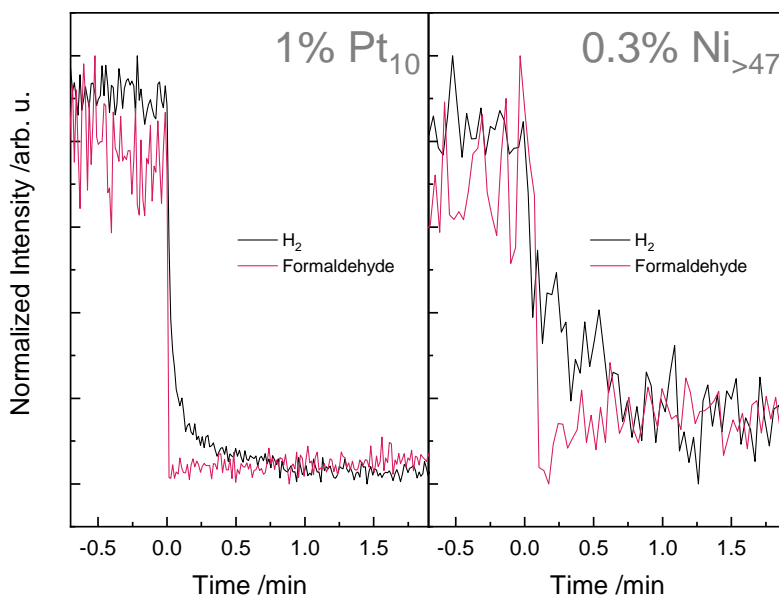


**Figure 5.** Excerpts of the QMS traces for hydrogen (black) and formaldehyde (red) during photocatalytic methanol oxidation on 1% ML Pt<sub>10</sub>/TiO<sub>2</sub>(110) (left) and 0.3% ML Ni<sub>>47</sub>/TiO<sub>2</sub>(110) (right) at 300 K in a methanol background pressure of  $5 \cdot 10^{-7}$  mbar. 0 min was defined as the moment when the light flux was blocked.

For both co-catalysts, the formaldehyde trace shows a sharp drop when the illumination is stopped (set to 0 min), while the H<sub>2</sub> trace tails off to the baseline in the dark. Although more clearly visible for the platinum-loaded sample due to the much better signal-to-noise ratio, the phenomenon is clearly evident on Ni<sub>>47</sub>/TiO<sub>2</sub>(110), too. In order to extract quantitative information from the peculiar behavior of the hydrogen trace, details of the reaction need to be considered: Since two surface hydrogen species are necessary for H<sub>2</sub> evolution, its formation is expected to follow a second-order behavior with respect to the concentration of surface hydroxyls ([H<sub>ad</sub>]), according to

$$-\frac{d[H_2]}{dt} = \frac{1}{2} \frac{d[H_{ad}]}{dt} = -k \cdot [H_{ad}]^2 \quad (\text{Eq. 1})$$

where  $k$  denotes the rate constant of this reaction and  $[H_2]$  to concentration of molecular hydrogen evolved (corresponding to its partial pressure). Integration (further details are given in the SI) yields the concentration for surface hydroxyls ( $[H_{ad}]_t$ ) at a particular time  $t$ :

$$[H_{ad}]_t = \frac{[H_{ad}]_0}{2k[H_{ad}]_0 \cdot t + 1} \quad (\text{Eq. 2})$$

where  $[H_{ad}]_0$  represents the initial concentration of surface hydroxyl (or its steady-state concentration during photocatalysis). Expressing the concentration of molecular hydrogen at the time  $t$  by the change in the concentration of hydroxyls over reaction time

$$[H_2]_t = \frac{1}{2}([H_{ad}]_0 - [H_{ad}]_t) \quad (\text{Eq. 3})$$

finally leads to

$$\frac{d[H_2]_t}{dt} = \frac{k[H_{ad}]_0^2}{(2k[H_{ad}]_0 \cdot t + 1)^2} \quad (\text{Eq. 4})$$

with (at  $t = 0$ )

$$k[H_{ad}]_0^2 = \text{TOF} \quad (\text{Eq. 5})$$

Consequently, the decay function can be fitted with:

$$r(t) = \frac{\text{TOF}}{\left(2 \frac{\text{TOF}}{[H_{ad}]_0} \cdot t + 1\right)^2} \quad (\text{Eq. 6})$$

in order to finally obtain the rate constant  $k'$ , which is defined by:

$$k' = k[H_{ad}]_0 \quad (\text{Eq. 7})$$

and serves as a quantitative measure for the decay rate. **Figure 6** shows baseline-corrected normalized QMS data extracted from different experiments with different amounts of co-catalyst loadings and the results from the second-order fitting procedure. A fast removal of hydrogen as  $H_2$  is expressed in high  $k'$  values (all values are given in **Table S1**), i.e. a steep slope of the decay. Clearly, the decay rate is significantly affected by the amount of co-catalyst on the surface. Higher co-catalyst loadings and catalytically more active cluster sizes show a higher rate constant and a faster decay. The differences are particularly evident for moderately active samples (i.e. slow decays), where the signal/noise ratio is sufficiently high but the reaction is not too fast so that it is limited by the time resolution of the QMS. It is found that samples decorated with  $Pt_5$  exhibit a doubling of the rate constant when their loading is increased two-fold. Furthermore, 0.6% ML  $Pt_5/TiO_2$  samples display a lower but somewhat comparable rate constant as 0.3% ML  $Pt_{10}/TiO_2$ .



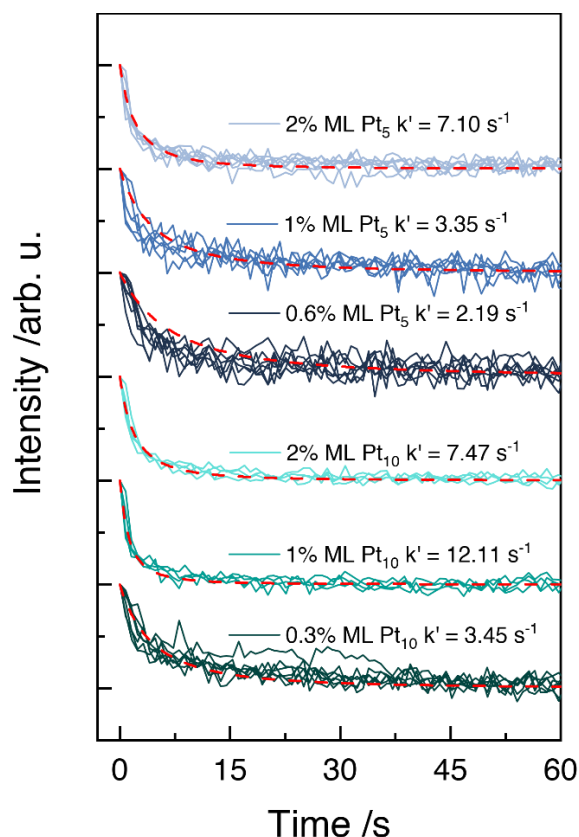


**Figure 6.** Excerpts of the normalized traces for hydrogen (black) during photocatalytic methanol oxidation experiments for different coverages of 1% ML and 2% ML of Pt<sub>5</sub> and Pt<sub>10</sub> at 300 K in a methanol background pressure of  $5 \cdot 10^{-7}$  mbar. The dashed red lines fit the decaying traces according to  $r(t) = \frac{k[H_{ad}]_0^2}{(2k[H_{ad}]_0 t + 1)^2}$ , where  $r(t)$  is the rate at a certain time  $t$  during the decay. The resulting  $k$  values are the respective rate constants.  $k[H_{ad}]_0^2$  was equalized to the TOF determined from the corresponding steady-state photoreforming interval.

## Discussion

### Photoactivity of Ni-Loaded TiO<sub>2</sub>(110)

For all cluster sizes and coverages, except for very low amounts of atomic Ni and Pt, hydrogen evolution on  $M_x/\text{TiO}_2(110)$  is facilitated and occurs stoichiometrically with formaldehyde. Thus, the reaction always follows the same mechanistic pathways (see ESI), but with significantly different rates in the different systems (**Figure 1 a – c**; **Figure 3**). The clusters act as hydrogen recombination centers by facilitating the desorption of H<sub>2</sub> and preventing the thermal back-reaction of the  $\alpha$ -H cleavage,<sup>16</sup> which strongly affect the overall product formation rate. On Ni<sub>x</sub>/TiO<sub>2</sub>(110), the activity in general benefits from larger clusters and higher coverages, and the total amount of Ni atoms on the surface governs the TOFs. Consequently, Ni<sub>>47</sub> clusters show the

highest catalytic activity, while 0.3% ML Ni<sub>10</sub> exhibit the same TOFs as 3% ML atomic Ni with the same metal content. Therefore, the kinetics of H<sub>2</sub> formation appears to be directly correlated to the total amount of the metal, while detectable cluster size-dependent effects are absent, different to thermal catalysis.<sup>35</sup> Larger areas of H<sub>2</sub> recombination sites thus allow for higher amounts being formed over a longer time span. Furthermore, the longer catalyst lifetime for higher amounts of Ni is explained by the increase in time which is required for the blocking of a bigger area with carbon. Independent of cluster size and coverage, eventual deactivation seems to be inevitable, as each Ni<sub>x</sub>/TiO<sub>2</sub>(110) catalyst investigated in this study features this unwanted property.

For Ni atoms (**Figure 1 c**)), only traces of H<sub>2</sub> are detected for a 1% ML coverage. After two minutes of illumination, no H<sub>2</sub> formation is observed anymore. Apart from that, the formation of photoproducts does not even seem to be stoichiometric (**Figure 1 d**)). Thus, the use of Ni atoms as co-catalyst in alcohol photoreforming may be questionable. The reaction behavior is in fact similar to the bare TiO<sub>2</sub>(110), where H<sub>2</sub> desorption is not observed at all.<sup>16</sup>

### **Photoactivity of Pt-Loaded TiO<sub>2</sub>(110)**

Pt-loaded titania exhibit a higher photocatalytic activity than Ni-loaded titania. For example, the activity of Pt<sub>10</sub>/TiO<sub>2</sub>(110) exceeds the activity of Ni<sub>10</sub>/TiO<sub>2</sub>(110) (**Figure 2**) roughly by an order of magnitude, which we attribute to the higher hydrogen evolution capability of Pt. Volcano plots from electrochemical studies suggest different metal-hydrogen bond strength as the origin of this difference.<sup>36, 37</sup> However, these plots have to be interpreted with caution,<sup>38</sup> especially since one has to extrapolate from electrochemical to photochemical systems. Unlike Ni-loaded titania, Pt<sub>x</sub>/TiO<sub>2</sub>(110) does not deactivate by photocorrosion and shows stable catalytic activity over hours.<sup>14</sup> While the Auger spectra of Ni<sub>x</sub>/TiO<sub>2</sub>(110) reveal persistent carbon deposits on the surface after catalysis and even after heating to 800 K,<sup>26</sup> no carbon is observed in comparable Auger spectra of Pt<sub>x</sub>/TiO<sub>2</sub>(110) after catalysis (see **Figure S1**). Overall, the high activity and long-term stability of Pt-loaded titania show Pt to clearly outperform Ni as co-catalyst material for the photocatalytic hydrogen evolution from alcohols on TiO<sub>2</sub>(110). This also holds for atomic systems, as 1% ML Pt atoms as co-catalyst enable a considerable, steady photocatalytic hydrogen evolution (see **Figure S2**), while 1% ML Ni<sub>1</sub> only evolves negligible amounts of H<sub>2</sub> during illumination (**Figure 1** bottom left). However, a lower metal loading of 0.3% ML of atomic Pt does also not exhibit detectable H<sub>2</sub> evolution activity during methanol photooxidation and, consequently, a certain amount of noble metal is needed for significant H<sub>2</sub> evolution. Within one specific cluster size, higher Pt co-catalyst coverages lead to enhanced TOFs (**Figure 3**). Obviously, a higher loading has a stronger beneficial effect on the

H<sub>2</sub> recombination rate. This is conceivable since the clusters act merely as H<sub>2</sub> recombination centers irrespective of their size; a higher cluster coverage therefore enhances the product formation rate (SI Eq. 2). Notably, different cluster size and coverage combinations which contain the same overall amount of Pt atoms (e.g. 0.6% ML Pt<sub>5</sub> and 0.3% ML Pt<sub>10</sub>) do not result in the same TOFs. As in the case of Ni, the total amount of metal on the surface remains an important parameter for H<sub>2</sub> evolution with Pt clusters, too, but the trend is overshadowed by size effects, which clearly affect the activity of Pt<sub>10</sub>/TiO<sub>2</sub>(110). This is different to Ni, where 0.3% ML Ni<sub>>47</sub> shows the highest TOF. These Pt cluster size effects (**Figure 3**) are in very good agreement with the recent literature. A first principles study by Wei and Liu predicted that Pt clusters without core atoms should show the highest H<sub>2</sub> formation activity.<sup>39</sup> Small particles with a high concentration of five or six coordinated apex sites per surface area (i.e. sizes below 20 atoms) were ascribed a dramatically higher activity than bigger clusters. Wang *et al.* calculated electronic properties of Pt clusters on anatase and concluded that two-layer structures of 0.7 – 1.5 nm in size are the ideal shape for photocatalytic hydrogen evolution.<sup>27</sup> These results were corroborated in a recent experimental study by Dessal *et al.* under ambient conditions.<sup>8</sup> In a theory-based work by Jiang *et al.*, Pt<sub>5-10</sub> clusters on TiO<sub>2</sub>(110) were indeed found to have two-layer structures.<sup>40</sup> Experimentally, two-layer structures for Pt<sub>>7</sub> on TiO<sub>2</sub>(110) were observed by Watanabe *et al.* by means of STM, although not for Pt<sub>5</sub>.<sup>41</sup> Thus, two-layer structures can be expected to occur for Pt<sub>10</sub> and possibly Pt<sub>5</sub>, whose comparably high activity agrees well with the theoretical predictions. Neuberger *et al.* investigated different sizes of Pt co-catalysts for the electrocatalytic hydrogen evolution on titania. They found that bulk Pt, Pt nanoparticles, Pt<sub>13</sub>, Pt<sub>10</sub>, and atomic Pt were all capable of H<sub>2</sub> production. Pt<sub>10</sub> and Pt<sub>13</sub> outperformed the others. Pt atoms showed the lowest activities. The results were explained with the overall amount of accessible Pt. No clear trend in the electronic structure emerged with respect to the Pt 4f<sub>7/2</sub> core levels.<sup>42</sup>

These theoretical and experimental results explain the behavior depicted in **Figure 3** thoroughly. The low or almost absent activity of Pt atoms is rationalized as follows: First, there is a low number of Pt sites when compared to a cluster at equal coverage. Second, a two-layer structure, which is favorable for H<sub>2</sub> evolution according to theory,<sup>27</sup> is absent. Third, the interaction of single Pt atoms with adsorbates and the support is most likely unfavorable for efficient H<sub>2</sub> evolution, because the Pt<sub>1</sub>-TiO<sub>2</sub> interaction is stronger than for bigger particles.<sup>40</sup> The enhanced H<sub>2</sub> rate of Pt<sub>5</sub> compared to single atoms is attributable to a larger total number of available Pt sites and probably one second-layer Pt atom as calculated by Jiang *et al.*<sup>40</sup> Pt<sub>10</sub> shows a 3D two layer structure<sup>41</sup> and the parameters governing the activity are combined optimally among the cluster sizes investigated herein, as proposed by theory studies in the literature<sup>27, 39</sup> (similar as in the work by Neuberger *et al.*).<sup>42</sup> Pt<sub>>47</sub> instead shows a high number of available Pt sites, but the particle size leads to a distinct bulk-like metallic character of

the majority of Pt atoms, which seems less favorable for H<sub>2</sub> evolution than the properties of small particles.<sup>27, 42</sup>

Furthermore, size effects are in general common for reactions involving hydrogen on metal cluster-loaded surfaces.<sup>43, 44</sup> Since H<sub>2</sub> formation on Pt<sub>x</sub>/TiO<sub>2</sub>(110) expectedly proceeds *via* a reverse spillover mechanism from the support to the cluster, the system appears similar to thermal size-sensitive cluster catalysts.<sup>45</sup> For example, some studies suggest an enhanced catalytic activity on the cluster perimeter.<sup>46, 47</sup> In a reverse spillover mechanism, differences in co-catalyst activity not only rely on the electronic structure and accessibility of certain cluster sites, but also on the width of the capture zone (that is, the area around the clusters where hydrogen can efficiently be scavenged). This capture zone will be larger for Pt<sub>10</sub> than for smaller Pt<sub>5</sub> particles, affecting the H<sub>2</sub> evolution capability more beneficially for the larger cluster. The size trends for Pt clusters in H<sub>2</sub> evolution discussed here are graphically summarized in **Figure 7**.

The asymptotic behavior of the Pt<sub>10</sub> curve in **Figure 4** and the very similar TOFs for coverages of 1% ML and 2% ML (**Figure 3**) indicate that at a specific coverage the amount of co-catalyst may not be limiting the reaction kinetics anymore, because the recombination of hydrogen is already facilitated quickly. While an upper TOF value of roughly four molecules per active site and s can be achieved, higher cluster coverages are not expected to enhance the TOF significantly further. In fact, it has already been observed that high metal loadings are detrimental for the photocatalytic activity on titania nanoparticles. Optimal values usually do not exceed more than only a few weight percent of platinum.<sup>48, 49</sup> Instead of increasing the surface coverage of the co-catalyst, a faster reactant supply will be more beneficial for higher reaction rates. Indeed, this is clearly visualized when the TOF is normalized by (and therefore independent of) the pressure (as exemplified for Pt<sub>5</sub> and Pt<sub>10</sub> in **Figure S3**). The kinetic limitation by reactant adsorption also leads to a saturation of the TOF at much lower cluster coverages for a lower pressure of methanol and only much lower maximal values are achieved (**Figure S4**). These impacts of cluster loading and reactant supply on the maximum TOF corroborate the mechanistic picture of thermal H<sub>2</sub> formation by surface hydroxyl recombination. If the concentration of surface hydrogen is too low due to insufficient supply of reactant, an increasing number of hydrogen recombination sites by a higher cluster density does not lead to notable changes in the overall reaction rate. A similar observation was made in a study by Teichner and co-workers about photocatalytic hydrogen generation from isopropanol on Pt/TiO<sub>2</sub> catalysts<sup>50</sup>, which indicates that similar mechanistic consequences may also result in that study, too.

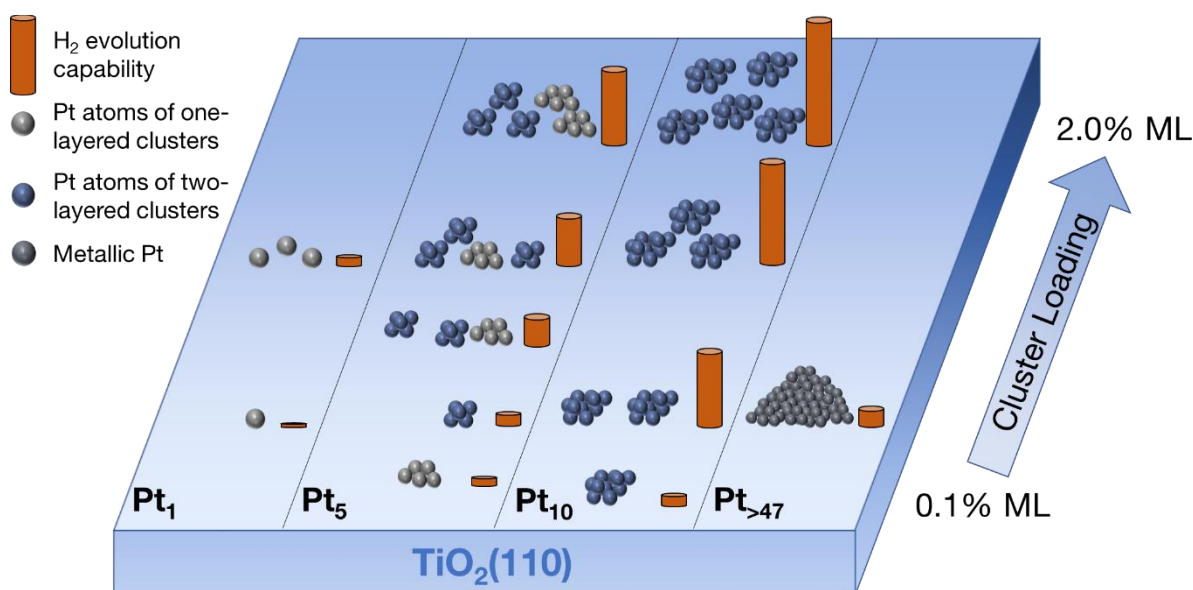


**Figure 7.** Graphic representation of the cluster size-dependent H<sub>2</sub> evolution capability (orange bars) of Pt clusters on TiO<sub>2</sub>(110) for different cluster coverages. 1<sup>st</sup> layer Pt atoms are depicted in grey, 2<sup>nd</sup> layer Pt atoms in orange. Pt<sub>>47</sub> clusters are depicted in dark grey to emphasize their more metallic character. The heights of the activity bars correspond to the numerical TOF values shown in Figure 3.

### Kinetics of H<sub>2</sub> Desorption from Pt- and Ni-loaded Titania

The size-coverage trends observed in the TOFs are also displayed in the H<sub>2</sub> decay kinetics of the corresponding QMS trace. The respective formaldehyde and hydrogen traces for both Ni<sub>x</sub> and Pt<sub>x</sub> co-catalysts decay in a similar fashion after the illumination has stopped. The qualitative behavior of the decay kinetics is thus specific to the product formed and not to the co-catalyst. This observation further evidences that the reaction mechanisms of product formation are presumably identical for Ni<sub>x</sub> and Pt<sub>x</sub>. In both cases H<sub>2</sub> evolution represents a consecutive reaction step to the photoreaction, which is formally independent of methanol photooxidation.<sup>16, 26</sup>

Furthermore, the H<sub>2</sub> evolution kinetics in photocatalytic studies can be quantified by evaluating the H<sub>2</sub> trace decay, which occurs after switching off the UV light. After extracting the data and performing baseline corrections, a second-order decay fit is used to model the datasets. The comparison with exponential fits (with values for R-square given in **Table S2** and the difference graphically exemplified for one experiment in **Figure S5**) reveals that the reaction indeed follows the behavior expected from the bimolecular nature of the hydrogen evolution. The better agreement of second-order kinetics further indicates that saturation effects in the surface hydroxyl concentration do not play a significant role in the reactions studied. The resulting rate constants (expressed as *k* values) allow more quantitative conclusions about the impact of the cluster sizes and loadings on the H<sub>2</sub> kinetics. They reflect several individual reaction steps, e.g. the diffusion of surface-hydrogen to the co-catalyst, the reverse spillover of

hydrogen from the TiO<sub>2</sub> surface to the metal clusters, and the hydrogen recombination there. Although the relative significance of these steps cannot yet be unambiguously determined, the 2<sup>nd</sup> order rate dependency tentatively suggests a limitation through hydrogen recombination rather than e.g. hydrogen migration. The comparison of different *k*'s reveals the same trend as the TOFs: Pt<sub>10</sub> shows faster decays than Pt<sub>5</sub> at equal coverages, which reflects the different size-dependent capabilities of removing hydrogen from the titania surface. Higher cluster loadings usually lead to a faster removal of surface hydrogen and, thus, to a higher value of *k*. The observation of this same trend in turn shows that the clusters do not influence the photoactive centers significantly at the coverages studied so that both partial reactions, surface hydroxyl formation and their recombination, occur largely unaffected from each other.

## Conclusion

This study shows that size-selected Ni and Pt co-catalysts influence the reactivity in photocatalytic methanol reforming on TiO<sub>2</sub>(110) in different ways. While the general mechanism of product formation is the same, catalyst deactivation occurs for all cluster sizes and coverages of nickel clusters. In contrast, such a behavior is not observed for Pt clusters, which exhibit a stable photocatalytic activity at least in the order of several hours. Moreover, Pt as co-catalyst on TiO<sub>2</sub>(110) generally leads to a much higher product formation rate than Ni. Regarding cluster size and coverage, an increase of the total amount of Ni on the surface, i.e. larger clusters or higher coverages, results in a TOF enhancement without size-specific impacts. In contrast, size-effects are observed for Pt, because a higher concentration of one particular cluster species (most notably Pt<sub>10</sub>) may improve the catalytic activity more than a simple increase in the metal content by the deposition of larger clusters. A two-layered geometry of small Pt clusters seems to be highly beneficial for H<sub>2</sub> evolution, in accordance with experimental studies from electrochemistry and theoretical predictions. Furthermore, the mechanistic picture of thermal H<sub>2</sub> evolution from alcohol photoreforming on TiO<sub>2</sub>(110) is corroborated and kinetically evaluated by investigating mass spectrometric data. A slow decay or sudden drop to the baseline upon ceasing illumination indicates different thermal desorption kinetics for H<sub>2</sub> (thermal recombination at clusters) and formaldehyde (direct desorption from titania), respectively. A faster decay of the H<sub>2</sub> trace is always associated with an increase in the TOF when the size or coverage of Pt clusters is changed. This can be traced back mechanistically to the inhibition of the back reaction by a faster rate of H<sub>2</sub> recombination.<sup>16</sup> Our work therefore shows that cluster size effects may play an important role in photocatalytic hydrogen evolution reactions, depending on the metal co-catalyst material. For platinum, it is found that higher metal loadings by an increase in the particle size is detrimental to the catalytic activity (similarly as it was reported for higher coverages).<sup>48, 49</sup>

## References

1. W. Y. Teoh, J. A. Scott and R. Amal, *J Phys Chem Lett*, 2012, **3**, 629-639.
2. L. Chen, J. Tang, L. N. Song, P. Chen, J. He, C. T. Au and S. F. Yin, *Appl Catal B-Environ*, 2019, **242**, 379-388.
3. Q. Wang and K. Domen, *Chem Rev*, 2020, **120**, 919-985.
4. B. A. Pinaud, J. D. Benck, L. C. Seitz, A. J. Forman, Z. B. Chen, T. G. Deutsch, B. D. James, K. N. Baum, G. N. Baum, S. Ardo, H. L. Wang, E. Miller and T. F. Jaramillo, *Energ Environ Sci*, 2013, **6**, 1983-2002.
5. M. Dilla, N. G. Moustakas, A. E. Becerikli, T. Peppel, A. Springer, R. Schlogl, J. Strunk and S. Ristig, *Phys Chem Chem Phys*, 2019, **21**, 13144-13150.
6. N. Fajrina and M. Tahir, *Int J Hydrogen Energ*, 2019, **44**, 540-577.
7. Z. H. N. Al-Azri, M. AlOufi, A. Chan, G. I. N. Waterhouse and H. Idriss, *Acs Catal*, 2019, **9**, 3946-3958.
8. C. Dessal, L. Martinez, C. Maheu, T. Len, F. Morfin, J. L. Rousset, E. Puzenat, P. Afanasiev, M. Aouine, L. Soler, J. Llorca and L. Piccolo, *J Catal*, 2019, **375**, 155-163.
9. D. Y. C. Leung, X. L. Fu, C. F. Wang, M. Ni, M. K. H. Leung, X. X. Wang and X. Z. Fu, *Chemosuschem*, 2010, **3**, 681-694.
10. U. Heiz, F. Vanolli, L. Trento and W. D. Schneider, *Rev Sci Instrum*, 1997, **68**, 1986-1994.
11. S. Vajda and M. G. White, *Acs Catal*, 2015, **5**, 7152-7176.
12. M. Arenz, S. Gilb and U. Heiz, *The Chemical Physics of Solid Surfaces*, 2007, **12**, 1-51.
13. F. F. Schweinberger, M. J. Berr, M. Doblinger, C. Wolff, K. E. Sanwald, A. S. Crampton, C. J. Ridge, F. Jackel, J. Feldmann, M. Tschurl and U. Heiz, *J Am Chem Soc*, 2013, **135**, 13262-13265.
14. C. A. Walenta, C. Courtois, S. L. Kollmannsberger, M. Eder, M. Tschurl and U. Heiz, *Acs Catal*, 2020, **10**, 4080-4091.
15. C. A. Walenta, S. L. Kollmannsberger, C. Courtois, R. N. Pereira, M. Stutzmann, M. Tschurl and U. Heiz, *Phys Chem Chem Phys*, 2019, **21**, 1491-1496.
16. C. Courtois, M. Eder, S. L. Kollmannsberger, M. Tschurl, C. A. Walenta and U. Heiz, *Acs Catal*, 2020, **10**, 7747-7752.
17. Q. Q. Hao, Z. Q. Wang, T. J. Wang, Z. F. Ren, C. Y. Zhou and X. M. Yang, *Acs Catal*, 2019, **9**, 286-294.
18. F. L. Li, X. Chen, Q. Guo and X. M. Yang, *J Phys Chem C*, 2020, **124**, 26965-26972.
19. K. Katsiev, G. Harrison, Y. Al-Salik, G. Thornton and H. Idriss, *Acs Catal*, 2019, **9**, 8294-8305.
20. M. A. Henderson, *Surf Sci Rep*, 2011, **66**, 185-297.
21. M. A. Henderson and I. Lyubinetsky, *Chem Rev*, 2013, **113**, 4428-4455.
22. R. F. Qian, H. X. Zong, J. Schneider, G. D. Zhou, T. Zhao, Y. L. Li, J. Yang, D. W. Bahnemann and J. H. Pan, *Catal Today*, 2019, **335**, 78-90.
23. G. Kolesov, D. Vinichenko, G. A. Tritsarlis, C. M. Friend and E. Kaxiras, *J Phys Chem Lett*, 2015, **6**, 1624-1627.
24. A. P. Muraca, M. D. Kershish, N. Camillone and M. G. White, *J Chem Phys*, 2019, **151**.
25. C. Courtois, M. Eder, K. Schnabl, C. A. Walenta, M. Tschurl and U. Heiz, *Angew Chem Int Edit*, 2019, **58**, 14255-14259.

26. M. Eder, C. Courtois, T. Kratky, S. Günther, M. Tschurl and U. Heiz, *Catal Sci Technol*, 2020, **10**, 7779-7779.
27. D. Wang, Z. P. Liu and W. M. Yang, *Acs Catal*, 2018, **8**, 7270-7278.
28. C. A. Walenta, S. L. Kollmannsberger, J. Kiermaier, A. Winbauer, M. Tschurl and U. Heiz, *Phys Chem Chem Phys*, 2015, **17**, 22809-22814.
29. S. L. Kollmannsberger, C. A. Walenta, C. Courtois, M. Tschurl and U. Heiz, *Acs Catal*, 2018, **8**, 11076-11084.
30. <https://webbook.nist.gov/>, 2021.
31. M. A. Henderson, *Langmuir*, 1996, **12**, 5093-5098.
32. M. A. Henderson, S. Otero-Tapia and M. E. Castro, *Faraday Discuss*, 1999, **114**, 313-329.
33. U. Diebold, *Surf Sci Rep*, 2003, **48**, 53-229.
34. L. T. Prahov, J. Disdier, J. M. Herrmann and P. Pichat, *Int J Hydrogen Energ*, 1984, **9**, 397-403.
35. U. Heiz, *Appl Phys a-Mater*, 1998, **67**, 621-626.
36. B. E. Conway and G. Jerkiewicz, *Electrochim Acta*, 2000, **45**, 4075-4083.
37. J. K. Nørskov, T. Bligaard, J. Rossmeisl and C. H. Christensen, *Nat Chem*, 2009, **1**, 37-46.
38. P. Quaino, F. Juarez, E. Santos and W. Schmickler, *Beilstein J Nanotech*, 2014, **5**, 846-854.
39. G. F. Wei and Z. P. Liu, *Chem Sci*, 2015, **6**, 1485-1490.
40. D. E. Jiang, S. H. Overbury and S. Dai, *J Phys Chem C*, 2012, **116**, 21880-21885.
41. Y. Watanabe, X. Y. Wu, H. Hirata and N. Isomura, *Catal Sci Technol*, 2011, **1**, 1490-1495.
42. F. Neuberger, J. Baranyai, T. Schmidt, T. Cottre, B. Kaiser, W. Jaegermann and R. Schäfer, *Zeitschrift Für Physikalische Chemie - International Journal of Research in Physical Chemistry & Chemical Physics*, 2020, **234**, 847-865.
43. A. S. Crampton, M. D. Rotzer, C. J. Ridge, B. Yoon, F. F. Schweinberger, U. Landman and U. Heiz, *Surf Sci*, 2016, **652**, 7-19.
44. H. W. Wang and J. L. Lu, *Chinese J Chem*, 2020, **38**, 1422-1444.
45. M. A. Röttgen, S. Abbet, K. Judai, J. M. Antonietti, A. S. Wörz, M. Arenz, C. R. Henry and U. Heiz, *J Am Chem Soc*, 2007, **129**, 9635-9639.
46. T. Ishida, T. Murayama, A. Taketoshi and M. Haruta, *Chem Rev*, 2020, **120**, 464-525.
47. A. S. Crampton, M. D. Rotzer, C. J. Ridge, F. F. Schweinberger, U. Heiz, B. Yoon and U. Landman, *Nat Commun*, 2016, **7**.
48. G. R. Bamwenda, S. Tsubota, T. Nakamura and M. Haruta, *J Photoch Photobio A*, 1995, **89**, 177-189.
49. A. Mills, M. Bingham, C. O'Rourke and M. Bowker, *J Photoch Photobio A*, 2019, **373**, 122-130.
50. I. A. Ichou, M. Formenti and S. J. Teichner, *Stud. Surf. Sci. Catal.*, 1983, **17**, 63-75.



# Supporting Information for

## Size and Coverage Effects of Ni and Pt Co-catalysts in Methanol Photoreforming on TiO<sub>2</sub>(110)

Moritz Eder<sup>‡</sup>, Carla Courtois<sup>‡</sup>, Philip Petzoldt, Sonia Mackewicz, Martin Tschurl, and Ueli Heiz<sup>\*</sup>

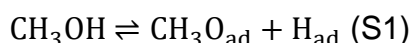
Chair of Physical Chemistry & Catalysis Research Center, Technical University of Munich, Lichtenbergstr. 4, 85748 Garching, Germany

<sup>‡</sup> The authors contributed equally.

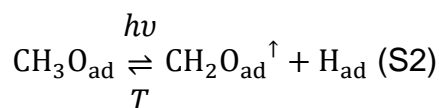
<sup>\*</sup>Corresponding Author: ulrich.heiz@mytum.de

### Mechanistic Details of Photocatalytic Methanol Conversion on Ni<sub>x</sub>/TiO<sub>2</sub>(110) and Pt<sub>x</sub>/TiO<sub>2</sub>(110)

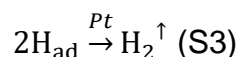
As the first step, methanol adsorbs onto the titania surface and partially dissociates, forming a methoxy and hydrogen surface species (Eq. S1):



Upon illumination, methoxy species at photoactive sites undergo  $\alpha$ -H bond cleavage, yielding formaldehyde and another surface hydrogen species. At room temperature, formaldehyde desorbs into the gas phase after a certain surface residence time, while hydrogen remains on the TiO<sub>2</sub>(110) surface (Eq. S2):[1,2]



Hydrogen cannot desorb from TiO<sub>2</sub>(110) at 300 K, i.e. a continued methanol photoconversion results in its accumulation on the surface. An increased hydrogen concentration will in turn shift the equilibrium of Eq. S2 to the left, finally leading to a total deactivation of the photocatalyst.[3] H<sub>ad</sub> diffuses considerably fast on the surface at room temperature in the presence of co-adsorbates such as water or alcohols.[4] In the presence of a metal cluster co-catalyst such as Pt, it will recombine with another H<sub>ad</sub> at the cluster and desorb as H<sub>2</sub> (Eq. S3).[5]



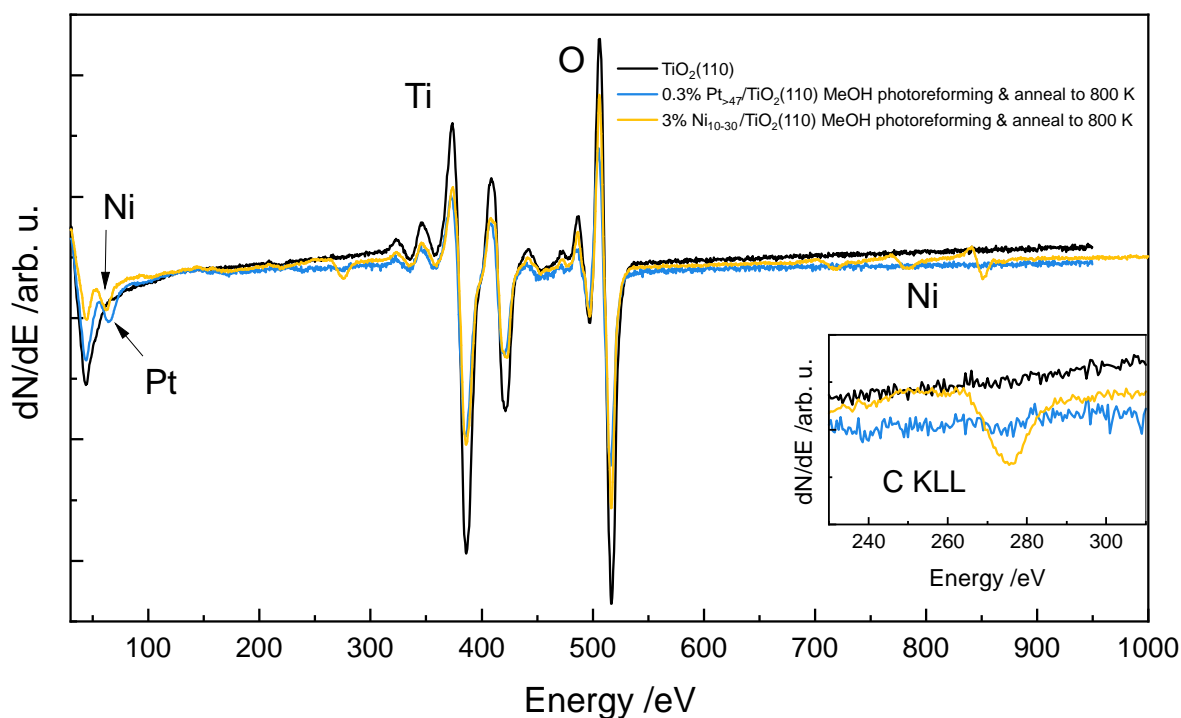


**Figure S1.** Auger spectra of bare, reduced  $\text{TiO}_2(110)$  (black), 0.3% ML  $\text{Pt}_{>47}/\text{TiO}_2(110)$  (blue) and 3% ML  $\text{Ni}_{>30}/\text{TiO}_2(110)$  (yellow) after methanol photoreforming experiments at 300 K and subsequent annealing to 800 K in order to desorb any surface species. The latter was measured above 380 K to show the persistence of the carbon KLL peak at 272 eV (inset on the bottom right). The peaks are assigned using Ref. [6].

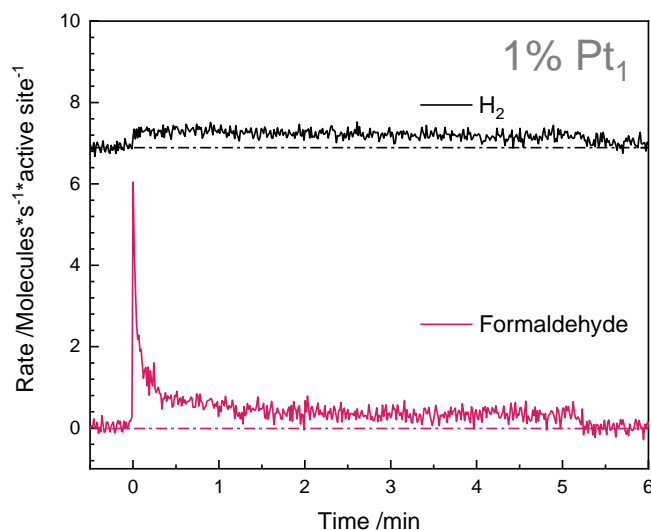


**Figure S2.** Product formation rates for hydrogen ( $m/z$  2, black), formaldehyde ( $m/z$  30, red) and methyl formate ( $m/z$  60, yellow) from photocatalytic methanol oxidation on 1% ML  $\text{Pt}_1/\text{TiO}_2(110)$  at 300 K in a methanol background pressure of  $5 \times 10^{-7}$  mbar. The signals are corrected for ionization cross section, QMS transmission, and their fragmentation pattern. The traces are offset for clarity.

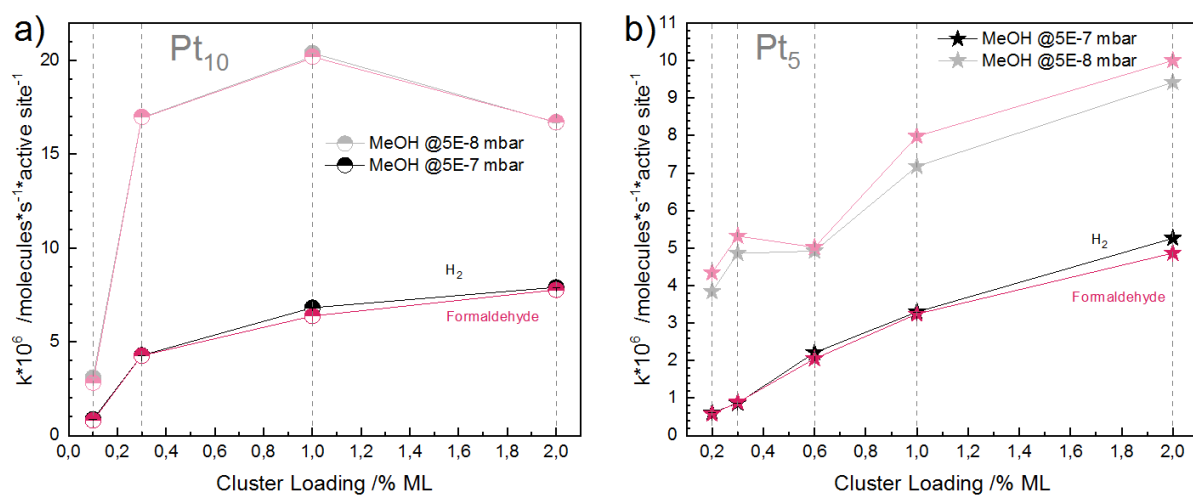


**Figure S3.** Pressure-normalized TOFs for hydrogen (black) and formaldehyde (red) from photocatalytic methanol reforming on a) Pt<sub>10</sub>/TiO<sub>2</sub>(110) and b) Pt<sub>5</sub>/TiO<sub>2</sub>(110) at 300 K as a function of cluster loading in a methanol background pressure of  $5 \times 10^{-7}$  mbar (light color) and  $5 \times 10^{-8}$  mbar (dark color) after one hour.

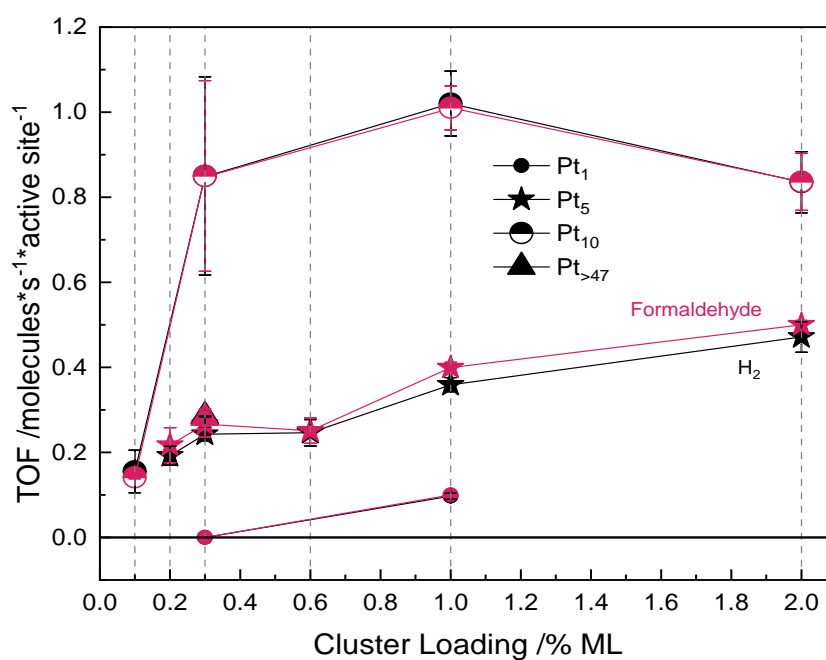
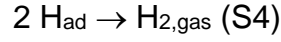


**Figure S4.** TOFs for hydrogen (black) and formaldehyde (red) from photocatalytic methanol oxidation on Pt<sub>x</sub>/TiO<sub>2</sub>(110) with x=1,5,10,>47 at 300 K as a function of cluster loading in a methanol background pressure of  $5 \times 10^{-8}$  mbar after one hour.

## H<sub>2</sub> Decay Analysis

The second-order fit function can be derived from the hydrogen recombination reaction:



Consequently, the kinetics of this reaction are give by:

$$-\frac{d[\text{H}_2]}{dt} = \frac{1}{2} \frac{d[\text{H}_{\text{ad}}]}{dt} = -k \cdot [\text{H}_{\text{ad}}]^2; \quad (\text{S5})$$

$$\frac{1}{[\text{H}_{\text{ad}}]^2} \cdot d[\text{H}_{\text{ad}}] = -2k dt; \quad (\text{S6})$$

$$-\frac{1}{[\text{H}_{\text{ad}}]} + C \Big|_{[\text{H}_{\text{ad}}]_0}^{[\text{H}_{\text{ad}}]_t} = -2kt + C' \Big|_0^t; \quad (\text{S7})$$

$$\frac{1}{[\text{H}_{\text{ad}}]_t} - \frac{1}{[\text{H}_{\text{ad}}]_0} = 2kt; \quad \frac{1}{[\text{H}_{\text{ad}}]_t} = \frac{1}{[\text{H}_{\text{ad}}]_0} + 2kt \quad (\text{S8})$$

$$\frac{1}{[\text{H}_{\text{ad}}]_t} = \frac{1+2k[\text{H}_{\text{ad}}]_0 t}{[\text{H}_{\text{ad}}]_0}; \quad [\text{H}_{\text{ad}}]_t = \frac{[\text{H}_{\text{ad}}]_0}{2k[\text{H}_{\text{ad}}]_0 t + 1} \quad (\text{S9})$$

with  $[\text{H}_2]$  being the concentration of molecular hydrogen in the gas phase (corresponding to its partial pressure),  $[\text{H}_{\text{ad}}]$  the concentration of surface hydroxyls right after the illumination is stopped ( $[\text{H}_{\text{ad}}]_0$  at  $t = 0$ ) or at a particular time  $t$  ( $[\text{H}_{\text{ad}}]_t$ ) and  $k$  the rate constant of the reaction.

As the reaction is evaluated over the evolution of the reaction product  $\text{H}_2$ , the concentration of surface hydroxyl is replaced by the concentration of hydrogen evolved at a certain time  $t$  ( $[\text{H}_2]_t$ ):

$$[\text{H}_2]_t = \frac{1}{2} ([\text{H}_{\text{ad}}]_0 - [\text{H}_{\text{ad}}]_t) = \frac{1}{2} \left( [\text{H}_{\text{ad}}]_0 - \frac{[\text{H}_{\text{ad}}]_0}{2k[\text{H}_{\text{ad}}]_0 t + 1} \right) \quad (\text{S 10})$$

$$\frac{d[\text{H}_2]_t}{dt} = \frac{d \left( [\text{H}_{\text{ad}}]_0 - \frac{[\text{H}_{\text{ad}}]_0}{2k[\text{H}_{\text{ad}}]_0 t + 1} \right)}{2dt} = \frac{k[\text{H}_{\text{ad}}]_0^2}{(2k[\text{H}_{\text{ad}}]_0 t + 1)^2} \quad (\text{S 11})$$

$$\frac{d[\text{H}_2]_t}{dt} = \frac{k[\text{H}_{\text{ad}}]_0^2}{(2k[\text{H}_{\text{ad}}]_0 t + 1)^2} \quad (\text{S 12})$$

$k$  and  $[\text{H}_{\text{ad}}]_0$  represent constant values and can be expressed by  $k'$ :

$$k' = k[\text{H}_{\text{ad}}]_0 \Rightarrow \frac{d[\text{H}_2]_t}{dt} = \frac{k'[\text{H}_{\text{ad}}]_0}{(2k't + 1)^2} \quad (\text{S 13})$$

Furthermore, the TOF equals the product of the rate constant and square of the hydroxyl concentration when the illumination is stopped:

$$t = 0 \Rightarrow \frac{d[\text{H}_2]_t}{dt} = k[\text{H}_{\text{ad}}]_0^2 = \text{TOF} \quad (\text{S 14})$$

In case of a pseudo first-order dependence with respect to the surface hydroxyl concentration, the commonly known exponential decay function for the rate of the reaction ( $r(t)$ , which may be obtained directly from the ion current) will result:

$$r(t) = TOF \times e^{-k \cdot t} \quad (\text{S } 15)$$

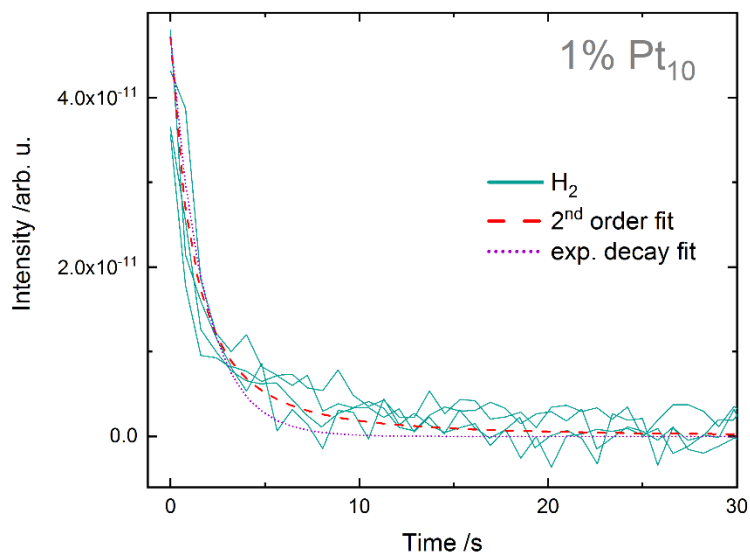


**Figure S5.** Visual comparison of the hydrogen trace (greenish), the 2<sup>nd</sup> order decay fit (eq. 13), and the exponential decay fit (eq. S15).

**Table S1.** Entities and numbers for calculating the rate constant  $k'$  as obtained from the second order decay fit. The calculation of the TOF is described in detail in previous work.[5] The TOF and  $k$  can be expressed in units of the measured ion current (A) or as the amount of adsorbed molecules (monolayer). The charge in the EI-QMS amounts to  $9.85 \times 10^{-10}$  A per monolayer as determined from methanol TPD experiments. Converting  $k$  from column 4 to column 5 therefore yields  $(\text{A} \times \text{s}^2)^{-1} \times \text{C}/\text{monolayer} = (\text{monolayer} \times \text{s})^{-1}$ , since  $\text{A} = \text{C} \times \text{s}^{-1}$ .

Sample	TOF /molecules $\text{s}^{-1}$ active site $^{-1}$	TOF $\times 10^{-11}$ (A)	$k \times 10^{11}$ ( $\text{A}^{-1} \text{s}^2$ )	$k$ (monolayer $^{-1} \text{s}^{-1}$ )	$[\text{H}_{\text{ad}}]_0 \times 10^{-12}$ (A s)	$[\text{H}]$ (monolayer $^{-1}$ )	$k'$ ( $\text{s}^{-1}$ )
0.6% ML Pt <sub>5</sub>	1.03	1.51	$3.2 \pm 0.2$	$4.7 \pm 0.3$	$6.9 \pm 0.2$	$0.47 \pm 0.01$	2.19
1% ML Pt <sub>5</sub>	1.62	2.39	$4.7 \pm 0.3$	$6.9 \pm 0.4$	$7.1 \pm 0.2$	$0.48 \pm 0.01$	3.35
2% ML Pt <sub>5</sub>	2.43	3.59	$14.0 \pm 0.8$	$21 \pm 1$	$5.1 \pm 0.1$	$0.34 \pm 0.01$	7.10
0.3% ML Pt <sub>10</sub>	2.13	3.15	$3.8 \pm 0.2$	$5.6 \pm 0.2$	$9.1 \pm 0.2$	$0.62 \pm 0.01$	3.45
1% ML Pt <sub>10</sub>	3.19	4.71	$31.1 \pm 0.2$	$45.9 \pm 3$	$3.9 \pm 0.1$	$0.26 \pm 0.01$	12.11
2% ML Pt <sub>10</sub>	3.89	5.74	$9.7 \pm 0.5$	$14.3 \pm 0.7$	$7.7 \pm 0.2$	$0.52 \pm 0.01$	7.47

**Table S2.** R-square values obtained with a 2<sup>nd</sup> order decay fit (eq. 4) and the exponential decay fit (eq. 5). Note that only one parameter was varied both for the 2<sup>nd</sup> order fit and for the exponential decay fit.

Sample	2 <sup>nd</sup> Order Fit R-square	Exponential Decay Fit R-square
0.6% ML Pt <sub>5</sub>	0.59	0.53
1% ML Pt <sub>5</sub>	0.63	0.54
2% ML Pt <sub>5</sub>	0.69	0.62
0.3% ML Pt <sub>10</sub>	0.63	0.53
1% ML Pt <sub>10</sub>	0.68	0.64
2% ML Pt <sub>10</sub>	0.63	0.53

## References

- [1] Shen, M.; Henderson, M. A. Identification of the Active Species in Photochemical Hole Scavenging Reactions of Methanol on TiO<sub>2</sub>. *J. Phys. Chem. Lett.* **2011**, *2* (21), 2707– 2710
- [2] Phillips, K. R.; Jensen, S. C.; Baron, M.; Li, S.-C.; Friend, C. M. Sequential Photo-Oxidation of Methanol to Methyl Formate on TiO<sub>2</sub>(110). *J. Am. Chem. Soc.* **2013**, *135* (2), 574– 577
- [3] Courtois, C.; Eder, M.; Kollmannsberger, S. L.; Tschurl, M.; Walenta, C. A.; Heiz, U. Origin of Poisoning in Methanol Photoreforming on TiO<sub>2</sub>(110): The Importance of Thermal Back-Reaction Steps in Photocatalysis. *ACS Catal.* **2020**, *10*, 7747– 7752
- [4] Zhang, Z.; Bondarchuk, O.; White, J. M.; Kay, B. D.; Dohnálek, Z. Imaging Adsorbate O–H Bond Cleavage: Methanol on TiO<sub>2</sub>(110). *J. Am. Chem. Soc.* **2006**, *128*, 4198 – 4199.
- [5] Walenta, C. A.; Kollmannsberger, S. L.; Courtois, C.; Pereira, R. N.; Stutzmann, M.; Tschurl, M.; Heiz, U. Why Co-Catalyst-Loaded Rutile Facilitates Photocatalytic Hydrogen Evolution. *Phys. Chem. Chem. Phys.* **2019**, *21* (3), 1491– 1496
- [6] Davis, L. E.; MacDonald, N. C.; Palmberg, P. W.; Riach, G. E.; Weber, R. E., *Handbook of Auger Electron Spectroscopy*, 2<sup>nd</sup> ed.; Physical Electronics Industries, Inc., 1976.